ALMA MATER STUDIORUM
UNIVERSITÀ DEGLI STUDI DI BOLOGNA

Dottorato di Ricerca in Ingegneria Elettronica, Telecomunicazioni e Tecnologie dell'Informazione

Dipartimento di Ingegneria dell'Energia Elettrica e dell'Informazione "Guglielmo Marconi" - DEI

Ciclo XXVIII

Settore concorsuale: 09/F2 - TELECOMUNICAZIONI

Settore scientifico disciplinare: ING-INF/03 - TELECOMUNICAZIONI

LOCATION AND MAP AWARENESS TECHNOLOGIES IN NEXT WIRELESS NETWORKS

Presentata da:
ANNA GUERRA

Coordinatore Dottorato:
Chiar.mo Prof. Ing.
ALESSANDRO
VANELLI-CORALLI

Relatore:
Chiar.mo Prof. Ing.
DAVIDE DARDARI

ESAME FINALE 2016

INDEX TERMS

Personal radar

Millimeter-wave technology

Massive Array

Localization and Mapping

RFID

Contents

Typeset using LaTeX.

List of Acronyms

5G fifth generation

AF amplify & forward

AOA angle-of-arrival

AOD angle-of-departure

AP access point

ASK amplitude shift keying

AWGN additive white Gaussian noise

BPE beam pointing error

BS base station

BSA beam solid area

CCF cross correlation function

CDF cumulative distribution function

CDMA code division multiple access

CIR channel impulse response

CRB Cramér-Rao bound

CRLB Cramér-Rao lower bound

CSI channel state information

CW continuous wave

D2D device-to-device

DF detect & forward

DOA direction-of-arrival

DS delay spread

EH energy harvesting

EIRP effective radiated isotropic power

EKF extended Kalman-Filter

FCC Federal Communications Commission

FCC Federal Communications Commission

FCC Federal Communications Commission

FIM Fisher information matrix

GDOP geometric dilution of precision

GPS Global Positioning System

HPBW half power beam width

i.i.d. independent and identically distributed

IMU inertial measurement unit

IR-UWB impulse radio-UWB

JF just forward

LEO localization error outage

LOS line-of-sight

MAC medium access control

MF matched filter

MIMO multiple-input multiple-output

ML maximum likelihood

mmW millimeter-wave

MPC multipath components

MSE mean square error

NCR normalized channel response

NLOS non-line-of-sight

OEB orientation error bound

PDP power delay profile

PEB position error bound

PN pseudo-noise

POC path overlap coefficient

PRMSE pointing root mean square error

PRP pulse repetition period

PSD power spectral density

RCS radar cross section

RF radiofrequency

RFID radio frequency identification

RMS root mean square

rms root mean square

RMSE root mean square error

RRC root raised cosine

RRCS root radar cross section

RSSI received signal strength indicator

RTLS real time locating systems

RTT round-trip time

RV random variable

SIW substrate integrated waveguide

SLAM simultaneous localization and mapping

SLL side lobe level

SNR signal-to-noise ratio

SOEB squared orientation error bound

SPEB squared position error bound

TA transmitarray

TDL tapped delay line

TDMA time division multiple access

TDOA time difference-of-arrival

TOA time-of-arrival

TOF time-of-flight

UHF ultra-high frequency

UWB ultra-wideband

VNA vector network analyzer

WiFi Wi-Fi

WSN Wireless Sensor Network

Executive Summary

In a future perspective, the need of mapping an unknown indoor environment, of localizing and retrieving information from objects with zero cost and effort will be satisfied by the adoption of next 5G technologies. Thanks to the mix of millimeter-wave (mmW) and massive arrays technologies, it will be possible to achieve a higher indoor localization accuracy without relying on a dedicated infrastructure for localization but exploiting that designed for communication purposes. Besides users localization and navigation objectives, mapping and thus, the capability of reconstructing indoor scenarios, will be an important field of research with the possibility of sharing environmental information via crowd-sourcing mechanisms between users. Finally, in the Internet of Things vision, it is expected that people, objects and devices will be interconnected to each other with the possibility of exchanging the acquired and estimated data including those regarding objects identification, positioning and mapping contents. To this end, the union of radio frequency identification (RFID), Wireless Sensor Network (WSN) and ultra-wideband (UWB) technologies has demonstrated to be a promising solution. Stimulated by this framework, this work describes different technological and signal processing approaches to ameliorate the localization capabilities and the user awareness about the environment. From one side, it has been focused on the study of the localization and mapping capabilities of multi-antenna systems based on 5G technologies considering different technological issues, as for example those related to the existing available massive arrays. From the other side, the investigation of the localization coverage of UWB-RFID systems relying on passive communication schemes has been undertaken by developing different techniques to improve the accuracy even in presence of non-line-of-sight (NLOS) conditions.

In particular, the main contributions of this dissertation are:

- Chapter 1: *Millimeter-wave Massive Arrays: Technological Potentials and Challenges*

  In Chapter 1 a description of massive antenna arrays working at mmW will be presented. In particular, the technological constraints encountered when operating in these range of frequencies will be highlighted as well as possible solutions to find a trade-off between array architecture complexity and well defined radiation characteristics. The effects of frequency selectivity and quantization beamforming weights will be analysed either from the antenna radiation characteristic perspective and from the map reconstruction accuracy point-of-view. Finally, a mmW measurement campaign conducted at CEA-Leti (Grenoble, France) will be described with the objective to characterize the potentialities of transmitarrays (TAs) when employed in a radar system. Part of the materials (text, tables and illustrations) of this chapter have been published in [J3], [C3], [C4], [C7] © IEEE.

- Chapter 2: *Personal Mobile Radars*

  In Chapter 2 the idea of personal radars will be presented and investigated. The main novelties of the mapping algorithm will be underlined in comparison with the traditional mapping techniques, for example those adopted in the simultaneous localization and mapping (SLAM) problem. Moreover, from a technological point-of-view two different kind of massive antenna arrays will be adopted for mapping purposes. From the results obtained in Chapter 2, an analysis on how radiation characteristics impact the mapping process will be undertaken. Finally, real data collected during mmW measurements campaign will be exploited as an input for the mapping algorithm, thus providing an experimental validation of the personal radar concept. Part of the materials (text, tables and illustrations) of this chapter have been published or submitted for publication in [J2], [J3], [C2], [C9], [C11] © IEEE.

- Chapter 3: *Single-Anchor Position and Orientation Bounds*

  Chapter 3 is focused on the analysis of the single access point (AP) position and orientation accuracy achievable when mmW massive antenna arrays are adopted both at AP and mobile side. First a general signal model valid for any antenna array geometry and configuration (e.g. timed, phased, and multiple-input multiple-output (MIMO) arrays) will be presented. Successively, the derivation of the Cramér-Rao lower bound (CRLB) for position and orientation estimation error will be undertaken considering multipath components (MPC), massive antenna array structure characteristics (e.g., quantization errors) and the synchronization error. Through a CRLB analysis, it will be shown that the perfect signal alignment by steering the beam is favourable for signal-to-noise ratio (SNR) enhancement towards a certain direction but it leads to a reduced diversity of available measurements that might drastically degrade the localization performance depending on the signal bandwidth. As a consequence, the performance depends on a compromise between diversity, SNR enhancement due to beamforming, and spatial filtering of multipath. Part of the materials (text, tables and illustrations) of this chapter have been published or submitted for publication in [J1], [C8] © IEEE.

- Chapter 4: *RFID Relaying and Energy Sprinklers Techniques*

  In Chapter 4, two techniques to enhance the indoor localization coverage of RFID systems will be analysed. Firstly, a multistatic RFID system employing energy sprinklers will be introduced with the purpose of exploiting low-cost passive tags. Secondly, the idea of adopting UWB non-regenerative relays for network localization will be described. Both techniques are demonstrated to provide a localization performance improvement and coverage extension in indoor environment even when NLOS propagation conditions are present by using extremely low-cost devices. Part of the materials (text, tables and illustrations) of this chapter have been published or submitted for publication in [J4], [C10], [C13] © IEEE.

Author Contributions

The thesis activity has been conducted at the Department of Electronical, Electronic, and Information Engineering “Guglielmo Marconi” at University of Bologna (UNIBO) in Italy for about three years interleaved with a visiting period of seven months at the Antenna and Propagation Laboratory of the Department of System Integration at CEA-Leti in Grenoble, France.

During the work at University of Bologna, two different activities have been conducted. Firstly, a study oriented to the localization coverage enhancement in UWB-RFID systems scenario has been undertaken. This analysis has been carried in the context of the European FP7 Project SELECT and the Italian Ministerial PRIN project GRETA. Chapter 4 shows the results of this investigation. The work presented in Chapter 4 is the result of the collaboration with the partners of the two projects consortium and mainly with Davide Dardari, Nicoló Decarli and Francesco Guidi.

A second activity has been the development of the personal radar idea conceived at UNIBO for mapping applications. Massive arrays and mmW technologies have been studied as a mix to be adopted in a radar system thanks to the higher ranging and angular definition achievable. This work has been carried on in collaboration with Davide Dardari and Francesco Guidi.

Following this research subject, the collaboration at CEA-Leti has permitted to deeply analyse the most suitable existing antenna array technologies for personal radar application as well as to conduct a measurement campaign at mmW frequencies to validate the theoretical and simulation results. During the visiting period, the author has collaborated with the Antenna and Propagation Laboratory of the Department of System Integration and, in particular, with Raffaele D'Errico and Antonio Clemente.

The research activity led to the publication of 2 journal papers and 2 under submission, and 12 conference papers. The candidate was the recipient of the Best Student Paper Award at the 2014 IEEE International Conference on Ultra-Wideband in Paris (France).

Introduction

Thesis motivations

In the new social era, characterized by the Internet of Things paradigm and by the widespread use of fifth generation (5G) smartphones and tablets, it is expected that mobile users will be able to communicate at an unprecedented speed, localize themselves with sub-centimeter precision and map unknown indoor environments while sharing information with other users [1].

In this future scenario, see for example Fig. 1, localization and communication will be intrinsically interconnected to each other. In fact, the possibility to adopt massive antenna array at APs will tremendously increase the spectral and energy efficiency but, besides communications, the AP could be used as a single-anchor node, i.e. node whose position is *a-priori* known, in a radio-localization perspective permitting the mobile users to be aware of their own positions even in indoor environments where the Global Positioning System (GPS) signals could be weak or totally absent. In Fig. 1, a mobile user (MU) is moving in an indoor environment and exploits the nearest AP for both communication and localization purposes. In this framework, localization knowledge is an essential information to further improve the communication capability [2]: in fact, APs, once aware of the intended users positions, could orient their power flux towards them increasing the SNR and reducing the level of interference and jammings. On the other side, while in traditional scenarios a dedicated infrastructure consisting of multiple anchor nodes with a single antenna is necessary for localization purposes to allow classic triangulation/multilateration techniques, the ability

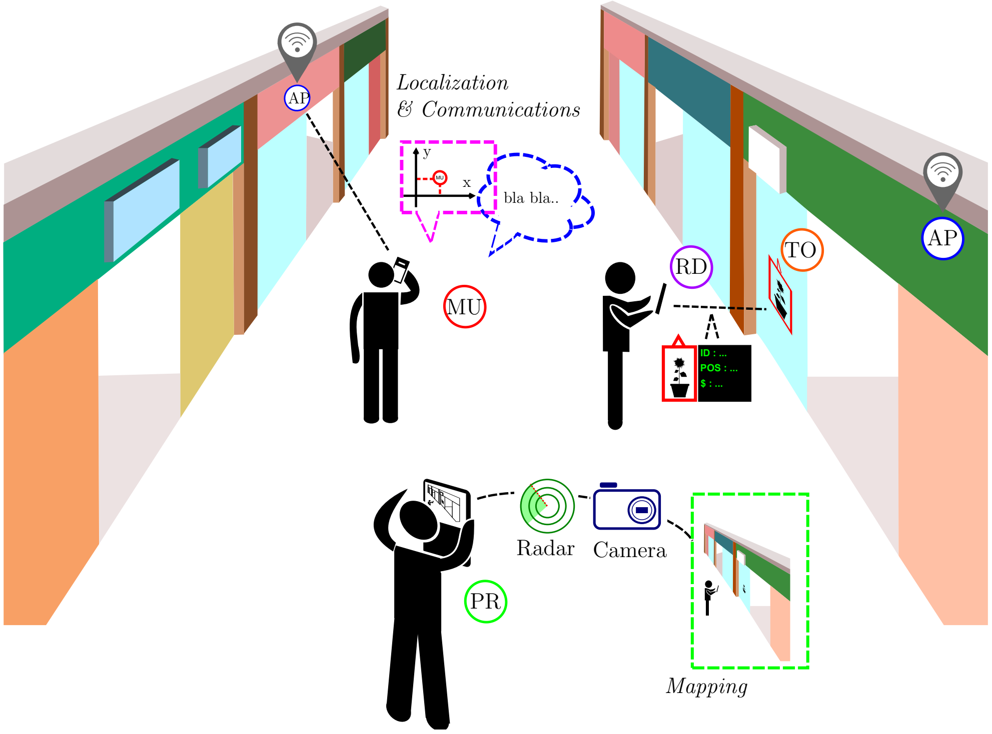

Figure 1: Examples of smartphone-centric systems.

to centralise in a single AP communication and localization capabilities will drastically decrease the overall system complexity and cost. In addition, not only APs but also smartphones could be embedded with massive antenna arrays, provided that high frequencies are considered, allowing an even more accurate localization capability [3, 4].
Starting from these considerations, the first research questions that this thesis aims at answering are

1) What are the fundamental limits in localization (positioning and orientation) error when employing a single AP as anchor node and a large (massive) number of antennas are adopted at both the AP and mobile?

2) Which massive array technologies can be employed for localization applications and how the massive antenna array technology constraints impact the localization and mapping performance?

Going a step ahead, once portable devices are embedded with massive

arrays, beamforming/beamsteering operations could be performed not only to strengthen the communication/localization capabilities but also to reinforce the user awareness of the environment. To take a possible application example, personal devices could help their owners to explore and navigate unknown environments assuming more and more the role of *personal radars.* Personal radars are based on the possibility to integrate a large number of antennas in the user device and to exploit the beamforming operation to scan the environment for mapping purposes [5]. In Fig. 1, personal radars are indicated with the acronym PR. The depth information retrieved during the scanning process can be finally fused with the embedded camera output to have a more precise environmental knowledge and to allow secure independent user navigation. The latter does not only mean following a specific path, but it includes also problem solving capabilities: for instance, the ability to select the safest route, avoid obstacles and recognize landmarks properties in unfamiliar environments. All these features imply a cognitive ability related to vision perception aimed at understanding the surrounding world [5, 6, 7]. The pervasive availability of personal radar capabilities on smartphones will enables several applications as for example high-definition and zero-effort indoor building mapping, blind people aid or the pictorial 3D environmental mapping where the third dimension results by the integration of the angle/range information collected by the personal radar with the 2D picture coming from the conventional embedded camera.
Stimulated by this perspective, the second research questions are

3) What is a *personal radar* and what are the main technological requirements that a *personal radar* has to accomplish?

4) What are the main constraints to be considered when a portable device (e.g., a smartphone or a tablet) becomes a *personal radar* from both a signal processing and technological point-of-view?

5) What is the mapping reconstruction level achievable as a function of the technology chosen?

Another essential requirement that we expect in future portable devices is the capability to interact and recognize objects deployed in the surrounding environment. In this direction, the integration of RFID, real time locating systems (RTLS) and WSN will allow the possibility to detect, identify and localize tagged objects and also to retrieve other type of information, as for example those sensed by tags integrated sensors [8, 9, 10]. In Fig. 1, the person indicated with the acronym RD (i.e. reader) uses his/her portable device to interrogate a tagged object (TO).

Tags are required to be cheap, simple, eco-friendly and able to sense physical quantities. To meet these specifications, passive tags, i.e. tags that are not equipped with batteries and exploiting energy harvesting techniques to power up themselves, are of particular interest. Nevertheless passive tags do not present any active transmitting section and, consequently, they rely on backscattering communication techniques to transmit their information (position, identity or sensing information) [11, 12]. As a result of the two-hop nature of backscatter communication, the SNR, and thus the ability to detect and localize tags, drastically decrease. This shortcoming together with the localization ambiguities arising when NLOS situations emerged, give rise to the last two questions

6) In a RFID scenario, how could it be possible to extend the localization coverage to counteract the poor link-budget experienced when passive tags are adopted?

7) Which solutions could be envisioned to overcome the indoor harsh propagation conditions, e.g. the obstacles blockage, without increasing the number of anchor nodes in the localization network?

To deal with all these issues, new solutions at technological, signal processing as well as network levels have to be proposed. In this direction, some of the main topics that will be further detailed in this thesis chapters will be introduced in the following sections.

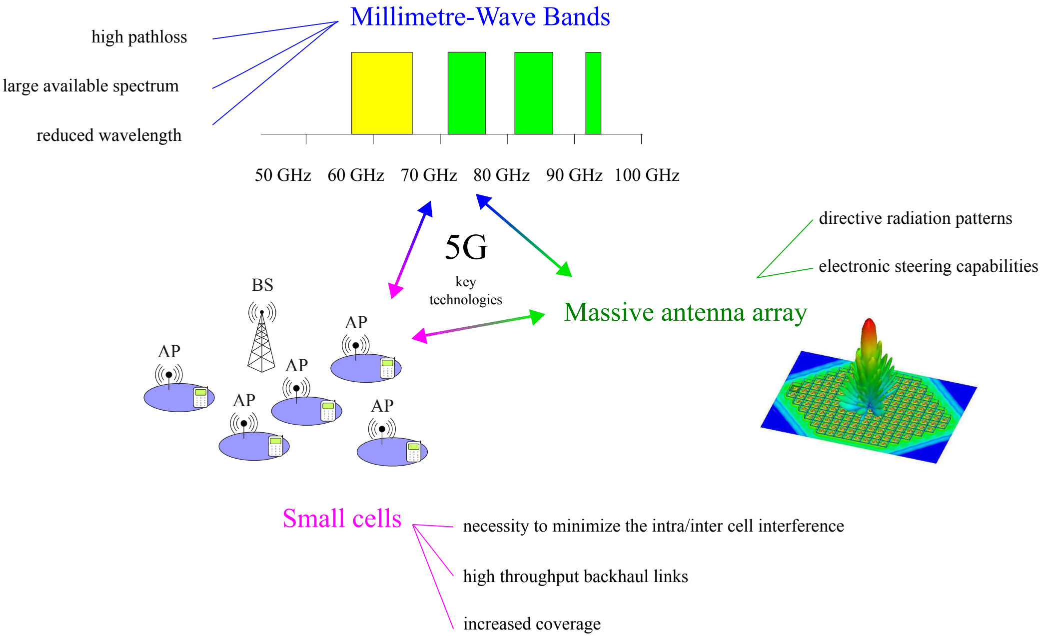

Figure 2: 5G enabling technologies.

Massive arrays and millimeter-wave technology

Millimetre-wave technology, massive antenna array and heterogeneous densification approaches have been identified as possible key players for next generation (5G) mobile wireless communications [13]. Specifically, great advantages can be experienced from the mix of these technologies, see Fig. 2: indeed, thanks to the reduced wavelength, massive antenna array could be packed in small-size space while the available bandwidth, the realized narrow beam and beamsteering capabilities enables a higher data rate and improved mapping performance. A densification approach based on smaller sized cells will also help to counteract the poor link budget and the high level of attenuation from oxygen absorption typical of mmW propagation.

Millimeter-wave frequencies occupy the spectrum from 30 to 300 GHz and open up a clean unlicensed bandwidth (up to 7 GHz), as for example that around 60 GHz [14, 15, 16]. Another main strength is the small wavelength that leads to very compact antenna arrays. For example, considering a central frequency of 60 GHz, the distance between two antenna elements will be 2.5 mm that makes possible the integration of hundreds of antennas in small areas. Besides these benefits, the main drawback of this technology is the high path-loss due to the reduced wavelength and the high atmosphere absorption. This is the reason why high antenna gains and small/femtocells are needed to counteract the link budget limitation.

As already introduced, high antenna directivity and gain, narrower beams and beamforming capabilities are characteristic elements of massive antenna arrays. The term ‘massive array’ will be used in this thesis to indicate an array with at least 100 antenna elements. While at microwave frequencies the antenna array technology is quite mature, even though device dimensions limits the maximum integrable number of antenna elements, at mmW severe technological constraints are still present and must be taken into account when designing positioning systems. Nevertheless, significant progresses have been recently done. For example, efforts for integrating large arrays on smartphones [17], for realizing massive arrays adopting digital phase shifters and operating at 60 GHz and 10 GHz [18, 19, 20] have been made, as well as preliminary performance studies on their adoption in new applications [5, 21].

In the following a distinction between different types of massive arrays will be drawn based on the feeding technique used. In particular, we will refer to corporate arrays when the antenna elements are fed with transmission lines and with TAs when a focal source illuminates the array (spatial feeding technique). The main advantage of corporate arrays is the precise radiation pattern control they could reach even if transmission lines introduce losses and when operating at mmW are difficult to realize. Moreover, in the family of corporate arrays we can distinguish between phased and timed arrays depending on the type of beamsteering architecture used. Contrarily, the spatial feeding technique adopted in TAs permits to illuminate a large number of antenna elements without increasing the array complexity and cost. However, the three-dimensional structure of the resulting array implies a less integrability in small spaces, e.g. in portable devices [22].

The benefits of all these array structures stand in the possibility of adaptively tuning the set of beamforming weights to realize an intended radiation

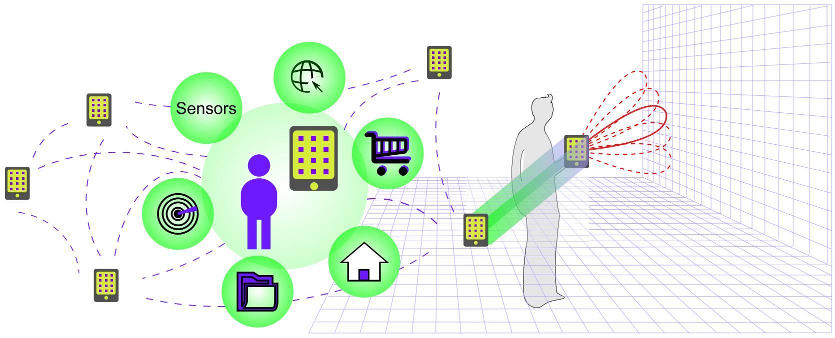

Figure 3: Personal radar mapping application.

pattern. More precisely, if the objective is to point the main beam towards a desired user or to scan an environment emulating the angular definition of a laser in personal radar applications, the beamsteering process will permit to electronically reconfigure the array weights to realize a pencil beam towards the useful direction and to change it in real-time. Finally, thanks to the possibility to accommodate massive antenna arrays in small spaces, both femtocells APs and user terminals could exploit the available beamforming antenna capabilities and the potential rich set of measurements to achieve a high localization accuracy using only 1-AP, as already introduced.

Localization and mapping applications

Motivated by this framework, one of the objective of this Ph.D. thesis is to investigate how multi-antenna arrays, enabling higher gains and real-time beamforming capabilities, together with the advantages of mmW technologies can be employed in a portable device providing an improved accuracy in mapping and positioning applications. In this context, two scenarios can be envisioned:

- The first is related to the *personal radar concept* and is *mapping-oriented*, see for example Fig. 3. As already mentioned, the personal radar might be embedded in new 5G smartphones or tablets and consists of a massive antenna array operating at mmW. Different new functionalities could be enabled by this system such as a real-time 3D map reconstruction or assisted navigation inside buildings. Traditionally, in SLAM applications, robots are equipped with a laser-based radar that mechanically steers its beam to scan the environment. Contrarily, when adopting a radar working with a mmW massive array, the steering process can be performed electronically and without any human intervention making the device simpler and more accessible to anyone. As the mapping algorithm is regarding, a non-coherent processing scheme will be adopted where all the available raw energy measurements coming from the massive array are exploited. From a signal processing perspective, an analysis of the steering and ranging capabilities of the proposed mmW personal radar concept as a function of the signal bandwidth and the number of antennas composing the array will be performed.

- The second application that will be analysed is *localization-oriented*. In this framework, a femtocell AP plays the role of the reference node, i.e. of the anchor node, whose main aim is to infer the user mobile position and orientation. A CRLB analysis on position and orientation estimation errors will be undertaken to better characterize the ultimate localization performance when different antenna array systems are adopted at the mobile side.

Finally, to better investigate the technological aspects related to mmW massive arrays, part of the PhD has been spent at the Antenna and Propagation Laboratory of the Department of System Integration at CEA-Leti in Grenoble, France. During this visiting period, an analysis regarding the most suitable antenna array technologies for personal radar application as well as a measurement campaign at mmW frequencies have been carried on [6, 7].

RFID systems and UWB technology

One step ahead, the ability to interact with objects present in the surrounding, to identify and localize them with sub-meter precision becomes more and more important. In this direction the adoption of the UWB technology and RFID systems plays a crucial role. Specifically, the adoption of the two-hop backscattering communication technique permits to employ low-cost passive tags attached to objects from which identification and positioning information could be retrieved. In this context, part of the Ph.D. research activities has been devoted to the enhancement of the localization coverage of monostatic and multistatic UWB RFID systems. These activities have been conducted in the framework of the European FP7 project SELECT and the Italian ministerial project GRETA [23, 24].

A traditional RFID system consists of readers and tags applied to objects. The reader interrogates the tags via a wireless link to obtain the data stored on them. Tags equipped with a complete radiofrequency (RF) transmitter are denoted as *active*. The cheapest RFID tags with the largest commercial potential are *passive* or *semi-passive*, where the energy necessary for tag-reader communication is harvested from the reader's signal or the surrounding environment. As an alternative to the monostatic configuration (i.e. that implying the co-location of the transmitter and the receiver in the same device), the possibility to isolate the transmitting section in simple devices and to keep all the complexity in few receiver nodes could provide some benefits in terms of tags detection. Advantages of bistatic and multistatic configurations have been recently highlighted in [25]. In Fig. 4, the different RFID configurations just introduced are depicted.

Besides the possibility of identifying tags, future advanced RFID systems are expected to provide high-definition tags localization combining the capability of RTLS and WSN that today are provided by different technologies [26]. As a consequence, accurate real-time localization at sub-meter level, high security, large number of tags management, in addition to extremely low power consumption, small size and low cost, will be new important requirements.

Unfortunately, most of these requirements cannot be completely fulfilled by the current first and second generation RFID or WSN technologies such as those based on ZigBee standard [27]. In fact, RFID systems using standard continuous wave (CW)-oriented communication in the ultra-high frequency (UHF) band have an insufficient range resolution to achieve accurate localiza-

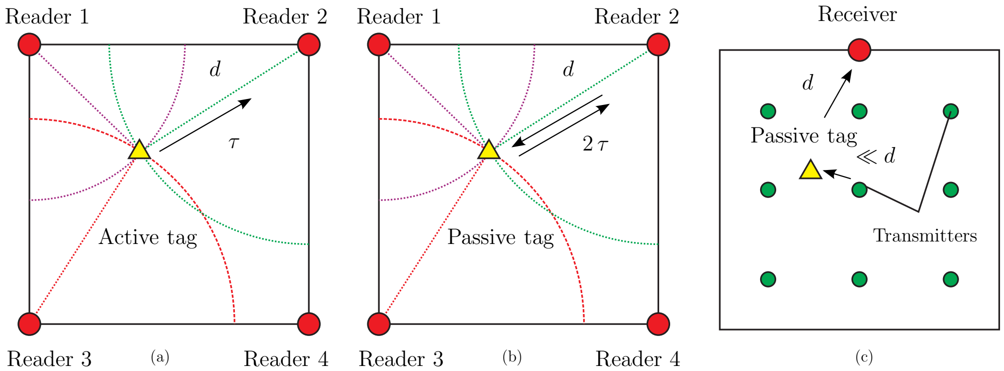

Figure 4: Different RFID scenario implying a monostatic configuration with active tags (a) and with passive or semi-passive tags (b), and a multistatic configuration with passive tags (c).

tion, are affected by multipath signal cancellation (due to the extreme narrow bandwidth signal), are very sensitive to narrowband interference and multi-user interference, and have an intrinsic low security [8]. A promising wireless technique for future identification and localization systems is the UWB technology characterized, in its impulse radio-UWB (IR-UWB) implementation, by the transmission of sub-nanosecond duration pulses [28, 12, 29, 30]. The employment of wideband signals enables the resolution of multipath, and extraordinary localization precision based on time-of-arrival (TOA) estimation signals. In addition, UWB allows for low power consumption at the transmitter side, extremely accurate ranging and positioning capability at sub-meter level, robustness to multipath, low detection probability, efficient multiple channel access and interference mitigation thus leading to potentially large number of devices operating and co-existing in small areas [31].

As anticipated, passive tags solutions are of particular interest thanks to their potential lower cost and power consumption. Different tags architectures will be presented in Chapter 4 to meet the following requirements:

- localizability with sub-meter precision even in indoor scenarios or in the presence of obstacles;
- small-size (with an area in the order of a few square centimeters) and lightness (i.e, without cumbersome batteries);

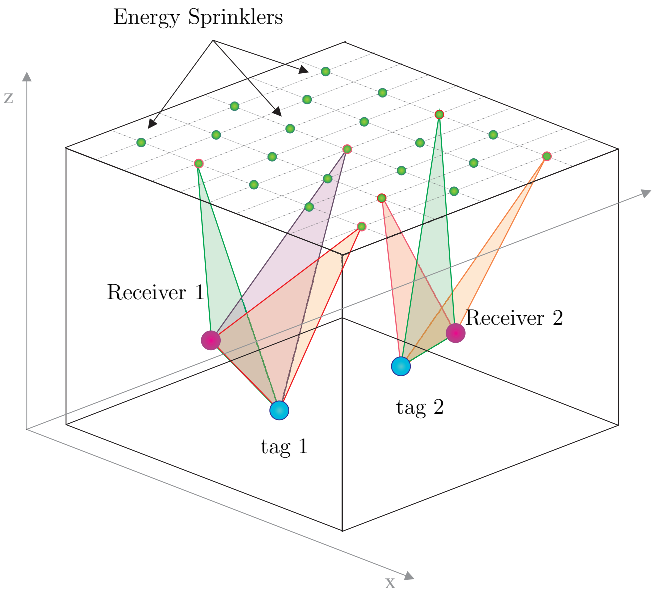

Figure 5: UWB-RFID scenario adopting energy sprinklers.

- energy-autonomy;
- eco-compatibility (i.e., made with recyclable materials as paper);
- easy integrability in goods, clothes and packages;
- low-cost to permit the employment of several tags in the environment;
- capability of sensing physical quantities of the environment.

To accomplish the first three points environmental energy gathering techniques, together with passive transmission techniques based on backscattering modulation have to been adopted. The idea of passive tags based on UWB backscatter signaling was introduced in [12] and further investigated in [11], where tag architectures as well as backscatter signaling schemes robust to the presence of clutter (i.e., reflections coming from surrounding objects) are presented. The backscatter modulator performs the signal modulation of the electromagnetic waves generated by the transmitting section of the reader just adopting an UWB switch alterning between two different load conditions (open and short circuits). Nevertheless, the two-hop link charac-

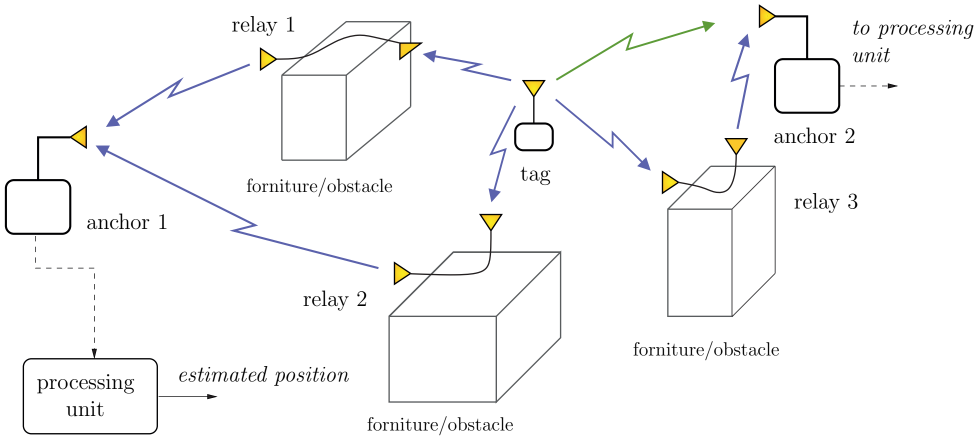

Figure 6: Example of localization system with non-regenerative relays.

terizing passive communications drastically decrease the SNR and thus, the reading range.

Energy sprinklers and relaying techniques

To overcome power transfer and low SNR limitations multistatic, RFID configurations will be presented in Chapter 4 where several low complexity transmitters, called *energy sprinklers* or *energy showers*, spread UHF/UWB signals to power up and interrogate tags around them [32]. Specifically, energy sprinklers are simple active transmitters which operate either in UHF and UWB bands: a UWB interrogation signal, fundamental to guarantee accurate ranging, is emitted in parallel with a UHF signal used for energy harvesting and for synchronizing the whole network [33]. The backscattered response is then collected by one or more receivers located in different positions. With the proposed configuration, it is expected that even tags placed far from the receiver can be detected and localized with an improved localization accuracy thanks to a reduced transmitter-tag distance. In Fig. 5, a potential RFID scenario implying energy sprinklers is presented.

Nevertheless when operating in indoor scenarios, NLOS situations can arise blocking the signals between readers and tags. To overcome such an issue, the adoption of relaying techniques is presented in the final part of Chapter 4. Relays are not new in communication-oriented scenarios but they could play an important role as repeaters of localization information [34]. To keep the system cost affordable, an analysis of non-regenerative relays for localization coverage will be undertaken. Differently from their regenerative counterpart, non-regenerative relays repeat the received signal as it is, indeed neither modulator nor demodulator sections are present in their structure. Non-regenerative relays can be active, namely amplify & forward (AF), or passive, namely just forward (JF). Figure 6 reports a RFID system exploiting the benefits of relaying techniques to overcome NLOS situations.

Chapter 1

Millimeter-wave Massive Arrays: Technological Potentials and Challenges

This chapter aims at introducing some massive arrays architectures considering the technological constraints present when operating at mmW frequencies. The trade-off between the intended radiation pattern to realize and the pursuit of simple and low-complex array architecture will be theoretically analysed in terms of beampointing error and beamwidth spread. Moreover, the results of a mmW measurement campaign using existing massive arrays as an essential part of a radar system will be presented.

1.1 Massive antenna array technology

In this section some massive antenna array structures will be described. Specifically, a distinction between massive arrays will be made based on the feeding techniques used. As already introduced, we will discern between corporate arrays relying on transmission lines, and spatial arrays in which the array illumination is provided by a focal source. The solution of adopting transmission lines will cause dissipation losses and a higher cost and complexity, but it guarantees at the same time a precise control on amplitude and

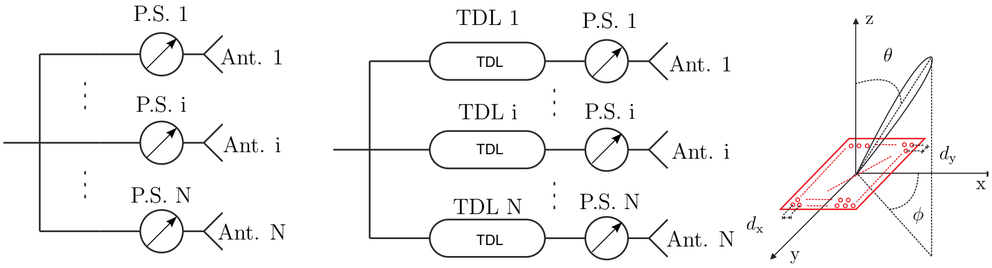

(a) (b) (c)

Figure 1.1: Corporate arrays architecture: phased arrays (a), timed arrays (b), planar arrays (c).

phase illumination allowing an accurate radiation pattern definition. Nevertheless when operating at mmW and when a large number of antennas are adopted, spatial-fed arrays could be an alternative solution. The adoption of this kind of arrays leads to a less pattern control and to spill over losses but it allows a simpler illumination strategy for large arrays together with a simpler structure and lower cost. In the following we will analyse timed and phased arrays from the first family and TAs as an example of spatial arrays.

1.1.1 Timed and phased array

Timed and phased arrays are based on the idea of assigning beamforming weights at each antenna branch to shape the radiation pattern in order to have the main beam pointing in a specific direction in space. From a signals point-of-view, this translates in a transmitted signal alignment performed by compensating the phase shifts and the time delays related to the antennas spatial distribution.

In narrowband system this beamforming/beamsteering operation could be performed using only phase shifters and the corresponding array structure is called *phased array*, see Fig. 1.1-left. Contrarily when wideband signals are adopted, it is no longer sufficient to use only phase shifters but tapped delay lines (TDLs) become necessary to compensate array inter-antenna delays. In such situation the array structure takes the name of *timed array*, see Fig. 1.1-center. At mmW, the fractional bandwidth, i.e. the ratio between the bandwidth and the central frequency W/f_c, is small (e.g, when $W =$

1 GHz and $f_\mathrm{c} = 60$ GHz even if the bandwidth could be considered wide, the fractional bandwidth is $\approx 0.017 \ll 1$ due to the high frequency used). As a consequence a phased array structure could be adopted instead of its timed counterpart reducing array cost and complexity. Nevertheless in the following sections the frequency effect on the beam pointing error and beamwidth spread is analysed.

Consider the scheme reported in Fig. 1.1-right, where $N_\mathrm{array} = MN$ antenna elements are placed in a rectangular area of dimension $L_\mathrm{x} \times L_\mathrm{y}$, with $L_\mathrm{x} = Md_\mathrm{x}$ and $L_\mathrm{y} = Nd_\mathrm{y}$. The elements are spaced apart of d_x (d_y) in the x (y) dimension. According to [35], and considering a uniform array, the AF at frequency f is defined as[1]

$$\mathrm{AF}(\Theta, f) = \sum_{m=1}^{M} \sum_{n=1}^{N} e^{j[(m-1)\Psi_\mathrm{x} + (n-1)\Psi_\mathrm{y}]} \tag{1.1}$$

with

$$\begin{aligned} \Psi_\mathrm{x} &= kd_\mathrm{x} \sin(\theta)\cos(\phi) + \beta_\mathrm{x} \\ \Psi_\mathrm{y} &= kd_\mathrm{y} \sin(\theta)\sin(\phi) + \beta_\mathrm{y} \end{aligned} \tag{1.2}$$

with $\Theta = (\theta, \phi)$ being the considered direction identified by the elevation and the azimuthal angles, θ and ϕ, respectively, and $k = 2\pi f/c$ the wavenumber, with c indicating the speed of light. To steer the main lobe towards a specific direction Θ_0, parameters β_x and β_y have to be set to

$$\begin{aligned} \beta_x &= -k_0 d_x \sin(\theta_0)\cos(\phi_0) \\ \beta_y &= -k_0 d_y \sin(\theta_0)\sin(\phi_0) \end{aligned} \tag{1.3}$$

with $k_0 = 2\pi f_0/c$, and f_0 being the reference frequency for which the steering parameters are designed. In the steering direction, for $f = f_0$ and in the absence of array non-idealities, it is $\mathrm{AF}(\Theta_0, f_0) = N_\mathrm{array}$.

The complex beam-steering weights determining the beam shape and

---

[1] For simplicity and without loss of generality, isotropic array elements are considered.

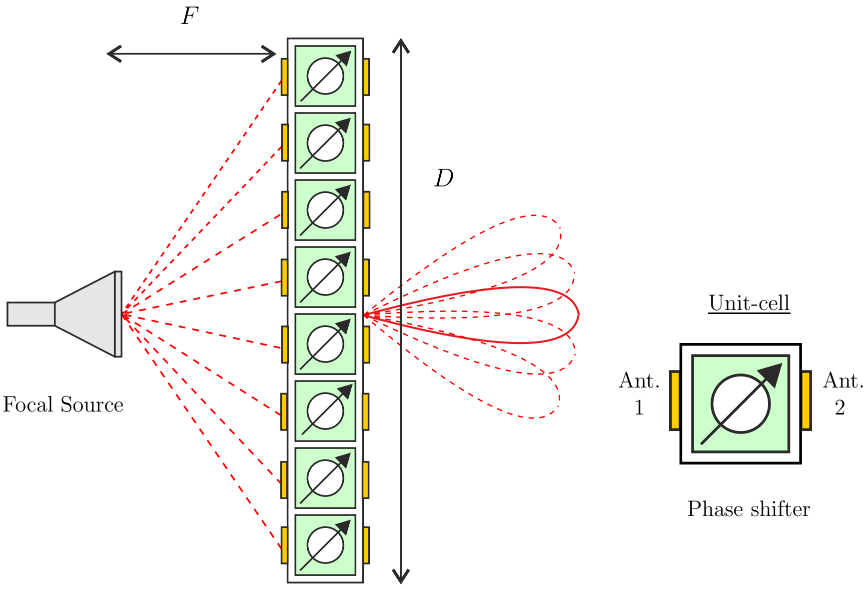

Figure 1.2: Transmitarray and unit-cell structure.

pointing direction can be expressed as

$$\omega_{mn} = e^{j\varphi_{mn}} = e^{j[(m-1)\beta_{\mathrm{x}}+(n-1)\beta_{\mathrm{y}}]} \tag{1.4}$$

where φ_{mn} is the weight phase, and β_{x} and β_{y} are defined in (1.3).

1.1.2 Transmitarray

Among the current different antenna arrays technologies, TAs could be a feasible solution to be adopted for future radar applications. A pictorial depiction of the TA is reported in Fig. 1.2. TAs consist of a focal source illuminating a planar array whose building blocks are the unit-cells. As reported in Fig. 1.2, each unit-cell consists of two antennas (indicated as Ant. 1 and 2) connected by a phase shifter. By tuning the transmission phase of the array elements, it is possible to obtain a specific phase distribution across the TA aperture and thus, to perform real-time beamsteering or beamforming by focusing, collimating, or shaping the incident power on the array in any direction in the free space. The TA is able to operate both in transmission and receive mode.

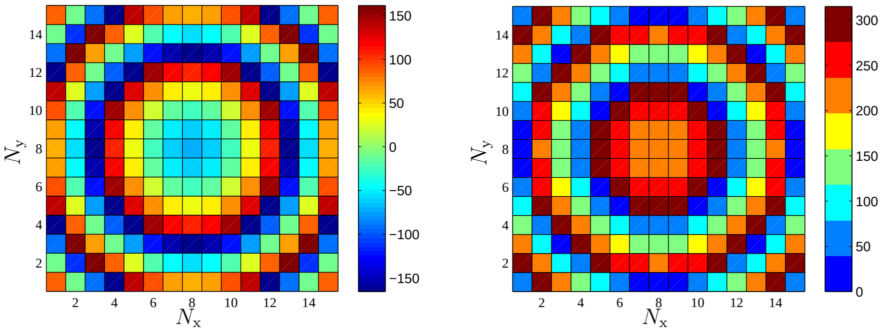

(a) Perfect (b) 3 bits

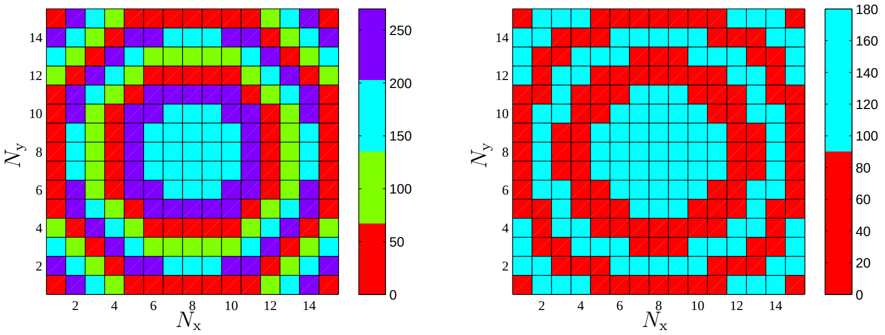

(c) 2 bits (d) 1 bit

Figure 1.3: Phase distribution in a 20 × 20 TA for different bit quantization values.

Thanks to their spatial feeding technique, TAs are extremely competitive compared to traditional phased arrays in terms of cost, complexity and power consumption. Unlike reflectarray antennas [36], TAs are free from focal source masking effects. Theoretical and experimental studies have been conducted to characterize and fully describe TAs [18, 37, 38]. Moreover, several electronically reconfigurable unit-cells and TAs have been proposed from the C- to the Ka-band using varactors diodes [39], phase shifters [40], PIN diodes [20, 41], or microelectromechanical system devices (MEMS) [42].

The TA radiation properties (i.e. radiation pattern as a function of the steering angle and frequency) have been extracted using an *ad-hoc* simulator experimentally validated in previous works at X-, Ka-, and V-band [18, 37,

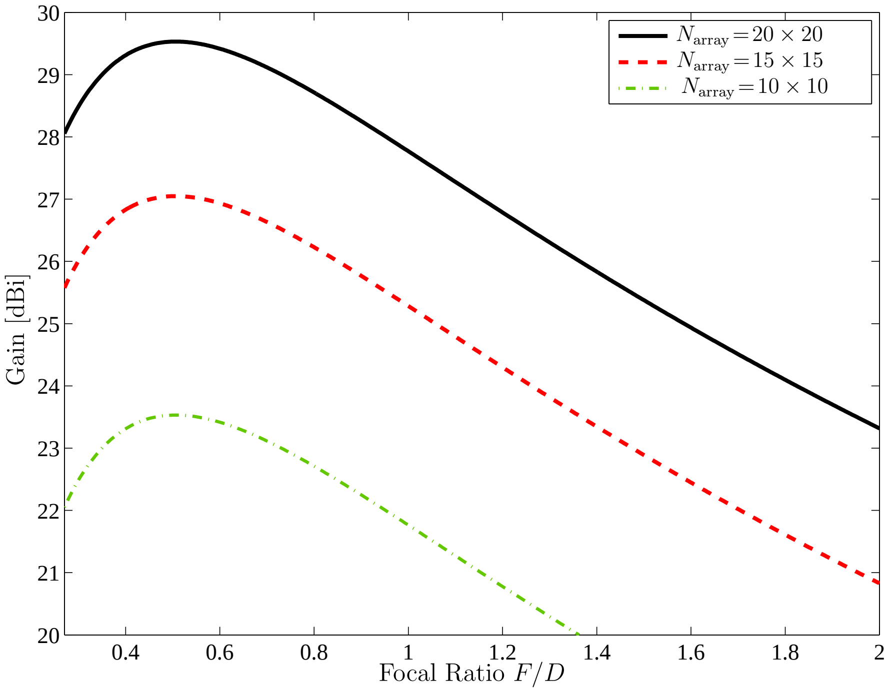

Figure 1.4: Theoretical gain of $N_{\text{array}} = 10 \times 10$, 15×15 and 20×20 TA as a function of the focal ratio at $f_0 = 60\,\text{GHz}$.

20, 38][2].

An ideal TA configuration is here considered at $f_0 = 60\,\text{GHz}$ with lossless and matched elements (i.e. the efficiency of the focal source η_{FS} and that of the unit-cells η_{IL} are both equal to 100%) in order to evaluate the best performance of such TAs for localization and mapping purposes.

The focal source has been modelled with a generic $\cos^n(\theta)$ radiation pattern with n being the focal source order [19]. Note that the directivity varies as a function of n: the transition from $n = 1$ to $n = 10$ results in a directivity increase from $D_{\text{FS}} = 6$ dBi to $D_{\text{FS}} = 13.4$ dBi. In the following, the focal source order is set to $n = 4$ representative of a standard gain horn with a directivity of 10 dBi, that is a typical choice for TAs [18, 37, 20, 38].

The linearly polarized unit-cell is modelled as a uniform aperture as described in [19]. Ideally, a continuous phase shift between 0° and 360° is nec-

---

[2] The possibility to use the TAs simulator and the 20×20 TAs for measurements is a courtesy of CEA LETI

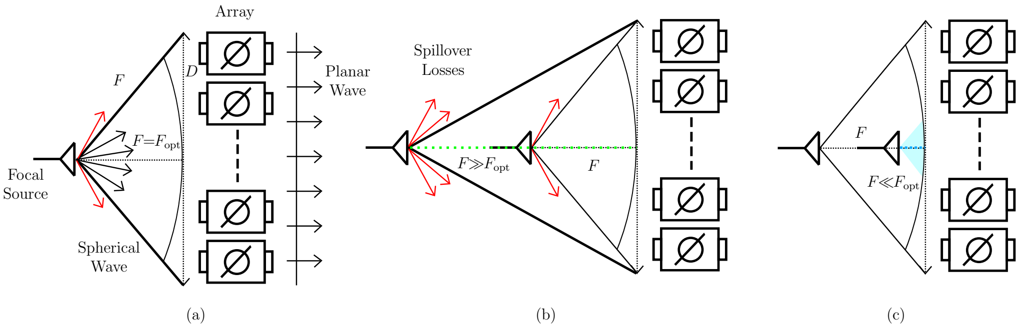

Figure 1.5: Focal ratio F/D parameter trade-off: a) when $F = F_{\text{opt}}$ the TA is maximized, b) when $F > F_{\text{opt}}$ spill-over losses increase, c) when $F < F_{\text{opt}}$ the planar array is bad illuminated.

essary to exactly compensate the phase on the array aperture at the cost of a higher complexity and losses in the case of electronically reconfigurable TA. A phase quantization can be introduced to avoid these drawbacks. Therefore, in our analysis, arrays with a 1-, 2-, 3-bit phase quantization have been considered. Figure 1.3 represent the phase values distribution as a function of the number of bits used for quantization for a planar 15×15 TA.

Denoting with N_x (N_y) the number of unit-cells elements in the x- (y-) direction and considering an inter-element spacing of $d_x = d_y = \lambda_0/2$, where λ_0 is the wavelength at f_0 (i.e. $\lambda_0 = 5\,\text{mm}$ at the center frequency 60 GHz), the TA side is set to $D = N_x d_x = N_y d_y$ (e.g. if the number of array elements is $N_{\text{array}} = N_x \times N_y = 15 \times 15$, then the side will be 37.5 mm).

One of the most important parameter in the design of the TA is the F/D ratio. The F/D ratio could be optimized by maximizing the TA gain, or equivalently, by finding the best trade-off between spillover losses and tapper efficiency. As graphically shown in Fig. 1.5, when F/D is higher than the optimum value (in terms of maximum gain) and the focal source is too distant from the receiving array, a great part of the power emitted by the focal source is not intercepted by the array aperture (spillover loss). On the contrary, when the focal source is close, the array surface is bad illuminated (low tapper efficiency). In Fig. 1.4, the simulated gains considering a perfect phase compensation and different sized TAs are reported as a function of the F/D ratio. The optimum $(F/D)_{\text{opt}}$ is between 0.4 and 0.5 and it corresponds

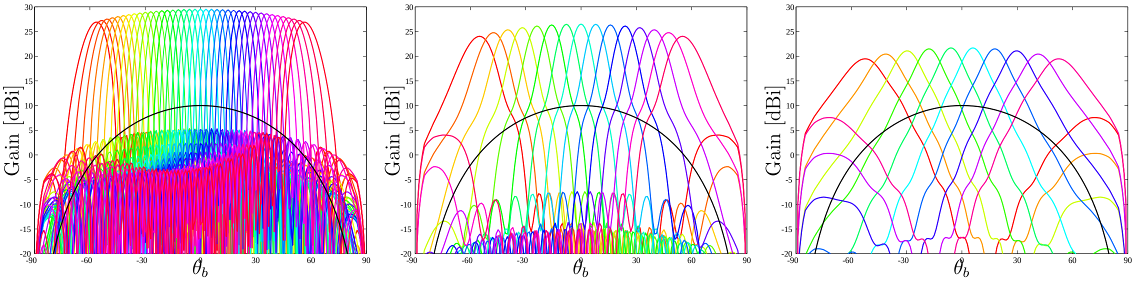

(a) Perfect, F_{opt} (b) Perfect, $F = 10\,\text{mm}$ (c) Perfect, $F = 5\,\text{mm}$

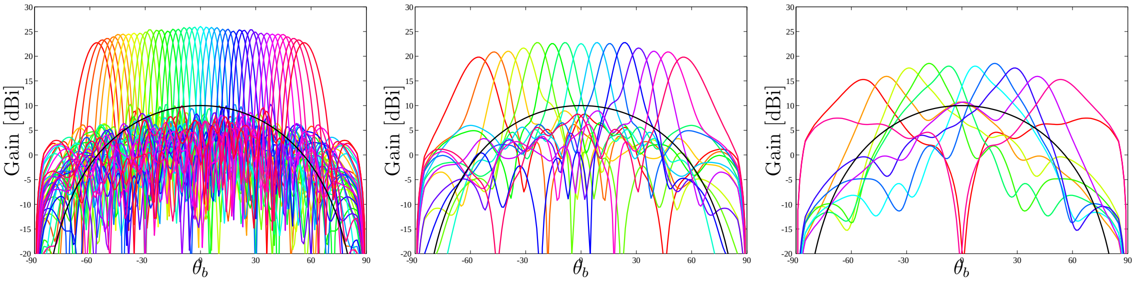

(d) 1 bit, F_{opt} (e) 1 bit, $F = 10\,\text{mm}$ (f) 1 bit, $F = 5\,\text{mm}$

Figure 1.6: Radiation pattern of a 20×20 TA as a function of the focal distance, phase quantization and steering angle

to different optimum focal distance values $F_{\text{opt}} = 25\,\text{mm}$, $F_{\text{opt}} = 19\,\text{mm}$, $F_{\text{opt}} = 13\,\text{mm}$ for $N_{\text{array}} = 20 \times 20$, $N_{\text{array}} = 15 \times 15$ and $N_{\text{array}} = 10 \times 10$, respectively. It is important to underline that the F/D ratio plays a key role on the integrability of the TA in portable devices as it defines the total volume occupied by the array. As a consequence, the effect of a reduced focal distance will be analysed to evaluate how a gain degradation impacts the mapping performance.

In Fig. 1.6 the gain of a 20×20 TA is reported as a function of the number of bits used for phase quantization and of the focal distance value. Note that, when considering a 20×20 array operating at $f_c = 60\,\text{GHz}$, the optimal focal distance is $F_{\text{opt}} = 25\,\text{mm}$. As we can see, reducing this value entails an increase of the half power beam width (HPBW) and the radiation pattern tends to coincide to the focal source one, reported in black in Fig. 1.6. This behaviour is due to the fact that when the focal source is too close to the array, not the entire array is illuminated but only a smaller set of unit cells

Table 1.1: Theoretical performance of transmitarrays optimized at $f_0 = 60\,\text{GHz}$ for maximum gain and different phase compensation conditions. The steering direction is $\theta_0 = 0°$.

	G [dBi]	SLL [dB]	HPBW [Degrees]	$(F/D)_{\text{opt}}$
Perfect	27.05	23.27	8	0.5
3 bits	26.88	24.62	8	0.44
2 bits	26.35	20.62	8	0.45
1 bit	23.53	20.25	9	0.49

(see also Fig. 1.5). At the same time when we consider a lower number of bits for phase quantization, both the side lobes level and the HPBW increase while the maximum gain decreases. In Fig. 1.6, the comparison between the case of perfect phase compensation and that using only 1 bit is reported.

In Table I, a comparison of the performance at $f_0 = 60\,\text{GHz}$ of the 15×15 TA is reported as a function of the number of bits used for the phase compensation process. The steering direction is here considered fixed to $\theta_0 = 0°$. The performances, obtained with perfect phase compensation, are also reported as a benchmark. It can be seen that the non-ideal phase compensation impacts the performance of the TA. Specifically, the maximum gain $G(\theta_0, f_0)$ decreases (quantization loss on directivity) while the level of the secondary lobes increases. The side lobe level (SLL) represents the difference (in [dB]) between the maximum gain and the peak of the main side lobe which has been reported in the Table I. The HPBW is here computed at f_0, which is a quite good approximation, despite the considered bandwidth $W = 1\,\text{GHz}$, because of the high f_0 involved. In the following, only 2 bits for phase compensation are considered (four different discrete phase values: 0°, 90° , 180°, and 270°) that could be a good compromise between structure complexity and radiation efficiency for an electronically reconfigurable TA.

Due to all the aforementioned characteristics, TA antennas represent excellent candidates for localization and environmental mapping applications at mmW. Note that the maximum steering angle θ_{b} is set to 60° according to the results reported in Fig. 1.7 for a 2-bit 15×15 TA. In Fig. 1.8 the theoretical gain of the 15×15 TA has been reported for two steering angles θ_b,

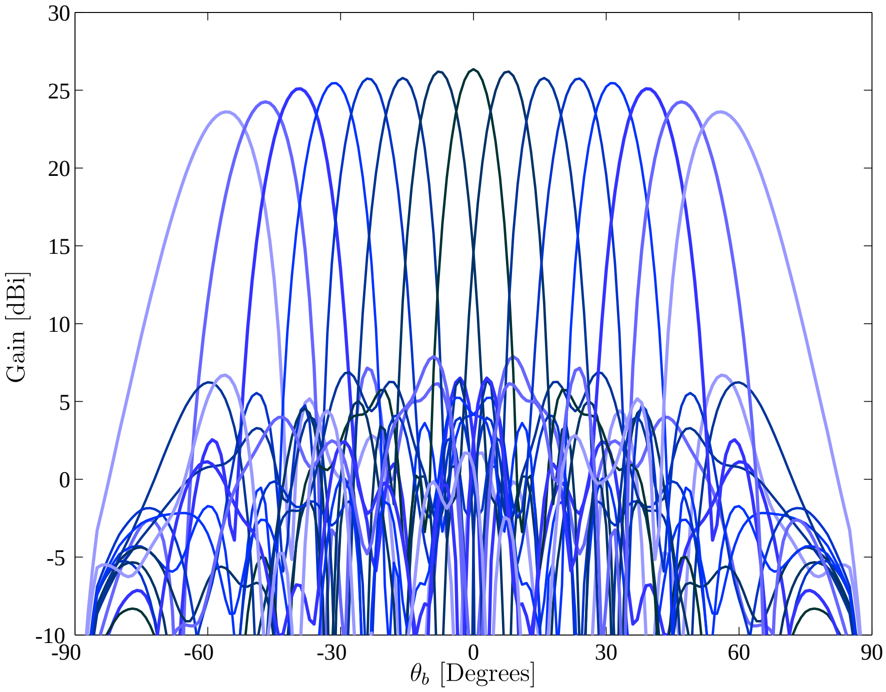

Figure 1.7: Gain of 2-bit 15×15 TA as a function of the steering angle θ_b at $f_0 = 60\,\mathrm{GHz}$ and for $(F/D)_{\mathrm{opt}}$ ratio.

namely 0° (continuous lines) and 60° (dashed lines) and for three frequencies in the considered band (lowest, central and highest frequencies). As previously mentioned, with a large bandwidth a slight difference in the radiation characteristic can be observed due to beamsquinting effect. However, as the fractional bandwidth W/f_0 is small, this effect is limited.

1.1.3 Sources of errors in massive antenna arrays

There are several issues that arise when massive wideband phased arrays are adopted and both accurate beamsteering and ranging have to be guaranteed. They are even more pronounced when working at very high frequencies due to technological and cost constraints [43].

This section deals with the effects of phase quantization errors and large signal bandwidth. The joint impact of such sources of error results in beam pointing errors and beamwidth spread that must be properly characterized when analyzing the performance of mapping schemes.

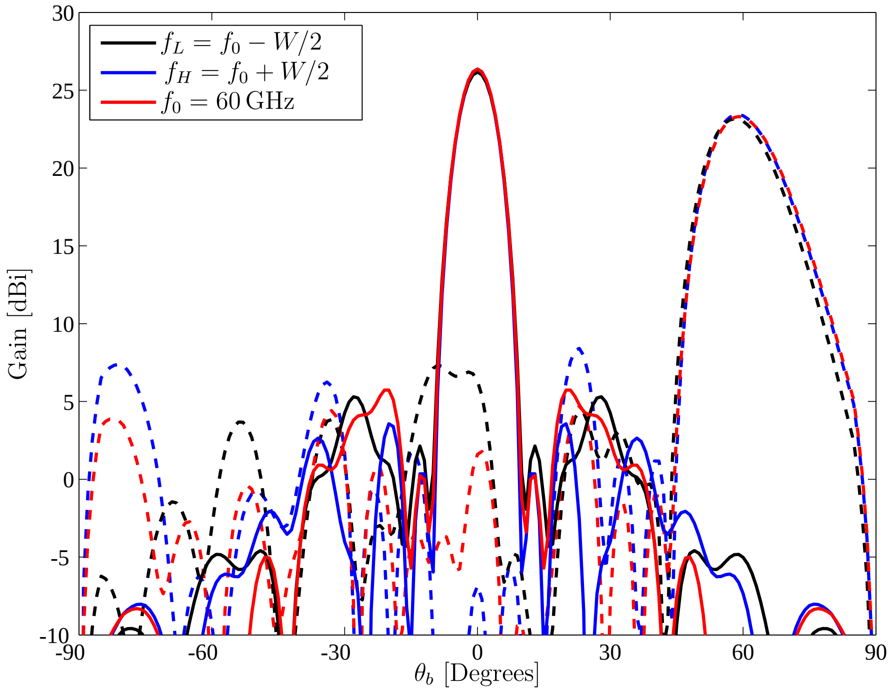

Figure 1.8: Theoretical gain of 2-bit 15×15 TA as a function of the steering angle θ_b with $W = 1\,\text{GHz}$ and for $(F/D)_{\text{opt}}$ ratio. Continuous lines refers to the case $\theta_b = 0°$, dashed lines refers to the case $\theta_b = 60°$.

Large signal bandwidth

A large bandwidth is in general desirable thanks to the corresponding achievable high ranging resolution [30]. However, in a wideband system, the received signal arrives at each antenna element with a delay that is not negligible compared to the signal duration, and hence it cannot be compensated by adopting only phase shifters, as typically done in narrowband systems. Unfortunately, the adoption of a huge number of time delay circuits represents a high-cost solution, especially at millimeter frequencies, then phase shifters remain at the moment the most viable solution [35]. Consequently, in the absence of time delays, the accumulation of the component received by each branch will result in a signal shape distortion. In other words, the actual steering direction and beamwidth would depend on frequency (beam squinting effect). For this reason the effects of signal bandwidth have to be carefully accounted for.

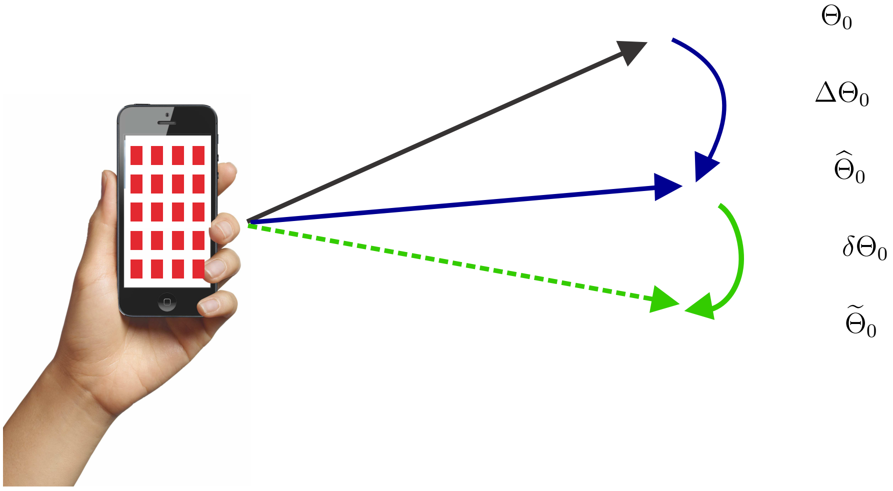

Figure 1.9: Beam pointing error scheme.

Array signal weights

Even the adoption of high resolution analog phase shifters might still not be a feasible solution for mmW massive antenna arrays if the aim is to keep low the system cost. Digitally controlled phase shifters implementing a discrete set of phase shifts represent a cheaper alternative at the expense of quantization errors [6]. Some new solutions have been investigated in [43] to find a compromise between the number of elements and the phase shifters accuracy.

Starting from the general model for the quantized version $\tilde{\omega}_{mn}$ of weights ω_{mn} proposed in [44], it is possible to express $\tilde{\omega}_{mn} = \omega_{mn} e^{j\delta_{mn}}$, with $\delta_{mn} \sim \mathcal{U}(-\Delta/2, \Delta/2)$ uniformly distributed random variables (RVs) in the quantization step Δ. Note that array weights errors affect the beam steering accuracy (see Fig. 1.9) and, consequently, the beamwidth characteristics. In addition, the misalignment of pulses at each array element causes temporal spread if it is not well counteracted. These effects can reduce the angle and ranging resolution as it will be detailed in the next section.

1.2 Impact of errors on pointing and angle resolution

This section investigates the impact of errors on the array characteristics. In particular, denote with $\widetilde{\mathrm{AF}}(\Theta, f)$ the actual AF in the presence of the aforementioned errors. Expression (1.1) becomes

$$\widetilde{\mathrm{AF}}(\Theta, f) = \sum_{m=1}^{M} \sum_{n=1}^{N} e^{j[(m-1)\Psi_{\mathrm{x}}+(n-1)\Psi_{\mathrm{y}}]} e^{j\delta_{mn}} \tag{1.5}$$

where δ_{mn}'s are the phase errors previously defined.

Now denote with $\widetilde{\Theta}_0 = (\tilde{\theta}_0, \tilde{\phi}_0)$ the actual beam pointing direction at frequency f and in presence of arrays non idealities. The actual beam pointing error could be related to the desired beam pointing direction as $\widetilde{\Theta}_0 = \Theta_0 + \Delta\widehat{\Theta}_0 + \delta\Theta_0$, with $\Delta\widehat{\Theta}_0 + \delta\Theta_0$ indicating the shift from the desired pointing direction consisting of both a deterministic $\Delta\widehat{\Theta}_0$ and random quantity $\delta\Theta_0 = (\delta\theta_0, \delta\phi_0)$ due to frequency selectivity and phase quantization, respectively (Fig. 1.9). Note that $\widehat{\Theta}_0 = (\hat{\theta}_0, \hat{\phi}_0) = \Theta_0 + \Delta\widehat{\Theta}_0$ is the actual beam pointing direction at frequency f and in absence of quantization error, with

$$\hat{\theta}_0 = \sin^{-1}\left(\frac{f_0}{f}\sin(\theta_0)\right), \quad \hat{\phi}_0 = \phi_0 \, . \tag{1.6}$$

For what follows it is convenient to derive the squared AF

$$\begin{aligned} |\widetilde{\mathrm{AF}}(\Theta, f)|^2 =& \sum_{mnpq} e^{j[(m-p)\Psi_x+(n-q)\Psi_y]} e^{j(\delta_{mn}-\delta_{pq})} \\ &= |\mathrm{AF}(\Theta, f)|^2 + \zeta_{\mathrm{err}}(\Theta, f) \end{aligned} \tag{1.7}$$

with

$$\zeta_{\mathrm{err}}(\Theta, f) = \sum_{mnpq} e^{j[(m-p)\Psi_x+(n-q)\Psi_y]} \left[e^{j(\delta_{mn}-\delta_{pq})} - 1\right] \tag{1.8}$$

and $\sum_{mnpq} = \sum_m^M \sum_n^N \sum_p^M \sum_q^N$. Equation (1.7) puts in evidence the deterministic and random terms composing the squared AF.

Considering δ_{mn}'s as independent and identically distributed (i.i.d.) RVs, the average squared AF is

$$\mathbb{E}\left\{|\widetilde{\mathrm{AF}}(\Theta,f)|^2\right\} = N_{\mathrm{array}} + \left(|\mathrm{AF}(\Theta,f)|^2 - N_{\mathrm{array}}\right)\chi^2 \tag{1.9}$$

where $\chi = \mathbb{E}\left\{e^{j\delta_{mn}}\right\} = \frac{2}{\Delta}\sin\left(\frac{\Delta}{2}\right)$. In the following the two effects that arise when phase errors and frequency selectivity are present will be described. First, the beampointing error phenomenon is investigated. Second, the beamwidth deviations caused by the joint influence of phase errors and squint effect will be addressed.

Beam pointing error

This section provides the evaluation of the impact of phase errors on the beam pointing direction. In particular the mean and the variance of the mean beam pointing error are derived.

The mean square error (MSE) of the beam pointing error is given by

$$\begin{aligned}\mathsf{MSE}_\theta(f,\theta_0) &= \mathbb{E}\left[\left(\delta\theta_0+\Delta\widehat{\theta}_0\right)^2\right] = \left[\Delta\widehat{\theta}_0\right]^2 + \mathbb{E}\left[\delta\theta_0^2(\widehat{\Theta}_0,f)\right]\\ \mathsf{MSE}_\phi(f,\phi_0) &= \mathbb{E}\left[\left(\delta\phi_0+\Delta\widehat{\phi}_0\right)^2\right] = \left[\Delta\widehat{\phi}_0\right]^2 + \mathbb{E}\left[\delta\phi_0^2(\widehat{\Theta}_0,f)\right]\end{aligned} \tag{1.10}$$

with

$$\left[\Delta\widehat{\phi}_0\right]^2 = 0, \quad \left[\Delta\widehat{\theta}_0\right]^2 = \left(\sin^{-1}\left(\frac{f_0}{f}\sin(\theta_0)\right) - \theta_0\right)^2. \tag{1.11}$$

In Appendix A it is shown that $\mathbb{E}[\delta\theta_0] = \mathbb{E}[\delta\phi_0] = 0$, and in Appendix B explicit expressions for $\mathbb{E}\left[\delta\theta_0^2(\widehat{\Theta}_0,f)\right]$ and $\mathbb{E}\left[\delta\phi_0^2(\widehat{\Theta}_0,f)\right]$ are derived and expressed by (1.47).

Given the transmitted signal power spectral density (PSD) $P_{\mathrm{t}}(f)$, with bandwidth W, the pointing root mean square error (PRMSE) could be defined as

$$\mathsf{PRMSE}(\Theta_0) = \sqrt{\frac{\int_W P_{\mathrm{t}}(f)\left[\mathsf{MSE}_\theta(f,\theta_0)+\mathsf{MSE}_\phi(f,\phi_0)\right]df}{\int_W P_{\mathrm{t}}(f)df}}\,. \tag{1.12}$$

It will be shown in Sec. 1.2.2 that small bandwidths W are better suited for high beam pointing accuracy. This is in contrast with the need to have large bandwidth signals for accurate ranging and a trade-off has to be found as will be reported in the numerical results.

Beamwidth spread

We are now interested in finding the 3 dB beamwidth spread, which varies with the frequency even if this is not explicitly indicated for notation convenience. It will be indicated as $\widetilde{\Theta}_{\mathrm{3dB}} = \left(\tilde{\theta}_0 \pm \delta\theta, \tilde{\phi}_0 \pm \delta\phi\right)$. In particular, the HPBW can be evaluated by solving the following equation

$$\left|\mathrm{AF}(\widetilde{\Theta}_{\mathrm{3dB}}, f)\right|^2 = \frac{1}{2}\left|\mathrm{AF}(\widetilde{\Theta}_0, f)\right|^2. \tag{1.13}$$

Consider now $\left(\tilde{\theta}_0 + \delta\theta, \tilde{\phi}_0 + \delta\phi\right)$, it follows that

$$\sum_{mnpq} \hat{w}_{mnpq} e^{j(m-p)\Psi_{\delta x}} e^{j(n-q)\Psi_{\delta y}} e^{j(\delta_{mn}-\delta_{pq})} = \frac{1}{2}\left|\mathrm{AF}(\widetilde{\Theta}_0, f)\right|^2 \tag{1.14}$$

where $\hat{w}_{mnpq} = e^{j\left[(m-p)\Psi_x|_{\Theta=\widetilde{\Theta}_0} + (n-q)\Psi_y|_{\Theta=\widetilde{\Theta}_0}\right]}$ and

$$\begin{aligned}\Psi_{\delta \mathrm{x}} &= kd_{\mathrm{x}}\left[\cos(\tilde{\theta}_0)\cos(\tilde{\phi}_0)\delta\theta - \sin(\tilde{\theta}_0)\sin(\tilde{\phi}_0)\delta\phi\right]\\ \Psi_{\delta \mathrm{y}} &= kd_{\mathrm{y}}\left[\sin(\tilde{\theta}_0)\cos(\tilde{\phi}_0)\delta\phi + \cos(\tilde{\theta}_0)\sin(\tilde{\phi}_0)\delta\theta\right]\,.\end{aligned} \tag{1.15}$$

In Appendix C a practical expression for the numerical evaluation of (1.13) is derived. From (1.51) and (1.52) in Appendix C we introduce the beam solid area (BSA)

$$\mathsf{BSA} = \Omega_{\mathrm{A}}(\Theta_0, f) = 4\,\mathbb{E}\left[\delta\tilde{\theta}_{x0}(\widetilde{\Theta}_0, f)\right]\mathbb{E}\left[\delta\tilde{\theta}_{y0}(\widetilde{\Theta}_0, f)\right]\sec\tilde{\theta}_0. \tag{1.16}$$

In addition, the *effective BSA* could be defined as

$$\Omega_{\mathrm{A,\,eff}}(\Theta_0) = \sqrt{\frac{\int_W P_{\mathrm{t}}(f)\Omega_{\mathrm{A}}^2(\Theta_0, f)df}{\int_W P_{\mathrm{t}}(f)df}}\,. \tag{1.17}$$

This parameter is an indicator of the angle resolution of the scanning process at direction Θ_0.

It will be shown in Sec. 1.2.2 through simulations that a large number of elements lets to reduce the impact of quantization errors as well as to narrow the beamwidth.

1.2.1 Ranging and steering accuracy

The ranging and angle resolution of massive antenna arrays will be now characterized accounting for bandwidth and sources of errors discussed in Sec. 1.1.3.

Target distance estimate (ranging) during each step of the scanning process is obtained through the measurement of the signal round-trip time (RTT). The fundamental limit of ranging accuracy of a target at distance d depends on the signal effective bandwidth W_{eff} and the received SNR as given by the CRLB [30]

$$\mathsf{CRLB} = \frac{c^2}{8\pi^2 \mathsf{SNR}\, W_{\mathrm{eff}}^2} \tag{1.18}$$

where W_{eff} is defined as

$$W_{\mathrm{eff}} \triangleq \sqrt{\frac{\int_{-\infty}^{+\infty} f^2 P_{\mathrm{t}}(f - f_0)\, df}{\int_{-\infty}^{+\infty} P_{\mathrm{t}}(f - f_0)\, df}} \approx W\,. \tag{1.19}$$

The mmW radar range equation related to a target at distance d, a test steering direction Θ_0, and considering a waveform with incident direction

$\Theta_i = (\theta_i, \phi_i)$ with respect to the target, can be expressed as

$$P_{\mathrm{r}}(\Theta_0, \Theta_i, d) = \int_W \frac{P_{\mathrm{t}}(f) c^2 \, G^2(\Theta_0, f) \, M(\Theta_0, \Theta_i, f, d)}{f^2 \, (4\pi)^3 \, d^4} \, df \tag{1.20}$$

with $G(\Theta_0, f) \approx \pi^2/\Omega_{\mathrm{A}}(\Theta_0, f)$ being the array gain [35] and $M(\Theta_0, \Theta_i, f, d)$ the target radar cross section (RCS).

Under the narrow beamwidth hypothesis, i.e. high N_{array}, the illuminated area on the target surface could be approximated with the beam area of the incident wave generated by the massive array (footprint area). Thus, the RCS of a target at mmW is given by [45, 46]

$$M(\Theta_0, \Theta_i, f, d) = 4\pi\rho A_{\mathrm{fp}}(\Theta_0, f, d)\zeta(\Theta_i) \tag{1.21}$$

where ρ is a parameter which depends on the type of scattering and the target material, and $\zeta(\Theta_i)$ is the incident/reflection coefficient of the target in the direction Θ_i. The footprint area is

$$A_{\mathrm{fp}}(\Theta, f, d) = \frac{\pi}{4} d^2 \Omega_{\mathrm{A}}(\Theta, d) \tag{1.22}$$

with $\Omega_{\mathrm{A}}(\Theta, f)$ given by (1.16).

Thus (1.20) results

$$P_{\mathrm{r}}(\Theta_0, \Theta_i, d) = \frac{\pi c^2}{64} \int_W \frac{\mathrm{EIRP}(f) \, \rho \, \zeta(\Theta_i)}{d^2 f^2} \, df \tag{1.23}$$

where $\mathrm{EIRP}(f) = P_{\mathrm{t}}(f) \, G(\Theta_0, f)$ is the effective radiated isotropic power (EIRP) typically constrained by regulatory power emission limits. Note the quadratic dependency of $P_{\mathrm{r}}(\Theta_0, \Theta_i, d)$ on the mobile-target distance d.

The actual SNR can be improved by increasing the transmission power or the observation time (e.g., by transmitting several pulses/symbols). However, both parameters have some constraints on spectrum emission regulations and the maximum tolerable scanning time, respectively. For what the latter is regarded, suppose we have to scan half of the full solid angle or half of the full angle, i.e. $\Omega_{\mathrm{o}} = 2\pi$ [sr] and $\Omega_{\mathrm{o}} = \pi$ [rad] in 3D and 2D scenarios, respectively.

The number N_{steer} of steering test directions to complete the scan process is strictly related to the array beamwidth, and thus to the number of antenna elements N_{array}, by the relation[3]

$$N_{\text{steer}} = \left\lfloor \frac{\Omega_{\text{o}}}{\Omega_{\text{mean}}} \right\rfloor \tag{1.24}$$

where Ω_{mean} denotes the mean BSA HPBW averaged over all the test directions Θ_0 given by

$$\Omega_{\text{mean}} = \frac{1}{\Omega_{\text{o}}} \int_{\Omega_{\text{o}}} \Omega_{\text{A,eff}}(\Theta)\, d\Omega \,. \tag{1.25}$$

Note that Ω_{mean} provides an indication on the scanning average angle resolution.

As a consequence, the scanning time is $T_{\text{scan}} = T_{\text{ob}} N_{\text{steer}}$, with T_{ob} representing the observation time for each test direction.

Note the dependency on the BSA: a narrow beam increases the scanning time, while the scanning angle resolution is improved. Under scanning time constraints, the SNR is given by

$$\mathsf{SNR} = \frac{P_{\text{r}}(\Theta_0, \Theta_i, d) T_{\text{ob}}}{N_0} = \frac{P_{\text{r}}(\Theta_0, \Theta_i, d) T_{\text{scan}}}{N_{\text{steer}} N_0} \tag{1.26}$$

where $N_0 = N_{\text{array}}\, \kappa \cdot T_0 \cdot F$, being κ the Boltzmann constant, $T_0 = 290\,[\text{K}]$ the receiver temperature, and F the receiver noise figure. Eq. (1.26) can be used in (1.18) to derive the fundamental limit of ranging as a function of the average BSA and scanning time constraint as it will be investigated in the numerical results.

1.2.2 Simulation results

Firstly, the impact of frequency selectivity and quantization errors on antenna array characteristics is evaluated in order to investigate the ranging and steering accuracy as a function of N_{array}. Successively, the mmW mea-

---

[3] $\lfloor x \rfloor$ denotes the biggest integer smaller than x.

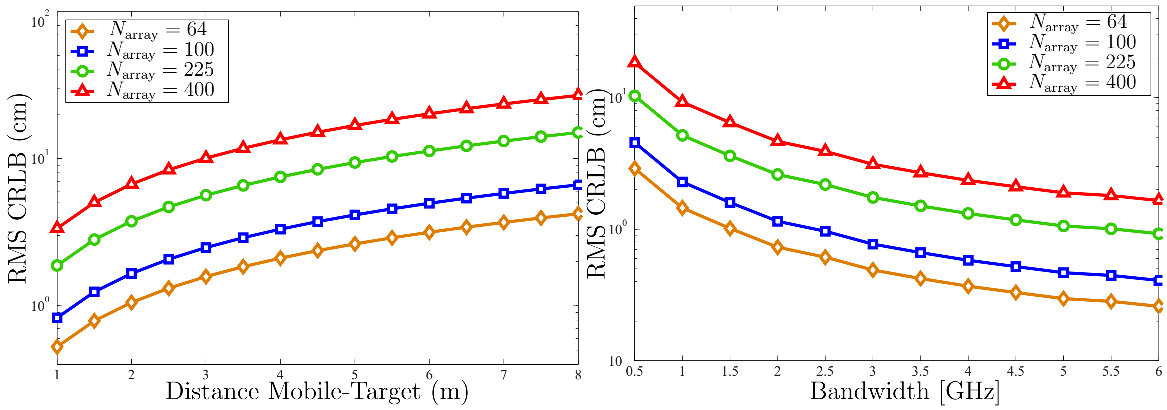

Figure 1.10: RMS CRLB vs. transmitted signal bandwidth W for a mobile-target distance of 10 m, and for $\Theta_0 = (45°, 45°)$ (left) and RMS CRLB vs. mobile-target distance for different values of N_{array}, $\Theta_0 = (45°, 45°)$, and $W = 500\,\text{MHz}$ (right).

surement campaign and the corresponding results will be discussed.

System parameters

According to the wavelength λ_0 and the object size L, there are different scattering regimes. Coherently with [46], it is assumed here to have $\lambda_0 \ll L$ (optics regime) even if in some cases it could result in a rough approximation. This assumption is reasonable in indoor environments where most of targets are constituted by walls that have an extension much larger than the wavelength. The approximation of a Lambertian scattering is considered [47], adopting the laser model proposed in [45] for the monostatic laser RCS, where ρ is defined as $\rho = \rho_{\text{d}}/\pi$, with ρ_{d} being the diffuse reflectivity (albedo), and Θ_{i} normal to the target. In addition, it is assumed that the targets are made of aerate concrete by approximating the albedo with the power reflection coefficient, evaluated by setting the concrete relative permittivity to $\epsilon_r = 2.26$ and its loss tangent to 0.0491 [48]. The scanning time is $T_{\text{scan}} = 0.1\,\text{ms}$, the noise figure $F = 4\,\text{dB}$ and it is assumed the transmission of a root raised cosine (RRC) signal compliant with the Federal Communications Commission (FCC) mask at 60 GHz [49], but with an average EIRP limited to 30 dBm to make the system suitable for battery-powered handset devices.

Ranging and steering accuracy trade-off

In this section, an example of trade-off between ranging and angle resolution is given considering a planar array working at 60 GHz with $d_\mathrm{x} = d_\mathrm{y} = \lambda_0/2$ and $M = N$.

The RMS CRLB on ranging is reported in Fig. 1.10-(right), obtained for different mobile-target distances and for different values of array elements N_array, where the transmitted signal bandwidth is set to $W = 500\,\mathrm{MHz}$. When N_array increases, the SNR decreases due to the reduced BSA and the constraint on EIRP according to (1.26).[4] In fact, N_array enters into N_0 and the array gain, which is inversely proportional to $\Omega_\mathrm{A}(\Theta, f)$. Thus, large values of N_array improve the scanning angle resolution, but worsen the SNR affecting (1.18). As an example, if the target ranging error is set to 5 cm at 5 m distance, from Fig. 1.10-(right) it must be $N_\mathrm{array} \leq 100$, provided that it is sufficiently high to satisfy our model. On the contrary, the bandwidth improves the ranging accuracy, as shown in Fig. 1.10-(left), but it has a detrimental effect on the PRMSE, as it can be noticed in Fig. 1.11-(left). From the same figure it can be seen that PRMSE is quite sensitive to the test steering elevation angle θ_0 and to phase quantization errors.

Finally, Fig. 1.11-(right) reports the BSA, evaluated according to (1.51) and (1.52), whose expectation is computed through Monte Carlo simulation. Note the weak dependence of the BSA on the frequency, and how large N_array results in lower BSA and lower sensitivity to quantization errors. In any case the effect of quantization errors on BSA can be neglected with good approximation. Moreover, if $\mathsf{BSA} \leq 0.04\,[\mathrm{sr}]$, it must be $N_\mathrm{array} \geq 64$.

Thus, it is possible to notice a strong impact of N_array on the BSA, which affects both the SNR and the ranging accuracy, and hence it needs to be properly taken into account during the system design.

Furthermore, there is also the trade-off in the choice of the bandwidth: the

---

[4] Note that here performance is strictly related to the adopted model, which is valid only for a high number of antenna elements, which justify the performance degradation when N_array increases.

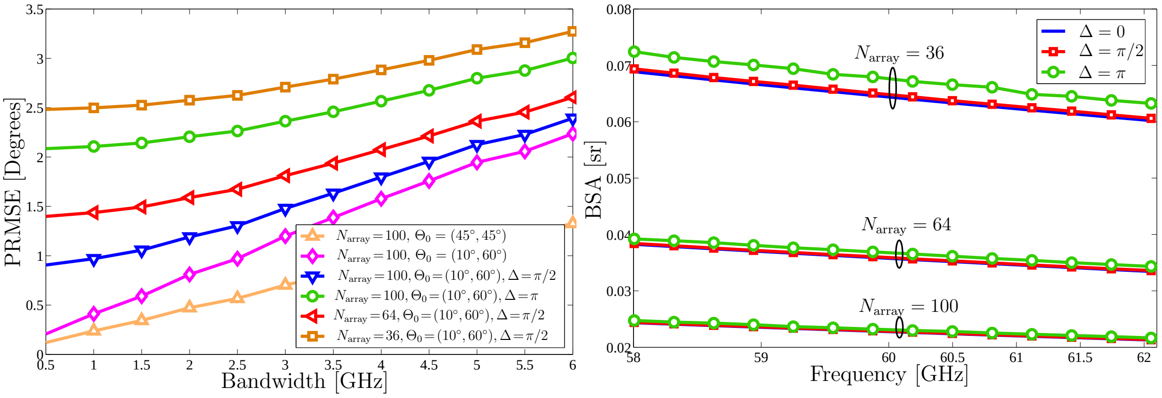

Figure 1.11: PRMSE vs. bandwidth for different values of N_{array}, different steering angles and in presence/absence of quantization effects (left) and BSA vs.frequency for different values of N_{array} and quantization errors (right).

ranging accuracy improves with a larger bandwidth but the array pointing error increases with W due to frequency selectivity effects. The bandwidth and the phase errors slightly affect the effective BSA and hence the scanning angle resolution. In our numerical example, $N_{\text{array}} = 100$ and $W = 1\,\text{GHz}$ represent a reasonable compromise.

1.3 Experimental results

This section aims at describing the mmW measurement campaign conducted in typical office environments using real-existing massive arrays.

Measurement set-up

In order to validate the personal radar concept, a measurement campaign has been conducted at CEA-Grenoble indoor premises. The map of the building floor is reported in Fig. 1.12. In particular, this experimental activity takes place in two different environments: and office room (Fig. 1.12-left) and a corridor (Fig. 1.12-right).

In particular, the measurement set-up is represented in Fig. 1.13 and it consists of:

- A 4-ports vector network analyzer (VNA) operating in the frequency

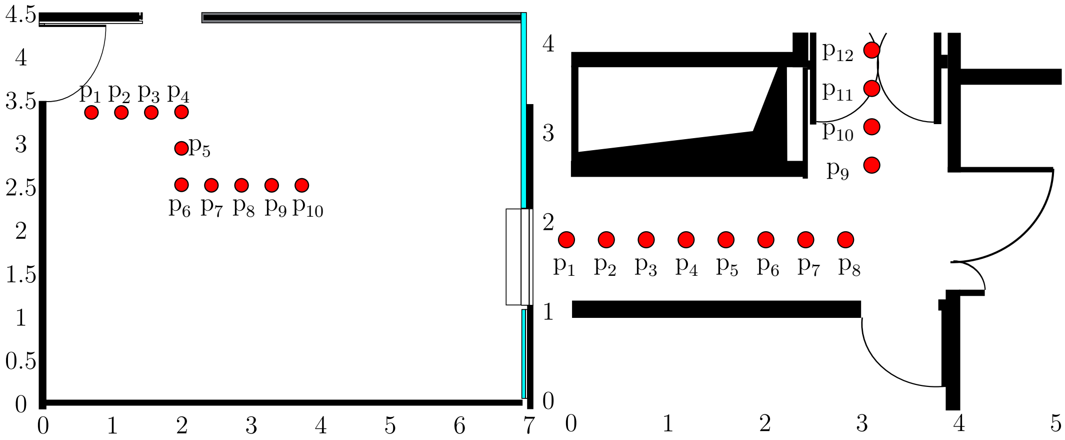

Figure 1.12: Plan of the indoor office environment.

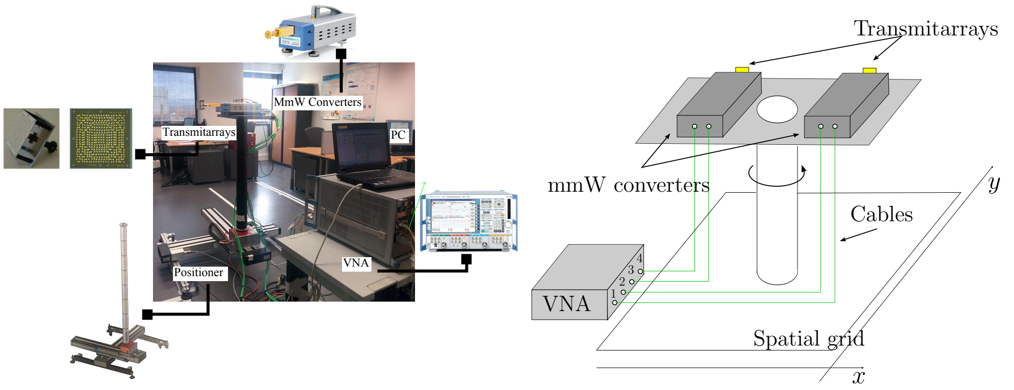

Figure 1.13: Measurement set-up.

range 10 MHz-24 GHz;

- 2 mmW converters operating in the frequency range 50 GHz-75 GHz;
- 2 Linearly polarized TAs (size 20×20, 1 bit, $F/D = 0.5$) [18];
- *X-Y-Azimuth* positioner.

A bistatic configuration has been considered with the TAs in order to mitigate the antenna coupling and to separate the transmitting and receiving channels. Specifically, as we can see in Fig. 1.12, where the plan of the office and the corridor are reported, measurements have been collected in 10 and

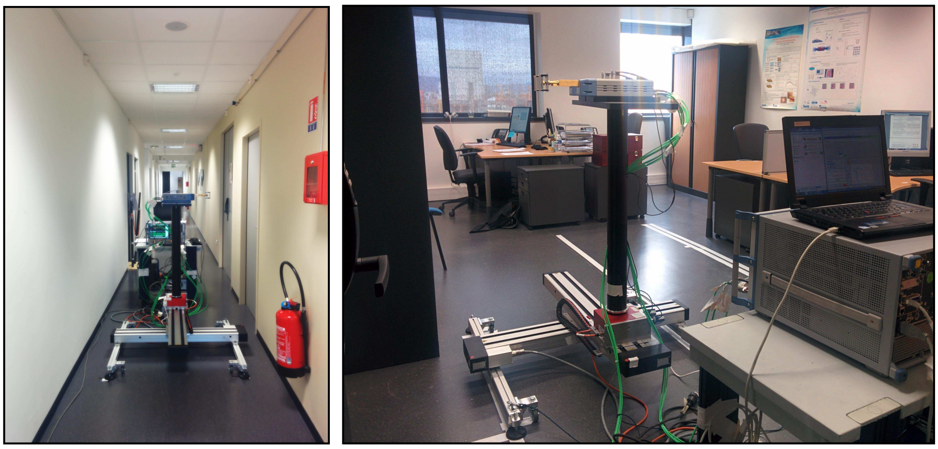

Figure 1.14: Photos of measurement campaign in corridor.

12 different positions spaced of 0.405 m [5] in the frequency range between $55 - 70$ GHz with a step of 5 MHz.

For each measurement position, the *X-Y-Azimuth* positioner permits to rotate the radar in the semi-plane from $-90°$ to $90°$ with a step of $5°$ (in accordance to the HPBW of the TA used) in order to emulate the beamforming operation. This mechanical steering is imposed by the fact that the considered TA is non-reconfigurable. Technological solutions to perform electronically beamsteering at V-band can be found in [50] where a multiple-source system is proposed. Fig. 1.14 shows two photos taken during the measurements campaign.

Transmitarray antenna used for measurements

The TAs used for measurements are fully described in [18]. In the considered TA structure, 20×20 unit-cells are adopted each with size of 2.5×2.5 mm^2 (i.e. the spacing between antennas is set to $\lambda_0/2 = 2.5$ mm where λ_0 is the wavelength at $f_0 = 60$ GHz). Each unit-cell is composed of two patch antennas (receiver and transmission one) printed on two identical substrates separated by a ground plane and connected by a metallised via hole. The transmission phase can be controlled by rotating the patch on the transmis-

---

[5] This step has been chosen in accordance to the value of the fully automated movement along the y-axis achievable with the positioner.

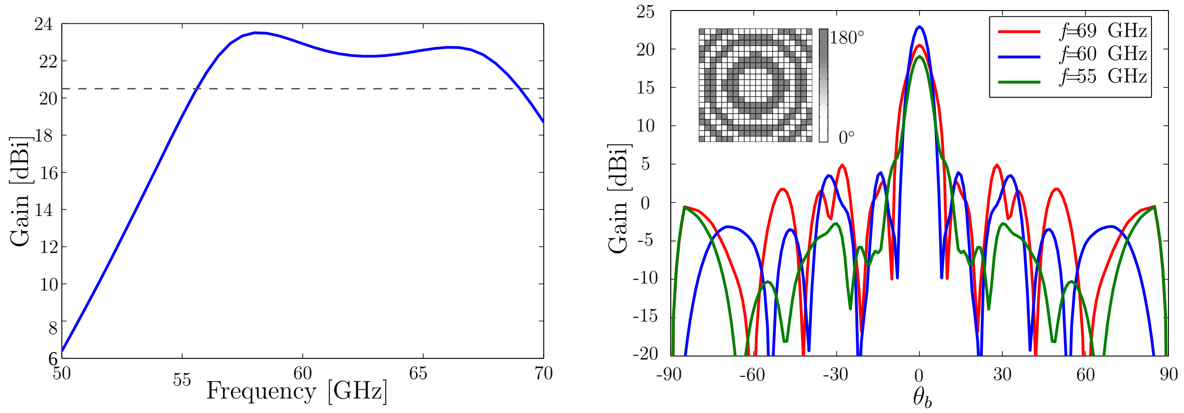

Figure 1.15: Computed maximum gain of the TA used for measurements for $\theta_b = 0°$ as a function of frequencies (top), phase distribution and realized gain for f_L, f_H and f_c (bottom) [18].

sion side. As previously introduced, this TA is non-reconfigurable because the patches rotation is fixed once the array is realized. The considered TA presents 1-bit of phase compensation corresponding to two possible phase values (0° and 180°). Finally, the focal source is a linearly-polarized pyramidal horn antenna with a gain equal to 10.2 dBi at 60 GHz and a full HPBW of 72° × 57°.

Given this array structure, in [18] simulations and measurements results report a maximum gain of 23.3 dBi, a directivity, spill-over loss and power efficiency equal to 26 dBi, 2.24 dB, and 53.6%, respectively.

In Fig. 1.15-(left) we report the maximum gain of the TA as a function of the frequency range used for measurements. The dashed lines correspond to the gain at 3 dB and intercept the continuous curve in correspondence of two frequency values, $f_L = 55$ GHz and $f_H = 69$ GHz, which define the extremes of the 3 dB bandwidth. In Fig. 1.15-(right) the phase distribution and the realized gain are shown. Note that we have reported the realized gain for f_L, f_H and for the frequency $f_c = 60$ GHz at which the TA has been optimized.

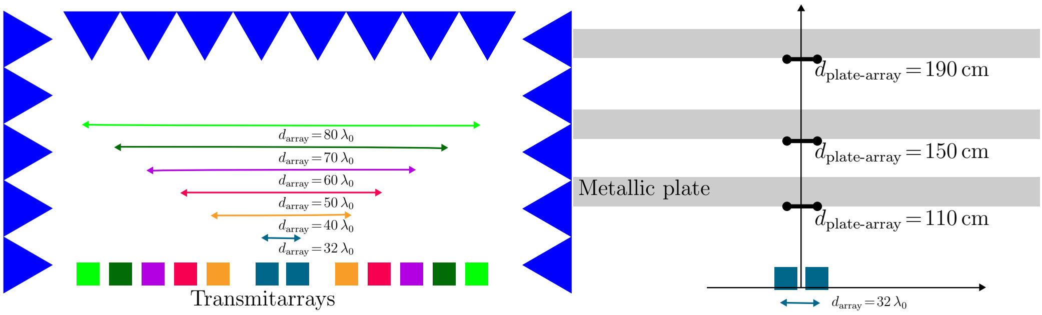

(a) Test coupling (b) Test distance

(c) Measurements scenario

Figure 1.16: Preliminary test with a metallic plate.

1.3.1 Preliminary tests using a metallic plate

Before performing the measurements campaign in the office environments described by Fig. 1.12, some preliminary measurements tests have been conducted with the main aim of

- evaluating the best TAs distance guaranteeing an acceptable coupling level and the separation of the tx-rx channels;
- evaluating the ranging performance of the TA-radar.

Figure. 1.16-(a) illustrates the configuration in which the measurements for testing the coupling have been performed. In particular, absorbers have been used to isolate the system under test reducing reflections coming from the surrounding environments and the radar support. Transmitarrays have been placed at different distances to each other, i.e. $d_{\text{array}} = 32 - 40 - 50 - 60 - 70 - 80\,\lambda_0$ $(16 - 20 - 25 - 30 - 35 - 40\,\text{cm})$, where $d_{\text{array}} = 32\,\lambda_0$ was the

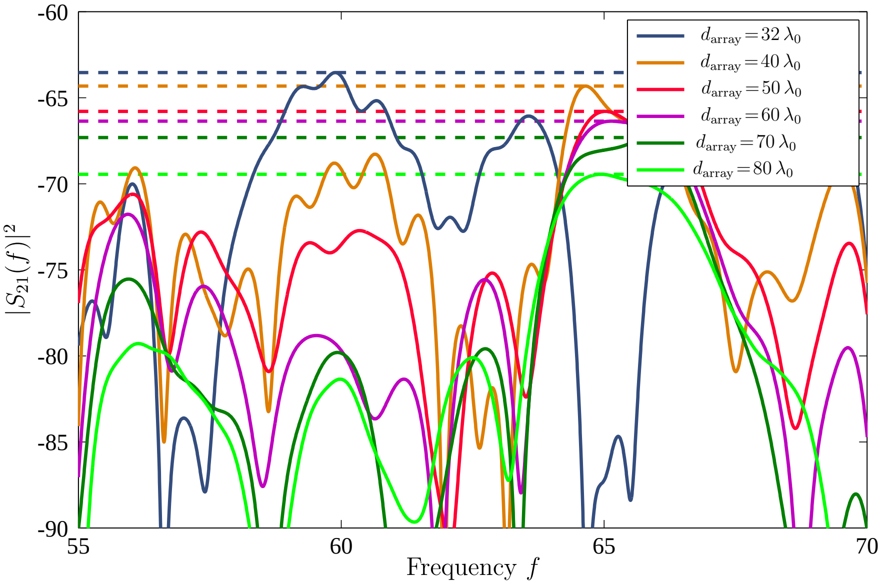

Figure 1.17: Coupling results considering different transmitarray distances.

closest distance at which the TAs could be located given the support and the converters. The result of this first test is reported in Fig. 1.17 in terms of power delay profile (PDP) in frequency domain. A time gating operation to isolate the array response has been operated to further reducing the level of the unintended environmental reflections. Thanks to the high antenna directivity, even when considering $d_{\text{array}} = 32\,\lambda_0$ the coupling level is lower then $-60\,\text{dB}$ ($\sim -63\,\text{dB}$) and thus, it does not strongly influence the line-of-sight (LOS) dominant direct contribution as we can notice from Fig. 1.18. Specifically, in Fig. 1.18 the squared channel impulse response (CIR) in the time domain has been represented as a function of the distance between the radar-system and a metallic plate, as graphically illustrated in Fig. 1.16-(b). As it can be seen, different TA-radar/metallic plate distances have been tested once fixed the TAs distances to $32\,\lambda_0$. In Fig. 1.18 the coupling component is the same for the three configurations and arrives with a delay of $0.5\,\text{ns}$ while the useful metallic plate reflection corresponds to the three main peaks at $110 - 150 - 190\,\text{cm}$, respectively.

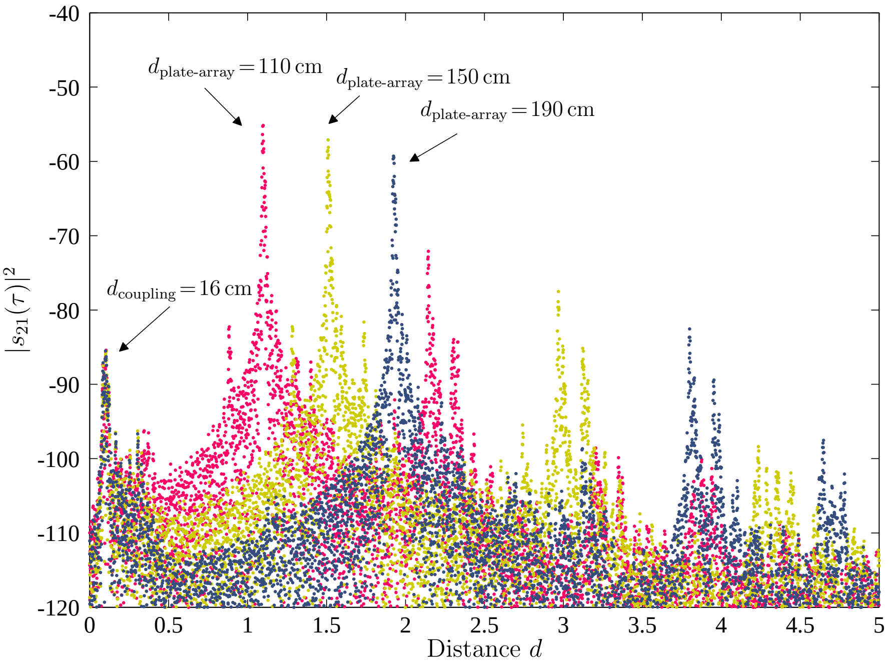

Figure 1.18: Results considering different metallic plate-radar distances.

1.3.2 RMS delay spread characterization

After these preliminary tests, we have performed measurements in the environments described in Fig. 1.12 where for each position and each TA steering direction, the S-matrix was measured in the frequency domain from 55 to 70 GHz (3 dB bandwidth) [18]. In particular, the measured $S_{21}(f)$ was reported in time-domain through the inverse Fourier transform, and time gating was performed in order to suppress the coupling between the two arrays.

In Fig. 1.19, 1.20 the PDP collected from different positions and for two different steering angles θ_b in the corridor and in the office room are shown.

In all the reported PDPs, there are a few components which are prominent with respect to the other extrapolating using an algorithm similar to that proposed in [51].

For the sake of simplicity, we now assume that the angle-of-departure (AOD) and the angle-of-arrival (AOA) are the same due to the high antenna directivity. Consequently, the antennas-embedded CIR for each radar

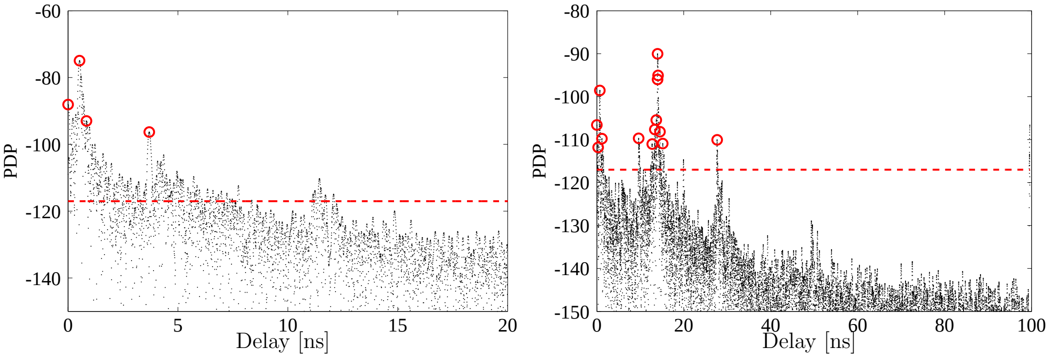

Figure 1.19: Example of PDP taken from p_1 with $\theta_b = -90°$ and p_6 with $\theta_b = -45°$ in the corridor environment.

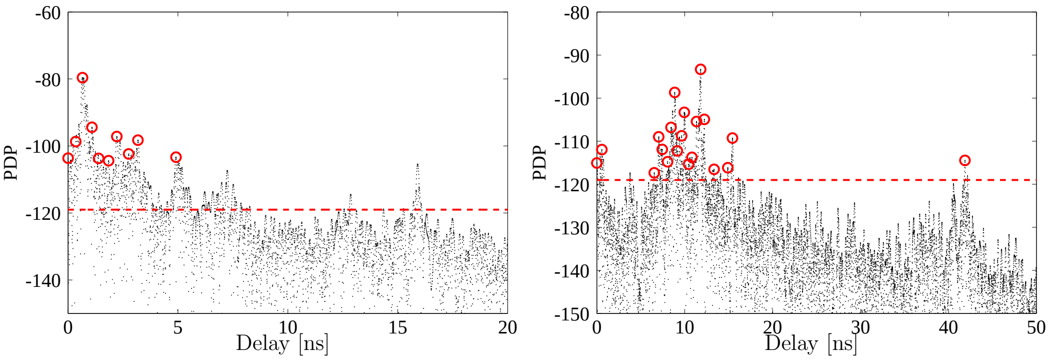

Figure 1.20: Example of PDP taken from p_1 with $\theta_b = -90°$ and p_8 with $\theta_b = -45°$ in the office environment.

position and steering direction can be written as

$$h_i^{\mathrm{b}}(\tau, \theta) = \sum_{k=1}^{N_{\mathrm{paths}}} a_{ik}\left(\theta - \theta_{\mathrm{b}}\right)\ \delta(\tau - \tau_k) \tag{1.27}$$

with $i = 1, \ldots, N_{\mathrm{pos}}$, where N_{pos} is the number of radar positions, N_{paths} is the number of paths, $\delta(\cdot)$ is the Dirac delta function and $a_{ik}\left(\cdot\right)$ is a term related to the array radiation characteristic. τ_k is the delay of the kth path and θ_{b} is the steering angle. Note that all paths angular direction could be associated to the steering direction thanks to the high antenna directivity. The PDP for each radar position and each steering direction is defined as

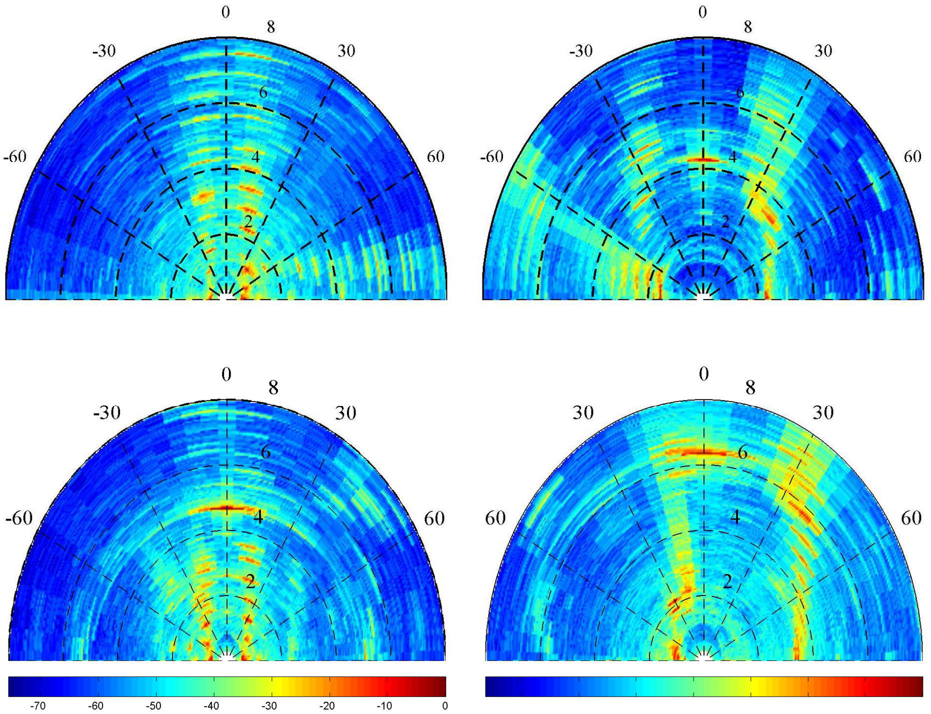

Figure 1.21: Radar map results for normalized PDP from radar position p_1 and considering all the steering directions in the corridor (left) and office (right).

$$\mathsf{PDP}_i(\tau, \theta) = \sum_{k=1}^{N_{\text{paths}}} |h_i^{\mathrm{b}}(\tau, \theta)|^2. \tag{1.28}$$

Thanks to the considered system, it was possible to merge all the collected measurements for each position. In Fig.1.21-top it is possible to observe the corridor and room reconstruction when the TAs are positioned in p_1. Notably, in such cases the contour of the two scenarios is quite well defined. On the contrary, Fig.1.21-bottom reports the maps for corridor in p_9 and for the room in p_7. While for the corridor it is still possible to recognize the lateral walls, for the room the image is less clear. These effects could be ascribed to the adoption of the TAs as laser, whereas the precision is lower especially at higher distances where the footprint area of the beam is larger. It is expected that those errors are corrected through the adoption

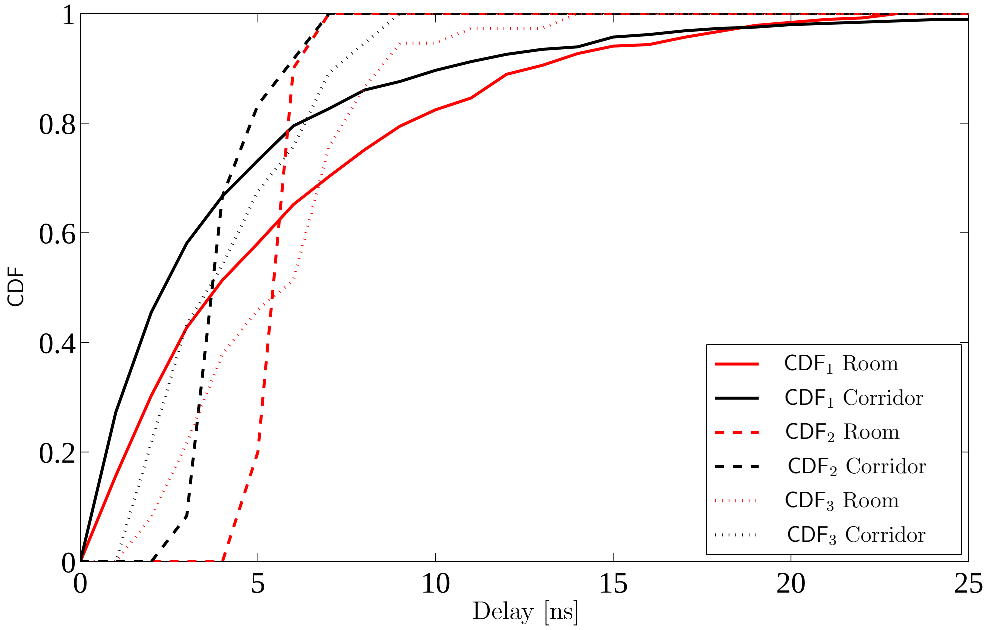

Figure 1.22: Obtained CDF.

of recursive filters, such as the one described in [5], where all measurements performed in different positions are kept into account in order to improve the quality of the maps. The root mean square (rms) delay spread is computed started from (1.28) as

$$\tau_i^{\mathrm{rms}}(\theta_b)=\sqrt{\frac{\sum_{k=1}^{N_{\mathrm{paths}}} \quad |h_i^{\mathrm{b}}(\tau,\, \theta)|^2\, (\tau_k - \bar{\tau})^2}{\sum_{k=1}^{N_{\mathrm{paths}}} \quad |h_i^{\mathrm{b}}(\tau,\, \theta)|^2}} \tag{1.29}$$

where $\bar{\tau}$ is the mean excess delay defined as

$$\bar{\tau}(\theta_b) = \frac{\sum_{k=1}^{N_{\mathrm{paths}}} \quad |h_i^{\mathrm{b}}(\tau,\, \theta)|^2\ \tau_k}{\sum_{k=1}^{N_{\mathrm{paths}}} \quad |h_i^{\mathrm{b}}(\tau,\, \theta)|^2} \tag{1.30}$$

The rms delay spread averaged over the steering direction or over the posi-

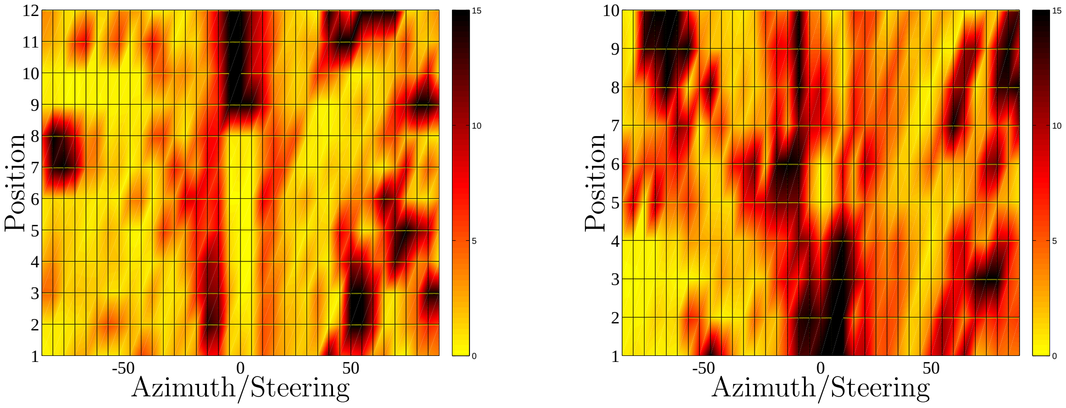

Figure 1.23: RMS delay spread averaged over steering direction as a function of the radar position in the corridor (right) and room (left) environment.

tions can be easily found, respectively, as

$$\begin{aligned}\bar{\tau}_i^{\mathrm{rms}} &= \frac{1}{N_{\mathrm{steer}}} \sum_{b=1}^{N_{\mathrm{steer}}} \tau_i^{\mathrm{rms}}(\theta_b) \\ \bar{\tau}_b^{\mathrm{rms}} &= \frac{1}{N_{\mathrm{pos}}} \sum_{i=1}^{N_{\mathrm{pos}}} \tau_i^{\mathrm{rms}}(\theta_b)\,. \end{aligned} \tag{1.31}$$

Define now $\mathcal{T}$ as the set of possible rms delay spread which is possible to experience due to channel characteristics. Consequently, the CDF with respect to $\tau_{i\,\mathrm{th}}^{\mathrm{rms}}$, with $\tau_{i\,\mathrm{th}}^{\mathrm{rms}} \in \mathcal{T}$, is given by

$$\begin{aligned}\mathsf{CDF}_1(\tau_{i\,\mathrm{th}}^{\mathrm{rms}}) &= \frac{1}{N_{\mathrm{steer}}N_{\mathrm{pos}}} \sum_{i=1}^{N_{\mathrm{pos}}} \sum_{b=1}^{N_{\mathrm{steer}}} \mathbf{1}\left(\tau_{i\,\mathrm{th}}^{\mathrm{rms}} - \tau_i^{\mathrm{rms}}(\theta_b)\right) \\ \mathsf{CDF}_2(\tau_{i\,\mathrm{th}}^{\mathrm{rms}}) &= \frac{1}{N_{\mathrm{pos}}} \sum_{i=1}^{N_{\mathrm{pos}}} \mathbf{1}\left(\tau_{i\,\mathrm{th}}^{\mathrm{rms}} - \bar{\tau}_i^{\mathrm{rms}}\right) \\ \mathsf{CDF}_3(\tau_{i\,\mathrm{th}}^{\mathrm{rms}}) &= \frac{1}{N_{\mathrm{steer}}} \sum_{b=1}^{N_{\mathrm{steer}}} \mathbf{1}\left(\tau_{i\,\mathrm{th}}^{\mathrm{rms}} - \bar{\tau}_b^{\mathrm{rms}}(\theta_b)\right) \end{aligned} \tag{1.32}$$

where $\mathbf{1}(x) = 1$ if $x \geq 0$, 0 otherwise. Fig.1.22 reports different distributions of the delay spread in the two environments, according to the fact that it is averaged over positions, over the steering directions, or all the values are separately considered as expressed in (1.32). As also in part suggested by the CIR previously reported, it is important to notice that the delay spread spans from values lower than 25 ns in both environments. We ascribe this effect to the adoption of high directive antennas, which operate as a spatial filter, and to the particular environment configuration especially for what the corridor is concerned. Notably, such results are in agreement with [52], where author observed a root delay spread of few nanoseconds, for the one-way channel, when high gain antennas are adopted. Moreover a small difference between the office and the corridor environment can be noticed.

1.4 Conclusions

This chapter presents an overview of massive antenna arrays operating at mmW frequencies. Firstly we have described phased and transmitarray antennas analysing the key structural parameters of the two configurations. Specifically, we have focused our attention in the number of bits used for phase compensation, the number of antennas composing the array and the focal distance value. All these parameters influence the radiation characteristics and thus, impact on the angular resolution capabilities of the arrays. Secondly the most important sources of errors have been illustrated. The quantization and frequency selectivity effects have been accounted for to derive the pointing error, the beamwidth spread and the ranging accuracy as a function of the number of antenna elements in the array. The analysis has highlighted how angular resolution, scanning time, signal bandwidth and ranging accuracy are tightly coupled and how a suitable trade-off has to be obtained. Finally, an indoor backscattering measurement campaign at millimeter-wave has been conducted using transmitarrays. The first step has been the evaluation of the coupling level between arrays when a bistatic configuration is adopted. Secondly, the two 1-bit 20×20 linearly polarized TAs have been used to scan a real office environment. The data collected have been exploited for the delay spread characterization of different steering direction, finding values lower in general of 25 ns due to the high-directivity TAs acting as spatial filters, and the two considered indoor scenarios. Moreover, the measurements results database will be exploited for mapping purposes as it will be detailed in the following chapter.

Appendix A

To evaluate $\mathbb{E}\left[\delta\Theta_0\right]$, consider that in the presence of non-ideal effects, the actual pointing direction can be derived by solving

$$S(\widetilde{\Theta}_0, f)=\frac{\partial|\widetilde{\mathrm{AF}}(\Theta, f)|^2}{\partial\theta}\bigg|_{\Theta=\widetilde{\Theta}_0}=0,\ F(\widetilde{\Theta}_0, f)=\frac{\partial|\widetilde{\mathrm{AF}}(\Theta, f)|^2}{\partial\phi}\bigg|_{\Theta=\widetilde{\Theta}_0}=0\,. \tag{1.33}$$

Considering the expansion with the first order of the Taylor series evaluated in $\widehat{\Theta}_0$, it is

$$\begin{aligned} S(\widetilde{\Theta}_0,f)&= S(\widehat{\Theta}_0+\delta\Theta_0, f) = S(\widehat{\Theta}_0, f)+\delta\theta_0\frac{\partial S(\Theta, f)}{\partial\theta}\bigg|_{\Theta=\widehat{\Theta}_0}=0 \\ F(\widetilde{\Theta}_0,f)&=F(\widehat{\Theta}_0+\delta\Theta_0,f) =F(\widehat{\Theta}_0, f)+\delta\phi_0\frac{\partial F(\Theta, f)}{\partial\phi}\bigg|_{\Theta=\widehat{\Theta}_0}=0\,. \end{aligned} \tag{1.34}$$

Thus, considering $\delta\Theta_0=(\delta\theta_0(\widehat{\Theta}_0, f), \delta\phi_0(\widehat{\Theta}_0, f))$, and the approach followed in [44], where the derivatives are approximated with their respective mean values, we have

$$\begin{aligned} \delta\theta_0(\widehat{\Theta}_0, f) &= \frac{-S(\Theta, f)}{\frac{\partial S(\Theta,f)}{\partial\theta}}\Bigg|_{\Theta=\widehat{\Theta}_0} \approx \frac{-S(\Theta, f)}{\mathbb{E}\left[\frac{\partial S(\Theta,f)}{\partial\theta}\right]}\Bigg|_{\Theta=\widehat{\Theta}_0} \\ \delta\phi_0(\widehat{\Theta}_0, f) &= \frac{-F(\Theta, f)}{\frac{\partial F(\Theta,f)}{\partial\phi}}\Bigg|_{\Theta=\widehat{\Theta}_0} \approx \frac{-F(\Theta, f)}{\mathbb{E}\left[\frac{\partial F(\Theta,f)}{\partial\phi}\right]}\Bigg|_{\Theta=\widehat{\Theta}_0} \end{aligned} \tag{1.35}$$

which allow us to write the mean components of $\delta\Theta_0$ as

$$\mathbb{E}\left[\delta\theta_0(\widehat{\Theta}_0, f)\right]=-\frac{\mathbb{E}\left[S(\Theta, f)\right]}{\mathbb{E}\left[\frac{\partial S(\Theta,f)}{\partial\theta}\right]}\Bigg|_{\Theta=\widehat{\Theta}_0},\ \mathbb{E}\left[\delta\phi_0(\widehat{\Theta}_0, f)\right]=-\frac{\mathbb{E}\left[F(\Theta, f)\right]}{\mathbb{E}\left[\frac{\partial F(\Theta,f)}{\partial\phi}\right]}\Bigg|_{\Theta=\widehat{\Theta}_0}. \tag{1.36}$$

To solve (1.36), let express $S(\Theta, f)$ as

$$S(\Theta, f) = \frac{\partial|\widetilde{\mathrm{AF}}(\Theta, f)|^2}{\partial\theta}=\frac{\partial|\mathrm{AF}(\Theta, f)|^2}{\partial\theta}+\frac{\partial\zeta_{\mathrm{err}}(\Theta, f)}{\partial\theta}\,. \tag{1.37}$$

By defining $\alpha_{mnpq} = [(m-p)\Psi_x + (n-q)\Psi_y]$ and $\frac{\partial \alpha_{mnpq}}{\partial \theta} = \psi_{mnpq}(\Theta, f)$ it is

$$\mathbb{E}\left[\frac{\partial \zeta_{\text{err}}(\Theta, f)}{\partial \theta}\right] = j\left[\chi^2 - 1\right] \sum_{mnpq} \psi_{mnpq}(\Theta, f)\, e^{j\alpha_{mnpq}} \tag{1.38}$$

where $\psi_{mnpq} = 0$ when $m = p$, $n = q$. Consequently we have

$$\mathbb{E}\left[S(\Theta, f)\right] = j\chi^2 \sum_{mnpq} \psi_{mnpq}(\Theta, f) e^{j\alpha_{mnpq}} \tag{1.39}$$

from which $\mathbb{E}\left[S(\widehat{\Theta}_0, f)\right] = 0$.

Analogously, we can make the same considerations for ϕ, obtaining $\mathbb{E}\left[\delta\theta_0(\widehat{\Theta}_0, f)\right] = \mathbb{E}\left[\delta\phi_0(\widehat{\Theta}_0, f)\right] = 0$, and consequently $\mathbb{E}\left[\delta\Theta_0\right] = 0$.

Appendix B

We express $\mathbb{E}\left[\delta\theta_0^2(\widehat{\Theta}_0, f)\right]$ and $\mathbb{E}\left[\delta\phi_0^2(\widehat{\Theta}_0, f)\right]$ as

$$\mathbb{E}\left[\delta\theta_0^2(\widehat{\Theta}_0, f)\right] = \left.\frac{\mathbb{E}\left[S^2(\Theta, f)\right]}{\left(\mathbb{E}\left[\frac{\partial S(\Theta, f)}{\partial \theta}\right]\right)^2}\right|_{\Theta = \widehat{\Theta}_0}, \quad \mathbb{E}\left[\delta\phi_0^2(\widehat{\Theta}_0, f)\right] = \left.\frac{\mathbb{E}\left[F^2(\Theta, f)\right]}{\left(\mathbb{E}\left[\frac{\partial F(\Theta, f)}{\partial \phi}\right]\right)^2}\right|_{\Theta = \widehat{\Theta}_0}. \tag{1.40}$$

For what the denominator of (1.40) is regarded, by taking the derivatives of (1.37), we have:

$$\frac{\partial S(\Theta, f)}{\partial \theta} = j \sum_{mnpq} e^{j\alpha_{mnpq}} e^{j(\delta_{mn} - \delta_{pq})} \left[\frac{\partial^2 \alpha_{mnpq}}{\partial \theta^2} + j\left(\frac{\partial \alpha_{mnpq}}{\partial \theta}\right)^2\right] \tag{1.41}$$

with

$$\frac{\partial^2 \alpha_{mnpq}}{\partial \theta^2} = -k\sin(\theta)\left[(m-p)d_x\cos(\phi) + (n-q)d_y\sin(\phi)\right] = \Lambda_{mnpq}(\Theta, f)\,. \tag{1.42}$$

Therefore it is

$$\mathbb{E}\left[\left.\frac{\partial S(\Theta,f)}{\partial\theta}\right|_{\Theta=\widehat{\Theta}_0}\right]=j\chi^2\sum_{mnpq}\Omega_{mnpq} \tag{1.43}$$

where

$$\Omega_{mnpq}=\Lambda_{mnpq}(\widehat{\Theta}_0,f)+j\,\psi^2_{mnpq}(\widehat{\Theta}_0,f)\,. \tag{1.44}$$

Regarding the numerator of (1.40) it is

$$\begin{aligned}&S^2(\widehat{\Theta}_0,f)=\\ -&\sum_{mnpq}\sum_{rstu}\psi_{mnpq}(\widehat{\Theta}_0,f)\psi_{rstu}(\widehat{\Theta}_0,f)e^{j(\delta_{mn}-\delta_{pq})}e^{j(\delta_{rs}-\delta_{tu})}\end{aligned} \tag{1.45}$$

whose expectation is given by (1.46)

$$\begin{aligned}\mathbb{E}\left[S^2(\widehat{\Theta}_0,f)\right]=&-\chi^4\sum_{mnpq}\sum_{\substack{rstu\\ mn\neq pq\neq rs\neq tu}}\psi_{mnpq}(\widehat{\Theta}_0,f)\psi_{rstu}(\widehat{\Theta}_0,f)+\left(1-\upsilon^2\right)\sum_{mnpq}\psi^2_{mnpq}(\widehat{\Theta}_0,f)\\ -2\,\upsilon\,\chi^2\sum_{mnpq}\sum_{\substack{rs\\ mn\neq rs}}\psi_{mnpq}(\widehat{\Theta}_0,f)\psi_{rspq}(\widehat{\Theta}_0,f)&-2\chi^2\sum_{mnpq}\sum_{\substack{rs\\ pq\neq rs}}\psi_{mnpq}(\widehat{\Theta}_0,f)\psi_{rsmn}(\widehat{\Theta}_0,f)\end{aligned} \tag{1.46}$$

where $\upsilon=\mathbb{E}\left[e^{-j2\delta_{mn}}\right]=\mathbb{E}\left[e^{j2\delta_{mn}}\right]=\frac{1}{\Delta}\sin(\Delta)$. We finally obtain

$$\mathbb{E}\left[\delta\theta_0^2(\widehat{\Theta}_0,f)\right]=\frac{\mathbb{E}\left[S^2(\widehat{\Theta}_0,f)\right]}{-\chi^4\left[\sum_{mnpq}\Omega_{mnpq}\right]^2},\quad \mathbb{E}\left[\delta\phi_0^2(\widehat{\Theta}_0,f)\right]=\frac{\mathbb{E}\left[F^2(\widehat{\Theta}_0,f)\right]}{-\chi^4\left[\sum_{mnpq}\Omega^{'}_{mnpq}\right]^2} \tag{1.47}$$

with

$$\mathbb{E}^2\left[\left.\frac{\partial S(\Theta,f)}{\partial\phi}\right|_{\Theta=\widehat{\Theta}_0}\right]=-\chi^4\left[\sum_{mnpq}\Omega^{'}_{mnpq}\right]^2. \tag{1.48}$$

Appendix C

Equation (1.14) can be rearranged by developing the second-order series expansion of the term $e^{j\left[(m-p)\Psi_{\delta x}+(n-q)\Psi_{\delta y}\right]}$ as

$$\sum_{mnpq} \hat{w}_{mnpq} e^{j\delta_{mnpq}} \Delta^2_{mnpq} = \sum_{mnpq} \hat{w}_{mnpq} e^{j\delta_{mnpq}} \tag{1.49}$$

where $\Delta_{mnpq} = (m-p)\Psi_{\delta x} + (n-q)\Psi_{\delta y}$, and $\delta_{mnpq} = \delta_{mn} - \delta_{pq}$. To derive the BSA we adopt an approach similar to that proposed in [35] and [53] where the beam is considered alternatively lying on the XZ- and YZ-plane. Specifically, consider the case in which $\tilde{\phi}_0 = 0$ and $\delta\phi = 0$ so that the beam lies on the XZ-plane, with deviation $\pm\delta\tilde{\theta}_{x0}$ from the beam pointing direction in that plane. We have that $\Delta_{mnpq} = (m-p)kd_x\delta\tilde{\theta}_{x0}\cos(\tilde{\theta}_0)$ and (1.49) can be written as

$$\sum_{mnpq} \hat{w}_{mnpq} e^{j\delta_{mnpq}} (m-p)^2 k^2 d_x^2 \delta\tilde{\theta}_{x0}^2 \cos^2(\tilde{\theta}_0) = |\mathrm{AF}(\widetilde{\Theta}_0, f)|^2. \tag{1.50}$$

It is possible to write

$$\mathbb{E}\left[\delta\tilde{\theta}_{x0}(\widetilde{\Theta}_0, f)\right] \approx \mathbb{E}\left[\pm\left[\frac{|\mathrm{AF}(\widetilde{\Theta}_0, f)|^2}{\sum_{mnpq} \hat{w}_{mnpq} e^{j\delta_{mnpq}} (m-p)^2 k^2 d_x^2 \cos^2(\tilde{\theta}_0)}\right]^{1/2}\right] \tag{1.51}$$

and analogously

$$\mathbb{E}\left[\delta\tilde{\theta}_{y0}(\widetilde{\Theta}_0, f)\right] \approx \mathbb{E}\left[\pm\left[\frac{|\mathrm{AF}(\widetilde{\Theta}_0, f)|^2}{\sum_{mnpq} \hat{w}_{mnpq} e^{j\delta_{mnpq}} (n-q)^2 k^2 d_y^2 \cos^2(\tilde{\theta}_0)}\right]^{1/2}\right]. \tag{1.52}$$

Solving (1.51) and (1.52) appears very complicated because the expected value regards the ratio of dependent RVs.

Chapter 2

Personal Mobile Radars

This chapter presents the idea of the *personal radar*, already briefly described in the Introduction. First a comparison with traditional mapping solutions is reported in Sec. 2.1. Section 2.2 introduces the main idea of adopting mmW massive arrays for indoor map reconstruction. The details of the mapping algorithm will be described in Sec. 2.3. Simulation and experimental results will be finally discussed in Sec. 2.4.1 and 2.4.2.

2.1 Related works

The last progresses in the robotic field made available robots and simultaneous localization and mapping (SLAM) techniques for automatic creation of indoor maps [54, 55]. Traditionally, SLAM is based on the concept that a robot, moving in an unknown environment, recognizes the surrounding objects being then able to reconstruct a 2D/3D map of the area. This is typically done by steering a laser beam across a dense number of test directions and estimating the RTT of the signal reflected by the obstacles (targets) for each test direction. In such a way, from RTT estimates, the distance of targets can be inferred and, consequently, an accurate map of the environment can be built.

Current accurate SLAM, for automatic creation of indoor maps [54, 55, 56], requires both high-definition distance estimates (ranging) and very narrow steering beams (angle resolution), traditionally accomplished by laser technology. In addition, the exploitation of Wi-Fi (WiFi) and sensors integrated in smartphones for zero-effort automatic indoor positioning and mapping applications relate very poorly to the actual mobile position, and topological environment information can be hardly inferred.

Under a different perspective, the proliferation of smartphones, tablets, and wireless connectivity, has enabled the possibility of crowd sourcing which has proven to be an effective way to generate and maintain outdoor maps. An example is given by the OpenStreetMap project that has focused on creating outdoor maps, and relies on GPS traces and satellite imagery [57]. The same concept has been also proposed for zero-effort automatic indoor mapping using various sensors already embedded in smartphones, such as magnetometer and WiFi [58, 59, 60, 61].

The idea to adopt mmW radars to overcome the shortcomings of laser is not new and it has been considered for outdoor applications in some previous works, such as [62, 63, 64, 65], where a dedicated very high-directional antenna is mechanically steered. The consequent near-pencil beam returns a precise angle and range information thus making the modeling and characterization of the environment with mmW radars very similar to that based on laser. Obviously, such systems can not be integrated into smartphones or tablets. Stimulated by this possibility, this chapter presents the idea of placing massive antenna arrays in smartphones or tablets thus realizing a high-definition and low-cost *personal mobile radar* by means of which crowd sourcing high-definition indoor mapping and cooperative SLAM capabilities could be enabled [5, 21, 66]. In fact, the availability of a large number of antennas on mobile devices opens the possibility of realizing narrow beams with electronic-driven steering capabilities that are fundamental for high-accuracy mapping as a cheap and energy efficient alternative to laser technology [6]. The pervasive availability of personal radar capabilities on smartphones will enable high-definition, zero-effort and automatic indoor building mapping by exploiting the possibility of crowd sourcing (crowd mapping) [59, 60, 58, 61]. In addition, other new applications are possible such as blind people aid or the pictorial 3D environmental mapping where the third dimension results

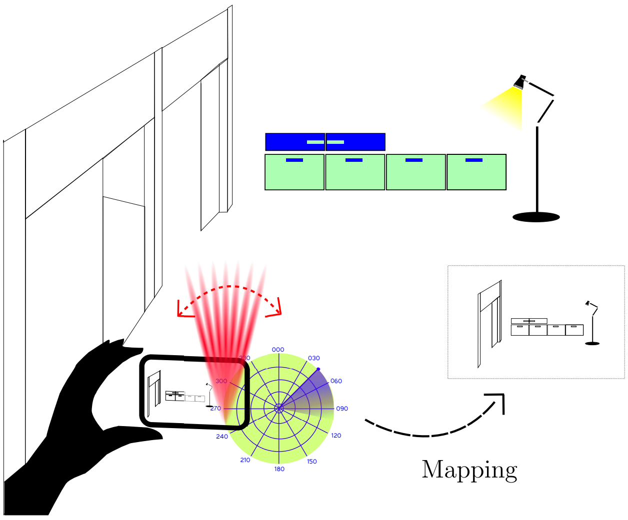

Figure 2.1: Personal radar idea.

by the integration of the angle/range information collected by the personal radar with the 2D picture coming from the conventional embedded camera. From a complementary perspective, in [67] a system of stereo cameras and integrated sensors is used to have the depth information and to create a 3D image of the environment. The main drawback of this solution is that cameras are not able neither to automatically scan the environment as they do not perform a beamforming operation (i.e. the user must be participatory as he/she has to "pilot" the scan process by properly moving the camera) nor to retrieve information about the electromagnetic properties of materials. The new approach proposed outperforms these weaknesses thanks to the adoption of mmW technology and of a multi-antenna radar system, which can scan the environment even if the smartphone is kept in the user pocket, i.e. without having the user participatory.

In the proposed mmW personal radar, wideband signals are employed to assure high ranging performance [4]. Unfortunately, technology constraints prevent the use of wideband time-delay components necessary to realize the required signals alignment from different array elements and only simple digitally-controlled phase shifters can be realistically adopted. Therefore, loss in steering and ranging accuracy due to quantized phase shifters and frequency selectivity might arise [44, 68]. In addition, even in case massive arrays are adopted, laser-like beams are not obtainable and each measurement might be affected by contributions coming from different directions due to the effect of an increased main lobe width and side-lobes level in the antenna radiation pattern. Thus, dedicated mapping approaches are needed to overcome these limitations and to make massive arrays an attractive candidate for environment mapping.

In the following, the state-of-the-art of existing mapping and SLAM techniques is presented together with an overview on mmW and massive array technologies. Secondly the steering and ranging capabilities of the proposed mmW personal radar concept will be analysed as a function of the signal bandwidth and the number of antennas composing the array. Specifically, the impact of frequency selectivity and quantization phase errors on the beam pointing error and beam width spread is jointly characterized. Successively the new mapping algorithm will be introduced. In particular, the low-complexity personal radar transceiver employs a massive antenna array and is based on the transmission of wideband signals with non-coherent processing of the corresponding backscatter response of the environment. Finally, the environment mapping capabilities of the personal radar are investigated by introducing a new Bayesian state-space model which considers a grid representation of the environment based on the electromagnetic characteristics of each space element and incorporating the new observation model able to properly account for the intrinsic characteristic of the massive antenna array and scanning process. Differently from the current state-of-the-art where a classic two-step approach is typically followed ("hard" decision) [64, 65], a new observation model is considered where all the available raw measurements ("soft" decision), and thus all the information coming from the antenna array, are exploited.

2.2 Personal radar concept

The previous analysis has highlighted how angle resolution, scanning time, signal bandwidth and ranging accuracy are tightly coupled. Now the mapping capabilities of the personal radar integrating massive arrays working

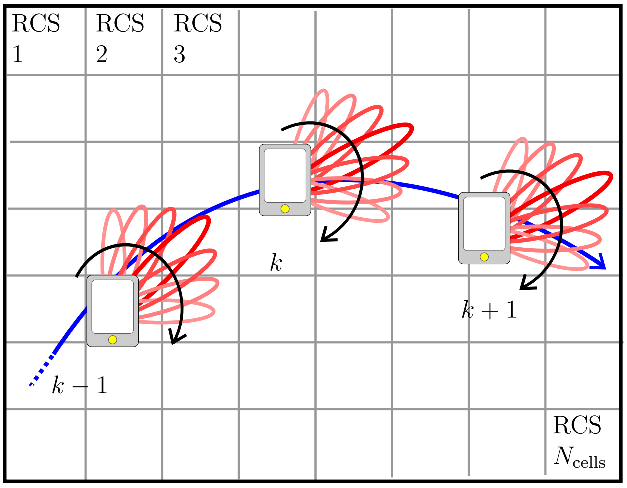

Figure 2.2: Grid-based mapping performed with the personal radar in three different positions at the instants $k-1$, k and $k+1$.

at mmW will be investigated. A person with a mobile terminal (e.g., a smartphone or a tablet) equipped with a mmW massive antenna array is considered walking with constant speed along a pre-determined trajectory. His/her position and orientation are constantly determined and updated by sensors integrated on the terminal or by external localization technologies [69]. The main task of personal radar is to incrementally build a consistent 2D/3D map of the surrounding environment. To this purpose, first a mmW radar collecting a rich set of measurements from the massive antenna array is proposed. Then a grid-based probabilistic mapping approach is adopted to fully exploit such measurements in a static environment. Hereafter, for simplicity of notation, the analysis is restricted to a 2D scenario even if the 3D extension is straightforward.

As it is well known from the literature, the environment mapping for moving radars needs three phases, once the initial step has been fixed: a prediction phase, an observation phase, and the final update phase. In the following, the first two phases will be characterized, with emphases the augmented state and the observation model of a massive array integrated into smartphones. Details on the implementation of extended Kalman-Filter (EKF), which is extensively described in the literature, is out of the scope of this

Ph.D thesis work.

The purpose of the personal radar is to provide a rich set of observations for the subsequent mapping phase starting from the analysis of the signals backscattered by the surrounding environment.

Let $\theta_b = -\pi/2\left(\frac{N_{\text{steer}}-1}{N_{\text{steer}}}\right) + (b-1)\pi/N_{\text{steer}}$, $b = 1, 2, \ldots N_{\text{steer}}$, be the set of N_{steer} steering directions considered during the scanning process defined, and θ_v the mobile orientation. Note that a large number of array elements implies a high angular resolution, and consequently a high number of steering directions and measurements. Consider a generic interrogation signal, for each steering direction θ_b, composed of N_{p} wideband pulses $p(t)$

$$g(t) = \sum_{l=0}^{N_{\text{p}}-1} p(t - lT_{\text{f}}) \tag{2.1}$$

with T_{f} being the time frame chosen so that all signals backscattered by the environment are received by the receiver before the transmission of the successive pulse, thus avoiding inter-frame interference. The consequent scanning time is $T_{\text{scan}} = T_{\text{ob}} N_{\text{steer}}$, where $T_{\text{ob}} = N_{\text{p}}\, T_{\text{f}}$.

Since each pulse is backscattered by the surrounding targets populating the environment, for the steering direction θ_b the received signal can be expressed as

$$r(t, \theta_b) = \sum_{l=0}^{N_{\text{p}}-1} s(t - lT_{\text{f}}, \theta_b) + n(t) \tag{2.2}$$

where $s(t, \theta_b) = p(t) \otimes h_{\text{C}}(t, \theta_b)$ is the channel response to the transmitted pulse $p(t)$ at direction θ_b, with $h_{\text{C}}(t, \theta_b)$ being the CIR taking the joint environment and antenna array response into account,[1] and with $n(t)$ being the additive white Gaussian noise (AWGN) with two-sided power spectral density $N_0/2$.

The received signal is first passed through an ideal bandpass filter with center frequency f_0 to eliminate out-of-band noise.[2] The filtered signal is

---

[1] $\otimes$ is the convolutional operator.

[2] This operation is necessary since the receiver is energy-based, as it will be described

denoted by

$$y(t,\theta_b) = \sum_{l=0}^{N_\mathrm{p}-1} x(t - lT_\mathrm{f}, \theta_b) + z(t) \tag{2.3}$$

where $x(t,\theta_b) = s(t,\theta_b) \otimes h_\mathrm{F}(t) \cong s(t,\theta_b)$ and $z(t) = n(t) \otimes h_\mathrm{F}(t)$, with $h_\mathrm{F}(t)$ being the impulse response of the filter.

To conjugate the need of having a manageable number of measurements and a low complexity receiver, a non-coherent approach based on energy measurements in a discretized time scale is considered . This approach also accounts for the complete uncertainty on the received waveform shape deriving from the a priori ignorance on environment electromagnetic characteristics. Specifically, energy measurements are taken during the time frame T_f after the transmission of each pulse by subdividing the time frame into $N_\mathrm{bin} = \lfloor T_\mathrm{f}/T_\mathrm{ED} \rfloor$ time slots (bins) of duration T_ED. Energy measurements are accumulated for each time bin over the N_p frames of the interrogation signal. The accumulated energy measurement at the sth time bin and bth steering angle θ_b is

$$e_{bs} = \sum_{k=0}^{N_\mathrm{p}-1} \int_{(s-1)\,T_\mathrm{ED}}^{s\,T_\mathrm{ED}} y^2(t + kT_\mathrm{f}, \theta_b)\, dt \tag{2.4}$$

with $s = 1, 2, \ldots, N_\mathrm{bin}$ and $b = 1, 2, \ldots\ N_\mathrm{steer}$. Note that T_ED must be chosen to accommodate most of the energy of the received pulse, i.e. $T_\mathrm{ED} \approx 1/W$.

According to [70], for each energy bin, the normalized energy measurement output can be well approximated by

$$\Lambda_{bs} = \frac{2}{N_0}\, e_{bs} \simeq \frac{1}{\sigma^2} \sum_{k=0}^{N_\mathrm{p}-1} \sum_{i=(s-1)N_\mathrm{d}}^{sN_\mathrm{d}} \left(x_i(\theta_b) + z_i^{(k)} \right)^2 \tag{2.5}$$

where $N_\mathrm{d} = 2WT_\mathrm{ED}$, $\sigma^2 = N_0 W$ is the noise variance, and $z_i^{(k)}$ are for odd i (even i) the samples of the real (imaginary) part of the equivalent low-pass of $z(t + kT_\mathrm{f})$, $k = 1, 2, \ldots, N_\mathrm{p}$, taken at Nyquist rate W in each interval T_ED.

---

later.

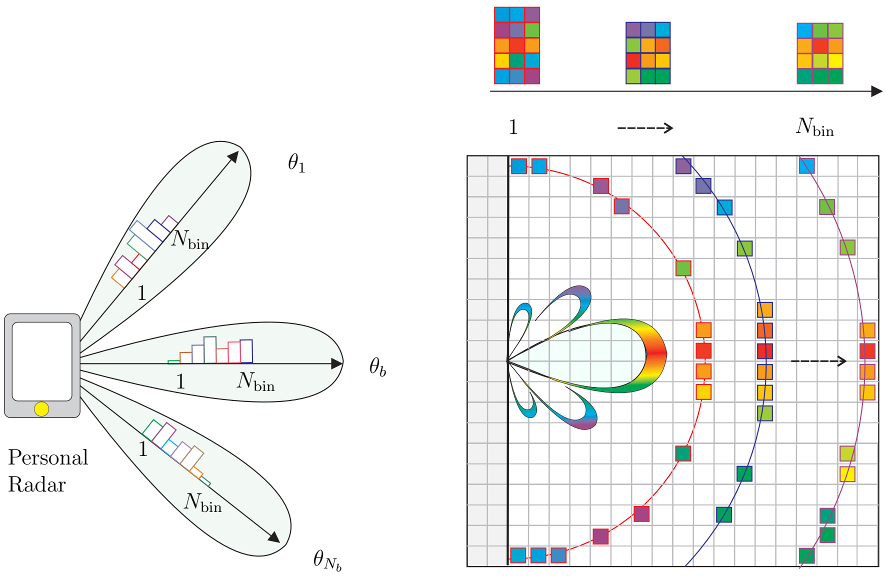

Figure 2.3: Grid-based mapping performed with the personal radar integrated in the smartphone.

In (2.5) the property $x(t+kT_{\rm f}, \theta_b) = x(t, \theta_b)$ is used, with $k = 1, 2, \ldots, N_{\rm p}$, so that $x_i(\theta_b)$ represents for odd i (even i) the samples of the real (imaginary) part of the equivalent low-pass of $x(t, \theta_b)$, taken at Nyquist rate W in each interval $T_{\rm ED}$, which does not depend on k.

It turns out that Λ_{bs} is a non-central Chi-square distributed RV with $N = N_{\rm p} N_{\rm d}$ degrees of freedom. The non-centrality parameter is $\lambda_{bs} = 2\gamma_{bs}$ [70] , where γ_{bs} is given by

$$\gamma_{bs} = \frac{N_{\rm p}}{2\sigma^2} \sum_{i=(s-1)N_{\rm d}}^{sN_{\rm d}} x_i^2(\theta_b) \simeq \frac{N_{\rm p}}{N_0} \int_{(s-1)\,T_{\rm ED}}^{s\,T_{\rm ED}} x^2(t, \theta_b)\, dt\ . \tag{2.6}$$

Note that (2.6) represents the accumulated SNR corresponding to the sth time bin and the bth steering direction which increases with the number $N_{\rm p}$ of pulses at the expense of a longer observation time $T_{\rm ob}$. Furthermore, each energy measurement e_{bs} does not depend only on the signal backscattered in the steering direction θ_b, but also on all contributions coming from different directions according to the shape of the array radiation pattern which affects $h_{\rm C}(t, \theta_b)$ and hence $x(t, \theta_b)$. During the mapping process these contributions could create ambiguities but, at the same time, permit to discriminate between different array configurations.

2.3 Mapping algorithm for personal radars

In the following, a state-space model for probabilistic mapping is introduced. Differently from literature, the model proposed is able to exploit the measurements from the massive array radar under a Bayesian filtering approach [21].

In a probabilistic mapping framework, the position and orientation of the mobile is known or partially known if resulting from an external localization system exploiting, for example, inertial measurement unit (IMU) and RF sensors measurements. The same mmW technology could be in principle exploited to provide extremely high accuracy positioning down to a few centimetres when interacting with base stations [4].

Different models can be adopted to represent the map. Feature-based models are privileged when a set of landmarks characterizes the environment and the sensors on the mobile device are able to well-discriminate them (i.e. using laser and video technologies). On the contrary, grid-based models for map representation are more suitable when sensors provide imprecise measurements from which it is difficult to discriminate between different features, such as when using radar [71]. In grid-based approaches, the environment is discretized in cells whose position is a-priori known and hence the number of states is fixed to the number of cells. In most of works, the state is a binary RV and represents the presence or not of any physical element in the corresponding cell (occupancy grid) [72].

In the following a RCS-based description of cells is adopted in a map-grid representation context. Moreover massive array radars with electronically steering beams are considered instead of mechanically steering devices. In particular, a 2D grid of $N_{\mathrm{L}} = X_{\mathrm{grid}} Y_{\mathrm{grid}}$ cells representative of the environment is considered. Differently from previous works, a one-step procedure is followed where a larger observation vector is introduced accounting for the specific massive antenna array radiation pattern and whose response could depend, in principle, on several cells, as illustrated in Fig. 2.3. Therefore, the mapping process works with a richer information set and no specific radar detection scheme and associated detection threshold evaluation strategy have to be designed, as required instead in conventional two-step approaches [64]. In the following, the adopted scheme is described, and the differences with classic Bayesian SLAM are highlighted.

2.3.1 State vector

The state vector at time k is defined as

$$\mathbf{x}(k) = \mathbf{m}(k) = [m_1(k),\, \ldots,\, m_i(k),\, \ldots,\, m_{N_\mathrm{L}}(k)]^\mathrm{T} \tag{2.7}$$

where $m_i(k)$ indicates the root radar cross section (RRCS) (with sign) of the ith cell of the grid. Obviously, if the cell is empty (only air), the corresponding RRCS is zero. Note that in the model herein adopted the dependency of $m_i(k)$ from the frequency is neglected and the environment is assumed stationary.

2.3.2 Observation model

Define $\mathbf{e}(k)$ the vector containing the accumulated measured energy at the output of the receiver at time k

$$\mathbf{e}(k) = [e_{11}(k),\, \ldots,\, e_{1N_\mathrm{bin}}(k),\, \ldots,\, e_{bs}(k),\, \ldots, e_{N_\mathrm{steer}1}(k),\, \ldots\, e_{N_\mathrm{steer}N_\mathrm{bin}}(k)]^\mathrm{T} \tag{2.8}$$

where $e_{bs}(k)$ is given by (2.4). As shown in the previous section, $e_{bs}(k)$ is proportional to a non-central Chi-square distributed RV that makes the formulation of the observation model challenging. However, for large N (typically > 50), i.e. for large N_p, the non-central Chi-square distribution can be approximated with a Gaussian distribution having mean $\lambda_{bs}+N$ and variance $2(N+2\lambda_{bs})$ [73]. We exploit this property to construct a tractable Gaussian observation model of the state-space model

$$\mathbf{z}(k) = \left[z_{11}(k), \ldots, z_{bs}(k), \ldots, z_{N_{\text{steer}}N_{\text{bin}}}(k)\right]^{\mathrm{T}} = \mathbf{h}(\mathbf{x}(k)) + \mathbf{v}(k) \tag{2.9}$$

where $z_{bs}(k)$ is the energy observation corresponding to the sth time bin and the bth steering angle, $\mathbf{h}(\cdot)$ is the observation function that relates the state vector to the observations, and

$$\mathbf{v}(k) = \left[v_{11}(k), \ldots, v_{bs}(k), \ldots, v_{N_{\text{steer}}N_{\text{bin}}}(k)\right]^{\mathrm{T}} \tag{2.10}$$

is the vector of uncorrelated Gaussian observation errors with zero mean and covariance matrix $\mathbf{R}(k) = \operatorname{diag}\left(\sigma_{11}^2(k), \ldots, \sigma_{bs}^2(k), \ldots, \sigma_{N_{\text{steer}}N_{\text{bin}}}^2(k)\right)$ with $\sigma_{bs}^2(k) = \operatorname{Var}\left(e_{bs}(k)\right)$. Note that the length $N_{\mathrm{m}} = N_{\text{steer}}N_{\text{bin}}$ of $\mathbf{z}(k)$ is related either to the number of the steering directions, depending on the antenna array pattern $G(\theta, f)$, and to the number of time bins depending on the signal bandwidth W through T_{ED}.

The generic element of $\mathbf{z}(k)$ can be written as

$$z_{bs}(k) = h_{bs}(\mathbf{x}(k)) + v_{bs}(k) = \mathbb{E}\left[e_{bs}(k)\right] + v_{bs}(k) \tag{2.11}$$

with $b = 1, 2, \ldots, N_{\text{steer}}$, $s = 1, 2, \ldots, N_{\text{bin}}$.

From (2.5) and (2.6) it is $\mathbb{E}\left[e_{bs}(k)\right] = T_{\mathrm{f}}P_{bs}(k)$ whereas $v_{bs}(k)$ is the measurement noise, as defined in (2.10), with variance $\sigma_{bs}^2(k) = N_0(N_{\mathrm{p}}WT_{\text{ED}}N_0 + 2T_{\mathrm{f}}P_{bs}(k))$. Using (1.21), the term $P_{bs}(k)$ depends on $\mathbf{x}(k)$ and represents the average received power at the bth steering angle and the sth time bin given by

$$P_{bs}(k) = \frac{\mathbb{E}\left[e_{bs}(k)\right]}{T_{\mathrm{f}}} = P_w + \sum_{i \in \mathcal{R}(s)} \int_W \frac{P_t(f)\, c^2\, m_i^2(k)\, G^2(\theta_i - \theta_v - \theta_b, f) N_{\mathrm{p}}}{f^2\, (4\pi)^3 d_i^4}\, df \tag{2.12}$$

where $P_w = \frac{\sigma^2 T_{\text{ED}} N_{\mathrm{p}}}{T_{\mathrm{f}}}$ is the noise power, d_i and θ_i are, respectively, the distance and angle between the mobile and the ith cell. Function $\mathcal{R}(s)$ returns the set of cells indexes contributing to the sth time bin (i.e. all the cells located at a distance close to $s \cdot d_{\mathrm{bin}}$ with $d_{\mathrm{bin}} = c \cdot T_{\mathrm{ED}}/2$).

Note that in (2.12) the actual footprint area corresponds to the aggregate area of the cells illuminated by the beam. In fact, $m_i(k)$ is evaluated using (1.21), by setting the footprint area A_{fp} to the area of a cell.

2.3.3 EKF-Mapping

There are several recursive approaches belonging to the Bayesian filtering theory to evaluate the posterior distribution $p(\mathbf{x}(k)|\mathbf{z}(1:k))$ of $\mathbf{x}(k)$ given the set of measurements $\mathbf{z}(1:k) = \{\mathbf{z}(1), \mathbf{z}(2), \ldots, \mathbf{z}(k)\}$ collected by the mobile device until time instant k. Among them, here the EKF is employed which offers a good trade-off between performance and complexity considering the intrinsic large state vector of dimension N_{L} resulting from the grid-based map representation.

The mean and covariance state matrix of the predicted state are, in linear, $\hat{\mathbf{x}}(k+1|k) = \hat{\mathbf{x}}(k|k)$ and $\mathbf{P}(k+1|k) = \mathbf{P}(k|k)$ respectively, due to the stationarity of the environment.[3] The prediction for the observation model is given by $\hat{\mathbf{z}}(k+1|k) = \mathbf{h}(\hat{\mathbf{x}}(k+1|k))$. Once the new measurement vector $\mathbf{e}(k+1)$ is available, the innovation in the model is

$$\boldsymbol{\nu}(k+1) = \mathbf{e}(k+1) - \hat{\mathbf{z}}(k+1|k)\,. \tag{2.13}$$

Consequently, the correction step performed by the EKF is described by

$$\begin{aligned} \hat{\mathbf{x}}(k+1|k+1) &= \hat{\mathbf{x}}(k+1|k) + \mathbf{W}(k+1)\,\boldsymbol{\nu}(k+1) \\ \mathbf{P}(k+1|k+1) &= \mathbf{P}(k+1|k) - \mathbf{W}(k+1)\mathbf{S}(k+1)\,\mathbf{W}^{\mathrm{T}}(k+1) \end{aligned} \tag{2.14}$$

where

$$\begin{aligned} \mathbf{S}(k+1) &= \nabla\mathbf{h}\,\mathbf{P}(k+1|k)\nabla\mathbf{h}^T + \mathbf{R}(k+1) \\ \mathbf{W}(k+1) &= \mathbf{P}(k+1|k)\nabla\mathbf{h}^T\mathbf{S}^{-1}(k+1) \end{aligned} \tag{2.15}$$

with $\nabla\mathbf{h}$ being the Jacobian of $\mathbf{h}(\cdot)$ evaluated in $\hat{\mathbf{x}}(k+1|k)$, which gives using

---

[3] The notation $(m|n)$ indicates at time m given the observations until time n.

(2.11) and (2.12)

$$\frac{\partial h_{bs}}{\partial m_i} = \begin{cases} 2\, m_i \int_W \frac{P_t(f)\, c^2\, G^2(\theta_i - \theta_\mathrm{v} - \theta_b, f) T_\mathrm{f} N_\mathrm{p}}{f^2\, (4\pi)^3 d_i^4}\, df & \text{if } \; i \in \mathcal{R}(s) \\ 0 & \text{otherwise.} \end{cases} \tag{2.16}$$

In the numerical results a case study is provided implementing the state-space model and the EKF mapping approach here introduced.

2.4 Results

Mapping capability is analysed in this section by exploiting the new state-space model proposed in Sec. 2.3. Results obtained through simulations are reported in Sec. 2.4.1 whereas those based on real collected radar measurements in Sec. 2.4.2.

2.4.1 Simulation results

System parameters

In the following, it is assumed the same scattering regime illustrated in Sec. 1.2.2. The scanning time is $T_{\mathrm{scan}} = 80\,\mu$s, the noise figure $N_{\mathrm{F}} = 4\,$dB and it is assumed the transmission of a RRC signal compliant with the FCC mask at 60 GHz [49], but with an average EIRP limited to 30 dBm to make the system suitable for battery-powered handset devices.

Mapping results considering phased-radar

The previously described mapping algorithm has been implemented in MATLAB in order to validate its theoretical performance.

The case study proposed refers to a typical indoor office environment of $20 \times 20\,\mathrm{m}^2$, whose layout is shown in Fig. 2.4, which has been discretized in a grid of cells having area $0.2 \times 0.2\,\mathrm{m}^2$ each, according to the high arrays resolution, and accounting for a wall attenuation, due to its thickness, of 40 dB [48]. The mobile device with personal radar capabilities moves along a

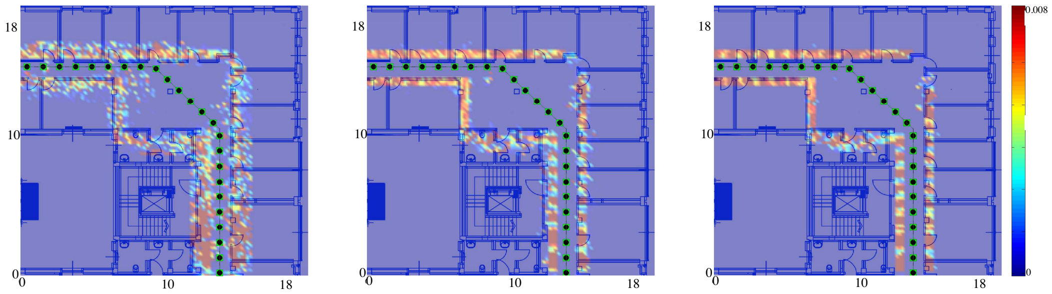

Figure 2.4: 2D mapping using 4×4 (top-left), 10×10 (top-right) and 15×15 (bottom) antenna arrays with a perfect knowledge of mobile position and no quantization errors.

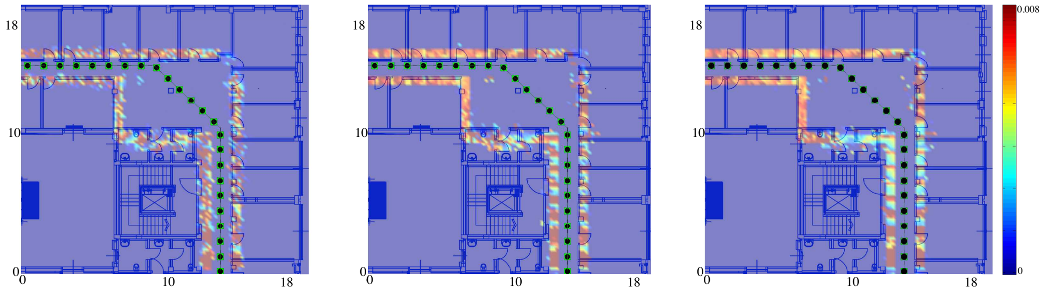

Figure 2.5: 2D mapping using 10×10 antenna arrays with $W = 500\,\text{MHz}$ (top-left), $W = 2\,\text{GHz}$ (top-right) and $W = 3\,\text{GHz}$ (bottom) with no quantization errors and a perfect knowledge of mobile position.

pre-determined trajectory and speed of 1m/s, and its reference orientation is always towards the direction of movement. Radar measurements are taken every second, and black circles refer to the true radar positions while the green squares to the positions perceived by the mobile device.

The personal radar performance are compared in three cases, $N_{\text{array}} = 15 \times 15$, $N_{\text{array}} = 10 \times 10$ and $N_{\text{array}} = 4 \times 4$, respectively. In the previous numerical results, the phased array with $N_{\text{array}} = 10 \times 10$ elements resulted as a value corresponding to a good compromise between ranging and steering accuracy. A time frame of $T_{\text{f}} = 100\,\text{ns}$ is considered with bandwidth $W = 1\,\text{GHz}$ and, consequently, $T_{\text{ED}} = 1\,\text{ns}$ if not otherwise indicated. The constraint on the scanning time is fixed to $T_{\text{scan}} = 80\mu\text{s}$ while the number

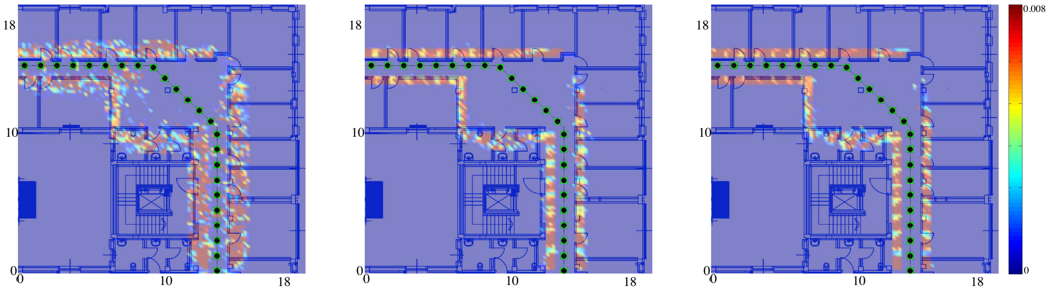

Figure 2.6: 2D mapping using 4 × 4 (top-left), 10 × 10 (top-right) and 15 × 15 (bottom) antenna arrays with a perfect knowledge of mobile position and with array quantization errors.

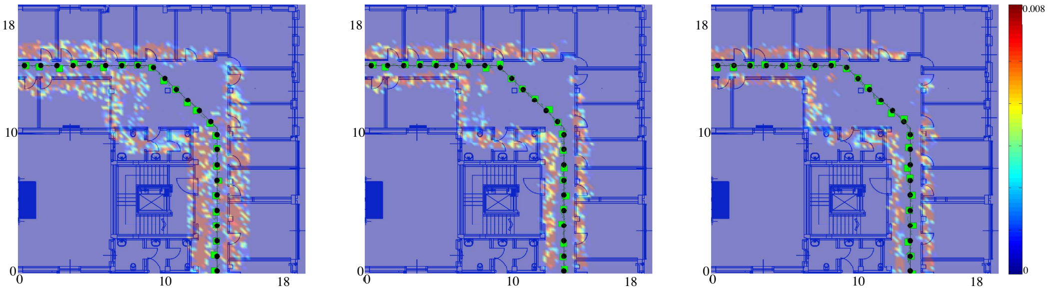

Figure 2.7: 2D mapping using 4 × 4 (top-left), 10 × 10 (top-right) and 15 × 15 (bottom) antenna arrays and with quantization and mobile position (10 cm) and orientation errors (5°).

of steering directions and of pulses per interrogation signal varies with the number of antenna elements, as N_{steer} increases with N_{array}. In fact, for $N_{\text{array}} = 16$, $N_{\text{array}} = 100$ and $N_{\text{array}} = 225$ antenna elements, it is $N_{\text{p}} = 100$, $N_{\text{p}} = 40$ and $N_{\text{p}} = 27$, respectively.

In the following results, the reconstructed map is represented in terms of RCS estimated through the EKF algorithm and it is juxtaposed to the true map of the office environment. Obviously, only the walls resulting in line-of-sight during the mobile movement are expected to be identified.

Performance in absence of system non-idealities Fig. 2.4 shows the estimated maps obtained with ideal (i.e. quantization error-free) antenna

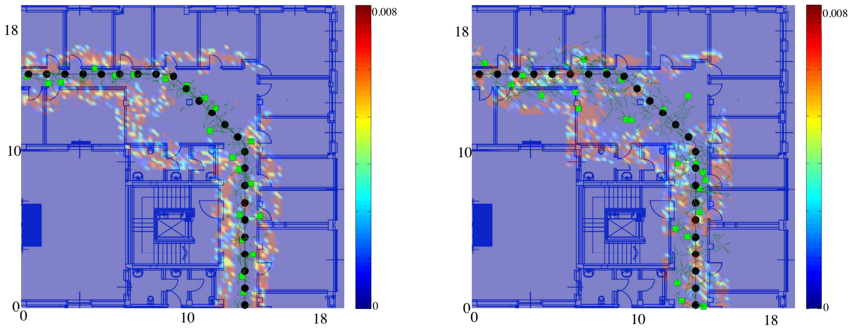

Figure 2.8: 2D mapping using 10 × 10 antenna arrays with mobile position errors of 0.5 m (left) and 1 m (right) and $W = 1$GHz.

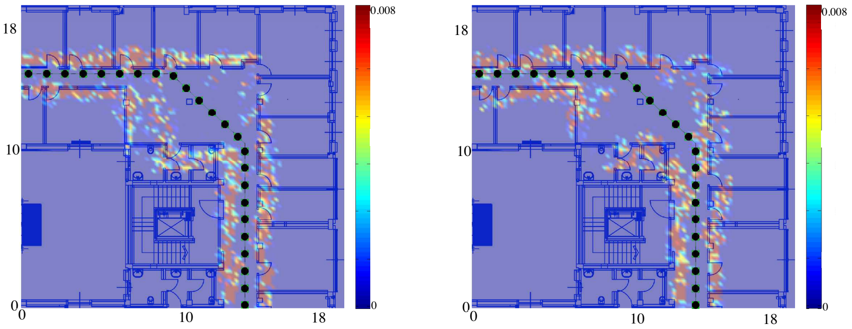

Figure 2.9: 2D mapping using 10×10 antenna arrays with mobile orientation errors of 10° (left) and 20° (right) and $W = 1$GHz.

arrays of 4×4 (left), 10×10 (right) and 15×15 (bottom) elements, and with perfect knowledge of the mobile position and orientation. The higher number of cells that are correctly identified using the 10×10 array with respect to 4×4 and 15×15 array puts in evidence that an enhanced performance in terms of map estimation accuracy can be found as a compromise between ranging accuracy and angular resolution, in agreement with the results of Sec. 1.2.2. In fact, for $N_{\text{array}} = 15 \times 15$, the map is well defined at the prize of a reduced SNR, and thus part of the map is not reconstructed, while for $N_{\text{array}} = 4 \times 4$ the higher number of pulses improves the SNR enabling the full reconstruction of the map, but with a lower angle resolution.

Fig. 2.5 reports the maps estimated through the adoption of an ideal

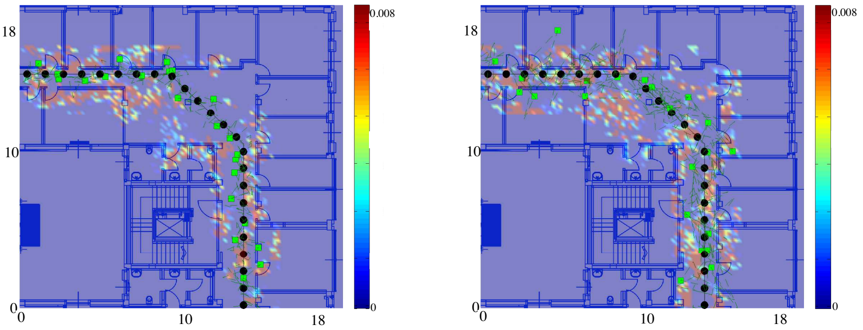

Figure 2.10: 2D mapping using 10 × 10 antenna arrays with position and mobile orientation errors 0.5 m+20° (left) and 1 m+20° (right) and W = 1GHz.

antenna array equipped with a 10 × 10 antenna array for different signal bandwidths. In particular, from the left to the right, the results obtained with $W = 500\,\text{MHz}$ (i.e. $T_{\text{ED}} = 2\,\text{ns}$), $W = 2\,\text{GHz}$ (i.e. $T_{\text{ED}} = 0.5\,\text{ns}$) and $W = 3\,\text{GHz}$ (i.e. $T_{\text{ED}} = 0.33\,\text{ns}$) are shown. As expected, when increasing the bandwidth the mapping performance improves due to the increased time resolution at the expense of an increased number N_{bin} of bins, and thus of receiver complexity.

Performance with System Non-Idealities The effect of phase quantization errors is shown in Fig. 2.6 where antenna arrays with very rough phasing capability of step $\Delta = \pi/2$ are considered. When compared to Fig. 2.4, it can be noted that, even if quantization errors might affect the array performance, their negative effect on map reconstruction can be significantly mitigated if their impact on radiation pattern is properly characterized in the measurement model (2.11) by adopting the analysis of Sec. 1.2.

In Fig. 2.7 mobile orientation and position errors caused by an imperfect external positioning system are included. In particular, orientation estimation errors with standard deviation of 5° are taken into account together with position estimation errors with 0.1 m standard deviation [74], both along the $x-$ and the $y-$axis. It is evident from the figure how estimated maps become much more degraded even if the performance of 10×10 antenna array is still

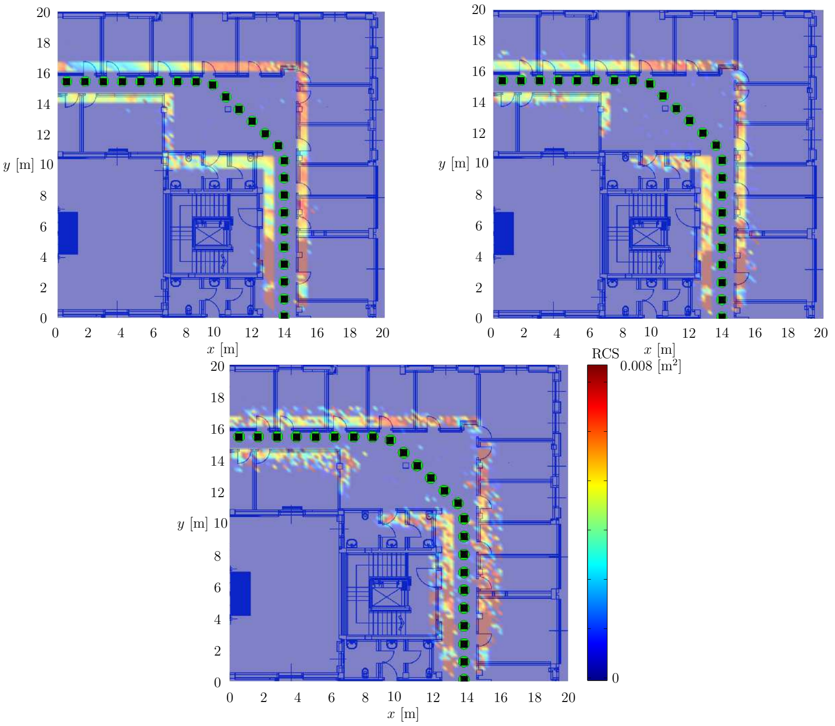

Figure 2.11: Mapping results using 20×20 (top-left), 15×15 (top-right) and 10×10 transmitarray (bottom) with 2 bits phase compensation, optimal F/D ratio and with a perfect knowledge of TA-radar position and orientation.

acceptable.

Despite future indoor location systems are expected to guarantee a self-localization with errors below 0.5 m, current technologies provide errors typically greater than 0.5 m. Thus, in Fig. 2.8 a mobile position error of 0.5 and 1 m is considered. Performance is evidently degraded, but it could be improved, for instance, through crowd sensing mechanism where users share their measurements in a cooperative way.

Fig. 2.9 reports the mapping results considering an augmented orientation estimation error of 10° and 20°, respectively. As we can see, the orientation estimation accuracy has a less detrimental effect on the mapping reconstruction with respect to the position.

Finally, Fig. 2.10 shows the results obtained when high position and orientation errors are present. As shown, the mapping quality is highly degraded and a crowd-sensing mechanism becomes essential to refine the map estima-

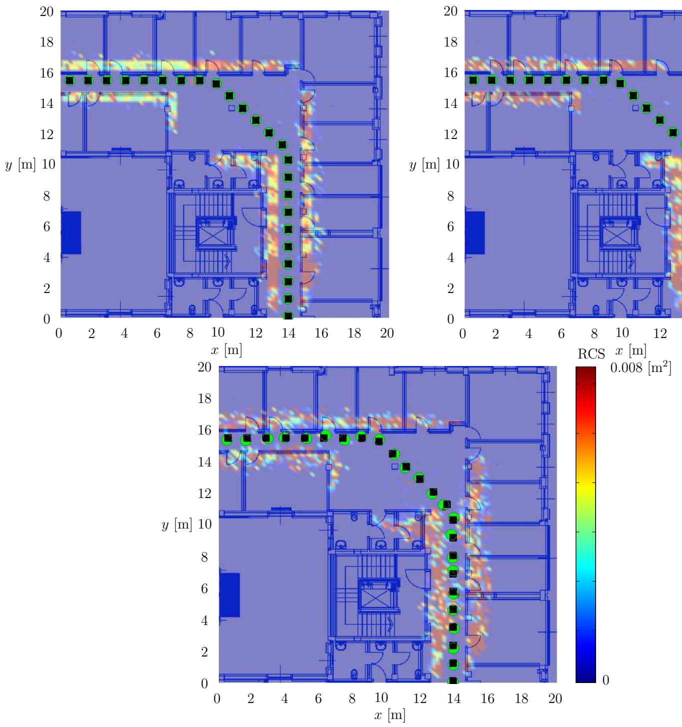

Figure 2.12: Mapping results using 15 × 15 TA with a perfect knowledge of TA-radar position and orientation and with a reduced focal distance F = 10mm (top-left) and F = 5mm (top-right), and with TA-radar position and orientation errors and F = 10mm (bottom).

tion.

Mapping results considering TA-radar

In this section the mapping results considering the radar equipped with a TA are presented. As before the radar explores the surrounding area and collects energy measurements by performing a scanning process over an angular range of $(-60°, 60°)$. The TA-radar moves along a determined and known path with a speed of $1\,\mathrm{m/s}$ and taking measurements every second. The path is indicated in Figs. 2.11 and 2.13; the black squares refer to the true TA-radar position while the green circles to the positions perceived by sensors. The orientation of the radar is always in the sense of the movement.

The results compare the TA mapping capabilities in terms of array size and focal distance degradation taking into account the quantization effect introduced by the discrete values of phase shifts. A 2-bit phase compensation is here adopted as a good compromise between maximum gain and TA unit-cells complexity.

As before, the time to complete an entire scan is fixed to $T_{\text{scan}} = 80\,\mu$s while the number of steering directions and of pulses per interrogation signal varies with the number of antenna elements, i.e. $N_{\text{p}} = 81$, $N_{\text{p}} = 62$, $N_{\text{p}} = 21$ with $N_{\text{array}} = 10 \times 10$, $N_{\text{array}} = 15 \times 15$, $N_{\text{array}} = 20 \times 20$, respectively.

Fig. 2.11 shows the RCS map estimation results considering a personal radar equipped with TAs of different size at $(F/D)_{\text{opt}}$ and without position and orientation errors. As can be seen, the mapping estimation accuracy increases with a higher number of antennas. In particular, an improved angular resolution is experienced with $N_{\text{array}} = 20 \times 20$ while the performance drastically decreases when $N_{\text{array}} = 10 \times 10$. In fact, the number of cells that are badly estimated is higher. Thus, a good trade-off between map's definition and TA complexity is represented by $N_{\text{array}} = 15 \times 15$, which guarantees good mapping performance while the personal radar complexity is kept affordable.

As previously discussed, another important parameter for array integrability in smart devices is the F/D ratio. Fig. 2.13-top shows the results obtained with $N_{\text{array}} = 15 \times 15$ and reduced F/D ratios, i.e. $F = 10\,\text{mm}$ and $F = 5\,\text{mm}$ instead of $F_{\text{opt}} = 19\,\text{mm}$. The reduced focal distance translates both in a gain degradation and in a larger main beam with a consequently reduction of the received SNR and of angular definition. Results for $F = 10\,\text{mm}$ show a slighter degradation of the mapping capability with respect to those obtained for F_{opt}. The effect of mobile radar positioning errors are investigated in Fig. 2.13-bottom where we have introduced orientation and position estimation errors with standard deviation of 5° and $0.1\,\text{m}$, both along the x- and the y- axis, respectively. It is evident from the figure how estimated maps become much more degraded even if the performance is still acceptable. Thus, if a key design parameter of the personal radar is represented by its compactness, which is the case when TAs have to be embedded into portable devices, $F = 10\,\text{mm}$ represents a valid and performing alternative to the solution with $F = F_{\text{opt}}$ which is less manageable.

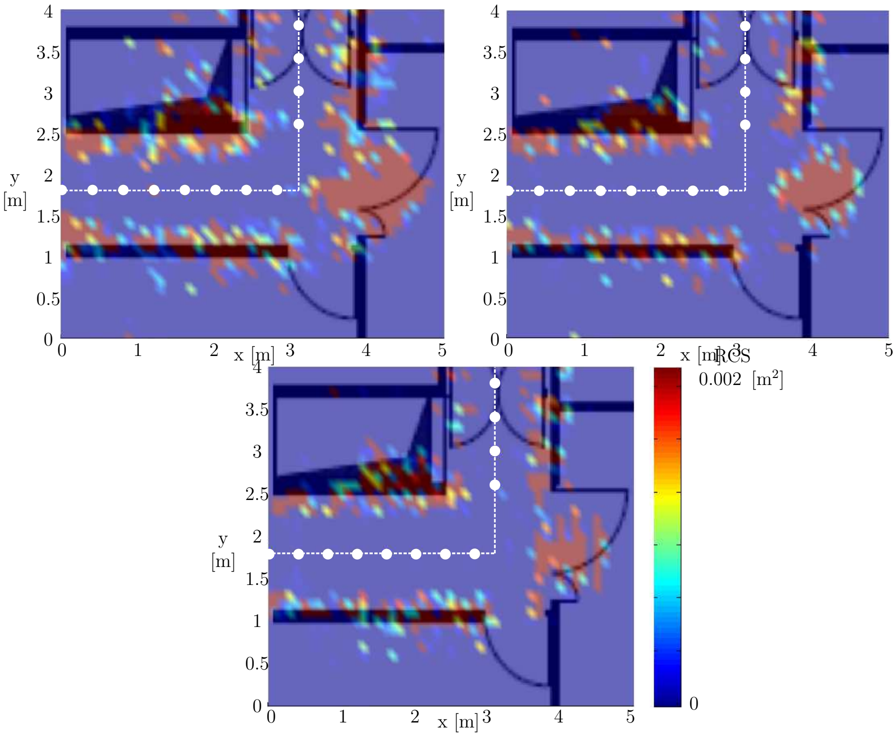

Figure 2.13: Mapping results using 1-bit 20×20 transmitarrays, $W = 1-2-3$ GHz (top-left, top-right and bottom, respectively), $N_\mathrm{p} = 100$ and exploiting real measured data.

2.4.2 Experimental results

Mapping using collected data

This section describes the mapping results obtained with the proposed model by including both simulated and measured data. The measurement campaign is illustrated in Sec. 1.3. The case study here described refers to the corridor environment described in Sec. 1.3 whose layout is juxtaposed to the estimated RCS maps in the results. As previously mentioned, a grid-based approach is adopted where the environment is discretized in cells having area $0.1 \times 0.1\,\mathrm{m}^2$ each according to the TA radiation patterns. The radar is equipped with the TA described in Sec. 1.3, exploring the surrounding area and collecting energy measurements by performing a scanning process over an angular range of $(-90°, 90°)$ with a step of 5° as described in previous sections. The TA-radar moves along a determined and known path with a spatial step of 0.405 m. In

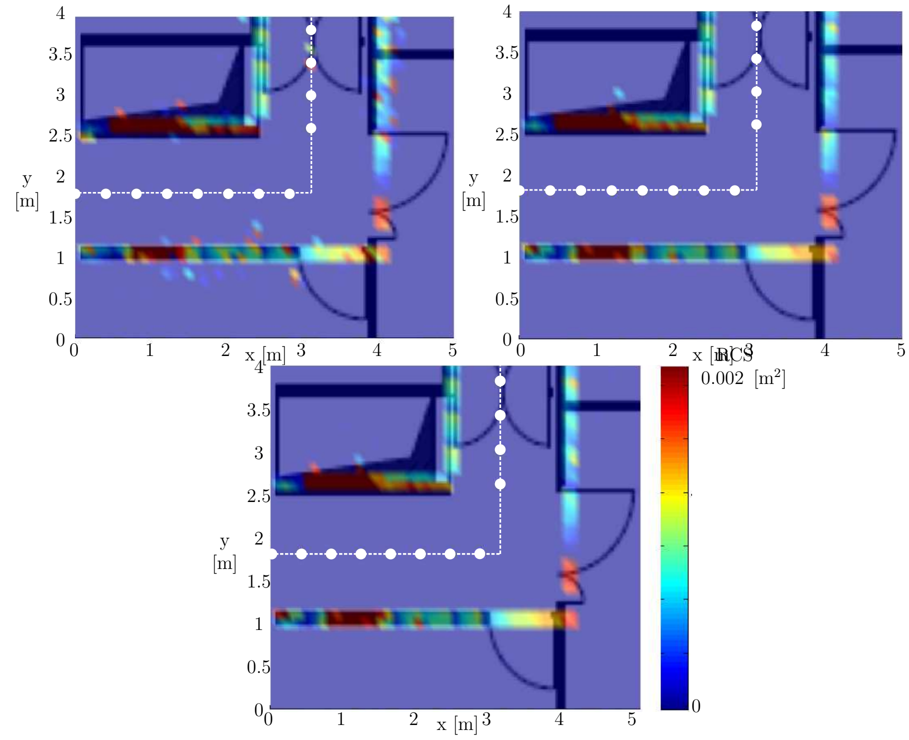

Figure 2.14: Mapping results using 1-bit 20×20 transmitarrays, $W = 1-2-3\,\text{GHz}$ (top-left, top-right and bottom, respectively), $N_\text{p} = 100$ and exploiting simulated data.

this scenario the TA-radar position and orientation are known.

The TA mapping capabilities are compared in terms of the signal bandwidth and by taking into account the quantization effect introduced by the 1-bit phase shift. A noise figure of $N_\text{F} = 4\,\text{dB}$, $T_0 = 290\,\text{K}$ and a signal bandwidth of $W = 1-2-3\,\text{GHz}$ (with $T_\text{ED} = 1/W$) are considered. RRC pulses centered at frequency $f_\text{c} = 60\,\text{GHz}$, roll-off factor $\alpha = 0.6$, and pulse width parameter $t_\text{p} = (1+\alpha)/W$ have been adopted. The time frame has been set to 100 ns and the number of transmitted pulses to $N_\text{p} = 100$. As before, results are obtained considering an EIRP of 30 dBm in accordance to Federal Communications Commission (FCC) mask at 60 GHz [49]. In this case, the measurement vector $\mathbf{e}(k)$ is given by data collected during measurements, where the energy profiles are directly included.

In Fig. 2.13 the mapping results exploiting the accumulated energy measurements are reported as a function of the signal bandwidth. Specifically, from the left to the right the RCS estimated map obtained with $W = 1\,\text{GHz}$ (i.e. $T_{\text{ED}} = 1\,\text{ns}$), $W = 2\,\text{GHz}$ (i.e. $T_{\text{ED}} = 0.5\,\text{ns}$) and $W = 3\,\text{GHz}$ (i.e. $T_{\text{ED}} = 0.34\,\text{ns}$) are shown. As expected, when increasing the bandwidth the mapping performance improves due to the increased temporal resolution.

Results obtained with $W = 3\,\text{GHz}$ are quite satisfactory as there is a nice match between the real maps and those estimated.

Then the measurements step has been simulated taking into account the RCS scattering model described in previous sections. In this scenario, the radar has been assumed moving with a speed of 1 m/s and taking measurements every 0.4 s. The radiation characteristics of the 1-bit 20×20 TAs used for measurements have been included in the simulator. As before, in Fig. 2.14 the simulation results are reported as a function of the signal bandwidth. Discrepancies between the previous results are due to different phenomena. First of all in the simulations a simple scattering model has been assumed. As a consequence, when considering collected measurements as an input for the mapping simulator a mismatch between the model and the real scattering behaviour can cause performance degradation. Secondly, in simulations a free space propagation condition is assumed for each interrogated cell supposing that the multipath effects are implicitly taken into account when including all the array pattern information in the grid-based approach. Obviously a more realistic channel model might help to fill the gap between simulations and measurements. Finally, in the simulation results the far-field assumption has been made. Thanks to this hypothesis, it is possible to exploit the far-field TA radiation pattern both in the prediction and the measurement phases when evaluating the mapping performance. Contrarily, in the real scenario where the measurements have been collected in a corridor (1.6 m width) the far-field condition is not always satisfied due to the high TA directivity with the consequence that the expected TA main beam could be not perfectly formed. This fact could cause a mismatch between the prediction and the measurement step of the mapping algorithm. Future works will be addressed in improving the mapping algorithm by properly accounting for such phenomena.

2.5 Conclusions

This chapter presents the idea of adopting massive antenna arrays at mmW as an effective way to embed personal radar capabilities in future smartphones. The environment mapping capabilities of the proposed personal radar have been investigated through the introduction of a non-coherent radar architecture and a new state-space model, within a grid-based Bayesian framework, in which each cell of the grid has been characterized by a specific RCS-based occupancy value. The peculiarities of the antenna array have been properly exploited by a direct integration of massive array radar measurements with the radar and mapping processes.

As an example of existing massive array technology to be embedded in personal radars TAs have been investigated . The performance of TAs has been extracted using an *ad-hoc* simulator experimentally validated at different bands. Different design parameters, such as the number of antenna elements, the focal distance, and the number of bits for phase compensation have been taken into account in the analysis. From this study, a 2-bit TA has been adopted for the mapping application because it could represent a good balance between complexity and radiation efficiency in view of the implementation of an electronically reconfigurable TA. The map reconstruction accuracy has been evaluated for different sized TAs and for reduced F/D values using a grid-based Bayesian state-space approach. Results have demonstrated that a 15×15 TA with a reduced focal distance of $F = 10\,\text{mm}$ permits to attain a good level of map reconstruction with the benefits of an easier integration and of a lower antenna array profile and cost.

Stimulated by these simulation results, an indoor backscattering measurement campaign using TAs at millimeter-wave has been conducted. The data collected have been exploited for map reconstruction using the grid-based Bayesian state-space approach. Results have demonstrated the feasibility of the mmW personal radar and that a good quality of map reconstruction can be achieved even when a limited set of phase values, i.e. only two in our case, are available.

Chapter 3

Single-Anchor Position and Orientation Bounds

Millimeter-wave massive arrays technology has been employed in Chapter 2 for mapping purposes. Another important field of application is mobile users localization. Specifically, 5G femtocells APs could be equipped with massive arrays to empower the communication. Besides more reliable and fast communication capabilities, APs can be exploited as reference nodes in a localization perspective. In this framework, this chapter will show the derivation of the fundamental limits in localization estimation error when massive arrays are used at both AP and mobile end. The analysis will compare different array structures working at mmW frequencies taking into account the sources of errors illustrated in Chapter 1.

3.1 Related works

The widespread use of tablets and smartphones generates new challenges such as an exponential increasing traffic demand, big data management issues, device-to-device (D2D) and devices-to-cloud interactions mechanisms. Moreover, the capability of localizing the nearest AP or self-localizing even in harsh propagation environments (i.e., indoor scenarios) will be an essential requirement for future portable devices [75, 3].

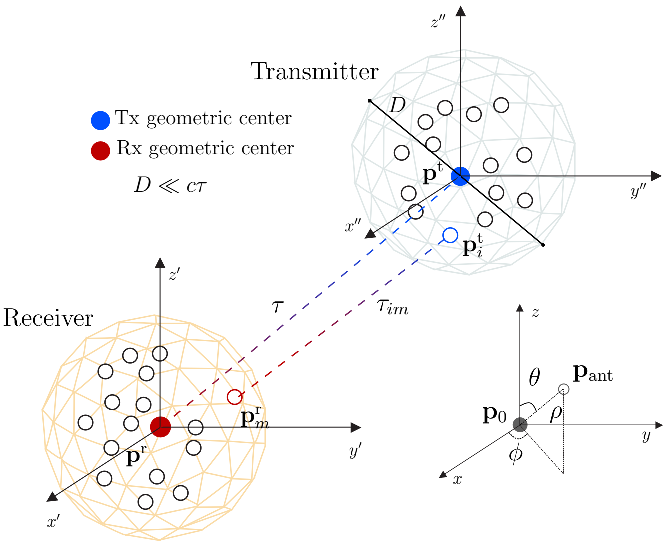

Figure 3.1: Multi-Antenna system configuration.

A possible solution to cope with the necessity to achieve an accurate positioning and navigation capability where the GPS signal is not available is that of exploiting the femtocells APs as reference nodes for localization purposes. However, localization coverage requires, in general, each location to be covered by at least 2 or 3 APs to allow multi-lateration/triangulation algorithms to work properly [76]. Indeed, in many positioning schemes, the APs must be tightly synchronized and, consequently, infrastructure cost could be unsustainable in typical indoor applications. Fortunately, the possibility to accommodate mmW massive antenna arrays both in APs and in the user terminals paves the way to high localization accuracy even with only one AP by exploiting the available beamforming antenna capabilities, the potential rich set of measurements and wideband signals [77].

Therefore it is of great interest to understand the fundamental limits on localization errors with wideband massive antenna arrays using only a single AP as reference node. Specifically, in a practical scenario both the AP and the mobile perform a beamsteering process: the AP scans the environment to focus the transmitted power in the direction of the mobile while the mobile sets its weights in order to maximize the received power. This coarse search represents itself a first step in the localization process which is followed by a fine search. The performance limits of the latter are given by the CRLB for position and orientation [30].

A rich literature has been produced for the analysis of the localization performance of wideband large antenna arrays. As we have already discussed in Chapter 1, wideband signals are the best candidate to achieve high ranging performance [78], but a strict phase control in beamforming, i.e. the adoption of precise and costly phase shifters and delay lines, becomes necessary to assure a perfect signal alignment. A cheaper and alternative solution is to adopt digitally controlled phase shifters implementing a discrete set of phase shifts and a reduced number of TDLs at the price of a reduced signal alignment capability. In addition, synchronization mismatch between the transmitter and the receiver might impact the localization accuracy. The impact of synchronization and array calibration errors has been addressed separately [79, 80, 81] or completely neglected in literature [82] when analyzing the CRLB on localization error.

The study on localization fundamental limits presented in this chapter has been inspired by the analysis conducted in [78, 83], and by the considerations presented in [84]. Specifically in [78, 83] authors explore the localization accuracy in terms of squared position error bound (SPEB) and squared orientation error bound (SOEB) for a wideband wireless network. In case the multiple anchors configuration is interpreted as a unique wideband antenna array, they demonstrate that the direction-of-arrival (DOA) information does not further improve the localization accuracy beyond that provided by the TOA alone when the entire wideband transmitted signal can be exploited to obtain TOA information. This astonishing result is further discussed in [84] where the narrowband assumption has been adopted to separate the baseband signal and the carrier frequency and where the TOA information can only be obtained from the baseband signal. Differently from [78, 83, 84], where different APs send orthogonal waveforms, we consider a system composed of two massive antenna arrays both at AP and mobile ends and according to the array configuration adopted, both orthogonal and non-orthogonal transmitted signals are accounted for.

Stimulated by these works, the derivation of the theoretical performance

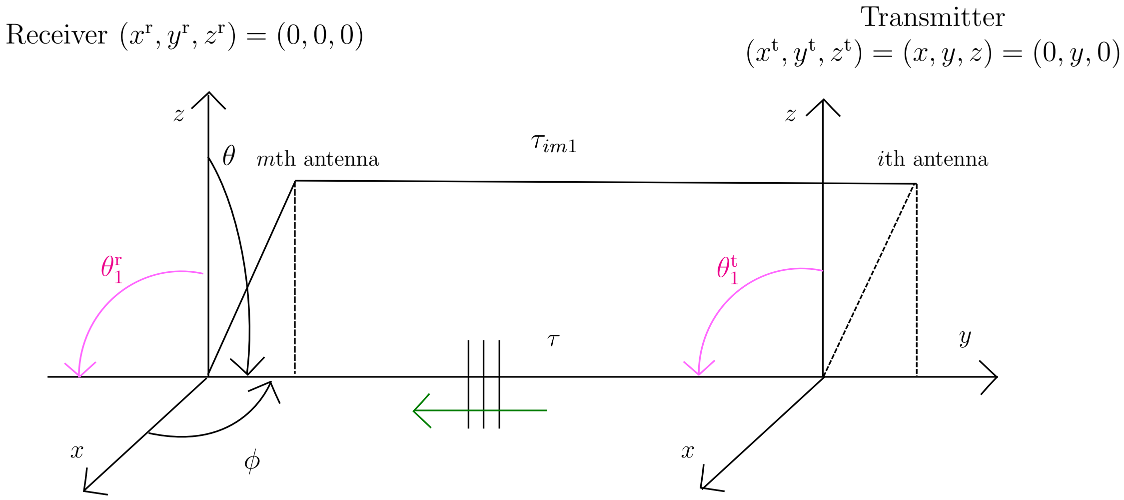

Figure 3.2: AWGN scenario.

limits on position and orientation error has been undertaken for different antenna array configurations, i.e. timed, phased, random and MIMO, for different effective bandwidths and in presence of multipath components. Quantized beamforming weights, antenna array technological constraints and synchronization mismatch between the AP and the mobile are taken into account in a unitary way.

3.2 Antenna array geometric configuration

We consider the 3D localization scenario, reported in Fig. 3.1, consisting of a single AP acting as reference node equipped with a receiving antenna array, with N_{rx} antenna elements, and a transmitting mobile terminal with a N_{tx}-elements antenna array. The localization process aims at directly inferring the position of the transmitter geometric center $\mathbf{p}^{\mathrm{t}} = [x_0^{\mathrm{t}}, y_0^{\mathrm{t}}, z_0^{\mathrm{t}}]^T = [x, y, z]^T$ and its orientation $\boldsymbol{\vartheta}^{\mathrm{t}} = [\vartheta^{\mathrm{t}}, \varphi^{\mathrm{t}}]^T$ when the receiver position $\mathbf{p}^{\mathrm{r}} = [x_0^{\mathrm{r}}, y_0^{\mathrm{r}}, z_0^{\mathrm{r}}]^T = [0, 0, 0]^T$ and orientation $\boldsymbol{\vartheta}^{\mathrm{r}} = [\vartheta^{\mathrm{r}}, \varphi^{\mathrm{r}}]^T = [0, 0]^T$ are known.[1] In a practical scenario, the mobile equipped with a transmitting antenna array scans the environment and orients its beam towards the receiving AP. Thanks to its multi-antenna configuration, the AP is able to infer the position

---

[1] Without loss of generality we put the receiver at the origin of the coordinate system.

and orientation of the transmitting mobile.

We indicate with $\mathbf{p}_i^{\mathrm{t}}$ the position of the ith transmitting antenna relative to the transmitter geometric center, and with $\mathbf{p}_m^{\mathrm{r}}$ the position of the mth receiving antenna relative to the receiver geometric center, whose coordinates are, respectively,

$$\begin{aligned}
\mathbf{p}_m^{\mathrm{r}}\left(\boldsymbol{\vartheta}^{\mathrm{r}}\right) &= \left[x_m^{\mathrm{r}},\ y_m^{\mathrm{r}},\ z_m^{\mathrm{r}}\right]^T \\
&= \mathbf{R}\left(\boldsymbol{\vartheta}^{\mathrm{r}}\right)\ \rho_m^{\mathrm{r}}\ \left[\sin(\theta_m^{\mathrm{r}})\cos(\phi_m^{\mathrm{r}}),\ \sin(\theta_m^{\mathrm{r}})\sin(\phi_m^{\mathrm{r}}),\ \cos(\theta_m^{\mathrm{r}})\right]^T \qquad (3.1) \\
\mathbf{p}_i^{\mathrm{t}}(\boldsymbol{\vartheta}^{\mathrm{t}}) &= \left[x_i^{\mathrm{t}},\ y_i^{\mathrm{t}},\ z_i^{\mathrm{t}}\right]^T \\
&= \mathbf{R}\left(\boldsymbol{\vartheta}^{\mathrm{t}}\right)\ \rho_i^{\mathrm{t}}\ \left[\sin(\theta_i^{\mathrm{t}})\cos(\phi_i^{\mathrm{t}}),\ \ \sin(\theta_i^{\mathrm{t}})\sin(\phi_i^{\mathrm{t}}),\ \ \cos(\theta_i^{\mathrm{t}})\right]^T, \qquad (3.2)
\end{aligned}$$

where $(\rho_m^{\mathrm{r}}, \theta_m^{\mathrm{r}}, \phi_m^{\mathrm{r}})$ $((\rho_i^{\mathrm{t}}, \theta_i^{\mathrm{t}}, \phi_i^{\mathrm{t}}))$ represents the spherical coordinates of the mth receiving (ith transmitting) antenna with respect to the receiver (transmitter) center. The rotational matrix $\mathbf{R}(\boldsymbol{\vartheta})$ is given by

$$\mathbf{R}(\boldsymbol{\vartheta}) = \mathbf{R}_z(\varphi)\,\mathbf{R}_x(\vartheta), \qquad (3.3)$$

where $\boldsymbol{\vartheta} = \{\vartheta, \varphi\}$ is the generic orientation angle, $\mathbf{R}_z(\varphi)$ and $\mathbf{R}_x(\vartheta)$ define the rotation around the z of φ and around x axis of ϑ, respectively

$$\mathbf{R}_z(\varphi) = \begin{bmatrix} \cos(\varphi) & -\sin(\varphi) & 0 \\ \sin(\varphi) & \cos(\varphi) & 0 \\ 0 & 0 & 1 \end{bmatrix}, \mathbf{R}_x(\vartheta) = \begin{bmatrix} 1 & 0 & 0 \\ 0 & \cos(\vartheta) & \sin(\vartheta) \\ 0 & -\sin(\vartheta) & \cos(\vartheta) \end{bmatrix}. \qquad (3.4)$$

Finally we designate with $\boldsymbol{\theta}_1 = (\theta_1, \phi_1)$ the incident angle at the receiving geometric centre in AWGN conditions and with $\boldsymbol{\theta}_0 = (\theta_0, \phi_0)$ the intended pointing direction in the steering process when applied.

We take L MPC into consideration as nuisance parameters in the localization process and we suppose that the first path always experiences a LOS propagation condition. For what the MPCs parameters are concerned, we follow the same notation introduced in [84]. We indicate with $\boldsymbol{\theta}_l^{\mathrm{t}} = (\theta_l^{\mathrm{t}}, \phi_l^{\mathrm{t}}) = (\theta_1 + \Delta\theta_l^{\mathrm{t}}, \phi_1 + \Delta\phi_l^{\mathrm{t}})$ and $\boldsymbol{\theta}_l^{\mathrm{r}} = (\theta_l^{\mathrm{r}}, \phi_l^{\mathrm{r}}) = (\theta_1 + \Delta\theta_l^{\mathrm{r}}, \phi_1 + \Delta\phi_l^{\mathrm{r}})$, $l = 1, 2, \ldots, L$, the angles of departure from the transmitting array and incidence at the receiver side of the lth path respectively. The angular biases $(\Delta\theta_l^{\mathrm{t}}, \Delta\phi_l^{\mathrm{t}})$ and $(\Delta\theta_l^{\mathrm{r}}, \Delta\phi_l^{\mathrm{r}})$ are the relative arrival-angle elevation and azimuth biases with respect to the direct path at the transmitter and receiver side. Obviously, it is $(\Delta\theta_1^{\mathrm{t}}, \Delta\phi_1^{\mathrm{t}}) = (\Delta\theta_1^{\mathrm{r}}, \Delta\phi_1^{\mathrm{r}}) = (0,0)$. Let

$$\tau_1 \triangleq \frac{\|\mathbf{p}^{\mathrm{r}} - \mathbf{p}^{\mathrm{t}}\|_2}{c} = \frac{d}{c}, \qquad \tau_{mi1} \triangleq \frac{\|\mathbf{p}_m^{\mathrm{r}} - \mathbf{p}_i^{\mathrm{t}}\|_2}{c} \tag{3.5}$$

be the propagation delay related to the direct path between the transmitting and receiving geometric centers and between the ith and mth antenna, respectively, where c is the speed of light and d is the distance between the arrays centers. Considering the multipath, we define the lth propagation delay between array centers as $\tau_l = \tau_1 + \Delta\tau_l$ where $\Delta\tau_l$ is the non-negative delay bias of the lth path with $\Delta\tau_1 = 0$ [84].

The geometric configuration assumption implies that the diameter D of the transmitting and receiving arrays is much smaller than the inter-array distance d, i.e., $D \ll d$. Note that this hypothesis is especially verified at mmW where the array dimensions are very small thanks to the reduced inter-antenna spacing. Moreover we suppose the arrays are sufficiently far from the surrounding scatterers thus obtaining identical incident angles at each receiver antenna, thus being valid the following approximation [82, 85, 84]

$$1)\ \tau_{mil} \approx \tau_l + \tau_i^{\mathrm{t}}(\boldsymbol{\theta}_l^{\mathrm{t}}, \boldsymbol{\vartheta}^{\mathrm{t}}) - \tau_m^{\mathrm{r}}(\boldsymbol{\theta}_l^{\mathrm{r}}, \boldsymbol{\vartheta}^{\mathrm{r}}), \qquad 2)\ a_{mil} \approx a_l \tag{3.6}$$

where a_{mil} is the amplitude of the lth path between the mth receiving and the ith transmitting antenna, and $\tau_m^{\mathrm{r}}(\boldsymbol{\theta}_l^{\mathrm{r}}, \boldsymbol{\vartheta}^{\mathrm{r}})$ and $\tau_i^{\mathrm{t}}(\boldsymbol{\theta}_l^{\mathrm{t}}, \boldsymbol{\vartheta}^{\mathrm{t}})$ are, respectively, the receiving and transmitting inter-antenna time delays with respect to the array geometric centers defined as

$$\tau_m^{\mathrm{r}}(\boldsymbol{\theta}_l^{\mathrm{r}}, \boldsymbol{\vartheta}^{\mathrm{r}}) = \frac{1}{c}\,\mathbf{d}\left(\boldsymbol{\theta}_l^{\mathrm{r}}\right)\,\mathbf{p}_m^{\mathrm{r}}\left(\boldsymbol{\vartheta}^{\mathrm{r}}\right), \qquad \tau_i^{\mathrm{t}}(\boldsymbol{\theta}_l^{\mathrm{t}}, \boldsymbol{\vartheta}^{\mathrm{t}}) = \frac{1}{c}\,\mathbf{d}\left(\boldsymbol{\theta}_l^{\mathrm{t}}\right)\,\mathbf{p}_i^{\mathrm{t}}\,\left(\boldsymbol{\vartheta}^{\mathrm{t}}\right) \tag{3.7}$$

with $\mathbf{d}(\boldsymbol{\theta}_1)$ being the direction cosine defined as

$$\mathbf{d}(\boldsymbol{\theta}_1) = [\sin(\theta)\cos(\phi),\ \sin(\theta)\sin(\phi),\ \cos(\theta)]\,. \tag{3.8}$$

Fig. 3.2 reports a graphical explanation of the considered system. As we can see the approximation in (3.6) lets to write the TOA as the summation between the inter-antenna delays and the delay between the array centers. The inter-antenna delay are considered as orthogonal projections in the direction of the wave propagation, as clearly depicted in Fig. 3.2.

3.3 Signal model

In antenna arrays, beamsteering is obtained by applying a progressive time delay at each array element so that the emitted signals result summed up coherently in the intended steering direction $\boldsymbol{\theta}_0$. When the signal bandwidth W is much less than its center frequency f_{c} ($W \ll f_{\text{c}}$), this process can be well approximated using only phase shifters (phased arrays). On the contrary, when $W \approx f_{\text{c}}$, phase shifts are no longer sufficient to align all frequency components of signals. As a consequence, to avoid distortion and beamsteering performance degradation (squinting effect), timed arrays consisting of phase shifters and TDLs must be introduced. An analysis of the beamwidth spread can be found in 1.2.

Differently, MIMO systems take advantage of the diversity given by multiple waveforms instead of performing beamsteering [86, 87]. However, to make the receiver able to discriminate the signal components coming from each single transmitting antenna, orthogonal waveforms are typically adopted [88, 89, 87, 90, 91]. As an example, in [87], a class of signals (i.e., frequency spread signals) are demonstrated to maintain orthogonality for time delays and frequency Doppler shifts.

3.3.1 Transmitted signal model

The complex envelope of the transmitted baseband signal at the ith transmitting antenna is denoted with $s_i(t)$. We consider a constraint on the total transmitted energy E_{tot} which is uniformly allocated among antennas, thus $E = E_{\text{tot}}/N_{\text{tx}} = \frac{1}{2} \int |s_i(t)|^2 dt$, $i = 1, 2, \ldots, N_{\text{tx}}$, represents the normalized RF energy at each antenna element. In addition we indicate with

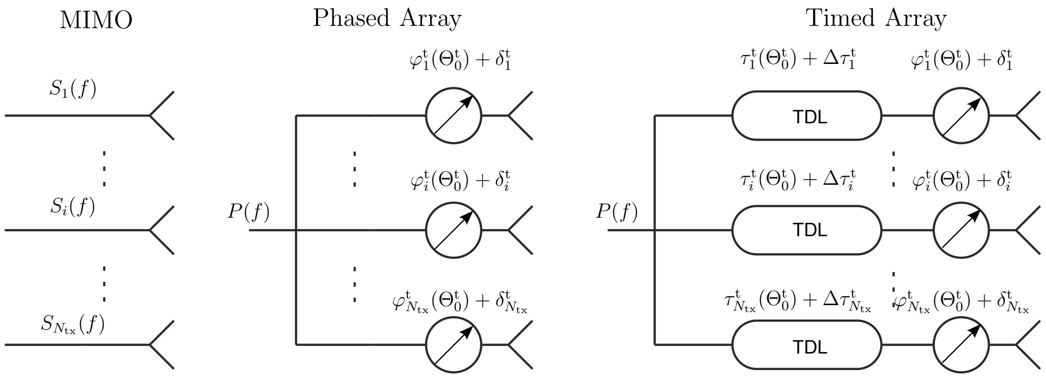

Figure 3.3: From the left to the right: MIMO, phased array and timed array scheme.

$S_i(f) = \mathcal{F}\{s_i(t)\}$, with $\mathcal{F}\{\cdot\}$ denoting the Fourier transform operation in a suitable observation interval T_{obs} containing the signal support. Then, we collect all the transmitted signals in a vector $\mathbf{S}(f) = [S_1(f), \ldots, S_{N_{\mathrm{tx}}}(f)]^T$.

The ideal beamforming matrix is[2]

$$\mathbf{B} = \mathrm{diag}\left(\omega_1, \omega_2, \ldots, \omega_i, \ldots \omega_{N_{\mathrm{tx}}}\right) \tag{3.9}$$

where the ith beamsteering weight is ω_i. Nevertheless, some technological issue could induce errors in the beamforming vector. In the presence of such non-perfect weights and synchronization error, a matrix containing all the non-idealities has to be introduced as

$$\mathbf{Q}(f) = e^{-j\,2\,\pi\,(f+f_{\mathrm{c}})\epsilon^{\mathrm{s}}}\,\mathrm{diag}\left(\varsigma_1, \varsigma_2, \ldots, \varsigma_i, \ldots, \varsigma_{N_{\mathrm{tx}}}\right) \tag{3.10}$$

where ϵ^{s} represents the synchronization error and ς_i takes into account the ith beamforming weights error.

After the transmitting beamforming process, the signal at each antenna element can be written as $\mathbf{Q}(f)\,\mathbf{B}(f, \boldsymbol{\theta}_0)\,\mathbf{S}(f)$. In the following we will detail the signal model for each system configuration.

---

[2] The ideality here refers to the absence of errors in the beamforming process (e.g, no quantization effects) and in time synchronization.

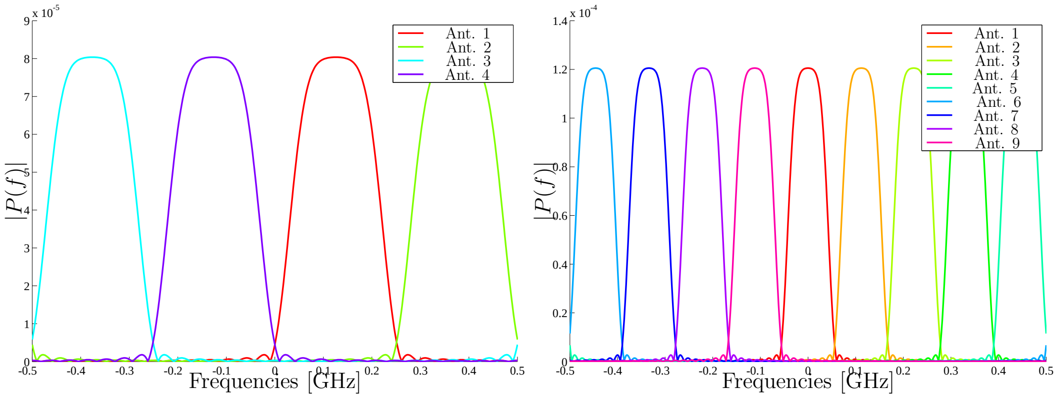

Figure 3.4: MIMO signal magnitude spectrum for $N_{\text{tx}} = 4$ and $N_{\text{tx}} = 9$ considering a total signal bandwidth of $W = 1\,\text{GHz}$.

MIMO arrays

In MIMO arrays, each transmit antenna sends out orthogonal waveforms $s_i(t) = \sqrt{2\,E}\,p_i(t)$, with $\int |p_i(t)|^2 dt = 1, i = 1, 2, \ldots, N_{\text{tx}}$. The orthogonality property implies

$$\int_W P_i(f)\,P_j^*(f)\,e^{-j2\pi f\left(\tau_{mil}-\tau_{njk}\right)}\,df = \begin{cases} 0 & i \neq j \\ \neq 0 & i = j \end{cases} \qquad \forall l, k, n, m. \tag{3.11}$$

with $P_i(f) = \mathcal{F}\{p_i(t)\}$. The possibility to provide orthogonal waveforms permits to increase the diversity gain as it will be detailed in next sections. However it translates in a greater bandwidth demand and in a more complex transmitter structure.

In MIMO case, the matrix in (3.9) is an identity matrix $\mathbf{B} = \mathbf{I}_{N_{\text{tx}}}$ while in presence of synchronization errors we have that (3.10) is $\mathbf{Q}(f) = e^{-j\,2\,\pi\,(f+f_c)\epsilon^{\text{s}}}\,\mathbf{I}_{N_{\text{tx}}}$. In Fig. 3.4, an example of the signals transmitted by an array of $N_{\text{tx}} = 4$ and $N_{\text{tx}} = 9$ antennas are reported in the frequency domain. A RRC pulse with a roll-off factor of $\beta = 0.6$, a bandwidth of $1\,\text{GHz}$ and a central frequency of $60\,\text{GHz}$ is considered.

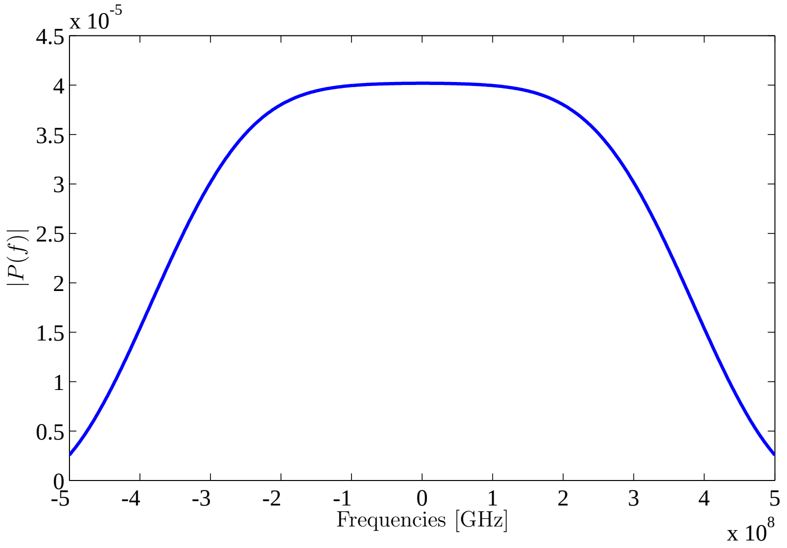

Figure 3.5: Timed signal magnitude spectrum.

Timed and phased arrays

Contrarily to MIMO, in timed and phased arrays the transmitted baseband signal is the same for all transmitting antennas (i.e. $s_i(t) = s(t) = \sqrt{2E}\ p(t)\ \forall i = 1, \ldots, N_{\text{tx}}$, see an example in Fig. 3.5) and beamsteering weights are applied to each branch of the array to focus the power flux in a precise direction in space, indicated hereafter as $\boldsymbol{\theta}_0 = (\theta_0, \phi_0)$. Specifically, the generic element inside (3.9) becomes $\omega_i = e^{j\left(2\,\pi\,f\,\tau_i^{\text{t}}(\boldsymbol{\theta}_0)+\varphi_i^{\text{t}}(\boldsymbol{\theta}_0)\right)}$ with $\varphi_i^{\text{t}}(\boldsymbol{\theta}_0)$ and $\tau_i^{\text{t}}(\boldsymbol{\theta}_0)$ being the transmitting steering phase and delay related to the ith phase shifter of the array respectively. When digitally controlled phase shifters are adopted in place of their high-resolution analog counterparts, the presence of quantization errors has to be accounted [5]. Consequently, the ith entry of $\mathbf{Q}(f)$ is $\varsigma_i = e^{j\left(2\,\pi\,f\,\Delta\tau_i^{\text{t}}+\delta_i^{\text{t}}\right)}$ and it takes into account the quantization effects on the beamforming weight with δ_i^{t} being the phase error and $\Delta\tau_i^{\text{t}}$ being the TDL error. The main difference between phased and timed array is the way in which the beamsteering process is performed: in the former only phase shifters are present (i.e., $\tau_i^{\text{t}}(\boldsymbol{\theta}_0) = 0$ and $\Delta\tau_i^{\text{t}} = 0\ \forall i = 1, \ldots, N_{\text{tx}}$) while in the latter TDLs and phase shifters are both employed to counteract the beamsquinting effect caused by a larger W/f_{c} ratio (see Fig. 3.3).

Moreover, thanks to the narrow beam formed, in timed and phased arrays a significant multipath spatial filtering effect is present as it will be analyzed in the numerical results.

3.3.2 Received signal model

In this section a general framework for the received signal model is illustrated. The aim of the system is to estimate the position $\mathbf{p}^{\mathrm{t}}$ of the transmitter and its orientation $\boldsymbol{\vartheta}^{\mathrm{t}}$ starting from the set of received waveforms $\mathbf{R}(f)$. The received signals are collected in a vector $\mathbf{R}(f) = [R_1(f), \ldots, R_m(f), \ldots \ldots, R_{N_{\mathrm{rx}}}(f)]^T$ where $R_m(f) = \mathcal{F}\{r_m(t)\}$ is evaluated in T_{ob} and $r_m(t)$ is the received signal at the mth receiving antenna. Specifically we can write

$$\mathbf{R}(f) = \sum_{l=1}^{L} \mathbf{A}^{\mathrm{r}}(f, \boldsymbol{\theta}_l^{\mathrm{r}}, \boldsymbol{\vartheta}^{\mathrm{r}})\, \mathbf{C}(f, \tau_l)\, \mathbf{A}^{\mathrm{t}}(f, \boldsymbol{\theta}_l^{\mathrm{t}}, \boldsymbol{\vartheta}^{\mathrm{t}})\, \mathbf{Q}(f)\, \mathbf{B}(f, \boldsymbol{\theta}_0)\, \mathbf{S}(f) + \mathbf{N}(f) \tag{3.12}$$

where

$$\mathbf{A}^{\mathrm{r}}(f, \boldsymbol{\theta}_l^{\mathrm{r}}) = \left[e^{j\,2\,\pi\,(f+f_{\mathrm{c}})\tau_1^{\mathrm{r}}(\boldsymbol{\theta}_l^{\mathrm{r}},\boldsymbol{\vartheta}^{\mathrm{r}})}, \ldots, e^{j\,2\,\pi\,(f+f_{\mathrm{c}})\tau_m^{\mathrm{r}}(\boldsymbol{\theta}_l^{\mathrm{r}},\boldsymbol{\vartheta}^{\mathrm{r}})}, \ldots, e^{j\,2\,\pi\,(f+f_{\mathrm{c}})\tau_{N_{\mathrm{rx}}}^{\mathrm{r}}(\boldsymbol{\theta}_l^{\mathrm{r}},\boldsymbol{\vartheta}^{\mathrm{r}})}\right]^T \tag{3.13}$$

$$\begin{aligned}\mathbf{A}^{\mathrm{t}}(f, \boldsymbol{\theta}_l^{\mathrm{t}}, \boldsymbol{\vartheta}^{\mathrm{t}}) = \mathrm{diag}\Big(&e^{-j\,2\,\pi\,(f+f_{\mathrm{c}})\tau_1^{\mathrm{t}}(\boldsymbol{\theta}_l^{\mathrm{t}},\boldsymbol{\vartheta}^{\mathrm{t}})}, \ldots, e^{-j\,2\,\pi\,(f+f_{\mathrm{c}})\tau_i^{\mathrm{t}}(\boldsymbol{\theta}_l^{\mathrm{t}},\boldsymbol{\vartheta}^{\mathrm{t}})}, \ldots \\ &\ldots, e^{-j\,2\,\pi\,(f+f_{\mathrm{c}})\tau_{N_{\mathrm{tx}}}^{\mathrm{t}}(\boldsymbol{\theta}_l^{\mathrm{t}},\boldsymbol{\vartheta}^{\mathrm{t}})}\Big)\end{aligned} \tag{3.14}$$

are the receiving and transmitting direction matrices for the inter antennas delays and transmitter orientation and $\mathbf{C}(f, \tau_l) = c_l\, \mathbf{1}_{1\times N_{\mathrm{tx}}}$ is the $1 \times N_{\mathrm{tx}}$ channel vector whose generic element is $c_l = a_l\, e^{-j\,2\,\pi\,(f+f_{\mathrm{c}})\,\tau_l} = \alpha_l\, e^{-j\,2\,\pi\,f\,\tau_l}$. Finally, $\mathbf{N}(f) = [N_1(f), \ldots, N_m(f), \ldots, N_{N_{\mathrm{rx}}}(f)]^T$ is the noise vector with $N_m(f) = \mathcal{F}\{n_m(t)\}$ and $n_m(t) \sim \mathcal{CN}(0, N_0/2)$ is a circularly symmetric, zero-mean, complex Gaussian noise.

When evaluating the ultimate performance of the estimator, MPCs, array quantization effects and the synchronization error are accounted for as nuisance parameters. Thus, define the unknown parameters vector as

$$\boldsymbol{\psi} = \left[\mathbf{q}^{T},\ \boldsymbol{\kappa}^{T},\ \epsilon^{\mathrm{s}}\right]^{T} \tag{3.15}$$

where we have collected the parameters of interest in $\mathbf{q} = \left[\mathbf{p}^{\mathrm{t}\ T},\ \boldsymbol{\vartheta}^{\mathrm{t}\ T}\right]^{T}$, the multipath parameters in

$$\boldsymbol{\kappa} = \left[\boldsymbol{\kappa}_1^{T}, \boldsymbol{\kappa}_2^{T}, \ldots, \boldsymbol{\kappa}_L^{T}\right]^{T}, \boldsymbol{\kappa}_l = \begin{cases} [a_1]^{T} & \text{if } l = 1 \\ \left[\alpha_l^{\Re},\ \alpha_l^{\Im}\ \right]^{T} & \text{if } l > 1. \end{cases} \tag{3.16}$$

The terms $\alpha_l^{\Re} = \Re\{\alpha_l\}$ and $\alpha_l^{\Im} = \Im\{\alpha_l\}$ indicate the real and imaginary part of the complex channel coefficient α_l, respectively [79, 92]. In particular, the dominant LOS component related to direct path (i.e., a_1) is considered deterministic while, for $l > 1$, $\alpha_l \sim \mathcal{CN}\left(0, \sigma_l^2\right)$ is a circularly symmetric Gaussian RV.

Note that one could consider a different set of MPC parameters vector as for example

$$\boldsymbol{\kappa}_l = \begin{cases} [a_1]^{T} & \text{if } l = 1 \\ \left[\alpha_l^{\Re},\ \alpha_l^{\Im}\ \Delta\tau_l,\ \Delta\theta_l^{\mathrm{r}},\ \Delta\phi_l^{\mathrm{r}}\right]^{T} & \text{if } l > 1. \end{cases} \tag{3.17}$$

or

$$\boldsymbol{\kappa}_l = \begin{cases} [a_1]^{T} & \text{if } l = 1 \\ \left[\alpha_l^{\Re},\ \alpha_l^{\Im},\ \tau_l,\ \theta_l^{\mathrm{r}},\ \phi_l^{\mathrm{r}}\right]^{T} & \text{if } l > 1. \end{cases} \quad . \tag{3.18}$$

The difference between (3.17) and (3.18) lies in considering the biases of the MPC with respect to the first path or the MPC itself. It can be demonstrated, see Appendix D, that in terms of Cramér-Rao bound (CRB) they are equivalent.

The motivation behind the choice of the simplified MPC parameters vector expressed in (3.16) stands for the fact that the position and orientation estimation are not affected by the information carried by $\left[\tau_l,\ \theta_l^{\mathrm{r}},\ \phi_l^{\mathrm{r}}\right]\ \forall l \neq 1$. Consequently we can discard them from $\boldsymbol{\kappa}_l$. This is analytically verified by noticing that $\nabla_{\boldsymbol{q}}\left(\tau_l\right)=\nabla_{\boldsymbol{q}}\left(\theta_l\right)=\nabla_{\boldsymbol{q}}\left(\phi_l\right)=0,\ \forall l\neq 1$.

The synchronization error is modeled as independent Gaussian zero-mean RVs with standard deviation σ_{ϵ}^2. Finally, we assume that the a-priori knowledge of the remaining parameters distribution is not available. In the following we will indicate with $\boldsymbol{\psi}_{\mathrm{r}}$ the set of parameters with available a-priori information and with $\boldsymbol{\psi}_{\mathrm{nr}}$ the set of deterministic parameters.

3.4 Position and orientation estimation error bound

3.4.1 General expression

The performance of any unbiased estimator $(\widehat{\boldsymbol{\psi}})$ can be bounded by the Bayesian CRLB [93]

$$\mathbb{E}_{\mathbf{r},\boldsymbol{\psi}_{\mathrm{r}}}\left\{\left(\widehat{\boldsymbol{\psi}}-\boldsymbol{\psi}\right)\left(\widehat{\boldsymbol{\psi}}-\boldsymbol{\psi}\right)^{T}\right\}\succeq \mathbf{J}_{\boldsymbol{\psi}}^{-1} \tag{3.19}$$

where $\mathbf{A}\succeq\mathbf{B}$ denotes that $\mathbf{A}-\mathbf{B}$ is a non-negative definite matrix and $\mathbf{J}_{\boldsymbol{\psi}}$ is the Bayesian Fisher information matrix (FIM) defined as

$$\mathbf{J}_{\boldsymbol{\psi}}\triangleq-\mathbb{E}_{\mathbf{r},\boldsymbol{\psi}_{\mathrm{r}}}\left\{\nabla^2_{\boldsymbol{\psi}\boldsymbol{\psi}}\ \ln f\left(\mathbf{r},\boldsymbol{\psi}_{\mathrm{r}}\right)\right\}=\mathbf{J}^{\mathrm{d}}_{\boldsymbol{\psi}}+\mathbf{J}^{\mathrm{p}}_{\boldsymbol{\psi}}=\left[\begin{array}{c|cc}\mathbf{J}^{\mathrm{d}}_{\mathbf{qq}} & \mathbf{J}^{\mathrm{d}}_{\mathbf{q}\boldsymbol{\kappa}} & \mathbf{J}^{\mathrm{d}}_{\mathbf{q}\epsilon^{\mathrm{s}}} \\ \hline \mathbf{J}^{\mathrm{d}}_{\boldsymbol{\kappa}\mathbf{q}} & \mathbf{J}^{\mathrm{d}}_{\boldsymbol{\kappa}\boldsymbol{\kappa}}+\mathbf{J}^{\mathrm{p}}_{\boldsymbol{\kappa}\boldsymbol{\kappa}} & \mathbf{J}^{\mathrm{d}}_{\boldsymbol{\kappa}\epsilon^{\mathrm{s}}} \\ \mathbf{J}^{\mathrm{d}}_{\epsilon^{\mathrm{s}}\mathbf{q}} & \mathbf{J}^{\mathrm{d}}_{\epsilon^{\mathrm{s}}\boldsymbol{\kappa}} & \mathbf{J}^{\mathrm{d}}_{\epsilon^{\mathrm{s}}\epsilon^{\mathrm{s}}}+\mathbf{J}^{\mathrm{p}}_{\epsilon^{\mathrm{s}}\epsilon^{\mathrm{s}}}\end{array}\right]$$

$$=\left[\begin{array}{cc}\mathbf{J}^{(1,1)}_{\boldsymbol{\psi}} & \mathbf{J}^{(1,2)}_{\boldsymbol{\psi}} \\ \mathbf{J}^{(2,1)}_{\boldsymbol{\psi}} & \mathbf{J}^{(2,2)}_{\boldsymbol{\psi}}\end{array}\right]. \tag{3.20}$$

The symbol $\nabla^2_{\boldsymbol{\psi}\boldsymbol{\psi}}=\partial^2/\partial\boldsymbol{\psi}\partial\boldsymbol{\psi}$ denotes the second partial derivatives with respect to the elements in $\boldsymbol{\theta}$ and

$$\mathbf{J}^{\mathrm{d}}_{\boldsymbol{\psi}}=-\mathbb{E}_{\mathbf{r},\boldsymbol{\psi}_{\mathrm{r}}}\left\{\nabla^2_{\boldsymbol{\psi}\boldsymbol{\psi}}\ \ln f\left(\mathbf{r}|\boldsymbol{\psi}_{\mathrm{r}}\right)\right\} \tag{3.21}$$

$$\mathbf{J}^{\mathrm{p}}_{\boldsymbol{\psi}}=-\mathbb{E}_{\boldsymbol{\psi}_{\mathrm{r}}}\left\{\nabla^2_{\boldsymbol{\psi}\boldsymbol{\psi}}\ \ln f\left(\boldsymbol{\psi}_{r}\right)\right\} \tag{3.22}$$

The log-likelihood function $\ln f\left(\mathbf{r}|\boldsymbol{\psi}_{\mathrm{r}}\right)$ can be written as

$$\ln f\left(\mathbf{r}|\boldsymbol{\psi}_{\mathrm{r}}\right) \propto -\frac{1}{N_0}\sum_{m=1}^{N_{\mathrm{rx}}}\int_{W}\left|R_m(f)-U_m(f)\right|^2 df\,, \tag{3.23}$$

whereas $\ln(f(\boldsymbol{\psi}_{\mathrm{r}}))$ represents the a-priori probability density function of parameters $\boldsymbol{\psi}_{\mathrm{r}}$ whose expression is derived in Appendix A. Finally, by using the Schur complement we can easily derive the CRLB expression related to the position and orientation parameters

$$\mathsf{CRB}\left(\mathbf{q}\right)=\left(\mathbf{J}_{\boldsymbol{\psi}}^{(1,1)}-\mathbf{J}_{\boldsymbol{\psi}}^{(1,2)}\,\left(\mathbf{J}_{\boldsymbol{\psi}}^{(2,2)}\right)^{-1}\,\mathbf{J}_{\boldsymbol{\psi}}^{(2,1)}\right)^{-1}. \tag{3.24}$$

Equation (3.24) is a general bound valid for different set-up (MIMO, phased and timed arrays) and accounting for signal weights quantization effects, synchronization mismatch and multipath. Specialized expression can be derived from (3.24) for specific cases to get insights on the key parameters affecting the performance as will be done in the following.

3.4.2 Alternative approaches followed

Some alternative approaches could be followed for the derivation of the localization error limit. Even if they have been discarded to the more compact and easy scheme suggested in 3.4.1, in the following we will report their formulation. Both are based on the observation that the parameters in $\boldsymbol{\psi}$ depend directly on signals TOAs and DOAs and thus it results convenient to map $\boldsymbol{\psi}$ into an alternative vector $\boldsymbol{\eta}$ containing the measured parameters.

Approach 2 (*Anchors-like approach*) In the first followed approach, the TOAs for each transmitter-receiver couple and MPC have been gathered in the alternative estimation parameters vector indicated as

$$\boldsymbol{\eta}=\left[\boldsymbol{\tau}^T,\,\boldsymbol{\alpha}^T,\,\epsilon^{\mathrm{s}}\right]^T=\left[\boldsymbol{\eta}_{\mathrm{nr}},\,\boldsymbol{\eta}_{\mathrm{r}}\right]^T \tag{3.25}$$

where $\boldsymbol{\tau} = [\boldsymbol{\tau}_1^T, \ldots, \boldsymbol{\tau}_l^T, \ldots, \boldsymbol{\tau}_L^T]^T$, $\boldsymbol{\tau}_l = \left[\boldsymbol{\tau}_{1l}^T, \ldots, \boldsymbol{\tau}_{ml}^T, \ldots, \boldsymbol{\tau}_{N_{\mathrm{rx}}l}^T\right]^T$ $\boldsymbol{\tau}_{ml} = [\tau_{1ml}, \ldots$ $\ldots \tau_{iml}, \ldots, \tau_{N_{\mathrm{tx}}ml}]^T$ are the measured TOAs whereas $\boldsymbol{\eta}_{\mathrm{r}} = \boldsymbol{\theta}_{\mathrm{r}} = [\boldsymbol{\alpha}_{\mathrm{R}}^T, \boldsymbol{\alpha}_{\mathrm{I}}^T, \epsilon^{\mathrm{s}}]^T$ is the random nuisance parameters vector with $\boldsymbol{\alpha}_{\mathrm{R}} = \left[\alpha_1^{\Re}, \ldots, \alpha_l^{\Re}, \ldots, \alpha_L^{\Re}\right]$ and $\boldsymbol{\alpha}_{\mathrm{I}} = \left[\alpha_1^{\Im}, \ldots, \alpha_l^{\Im}, \ldots, \alpha_L^{\Im}\right]$. The shortcoming of this solution is that Eq. (3.25) results in a vector of dimensions bigger and bigger as the number of antenna elements grows and thus, this turns in FIMs of higher dimensions. This approach has been inspired by the work in [78], where different anchors widely dislocated in the environment are adopted but it is not very suitable when arrays are adopted.

Approach 3 The second approach is an evolution of the first one where we consider only the TOA and DOA between the array centers. In this case the parameters vector will be

$$\boldsymbol{\eta} = [\boldsymbol{\xi}^T, \boldsymbol{\kappa}^T, \epsilon^{\mathrm{s}}]^T \tag{3.26}$$

where $\boldsymbol{\xi} = [\tau_1, \boldsymbol{\theta}_1, \boldsymbol{\vartheta}^{\mathrm{t}}]^T$ contains the TOA, DOA and orientation information. $\boldsymbol{\kappa}^T$ consists of the multipath parameters expressed as in (3.16) and ϵ^{s} is the synchronization error. The shortcoming of this approach is that while the position can be related to TOA-DOA measurements, the orientation needs the measurements of the phase difference between array elements. In this sense, mapping operation from $\boldsymbol{\psi}$ to $\boldsymbol{\eta}$ is useful only for the orientation-aware case. This solution has been suggested by the work in [94].

Once the new parameters vector has been defined, the *chain rule* is adopted to translates TOA measurements information into localization (i.e., position and orientation) information. The Bayesian FIM of $\boldsymbol{\psi}$ can be found as a function of the FIM of $\boldsymbol{\eta}$ as

$$\mathbf{J}_{\boldsymbol{\psi}} = \left(\nabla_{\boldsymbol{\psi}}\, \boldsymbol{\eta}\right) \mathbf{J}_{\boldsymbol{\eta}} \left(\nabla_{\boldsymbol{\psi}}\, \boldsymbol{\eta}\right)^H = \begin{bmatrix} \mathbf{J}_{\boldsymbol{\psi}}^{(1,1)} & \mathbf{J}_{\boldsymbol{\psi}}^{(1,2)} \\ \mathbf{J}_{\boldsymbol{\psi}}^{(2,1)} & \mathbf{J}_{\boldsymbol{\psi}}^{(2,2)} \end{bmatrix} \tag{3.27}$$

where $\nabla_{\boldsymbol{\psi}}(\boldsymbol{\eta}) = \partial \boldsymbol{\eta} / \partial \boldsymbol{\psi}$ is a vector containing the first-order partial derivatives of the elements in $\boldsymbol{\eta}$ with respect to those in $\boldsymbol{\psi}$, and $\mathbf{J}_{\boldsymbol{\eta}}$ is the FIM related to the new parameters vector defined as

$$\mathbf{J}_{\boldsymbol{\eta}} = -\mathbb{E}_{\mathbf{r},\boldsymbol{\eta}_\mathrm{r}}\left\{\nabla^2_{\boldsymbol{\eta}\boldsymbol{\eta}}\ \ln f\left(\mathbf{r},\boldsymbol{\eta}_\mathrm{r}\right)\right\} = \mathbf{J}^\mathrm{d}_{\boldsymbol{\eta}} + \mathbf{J}^\mathrm{p}_{\boldsymbol{\eta}}, \tag{3.28}$$

$$\mathbf{J}^\mathrm{d}_{\boldsymbol{\eta}} = -\mathbb{E}_{\mathbf{r},\boldsymbol{\eta}_\mathrm{r}}\left\{\nabla^2_{\boldsymbol{\eta}\boldsymbol{\eta}}\ \ln f\left(\mathbf{r}|\boldsymbol{\eta}_\mathrm{r}\right)\right\}, \tag{3.29}$$

$$\mathbf{J}^\mathrm{p}_{\boldsymbol{\eta}} = -\mathbb{E}_{\boldsymbol{\eta}_\mathrm{r}}\left\{\nabla^2_{\boldsymbol{\eta}\boldsymbol{\eta}}\ \ln f\left(\boldsymbol{\eta}_r\right)\right\}, \tag{3.30}$$

with $\nabla^2_{\boldsymbol{\eta}\boldsymbol{\eta}} = \partial^2/\partial\boldsymbol{\eta}\partial\boldsymbol{\eta}$ being the vector with the second partial derivatives with respect to the elements in $\boldsymbol{\eta}$, $\ln f\left(\boldsymbol{\eta}_r\right) = \ln f\left(\boldsymbol{\psi}_r\right)$ and $\ln f\left(\mathbf{r}|\boldsymbol{\eta}_\mathrm{r}\right) = \ln f\left(\mathbf{r}|\boldsymbol{\psi}_\mathrm{r}\right)$ since $\boldsymbol{\eta}_\mathrm{r} = \boldsymbol{\psi}_\mathrm{r}$. As before, we have indicated with $\mathbf{J}^\mathrm{d}_{\boldsymbol{\eta}}$ the FIM related to the data and with $\mathbf{J}^\mathrm{p}_{\boldsymbol{\eta}}$ the contribution brought by the a-priori information on the statistics of the synchronization error.

Let $\nabla_{\boldsymbol{\psi}} = \left[\nabla^T_{\mathbf{q}}, \nabla^T_{\boldsymbol{\kappa}}, \nabla^T_{\epsilon^\mathrm{s}}\right]^T$ and $\nabla^T_{\mathbf{q}} = \left[\nabla^T_{\mathbf{p}^\mathrm{t}}, \nabla^T_{\boldsymbol{\vartheta}^\mathrm{t}}\right]^T$, we can derive the expression of $(\nabla_{\boldsymbol{\psi}}\,\boldsymbol{\eta})$ for the two different approaches as well as the FIM. All the mathematical expressions are reported in Appendix E. Finally, through (3.24) the expression for the localization error bound can be computed.

It is important to remark that the three approaches proposed are equivalent but the one presented in Sec. 3.4.1 has been chosen for the following reasons.

- It permits in a single-step to derive the position and orientation estimation error variance without relying on an alternative vector containing the array measurements;
- It allows to consider large antenna arrays both at AP and mobile side without increasing the FIMs size;
- It enables the possibility to find a more compact expression for the CRB in simplified arrays geometry case.

3.4.3 Ideal AWGN scenario

Here we provide an example on how the general expression (3.24) can be simplified in absence of array calibration errors and MPCs. Specifically, in

AWGN conditions, (3.20) can be reduced to

$$\mathbf{J}_{\boldsymbol{\psi}} = \left[\begin{array}{c:c} \mathbf{J}_{\mathbf{qq}} & \mathbf{0} \\ \hdashline \mathbf{0} & \mathbf{J}_{\boldsymbol{\kappa}^{(1)}\boldsymbol{\kappa}^{(1)}} \end{array}\right] \tag{3.31}$$

where the elements of $\mathbf{J}_{\mathbf{qq}}$ and $\mathbf{J}_{\boldsymbol{\kappa}^{(1)}\boldsymbol{\kappa}^{(1)}}$ are reported in Appendix B and where we have omitted the superscript $^{\mathrm{d}}$ as in this case all the parameters to estimate are deterministic. Specifically, the elements of $\mathbf{J}_{\mathbf{qq}}$ are expressed in (3.61). Starting from (3.31), it can be easily found that

$$\mathsf{CRB}\left(\mathbf{q}\right) = \left(\mathbf{J}_{\mathbf{qq}}\right)^{-1}. \tag{3.32}$$

For further convenience, define $\nu_t = 2\, E_{\mathrm{t}}/N_0 = \nu\, N_{\mathrm{tx}}$, with $\nu = 2\, E/N_0$. The (total) SNR at each receiving antenna element is $\mathsf{SNR}_{\mathrm{t}} = N_{\mathrm{tx}}\mathsf{SNR}_1$, where $\mathsf{SNR}_1 = (a_1)^2\, \nu$ represents the SNR component at the generic transmitting antenna element.

With reference to (3.32), in the next sections we will discuss the two particular cases of MIMO and timed arrays.

MIMO array

According to Appendix C, we can explicit the matrix (3.32) as

$$\mathbf{J}_{\mathbf{qq}} = 8\pi^2\, \mathsf{SNR}_1 \left(\beta_i^2 + f_{\mathrm{c}}^2\right) \sum_{m=1}^{N_{\mathrm{rx}}} \sum_{i=1}^{N_{\mathrm{tx}}} \mathbf{G}_{mii} \tag{3.33}$$

where $\beta_i^2 = \frac{\beta^2}{N_{\mathrm{tx}}}$ is the squared baseband effective bandwidth of $p_i(t)$, and $\mathbf{G}_{mii}$ is a (5×5) matrix depending on the array geometry. Specifically, it provides the relationship between the TOA at each TX-RX couple with the transmitter position and orientation. The CRB can be written as

$$\mathsf{CRB}\left(\mathbf{q}\right) = \frac{1}{8\pi^2\, \mathsf{SNR}^{(1)} \left(\beta_i^2 + f_{\mathrm{c}}^2\right)} \left(\sum_{m=1}^{N_{\mathrm{rx}}} \sum_{i=1}^{N_{\mathrm{tx}}} \mathbf{G}_{mii} \right)^{-1}. \tag{3.34}$$

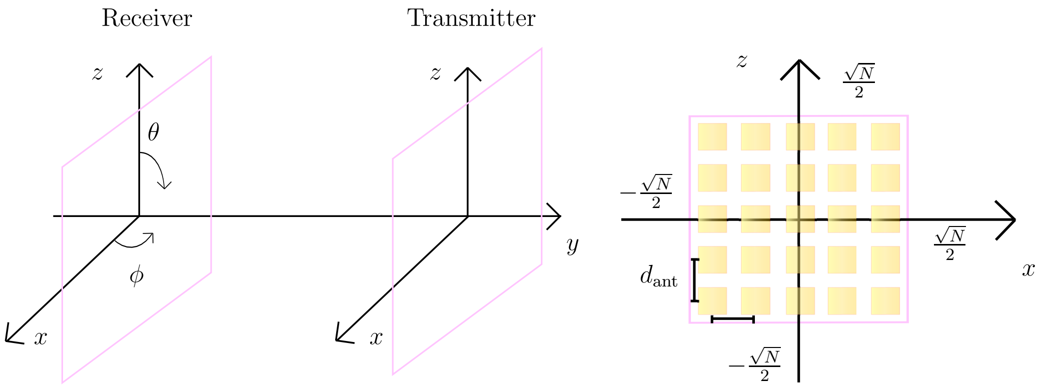

Figure 3.6: Squared arrays configuration with N elements.

When an ideal MIMO scheme is considered, the orthogonality property of the transmitted signals allows independent TOA measurements, one for each TX-RX antenna couple. Obviously the orthogonal property can be obtained only at the price of a low spectral efficiency (i.e., the squared effective bandwidth is $\beta_i^2 = \frac{\beta^2}{N_{\text{tx}}}$, contrarily to what happens if the same signal is transmitted by all array antennas) and unaffordable complexity, especially with massive antennas.

To improve the comprehension of (3.34) and to better clarify the role played by the geometry, we report a particular example valid for a planar array configuration. Specifically, we consider the transmitter (receiver) array being a planar square array of area $A_{\text{tx}} = d_{\text{ant}}^2 N_{\text{tx}}$ ($A_{\text{rx}} = d_{\text{ant}}^2 N_{\text{rx}}$), with the antenna elements equally spaced of d_{ant}. We consider both arrays lying in the XZ-plane and being located one in front of the other with $\mathbf{p}^{\text{r}} = [0,\, 0,\, 0]^T$ and $\mathbf{p}^{\text{t}} = [0,\, y,\, 0]^T$, so that $d = y$. Finally, we set $\boldsymbol{\vartheta}^{\text{t}} = [0, 0]^T$. In Fig. 3.6 is reported the considered simplified scenario.

For this geometric configuration, the diagonal elements in the position and orientation CRLB matrix derived starting from (3.34), are given by

$$\kappa_x = \kappa_z = \frac{12\,\kappa_0}{S\,(N_{\text{rx}} - 1)}, \quad \kappa_y = \frac{\kappa_0}{N_{\text{rx}}}, \quad \kappa_{\vartheta^{\text{t}}} = \kappa_{\varphi^{\text{t}}} = \frac{12\,\kappa_0\,(N_{\text{tx}} + N_{\text{rx}} - 2)}{A_{\text{rx}}\,(N_{\text{tx}} - 1)\,(N_{\text{rx}} - 1)} \tag{3.35}$$

where $\kappa_0 = c^2/(8\pi^2\,\mathsf{SNR}_{\text{t}}\,(\beta_i^2 + f_c^2))$ is the CRLB of the ranging error one would obtain using single antennas, and $S = A_{\text{rx}}/y^2$ represents the ratio between the receiver array area and the squared TX-RX distance. Note that κ_0 depends on the carrier frequency f_c, on the shape of the pulse through β_i^2, on the received SNR, and it does not depend on the number of transmitting antennas. From (3.35), it is possible to remark that the CRLB of the y-coordinate estimation error is inversely proportional to the number of the receiving antenna elements accounting for the number of independent measurements available at the receiver. Regarding the CRLB for the other two position coordinates, a key parameter on the accuracy is S which is related to the ratio between the dimension of the receiver array and the distance between the arrays: as this ratio becomes smaller (i.e. as the distance between the arrays becomes larger with respect to the array size), the positioning accuracy degrades. From (3.35) it is also possible to notice that the accuracy in estimating the orientation depends both on the transmitting and receiving antenna elements. Specifically, both N_tx and N_rx must be greater than one whereas for the position coordinates, the constraint is only on the number of receiving elements. Moreover, non-zero off-diagonal elements remark a correlation between the error on the estimation of the position and orientation parameters. Specifically, we have

$$\kappa_{z\vartheta^\mathrm{t}} = \kappa_{\vartheta^\mathrm{t}z} = \kappa_{x\varphi^\mathrm{t}} = \kappa_{\varphi^\mathrm{t}x} = \frac{12\,\kappa_0}{S\,y\,\left(N_\mathrm{rx}-1\right)}. \tag{3.36}$$

Contrarily, in the *orientation-aware* case, we have

$$\kappa_x = \kappa_z = \frac{12\,\kappa_0}{S\,\left(N_\mathrm{tx}+N_\mathrm{rx}-2\right)}, \quad \kappa_y = \frac{\kappa_0}{N_\mathrm{rx}}. \tag{3.37}$$

Note that when passing from a condition of orientation-unawareness to that of orientation-awareness the positioning accuracy increases, thanks to the additional information provided.

Timed array

Analogous considerations can be drawn for ideal timed arrays. In this case, we have that (3.32) is

$$\mathbf{J}_{\mathbf{qq}} = 8\pi^2 \,\mathsf{SNR}_1 \left(\beta^2 + f_{\mathrm{c}}^2\right) \sum_{m=1}^{N_{\mathrm{rx}}} \sum_{i=1}^{N_{\mathrm{tx}}} \sum_{j=1}^{N_{\mathrm{tx}}} \mathbf{G}_{mij} \tag{3.38}$$

where $\mathbf{G}_{mij}$ is the same 5×5 matrix defined for the MIMO case (see Appendix C). Differently from MIMO here we have an additional summation done with respect to the transmitting antennas due to the fact that in timed array the same signal is adopted for all the antennas composing the array instead of orthogonal waveforms. Therefore, the $\mathsf{CRB}\left(\mathbf{q}\right)$ is

$$\mathsf{CRB}\left(\mathbf{q}\right) = \frac{1}{8\,\pi^2\,\mathsf{SNR}_1 \left(\beta^2 + f_{\mathrm{c}}^2\right)} \left(\sum_{m=1}^{N_{\mathrm{rx}}} \sum_{i=1}^{N_{\mathrm{tx}}} \sum_{j=1}^{N_{\mathrm{tx}}} \mathbf{G}_{mij} \right)^{-1}. \tag{3.39}$$

As before, to improve the comprehension of (3.39), we report a particular example valid for the planar array configuration described above. Differenly from the MIMO case, here the equivalent FIM for position and orientation is singular. As a consequence, we assume that the transmitter orientation is a known parameter (*orientation-aware* case) and we discard it from the estimation parameters vector. In this case the elements of the CRLB matrix results in

$$\kappa_x = \kappa_z = \frac{12\,\kappa_0}{S} \frac{1}{N_{\mathrm{tx}}\left(N_{\mathrm{rx}} - 1\right)}, \quad \kappa_y = \kappa_0 \,\frac{1}{N_{\mathrm{tx}}\,N_{\mathrm{rx}}} \tag{3.40}$$

From (3.40), it is possible to remark that the CRLB of the y-coordinate estimation error is inversely proportional to N_{tx} and N_{rx}: in fact, the N_{tx} term accounts for the SNR enhancement due to the beamsteering process while the N_{rx} term accounts for the number of independent measurements available at the receiver. Note that when $N_{\mathrm{rx}} = 1$, the localization along the x and z axes is not possible (only ranging in the y direction), as for the MIMO case.

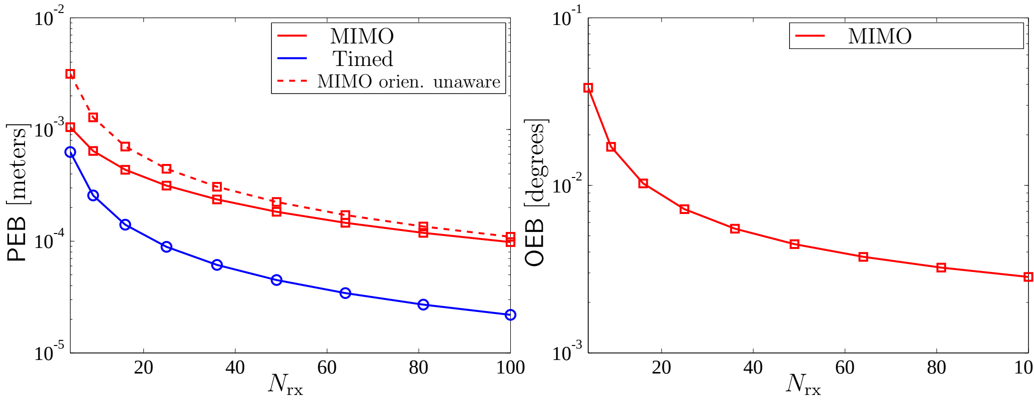

(a) PEB (b) OEB

Figure 3.7: Simulated and ideal PEB and OEB as a function of the receiving antenna elements considering $N_{\rm tx} = 25$, $\vartheta^{\rm t} = (0°, 0°)$, and $y = d = 5\,{\rm m}$. Continuous lines refers to the simulated values derived from (3.24), while markers those obtained from the analytical expressions in (3.35), (3.37) and (3.40).

Preliminary Comparison Between the Obtained Formula Let define the position and orientation error performance metrics as

$$\mathsf{PEB} = \sqrt{\kappa_x + \kappa_y + \kappa_z}, \quad \mathsf{OEB} = \sqrt{\kappa_{\vartheta^{\rm t}} + \kappa_{\varphi^{\rm t}}} \ . \tag{3.41}$$

In Fig. 3.7, PEB and OEB performance are reported for both orientation-aware and -unaware cases considering a transmitting array of $N_{\rm tx} = 25$ antennas and an AP equipped with a massive array ($N_{\rm rx} = 100$). Continuous lines refer to results evaluated in accordance to (3.24) while markers are obtained by the analytical expressions in (3.35), (3.37) and (3.40). It can be noticed that an accordance between simulated and analytical results is present. As can be graphically and analytically deduced, timed arrays outperforms the performance of MIMO for the particular steering and geometric configuration conditions chosen. This is due to the benefit carried by an increased processing gain proportional to the number of the transmitting antennas. Nevertheless, when timed arrays are adopted orientation estimation is not always possible as for certain receiver orientation the FIM is singular and cannot be inverted. In the numerical results it will be shown how different array configurations can help in increasing the diversity without resorting to orthogonal signals.

3.4.4 Ideal multipath scenario

In this section we aim at analysing the same array configurations in absence of array non-idealities and synchronization errors but in the presence of multipath. The main objective is to understand how the possibility of overlapping between MPCs could degrade the localization performance. As previously done, we start from (3.20) and we derive their simplified version as follows

$$\mathbf{J}_{\psi} = \left[\begin{array}{c|c} \mathbf{J}_{\mathbf{q}\mathbf{q}} & \mathbf{J}_{\boldsymbol{\kappa}\mathbf{q}} \\ \hline \mathbf{J}_{\mathbf{q}\boldsymbol{\kappa}} & \mathbf{J}_{\boldsymbol{\kappa}\boldsymbol{\kappa}} \end{array}\right], \tag{3.42}$$

where $\mathbf{J}_{\boldsymbol{\kappa}\boldsymbol{\kappa}}$ accounts for the a-priori information reported in Appendix A. The CRB in (3.24) becomes

$$\mathsf{CRB}\left(\mathbf{q}\right) = \left(\mathbf{J}_{\mathbf{q}\mathbf{q}} - \mathsf{POC}\right)^{-1} \tag{3.43}$$

with path overlap coefficient (POC) expressed as

$$\mathsf{POC} = \mathbf{J}_{\mathbf{q}\boldsymbol{\kappa}}\,\mathbf{J}_{\boldsymbol{\kappa}\boldsymbol{\kappa}}^{-1}\,\mathbf{J}_{\boldsymbol{\kappa}\mathbf{q}}. \tag{3.44}$$

Note that differently from [78], here the POC depends both on the TOA and AOA of the MPC. As it will be shown in the numerical results, once fixed the temporal overlap the POC varies in accordance to the angle of incidence at the receiving array.

Single-antenna scenario

To understand the effect of the multipath overlapping, it seems convenient to analyse what happens when deriving the CRB on the TOA related to the direct path. To simplify the derivation we consider the case in which the transmitter and the receiver consist of a single antenna and only 2 MPCs are present. In this simplified scenario considering a bandpass signal $S(f)$, the

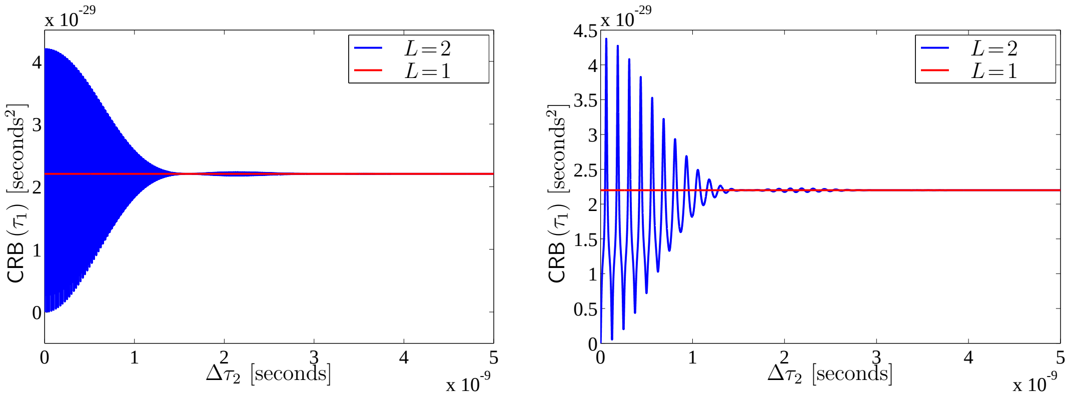

Figure 3.8: CRB as a function of $\Delta\tau_2$ for $f_c = 60\,\text{GHz}$ (left) and $f_c = 4\,\text{GHz}$ (right) (*orientation-aware* case).

received signal model becomes

$$R(f) = \left(\alpha_1\, e^{-j\,2\pi\, f\, \tau_1} + \alpha_2\, e^{-j\,2\pi\, f\, \tau_2}\right)\, S(f) \,+\, N(f) \tag{3.45}$$

Recalling the parameters vector in (3.15) and the considerations in Appendix D, it will be

$$\boldsymbol{\eta} = [\tau_1,\, \boldsymbol{\kappa}_1,\, \boldsymbol{\kappa}_2]^T = [\tau_1,\, \alpha_1,\, \alpha_2,\, \tau_2]^T \tag{3.46}$$

where we have discarded all the angular informations as for the moment we are interested at inferring the CRLB on the TOA. After some computations, it is possible to obtain

$$\mathsf{CRB}(\tau_1) = \frac{1}{2\,\nu\,|\alpha_1|^2}\left(\beta^2 - \left(\frac{\left(R_{\dot{p}}(\Delta\tau_2)\right)^2}{1-\left(R_p(\Delta\tau_2)\right)^2}\right)\right)^{-1} = \frac{1}{2\,\nu\,|\alpha_1|^2}\left(\beta^2 - \chi^2\right)^{-1} \tag{3.47}$$

where $R_p(\cdot)$, $R_{\dot{p}}(\cdot)$ and $R_{\ddot{p}}(\cdot)$ are defined in Appendix B and $\beta^2 = R_{\ddot{p}}(0)$. A graphical representation of (3.47) is reported in Fig. 3.8 for $W = 1\,\text{GHz}$, $f_c = 60\,\text{GHz}$ and $f_c = 4\,\text{GHz}$ and $d_{\text{tx-rx}} = 5\,\text{m}$. In Fig. 3.8-(left) the fractional bandwidth W/f_c is very small and consequently, for $L = 2$ the fluctuations around the AWGN case are very fast while for $f_c = 4\,\text{GHz}$ are more dis-

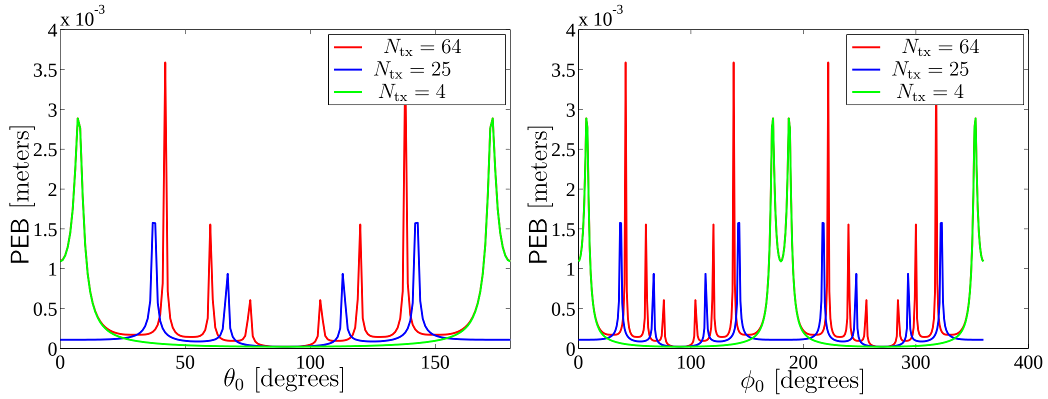

Figure 3.9: PEB as a function of the steering angle for timed arrays with $N_{\text{rx}} = 100$ and different N_{tx} (*orientation-aware* case).

cernible (see Fig. 3.8-(right)). One can notice that when $\Delta\tau_2 = 0$, i.e. the second path is completely overlapped to the first path, the coefficient $\chi^2 \to 0$ meaning that the MPCs sum both constructively and destructively and the overall effect is that the PEB tends to the AWGN case. Similarly, when the difference $\Delta\tau_2$ is greater than the signal duration, the two paths do not overlap and the localization performance only depends on the information provided by the direct path.

3.5 Numerical results

In this section some numerical results are reported considering different array configurations, propagation conditions and system non-idealities.

3.5.1 System configuration

We consider a scenario with a single AP equipped with a massive array of $N_{\text{rx}} = 100$ antennas, with the center placed in $\mathbf{p}^{\text{r}} = [0, 0, 0]^T$, and a transmitting antenna whose array center is located in $\mathbf{p}^{\text{t}} = [0, 5, 0]^T$ ($d = 5\,\text{m}$). Four AP's structures are analysed: the timed array equipped with delay lines and phase shifters, the phased array in which only phase shifters are adopted, and finally the MIMO array in which orthogonal waveforms are transmitted and neither phase shifters nor time delays are adopted. We assume, as in the

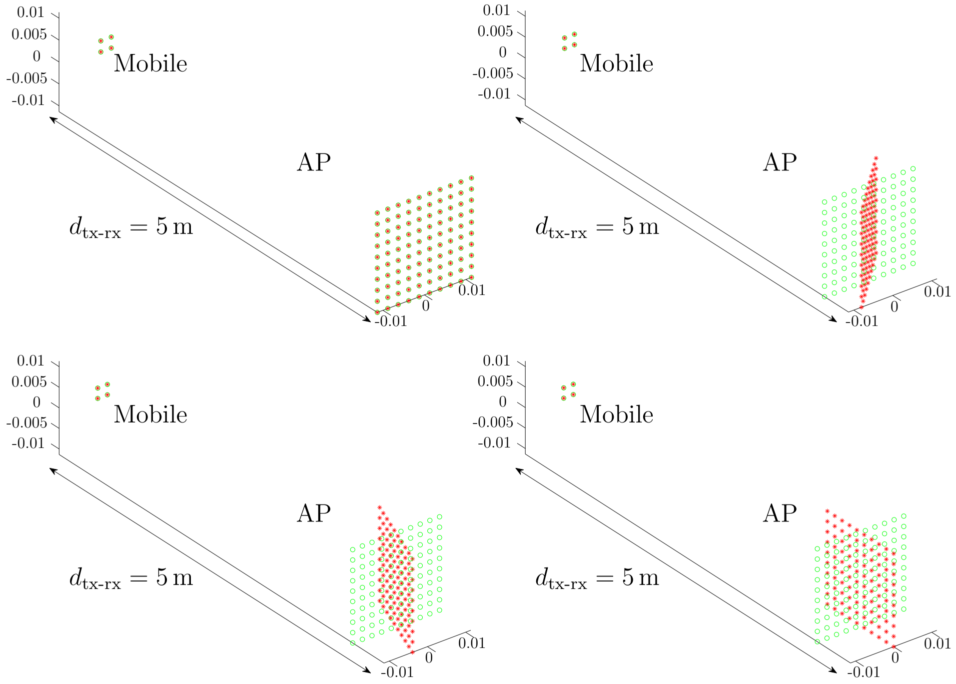

Figure 3.10: Array geometric configurations used in simulations results. From the top-left to the bottom-right, the AP orientation has been set to $\vartheta^{\text{r}} = 0°$, 45°, 70° and 90°.

mathematical model, that the receiver has a perfect knowledge of the transmitter steering direction, and we compare the results considering $f_{\text{c}} = 60\,\text{GHz}$ in AWGN and multipath conditions. Transmitted signals are compliant with the correspondent FCC energy mask [49]. The performance is evaluated in terms of PEB and OEB computed from Monte Carlo simulations as

$$\mathsf{PEB} = \frac{\sum_{k=1}^{N_{\text{cycle}}} \sqrt{\text{tr}\left(\mathsf{CRB}\left(\mathbf{p}^{\text{t}}\right)\right)}}{N_{\text{cycle}}}, \quad \mathsf{OEB} = \frac{\sum_{k=1}^{N_{\text{cycle}}} \sqrt{\text{tr}\left(\mathsf{CRB}\left(\boldsymbol{\vartheta}^{\text{t}}\right)\right)}}{N_{\text{cycle}}} \tag{3.48}$$

where $\text{tr}\left(\cdot\right)$ indicates the matrix trace and $N_{\text{cycle}} = 100$ is the number of Monte Carlo iterations. For each cycle, a different 3D array orientation and multipath scenario are generated. Specifically, the receiving (transmitting) antenna elements are spaced apart of $d_{\text{ant}} = \lambda_L/2$, where $\lambda_L = c/f_L$ and $f_L = f_{\text{c}} - W/2$, and a planar configuration as that reported in Fig. 3.10 has

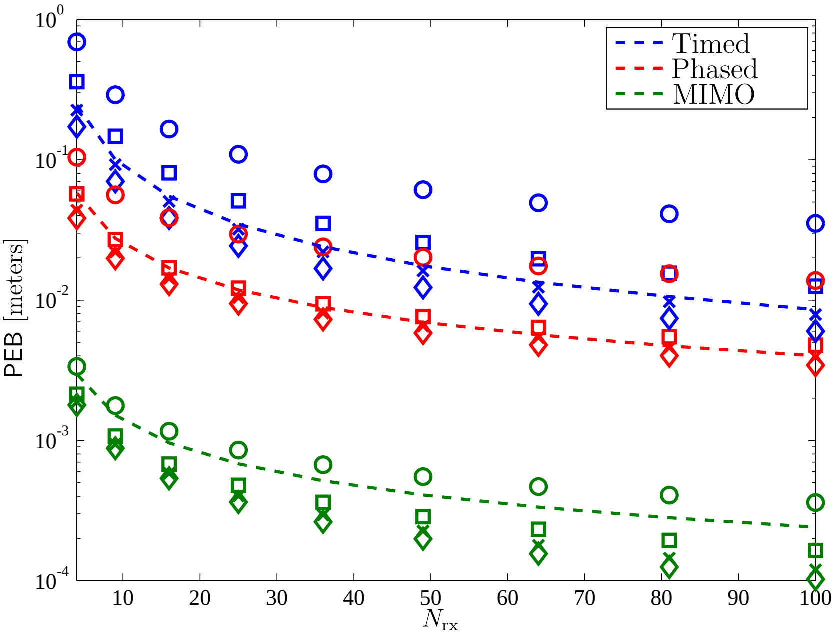

Figure 3.11: PEB vs number of receiving elements N_{rx} in *orientation-aware case* and with $N_{\mathrm{tx}} = 25$. Continuous lines refer to the case averaged over $(\boldsymbol{\vartheta}^{\mathrm{t}}, \boldsymbol{\vartheta}^{\mathrm{r}})$ while the markers lines have been averaged over $\boldsymbol{\vartheta}^{\mathrm{t}}$ and the receiver orientation has been set to $\boldsymbol{\vartheta}^{\mathrm{r}} = (0°, 0°)$ (marker: $\diamond$), $\boldsymbol{\vartheta}^{\mathrm{r}} = (0°, 45°)$ (marker: $\times$), $\boldsymbol{\vartheta}^{\mathrm{r}} = (0°, 70°)$ (marker: $\square$), $\boldsymbol{\vartheta}^{\mathrm{r}} = (0°, 90°)$ (marker: $\circ$).

been adopted.

A receiver noise figure of $N_{\mathrm{F}} = 4\,\mathrm{dB}$ and an observation time of $T_{\mathrm{f}} = 500\,\mathrm{ns}$ are considered. The signal bandwidth is set to $W = 1$ GHz (e.g., if RRC pulses are adopted with a roll-off factor of $\beta = 0.6$, the signal duration is $\tau_{\mathrm{p}} = (1 + \beta)/W = 1.6\,\mathrm{ns}$) if not otherwise indicated.

When present, the phase shifters' quantization errors are uniformly distributed between $\delta_i^{\mathrm{t}} \sim \mathcal{U}\left(-\pi/4, \pi/4\right)$ while the TDLs errors are $\Delta\tau_i^{\mathrm{t}} \sim \mathcal{U}\left(0, d_{\mathrm{ant}}/c\right)$. The standard deviation of the synchronization error is set to $\sigma_{\epsilon} = 100\,\mathrm{ps}$.

3.5.2 Results

The results of this section have been obtained as a function of the following quantities

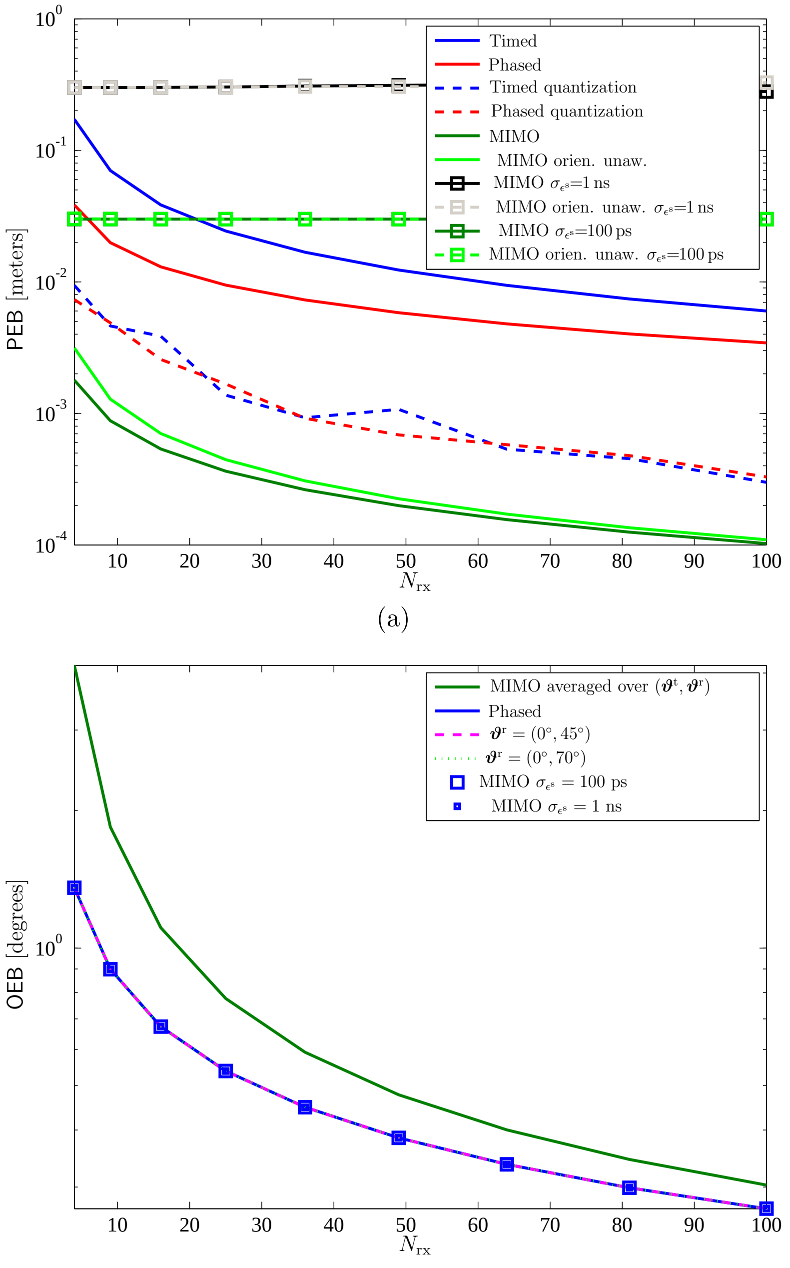

Figure 3.12: PEB and OEB vs number of receiving elements $N_{\rm rx}$ with $N_{\rm tx} = 25$ and $\boldsymbol{\vartheta}^{\rm r} = (0°, 0°)$. The results are averaged over 100 possible values of $\boldsymbol{\vartheta}^{\rm t}$.

- the transmitting antennas number;
- the steering directions;

- the array structure (i.e. timed, phased, random, MIMO);
- the multipath temporal and angular overlapping effect.

Free space scenario

In this section the results for the AWGN case are reported for both *orientation-aware* and *orientation-unaware* problems.

Firstly we have considered the PEB for timed arrays as a function of the steering directions when the receiver orientation is fixed to $\boldsymbol{\vartheta}^{\mathrm{r}} = \boldsymbol{\vartheta}^{\mathrm{t}} = (0^\circ, 0^\circ)$. The results varying both steering angles (θ_0, ϕ_0) can be found in Fig. 3.9. The number of receiving antenna elements is fixed to $N_{\mathrm{rx}} = 100$ whereas the performance are reported as a function of the number of transmitting elements. As expected when operating with a fixed EIRP, the localization performance for different N_{tx} coincide in the direction of the transmitter (i.e. when $\theta_0 = \theta$ and $\phi_0 = \phi$) as the maximum array gain increases proportional to N_{tx}. From the obtained results it can be noticed that when a low number of transmitting antennas (e.g. $N_{\mathrm{tx}} = 4$) is adopted, the PEB is more insensitive with respect to the steering direction due to the fact that the HPBW on both elevation and azimuth plane is larger. Contrarily, when the number of antennas increases, the main beam becomes narrower and consequently, the PEB changes according to the radiation pattern. This effect will play an important role of spatial filtering when MPCs are present.

Secondly, we aim at comparing different array structures considering different sized receiving arrays when the constraint is on the total emitted power. In this case we have considered different receiver orientation and we have averaged the PEB results over 100 possible transmitter orientations.

Figure 3.11 reports the PEB results in the *orientation-aware* case for different receiver orientation. As we can see, timed and phased arrays performance highly depends on receiver's orientation and some configurations could lead to a FIM singularity problem. Contrarily, in MIMO case this impact is less pronounced as different signals are transmitted for each antenna branch. The non-perfect alignment of phased arrays permits to preserve a good level of diversity gain and hence of PEB performance even in unlucky

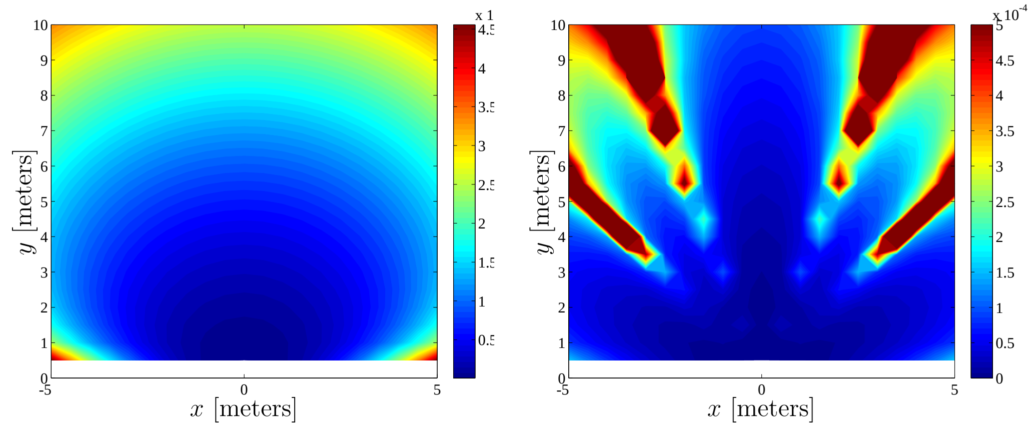

(a) MIMO, $\boldsymbol{\vartheta}^{\mathrm{t}} = (0°, 0°)$ (b) Timed, $\boldsymbol{\vartheta}^{\mathrm{t}} = (0°, 0°)$

Figure 3.13: PEB with $N_{\mathrm{rx}} = 100$ and $N_{\mathrm{tx}} = 9$ in *orientation-aware* case varying the transmitter orientation.

receiver's orientation. Consequently, contrarily to what happened in Fig. 3.7 where $\boldsymbol{\vartheta}^{\mathrm{t}} = (0°, 0°)$, timed and phased arrays localization accuracy appears degraded with respect to the MIMO array case. Figure 3.12-(a) shows the PEB results for both *orientation-aware* and *orientation-unaware* cases as a function of the receiver antennas number once the receiver's orientation is fixed to $\boldsymbol{\vartheta}^{\mathrm{r}} = (0°, 0°)$. Contrarily from what intuitively expected, when a large bandwidth is adopted, the performance of phased arrays exceeds that of timed arrays. We ascribe this effect to the fact that the perfect alignment of the transmitted signals in timed arrays increases the processing gain but reduces the transmitting diversity gain. On the other side, phased arrays preserve both a good level of diversity and of steering capabilities. Finally, when MIMO arrays are employed, a reduction in the received SNR is experienced again, but the number of independent measurements becomes equal to its maximum (i.e. $N_{\mathrm{tx}}N_{\mathrm{rx}}$). Following the same principle, array quantization errors, once characterized, can be fruitfully exploited to improve the diversity, and thus the localization performance. In all cases, the synchronization error degrades the localization performance.

Figure 3.12-(b) reports the OEB results as a function of the receiving elements. As it can be noticed, in this case only the performance of MIMO

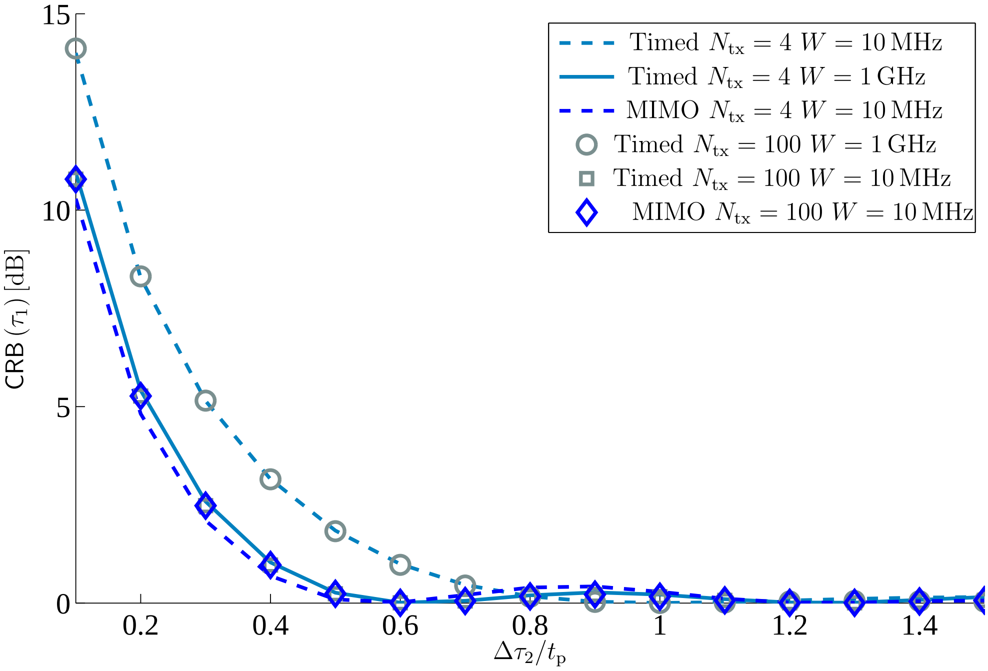

Figure 3.14: Normalized CRB on TOA of the first path considering different signal bandwidth and transmitting antenna number.

arrays are analysed because of the singularity problem arising in timed and phased arrays. Synchronization error and different receiver's orientation do not impact the orientation accuracy.

Grid results Figure 3.13 reports the PEB results for the *orientation-aware* case when the mobile can move in a grid of points spaced of 0.5m. We considered a 3D indoor scenario of $10 \times 10 \times 3\,\mathrm{m}^3$ where we have supposed that the mobile and the AP are at the same height. The receiver is placed at the origin $\mathbf{p}^\mathrm{r} = [0, 0, 0]^T$, its orientation is assumed equal to $\boldsymbol{\vartheta}^\mathrm{r} = (0°, 0°)$ and it is equipped with $N_\mathrm{rx} = 100$. Contrarily, we set the number of the mobile array antennas at a lower value in order to facilitate the integrability in portable devices (i.e. $N_\mathrm{tx} = 9$) and we analysed the results when the transmitter orientation is $\boldsymbol{\vartheta}^\mathrm{t} = (0°, 0°)$. The steering weights are always set to point towards the AP. Grid results confirm that MIMO arrays are more

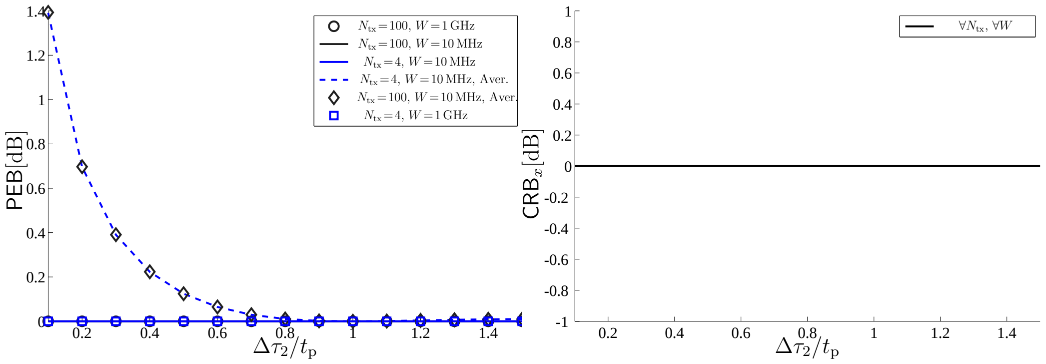

(a) PEB (b) CRB_x

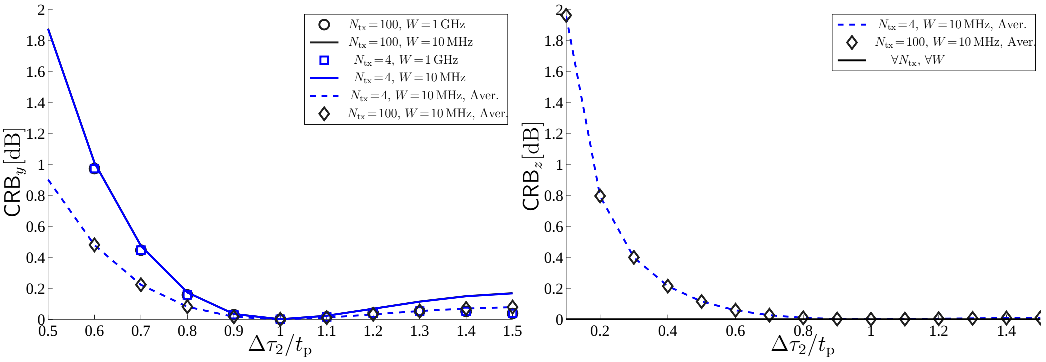

(c) CRB_y (d) CRB_z

Figure 3.15: Normalized PEB and CRB w.r.t. the AWGN case considering different signal bandwidth and transmitting antenna number.

insensitive from the transmitter orientations[3] than the timed arrays. Indeed, when comparing Fig. 3.13-(a) and Fig. 3.13-(b) we can see that if the mobile orientation is fixed, the localization accuracy is higher in a privileged direction in space corresponding to the best geometric configuration conditions.

---

[3] This is true at the exception of particular points in space where the transmitter and the receiver are perpendicular to each other. In fact, at the correspondence of these particular points the FIM related to the transmitter position becomes singular even for MIMO arrays. In Fig. 3.13-(a) the singularity points are white colored.

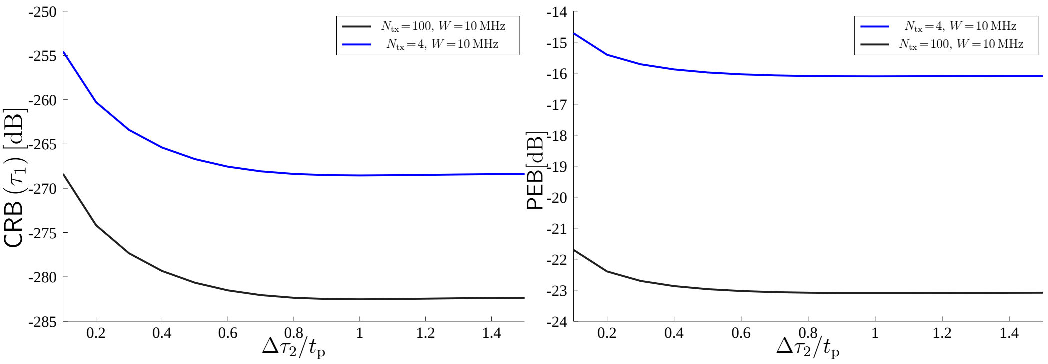

(a) CRB (b) PEB

Figure 3.16: CRB and PEB considering different transmitting antenna number.

Multipath scenario

In this section we consider the case of MPCs when the orientation between the AP and the mobile is known at the receiver side. The geometrical configuration is reported in Fig. 3.6, and in particular, we consider

- two squared antenna arrays lying in the XZ-plane one in front to the other;
- the orientation between the transmitter and the receiver fixed to $\boldsymbol{\vartheta}^{\mathrm{t}} = \boldsymbol{\vartheta}^{\mathrm{r}} = (0°, 0°)$;
- a scatterer moving between the two arrays.

Given this geometric configuration, we analyse the multipath effect separating the temporal and angular contribution. In particular, as expressed in Section 3.4.4, the POC in (3.44) depends on both delay and angle information and in the following, we will separately investigate each of them.

MPC temporal overlapping effect In this paragraph we report the results varying the value of the second path delay bias $\Delta\tau_2$. Specifically, we consider a geometric configuration with the transmitter and the receiver spaced of 5 m and the scatterers located behind the transmitter with a distance proportional to the delay bias. In this configuration, the second path

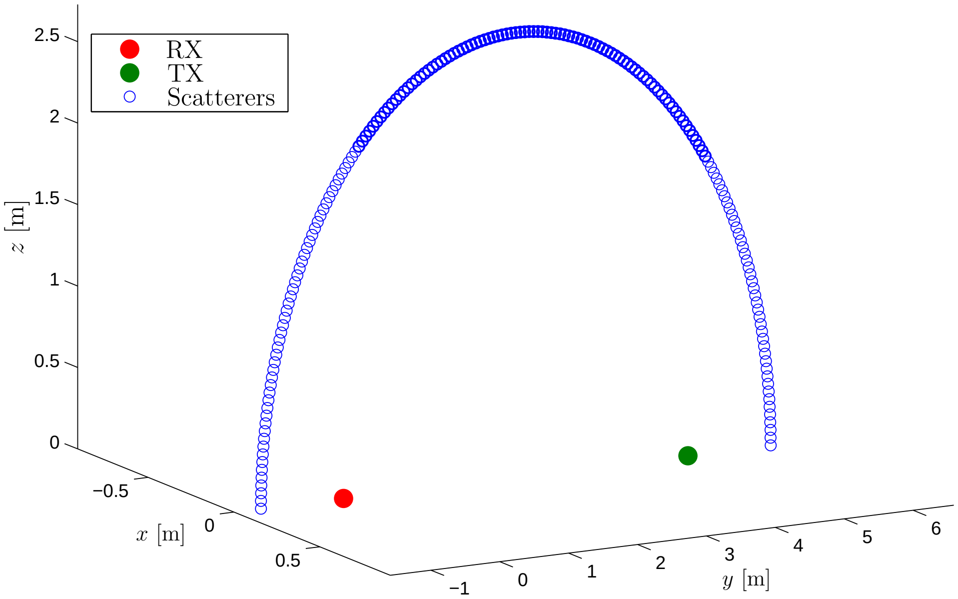

Figure 3.17: Scatterers geometric configuration.

arrives with the same AOA of the first one but with a difference delay value. The second path delay bias ranges from $10\%\,t_{\rm p}$ to $150\%\,t_{\rm p}$, where $t_{\rm p}$ is the transmitted signal duration (note that $t_{\rm p} \approx 1/W$). In Fig. 3.14 the results varying the the number of transmitting elements and the signal bandwidth ($W = 10\,\text{MHz}$ and $W = 1\,\text{GHz}$) are shown, with a fixed transmitted power of $-30\,\text{dB}$, a single receiving antenna, i.e., $N_{\rm rx} = 1$. As it can be seen, when the second path delay is greater than the transmitted signal duration the performance in terms of CRB is the same of that obtained in AWGN condition in accordance to what has been already proved in [78]. This is due to the fact that only the first path contributes to the localization accuracy.

By considering a greater number of receivers ($N_{\rm rx} = 9$), we can compare the same performance in terms of PEB. In Fig. 3.15 results in terms of CRB on the three position coordinates and of PEB are illustrated. Continuous lines refer to the case in which the receiver orientation is fixed to $\boldsymbol{\vartheta}^{\rm r} = (0°, 0°)$ while dashed lines to the averaged case. In this latter situation, $\varphi^{\rm r}$ varies from $0°$ to $180°$ degrees with a step of $5°$ while $\vartheta^{\rm r} = 0°$ has been fixed. As it can be

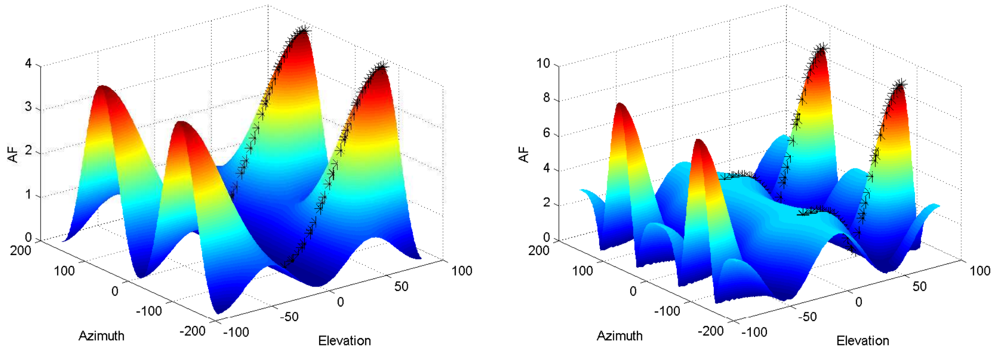

(a) $N_{\text{tx}} = 4$ (b) $N_{\text{tx}} = 9$

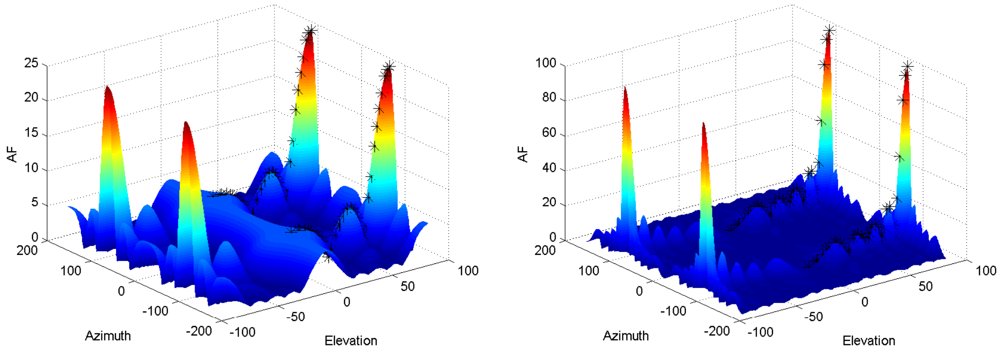

(c) $N_{\text{tx}} = 25$ (d) $N_{\text{tx}} = 100$

Figure 3.18: Array factor considering different transmitting array antenna .

noticed, when the receiving array lies on the XZ plane as the transmitting one, the CRB on the x and z coordinates are equal to that achieved in the AWGN condition. As a consequence, also the PEB reports a slight variation from the AWGN case as it is more influenced by the estimation accuracy of the x and z coordinates than that of the y one. Contrarily, when we change the receiver azimuthal rotational angle the performance on estimating the z coordinates and thus the PEB significantly varies from the AWGN scenario.

From results in Fig. 3.14 and 3.15, it seems that the localization performance considering a number of transmitting antenna equal to $N_{\text{tx}} = 4$ or to $N_{\text{tx}} = 100$ is the same. However, we recall the fact that they are normalized

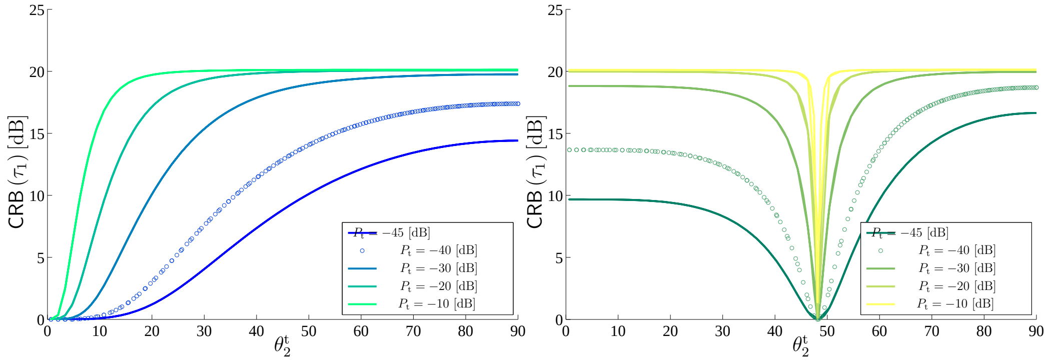

(a) $N_{\mathrm{tx}} = 4$ (b) $N_{\mathrm{tx}} = 9$

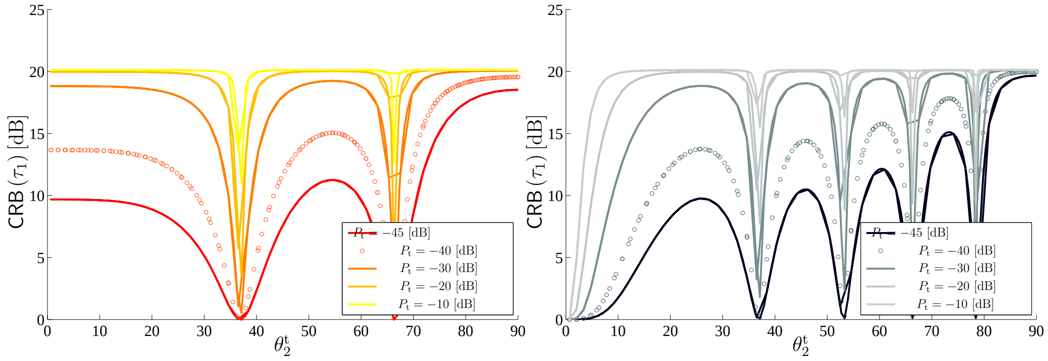

(c) $N_{\mathrm{tx}} = 25$ (d) $N_{\mathrm{tx}} = 100$

Figure 3.19: Normalized CRB w.r.t. the AWGN case considering different transmitted powers and transmitting antenna number.

to the correspondent AWGN case. To clarify this point, we report an example in Fig. 3.16 of non-normalized results in order to better appreciate the beneficial effect of an increased array gain.

MPC angular overlapping effect In this paragraph we analyse the spatial filtering effect by considering a set of scattering points located as in Fig. 3.17. Specifically, based on the results shown in the previous paragraph, we impose a temporal path overlap of $\Delta\tau_2 = 5\%\, t_{\mathrm{p}}$ (as before, the bandwidth is set to 10 MHz and the central frequency is fixed to $f_{\mathrm{c}} = 60\,\mathrm{GHz}$) so that all the scatterers are located in an ellipse whose foci are the transmitting and receiving array geometric centres. If we had considered a greater bandwidth, as for example $W = 1\,\mathrm{GHz}$, the delay of the second path would be smaller

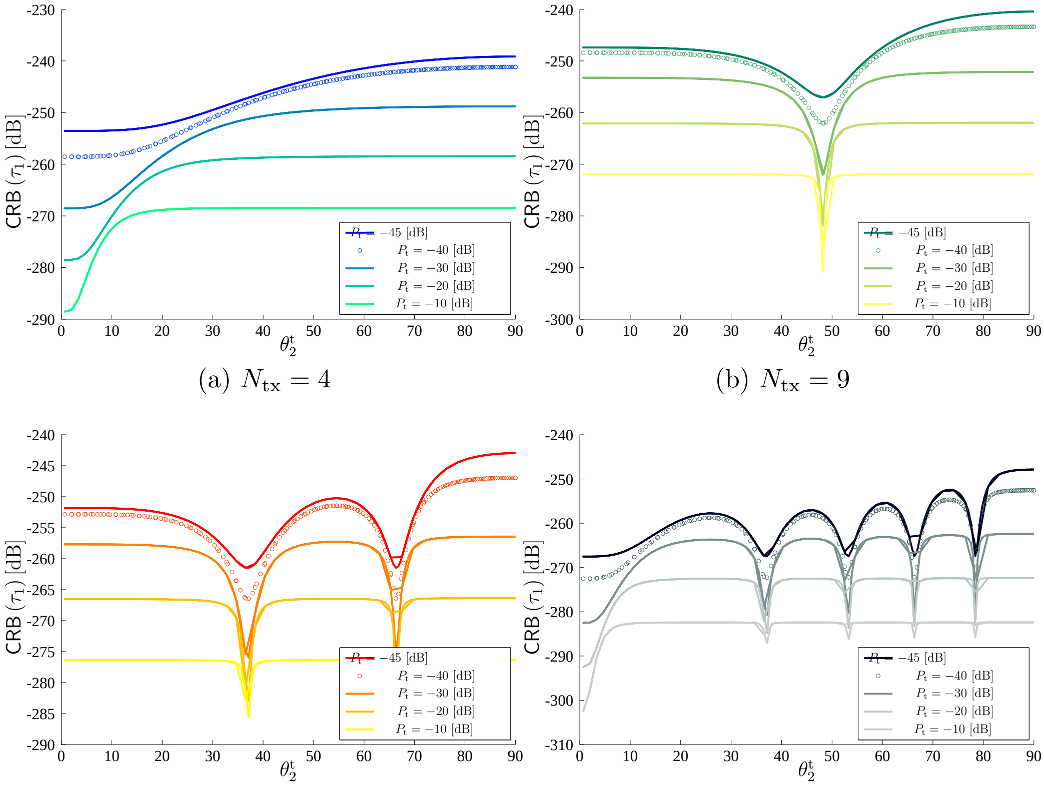

(a) $N_{\mathrm{tx}} = 4$ (b) $N_{\mathrm{tx}} = 9$

(c) $N_{\mathrm{tx}} = 25$ (d) $N_{\mathrm{tx}} = 100$

Figure 3.20: CRB w.r.t. the AWGN case considering different transmitted powers and transmitting antenna number.

causing all scatterers points fall in the main antenna lobe. As a result we would not appreciate the spatial effect. For simplicity, we consider an ellipse lying on the ZY plane and we aim at analysing the filtering capability of the transmitting array based on its radiation characteristic. To this end, in Fig. 3.18, we can see the 3D radiation considering different sized transmitting arrays. Black star markers represent the intersection between the transmitter array radiation pattern and scatterers positions. Figure 3.19 shows the results related to the CRB on the direct TOA estimation error normalized with respect to the AWGN case with $N_{\mathrm{rx}} = 1$ and as a function of the number of transmitting elements and of the transmitted power. Results are plotted with respect to the second path AOD. As we can see for $\theta_2^{\mathrm{t}} = 90°$, which corresponds to the scatterers behind the transmitter and the receiver, the

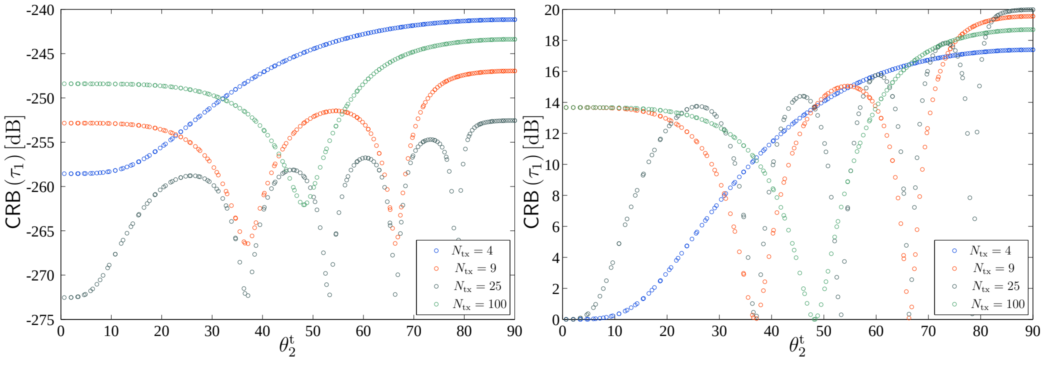

(a) (b)

Figure 3.21: CRB considering different transmitting antenna number.

second path intercepts the radiation pattern in the main lobe causing the maximum error in the TOA estimation. Then, by following the profile of the radiation pattern it is possible to remark different levels of filtering effect: for example, when a small number of antennas is considered (see Fig. 3.19-(a), $N_{\rm tx} = 4$) the angular overlap lasts several degrees contrarily to what happens when a higher number of antennas is adopted (see Fig. 3.19-(d), $N_{\rm tx} = 100$). For what the transmitted power is concerned, again in Fig. 3.19 the CRB is normalized to the AWGN case. In fact, as traditionally known, when increasing the transmitted power as shown in Fig. 3.20, the ranging accuracy increases.

3.6 Conclusions

In this chapter, a study on the theoretical localization performance by adopting massive arrays both at mmW in femtocells AP has been conducted. The performance has been evaluated by deriving the position and orientation CRLB for different array configurations, when the receiver array has the knowledge of the transmitter beamforming weights. Moreover, array calibration and synchronization error have been considered as nuisance parameters. Results have shown that in AWGN conditions, even though a perfect steering capability is desirable to maximize the SNR (perfect signal alignment), it could reduce the diversity level exploitable for positioning. This becomes essential in orientation-unaware situations, i.e. in situations in which the transmitter orientation knowledge is not available at receiver side and for particular array geometric configurations. Therefore phase misalignments caused by large signal bandwidth or the orthogonality properties of the MIMO arrays can be fruitfully exploited to improve the diversity, and thus the localization, position and orientation, performance. Nevertheless when a more realistic propagation scenario is considered, the possibility to exploit a well-defined radiation pattern with a main privileged beam translates in the generation of a spatial filtering effect for MPCs and in a more accurate localization accuracy.

Appendix A

In this Appendix, we want to derive the elements of (3.22). As we have previously mentioned, we will support that the position and the orientation are deterministic parameters and that a prior knowledge of the synchronization errors is available. Moreover, the dominant LOS component related to direct path (i.e. $l = 1$) is considered deterministic while, for $l > 1$, $\alpha_l \sim \mathcal{CN}\left(0, \sigma_l^2\right)$ is a circularly symmetric Gaussian RV . Since we are interested in deriving $\mathbf{J}_{\boldsymbol{\psi}}^{\mathrm{p}}$, we derive $\ln\left(f(\boldsymbol{\psi}_{\mathrm{r}})\right)$ where $\boldsymbol{\psi}_{\mathrm{r}} = \left[\boldsymbol{\alpha}^{\Re\,T},\, \boldsymbol{\alpha}^{\Im\,T},\, \epsilon^{\mathrm{s}}\right]^T$.
As ϵ^{s}, $\boldsymbol{\alpha}^{\Re\,T}$ and $\boldsymbol{\alpha}^{\Re\,T}$ are independent RVs we can write

$$\ln\left(f(\boldsymbol{\psi}_{\mathrm{r}})\right) = \ln\left(f(\boldsymbol{\alpha}^{\Re\,T})\right) + \ln\left(f(\boldsymbol{\alpha}^{\Im\,T})\right) + \ln\left(f(\epsilon^{\mathrm{s}})\right) \tag{3.49}$$

where

$$J_{\epsilon^{\mathrm{s}}\epsilon^{\mathrm{s}}}^{\mathrm{p}} = \frac{1}{\sigma_\epsilon^2}, \quad J_{\alpha_k^{\Re}\alpha_l^{\Re}}^{\mathrm{p}} = J_{\alpha_k^{\Im}\alpha_l^{\Im}}^{\mathrm{p}} = \begin{cases} \frac{1}{\sigma_l^2} & \text{if } l = k \\ 0 & \text{if } l \neq k \end{cases}. \tag{3.50}$$

Appendix B

In this Appendix we want to derive the elements of (3.20). To accomplish this task, we introduce the following quantities relative to the correlation between signals coming from different transmitting antennas and their derivatives

$$R_p(\tau_1 - \tau_2) = \int_W e^{-j\,2\,\pi\,f\,(\tau_1-\tau_2)}\, P_i(f)\, P_j^*(f)\, df \tag{3.51}$$

$$R_{\ddot{p}}(\tau_1 - \tau_2) = \int_W f^2\; e^{-j\,2\,\pi\,f\,(\tau_1-\tau_2)}\, P_i(f)\, P_j^*(f)\, df. \tag{3.52}$$

Based on (3.51), we also introduce some composite terms

$$\chi_{ij}^{(1,1)}(2) = \int_W (f+f_\mathrm{c})^2 \; e^{-j\,2\,\pi\,f\,(\tau_{im1}-\tau_{jm1})}\, P_i(f)\, P_j^*(f)\, df \tag{3.53}$$

$$\chi_{ij}^{(1,1)}(0) = \int_W (f+f_\mathrm{c}) \; e^{-j\,2\,\pi\,f\,(\tau_{im1}-\tau_{jm1})}\, P_i(f)\, P_j^*(f)\, df \tag{3.54}$$

$$\chi_{ij}^{(l,k)}(0) = \int_W (f+f_\mathrm{c}) \; e^{-j\,2\,\pi\,f\,\left(\tau_{iml}-\tau_{jmk}\right)}\, P_i(f)\, P_j^*(f)\, df. \tag{3.55}$$

Finally, it will result useful to collect the exponential terms in the following variables

$$\xi_{ij}^{(1,k)} = e^{-j\,2\,\pi\,f_\mathrm{c}\,\left(\tau_{im1}+\tau_m^\mathrm{r}(\theta_k)-\tau_j^\mathrm{t}(\theta_k)\right)} \tag{3.56}$$

$$\xi_{ij}^{(l,1)} = e^{-j\,2\,\pi\,f_\mathrm{c}\,\left(-\tau_{jm1}-\tau_m^\mathrm{r}(\theta_l)+\tau_i^\mathrm{t}(\theta_l)\right)} \tag{3.57}$$

$$\xi_{ij}^{(1,1)} = e^{-j\,2\,\pi\,f_\mathrm{c}\,(\tau_{im1}-\tau_{jm1})} \tag{3.58}$$

$$\xi_{ij}^{(l,l)} = e^{-j\,2\,\pi\,f_\mathrm{c}\,\left(-\tau_j^\mathrm{t}(\theta_l)+\tau_i^\mathrm{t}(\theta_l)\right)} \tag{3.59}$$

$$\tag{3.60}$$

and the steering in $b_{ij} = \omega_i(\theta_0)\omega_j^*(\theta_0)$. The elements of $\mathbf{J}^\mathrm{d}_{\mathbf{q}\mathbf{q}}$ are

$$J^\mathrm{d}_{q_a\,q_b} = 8\,\pi^2\,\nu\,a_1^2\,\Re\left\{\sum_{m=1}^{N_\mathrm{rx}}\sum_{i=1}^{N_\mathrm{tx}}\sum_{j=1}^{N_\mathrm{tx}} b_{ij}\,\xi_{ij}^{(1,1)}\,\chi_{ij}^{(1,1)}(2)\,\nabla_{q_a}(\tau_{im1})\,\nabla_{q_b}(\tau_{jm1})\right\} \tag{3.61}$$

with $\nu = E/N_0$. The elements of $\mathbf{J}^\mathrm{d}_{\mathbf{q}\epsilon^\mathrm{s}}$ and $\mathbf{J}^\mathrm{d}_{\epsilon^\mathrm{s}\mathbf{q}}$ are

$$J^\mathrm{d}_{q_a\,\epsilon^\mathrm{s}} = 8\,\pi^2\,\nu\,a_1^2\,\Re\left\{\sum_{m=1}^{N_\mathrm{rx}}\sum_{i=1}^{N_\mathrm{tx}}\sum_{j=1}^{N_\mathrm{tx}} b_{ij}\,\xi_{ij}^{(1,1)}\,\chi_{ij}^{(1,1)}(2)\,\nabla_{q}(\tau_{jm1})\right\} \tag{3.62}$$

$$J^\mathrm{d}_{\epsilon^\mathrm{s}\,q_a} = 8\,\pi^2\,\nu\,a_1^2\,\Re\left\{\sum_{m=1}^{N_\mathrm{rx}}\sum_{i=1}^{N_\mathrm{tx}}\sum_{j=1}^{N_\mathrm{tx}} b_{ij}\,\xi_{ij}^{(1,1)}\,\chi_{ij}^{(1,1)}(2)\,\nabla_{q}(\tau_{im1})\right\} \tag{3.63}$$

The elements of $\mathbf{J}^{\mathrm{d}}_{\boldsymbol{\kappa}\boldsymbol{\kappa}}$ are

$$J^{\mathrm{d}}_{a_1\,a_1} = 2\,\nu\Re\left\{\sum_{m=1}^{N_{\mathrm{rx}}}\sum_{i=1}^{N_{\mathrm{tx}}}\sum_{j=1}^{N_{\mathrm{tx}}} b_{ij}\,\xi_{ij}^{(1,1)}\,R_p(\tau_{im1}-\tau_{jm1})\right\} \tag{3.64}$$

$$J^{\mathrm{d}}_{\alpha^{\Re}_k\,\alpha^{\Re}_l} = J^{\mathrm{d}}_{\alpha^{(k)}_I\,\alpha^{(l)}_I} = 2\,\nu\Re\left\{j\sum_{m=1}^{N_{\mathrm{rx}}}\sum_{i=1}^{N_{\mathrm{tx}}}\sum_{j=1}^{N_{\mathrm{tx}}} b_{ij}\,\xi_{ij}^{(l,k)}\,R_p(\tau_{iml}-\tau_{jmk})\right\} \tag{3.65}$$

$$J^{\mathrm{d}}_{a_1\,\alpha^{\Re}_l} = 2\,\nu\Re\left\{\sum_{m=1}^{N_{\mathrm{rx}}}\sum_{i=1}^{N_{\mathrm{tx}}}\sum_{j=1}^{N_{\mathrm{tx}}} b_{ij}\,\xi_{ij}^{(l,1)}\,R_p(\tau_{iml}-\tau_{jm1})\right\} \tag{3.66}$$

$$J^{\mathrm{d}}_{\alpha^{\Re}_k\,a_1} = 2\,\nu\Re\left\{\sum_{m=1}^{N_{\mathrm{rx}}}\sum_{i=1}^{N_{\mathrm{tx}}}\sum_{j=1}^{N_{\mathrm{tx}}} b_{ij}\,\xi_{ij}^{(1,k)}\,R_p(\tau_{im1}-\tau_{jmk})\right\} \tag{3.67}$$

$$J^{\mathrm{d}}_{a_1\,\alpha^{\Im}_l} = 2\,\nu\Re\left\{j\sum_{m=1}^{N_{\mathrm{rx}}}\sum_{i=1}^{N_{\mathrm{tx}}}\sum_{j=1}^{N_{\mathrm{tx}}} b_{ij}\,\xi_{ij}^{(l,1)}\,R_p(\tau_{iml}-\tau_{jm1})\right\} \tag{3.68}$$

$$J^{\mathrm{d}}_{\alpha^{\Im}_k\,a_1} = -2\,\nu\Re\left\{j\sum_{m=1}^{N_{\mathrm{rx}}}\sum_{i=1}^{N_{\mathrm{tx}}}\sum_{j=1}^{N_{\mathrm{tx}}} b_{ij}\,\xi_{ij}^{(1,k)}\,R_p(\tau_{im1}-\tau_{jmk})\right\} \tag{3.69}$$

$$J^{\mathrm{d}}_{\alpha^{\Im}_k\,\alpha^{\Re}_l} = 2\,\nu\Re\left\{-j\sum_{m=1}^{N_{\mathrm{rx}}}\sum_{i=1}^{N_{\mathrm{tx}}}\sum_{j=1}^{N_{\mathrm{tx}}} b_{ij}\,\xi_{ij}^{(l,k)}\;R_p(\tau_{iml}-\tau_{jmk})\right\} \tag{3.70}$$

The elements of $\mathbf{J}^{\mathrm{d}}_{\epsilon^{\mathrm{s}}\boldsymbol{\kappa}}$ are

$$J^{\mathrm{d}}_{\epsilon^{\mathrm{s}}\,a_1} = 4\,\pi\,a_1\,\nu\,\Re\left\{-j\;\sum_{m=1}^{N_{\mathrm{rx}}}\sum_{i=1}^{N_{\mathrm{tx}}}\sum_{j=1}^{N_{\mathrm{tx}}} b_{ij}\,\xi_{ij}^{(1,k)}\chi_{ij}^{(1,1)}(0)\right\} \tag{3.71}$$

$$J^{\mathrm{d}}_{\epsilon^{\mathrm{s}}\,\alpha^{\Re}_l} = 4\,\pi\,a_1\,\nu\Re\left\{j\;\sum_{m=1}^{N_{\mathrm{rx}}}\sum_{i=1}^{N_{\mathrm{tx}}}\sum_{j=1}^{N_{\mathrm{tx}}} b_{ij}\,\xi_{ij}^{(l,1)}\chi_{ij}^{(l,1)}(0)\right\} \tag{3.72}$$

$$J^{\mathrm{d}}_{\epsilon^{\mathrm{s}}\,\alpha^{\Im}_l} = 4\,\pi\,a_1\,\nu\Re\left\{\sum_{m=1}^{N_{\mathrm{rx}}}\sum_{i=1}^{N_{\mathrm{tx}}}\sum_{j=1}^{N_{\mathrm{tx}}}\; b_{ij}\,\xi_{ij}^{(l,1)}\,\chi_{ij}^{(l,1)}(0)\right\} \tag{3.73}$$

$$J^{\mathrm{d}}_{\alpha^{\Re}_k\,\epsilon^{\mathrm{s}}} = 4\,\pi\,a_1\,\nu\Re\left\{-j\;\sum_{m=1}^{N_{\mathrm{rx}}}\sum_{i=1}^{N_{\mathrm{tx}}}\sum_{j=1}^{N_{\mathrm{tx}}} b_{ij}\,\xi_{ij}^{(1,k)}\,\chi_{ij}^{(1,k)}(0)\right\} \tag{3.74}$$

$$J^{\mathrm{d}}_{\alpha^{\Im}_k\,\epsilon^{\mathrm{s}}} = 4\,\pi\,a_1\,\nu\Re\left\{\sum_{m=1}^{N_{\mathrm{rx}}}\sum_{i=1}^{N_{\mathrm{tx}}}\sum_{j=1}^{N_{\mathrm{tx}}} b_{ij}\,\xi_{ij}^{(1,k)}\chi_{ij}^{(1,k)}(0)\right\} \tag{3.75}$$

The elements of $\mathbf{J}^{\mathrm{d}}_{\epsilon^{\mathrm{s}}\,\epsilon^{\mathrm{s}}}$ is

$$J^{\mathrm{d}}_{\epsilon^{\mathrm{s}}\,\epsilon^{\mathrm{s}}} = 8\,\pi^2\,\nu\,a_1^2\,\Re\left\{\sum_{m=1}^{N_{\mathrm{rx}}}\sum_{i=1}^{N_{\mathrm{tx}}}\sum_{j=1}^{N_{\mathrm{tx}}} b_{ij}\,\xi_{ij}^{(1,1)}\,\chi_{ij}^{(1,1)}(2)\,+\sum_{l=2}^{L}\sigma_l^2\,\xi_{ij}^{(l,l)}\,R_{\ddot{p}}\left(\tau_{mil}-\tau_{jml}\right)\right\} \tag{3.76}$$

The elements of $\mathbf{J}^{\mathrm{d}}_{\mathbf{q}\boldsymbol{\kappa}}$ are

$$J^{\mathrm{d}}_{q_a\,a_1} = 4\,\nu\pi\,a_1\,\Re\left\{-j\sum_{m=1}^{N_{\mathrm{rx}}}\sum_{i=1}^{N_{\mathrm{tx}}}\sum_{j=1}^{N_{\mathrm{tx}}} b_{ij}\,\xi_{ij}^{(1,1)}\,\chi_{ij}^{(1,1)}(0)\nabla_{q_a}\left(\tau_{im1}\right)\right\} = 0 \tag{3.77}$$

$$J^{\mathrm{d}}_{q_a\,\alpha_l^{\Re}} = 4\,\pi\,a_1\,\nu\Re\left\{j\sum_{m=1}^{N_{\mathrm{rx}}}\sum_{i=1}^{N_{\mathrm{tx}}}\sum_{j=1}^{N_{\mathrm{tx}}} b_{ij}\,\xi_{ij}^{(l,1)}\chi_{ij}^{(l,1)}(0)\nabla_{q_a}\left(\tau_{jm1}\right)\right\} \tag{3.78}$$

$$J^{\mathrm{d}}_{\alpha_k^{\Re}\,q_a} = 4\,\pi\,a_1\,\nu\Re\left\{-j\sum_{m=1}^{N_{\mathrm{rx}}}\sum_{i=1}^{N_{\mathrm{tx}}}\sum_{j=1}^{N_{\mathrm{tx}}} b_{ij}\,\xi_{ij}^{(1,k)}\,\chi_{ij}^{(1,k)}(0)\nabla_{q_a}\left(\tau_{im1}\right)\right\} \tag{3.79}$$

$$J^{\mathrm{d}}_{q_a\,\alpha_l^{\Im}} = 4\,\pi\,a_1\,\nu\Re\left\{\sum_{m=1}^{N_{\mathrm{rx}}}\sum_{i=1}^{N_{\mathrm{tx}}}\sum_{j=1}^{N_{\mathrm{tx}}} b_{ij}\,\xi_{ij}^{(l,1)}\,\chi_{ij}^{(l,1)}(0)\nabla_{q_a}\left(\tau_{jm1}\right)\right\} \tag{3.80}$$

$$J^{\mathrm{d}}_{\alpha_k^{\Im}\,q_a} = 4\,\pi\,a_1\,\nu\Re\left\{\sum_{m=1}^{N_{\mathrm{rx}}}\sum_{i=1}^{N_{\mathrm{tx}}}\sum_{j=1}^{N_{\mathrm{tx}}} b_{ij}\,\xi_{ij}^{(1,k)}\chi_{ij}^{(1,k)}(0)\nabla_{q_a}\left(\tau_{im1}\right)\right\} \tag{3.81}$$

Appendix C

In this Appendix we will report the expression of the matrix $\mathbf{G}_{mij}$ reported in (3.33) and (3.38). We aim at deriving the following matrix implementing the geometric relationship between TOA and positioning information

$$\mathbf{G}_{mijl} = \nabla_{\mathbf{qq}}(\tau_{mil}, \tau_{jml}). \tag{3.82}$$

The Jacobian operator $\nabla_{\mathbf{qq}}\left(\cdot,\cdot\right)$ corresponds to

$$\nabla_{\mathbf{qq}}\left(\cdot,\cdot\right)=\begin{bmatrix} \nabla_{xx}(\cdot,\cdot) & \nabla_{xy}(\cdot,\cdot) & \nabla_{xz}(\cdot,\cdot) & \nabla_{x\vartheta^{\mathrm{t}}}\ (\cdot,\cdot) & \nabla_{x\varphi^{\mathrm{t}}}(\cdot,\cdot) \\ \nabla_{yx}(\cdot,\cdot) & \nabla_{yy}(\cdot,\cdot) & \nabla_{yz}(\cdot,\cdot) & \nabla_{y\vartheta^{\mathrm{t}}}\ (\cdot,\cdot) & \nabla_{y\varphi^{\mathrm{t}}}(\cdot,\cdot) \\ \nabla_{zx}(\cdot,\cdot) & \nabla_{zy}(\cdot,\cdot) & \nabla_{zz}(\cdot,\cdot) & \nabla_{z\vartheta^{\mathrm{t}}}\ (\cdot,\cdot) & \nabla_{z\varphi^{\mathrm{t}}}(\cdot,\cdot) \\ \nabla_{\vartheta^{\mathrm{t}}x}(\cdot,\cdot) & \nabla_{\vartheta^{\mathrm{t}}y}(\cdot,\cdot) & \nabla_{\vartheta^{\mathrm{t}}z}(\cdot,\cdot) & \nabla_{\vartheta^{\mathrm{t}}\vartheta^{\mathrm{t}}}\ (\cdot,\cdot) & \nabla_{\vartheta^{\mathrm{t}}\varphi^{\mathrm{t}}}(\cdot,\cdot) \\ \nabla_{\varphi^{\mathrm{t}}x}(\cdot,\cdot) & \nabla_{\varphi^{\mathrm{t}}y}(\cdot,\cdot) & \nabla_{\varphi^{\mathrm{t}}z}(\cdot,\cdot) & \nabla_{\varphi^{\mathrm{t}}\vartheta^{\mathrm{t}}}\ (\cdot,\cdot) & \nabla_{\varphi^{\mathrm{t}}\varphi^{\mathrm{t}}}(\cdot,\cdot) \end{bmatrix} \tag{3.83}$$

where the generic element can be written as $\nabla_{q_a\,q_b}(\tau_{mil},\tau_{mjl})=\nabla_{q_a}(\tau_{mil})\nabla_{q_b}(\tau_{mjl})$. For the particular antenna configuration chosen, see Fig. 3.2, in which the array antennas are spaced of d_{ant}, we can write (3.1) as

$$\mathbf{p}_i^{\mathrm{t}}{=}R(\boldsymbol{\vartheta}^{\mathrm{t}})\begin{bmatrix} i_x d_{\mathrm{ant}} \\ 0 \\ i_z d_{\mathrm{ant}} \end{bmatrix} = \begin{bmatrix} i_x d_{\mathrm{ant}}\cos(\varphi^{\mathrm{t}}) - i_z d_{\mathrm{ant}}\sin(\vartheta^{\mathrm{t}})\sin(\varphi^{\mathrm{t}}) \\ i_x d_{\mathrm{ant}}\sin(\varphi^{\mathrm{t}}) + i_z d_{\mathrm{ant}}\sin(\vartheta^{\mathrm{t}})\cos(\varphi^{\mathrm{t}}) \\ i_z d_{\mathrm{ant}}\cos(\vartheta^{\mathrm{t}}) \end{bmatrix} \tag{3.84}$$

$$\mathbf{p}_m^{\mathrm{r}}{=}R(\boldsymbol{\vartheta}^{\mathrm{r}})\begin{bmatrix} m_x d_{\mathrm{ant}} \\ 0 \\ m_z d_{\mathrm{ant}} \end{bmatrix}. \tag{3.85}$$

where d_{ant} is the antenna inter-spacing, $m_x = m_z = -\frac{\sqrt{N_{\mathrm{rx}}}-1}{2}, -\frac{\sqrt{N_{\mathrm{rx}}}-1}{2}+1,\ldots,\frac{\sqrt{N_{\mathrm{rx}}}-1}{2}$ and $i_x = i_z = -\frac{\sqrt{N_{\mathrm{tx}}}-1}{2}, -\frac{\sqrt{N_{\mathrm{tx}}}-1}{2}+1,\ldots,\frac{\sqrt{N_{\mathrm{tx}}}-1}{2}$. Moreover, the array centers are placed so that $\boldsymbol{\theta}_1=(\theta,\phi)=(-\pi/2,\pi/2)$ and

$$\mathbf{p}^{\mathrm{r}}=[0\ 0\ 0]^{\mathsf{T}} \quad \mathbf{p}^{\mathrm{t}}=[0\ y\ 0]^{\mathsf{T}}. \tag{3.86}$$

As a consequence (3.82) reduces to

$$\mathbf{G}_{mij1} = \mathbf{G}_{mij} = \frac{d_{\text{ant}}^2}{(c\,y)^2}$$

$$\times \left[\begin{array}{c:c:c:c:c} (m_x - i_x)\,(m_x - j_x) & \frac{y}{d_{\text{ant}}}(m_x - i_x) & (m_x - i_x)(j_z - m_z) & y\,(i_x - m_x)\,j_z & y\,(i_x - m_x)\,j_x \\ \frac{y}{d_{\text{ant}}}(m_x - i_x) & \frac{y^2}{d_{\text{ant}}^2} & \frac{y}{d_{\text{ant}}}(j_z - m_z) & -\frac{y^2}{d_{\text{ant}}}j_z & -\frac{y^2}{d_{\text{ant}}}j_x \\ (m_x - i_x)(j_z - m_z) & \frac{y}{d_{\text{ant}}}(j_z - m_z) & (i_z - m_z)\,(j_z - m_z) & y\,(m_z - i_z)\,j_z & y\,(m_z - i_z)\,j_x \\ y\,(i_x - m_x)\,j_z & -\frac{y^2}{d_{\text{ant}}}j_z & y\,(m_z - i_z)\,j_z & y^2 i_z j_z & y^2 i_z j_x \\ y\,(i_x - m_x)\,j_x & -\frac{y^2}{d_{\text{ant}}}j_x & y\,(m_z - i_z)\,j_x & y^2 i_z j_x & y^2 i_x j_x \end{array}\right] \tag{3.87}$$

with $j_x = j_z = -\frac{\sqrt{N_{\text{tx}}}-1}{2}, -\frac{\sqrt{N_{\text{tx}}}-1}{2} + 1, \ldots, \frac{\sqrt{N_{\text{tx}}}-1}{2}$.

Appendix D

In this Appendix we aim at demonstrating that the MPC parameters vector in (3.17) and in (3.18) are equivalent when considering the CRB on the TOA of the first path. To this purpose we consider a single antenna scenario, only two paths and a simplified received signal model:

$$R(f) = \sum_{l=1}^{2} \alpha_l \, e^{-j\,2\pi\,f\,\tau_l}\, S(f) \,+\, N(f). \tag{3.88}$$

Then, we test two different parameters vector:

$$\boldsymbol{\eta} = \left[\tau_1,\, \alpha_1\ \tau_2,\, \alpha_2\right]^T \tag{3.89}$$

$$\boldsymbol{\psi} = \left[\tau_1,\, \alpha_1\ \Delta\tau_2,\, \alpha_2\right]^T \tag{3.90}$$

and the following definitions

$$R_p(\Delta\tau) = \int_T p(t+\Delta\tau)\, p(t)\, dt = \int_W e^{-j\,2\,\pi\,f\,\Delta\tau}\, |P(f)|^2\, df \tag{3.91}$$

$$R_{\dot{p}}(\Delta\tau) = \int_T p(t+\Delta\tau)\, \dot{p}(t)\, dt = \int_W j\,2\,\pi\,f\, e^{-j\,2\,\pi\,f\,\Delta\tau}\, |P(f)|^2\, df \tag{3.92}$$

$$R_{\ddot{p}}(\Delta\tau) = \int_T p(t+\Delta\tau)\, \ddot{p}(t)\, dt = \int_W 4\,\pi^2\, f^2\, e^{-j\,2\,\pi\,f\,\Delta\tau}\, |P(f)|^2\, df \tag{3.93}$$

with $R_p(0) = 1$, $R_{\dot{p}}(0) = 0$ and $R_{\ddot{p}}(0) = \beta^2$.

After some computations, the FIMs could be computed resulting in

$$\begin{aligned}
\mathbf{J}_{\boldsymbol{\eta}} &= 2\;\nu \left[\begin{array}{c|ccc}
|\alpha_1|^2\;\beta^2 & 0 & 0 & \alpha_1\;R_{\dot{p}}(\Delta\tau^{(2,1)}) \\ \hline
0 & 1 & 0 & R_p(\Delta\tau^{(2,1)}) \\
0 & 0 & \sigma_2^2\;\beta^2 & 0 \\
-\alpha_1\;R_{\dot{p}}(\Delta\tau^{(1,2)}) & R_p(\Delta\tau^{(1,2)}) & 0 & 1
\end{array} \right] \\
&= \begin{bmatrix} \mathbf{A}_{\boldsymbol{\eta}} & \mathbf{B}_{\boldsymbol{\eta}} \\ \mathbf{B}_{\boldsymbol{\eta}}^H & \mathbf{C}_{\boldsymbol{\eta}} \end{bmatrix}
\end{aligned} \tag{3.94}$$

$$\begin{aligned}
\mathbf{J}_{\boldsymbol{\psi}} &= 2\;\nu \left[\begin{array}{c|ccc}
(|\alpha_1|^2 + \sigma_2^2)\;\beta^2 & 0 & \sigma_2^2\;\beta^2 & -\alpha_1\;R_{\dot{p}}(\Delta\tau^{(2,1)}) \\ \hline
0 & 1 & 0 & R_p(\Delta\tau^{(1,2)}) \\
\sigma_2^2\;\beta^2 & 0 & \sigma_2^2\;\beta^2 & 0 \\
-\alpha_1\;R_{\dot{p}}(\Delta\tau^{(1,2)}) & R_p(\Delta\tau^{(2,1)}) & 0 & 1
\end{array} \right] \\
&= \begin{bmatrix} \mathbf{A}_{\boldsymbol{\psi}} & \mathbf{B}_{\boldsymbol{\psi}} \\ \mathbf{B}_{\boldsymbol{\psi}}^H & \mathbf{C}_{\boldsymbol{\psi}} \end{bmatrix}
\end{aligned} \tag{3.95}$$

Note that $\mathbf{C}_{\boldsymbol{\eta}} = \mathbf{C}_{\boldsymbol{\psi}} = \mathbf{C}$ and its inverse is equal to

$$\mathbf{C} = \begin{bmatrix}
-\frac{1}{\left(R_p(\Delta\tau^{(1,2)})\right)^2 - 1} & 0 & \frac{R_p(\Delta\tau^{(1,2)})}{\left(R_p(\Delta\tau^{(1,2)})\right)^2 - 1} \\
0 & \frac{1}{\sigma_2^2\;\beta^2} & 0 \\
\frac{R_p(\Delta\tau^{(1,2)})}{\left(R_p(\Delta\tau^{(1,2)})\right)^2 - 1} & 0 & -\frac{1}{\left(R_p(\Delta\tau^{(1,2)})\right)^2 - 1}
\end{bmatrix}. \tag{3.96}$$

Finally, the CRB based on $\boldsymbol{\eta}$ can be found as

$$\begin{aligned}\mathsf{CRB}_{\boldsymbol{\eta}}(\tau_1) &= \frac{1}{2\,\nu}\left(|\alpha_1|^2\,\beta^2 - |\alpha_1|^2\,R_{\dot{p}}(\Delta\tau^{(2,1)})\left(\frac{1}{1-\left(R_p(\Delta\tau^{(1,2)})\right)^2}\right)R_{\dot{p}}(\Delta\tau^{(2,1)})\right)^{-1}\\ &= \frac{1}{2\,\nu\,|\alpha_1|^2}\left(\beta^2 + \left(\frac{\left(R_{\dot{p}}(\Delta\tau^{(2,1)})\right)^2}{\left(R_p(\Delta\tau^{(1,2)})\right)^2-1}\right)\right)^{-1} \qquad (3.97)\end{aligned}$$

and it results equal to that obtained considering $\boldsymbol{\psi}$

$$\begin{aligned}\mathsf{CRB}_{\boldsymbol{\psi}}(\tau_1) &= \frac{1}{2\,\nu}\,\Big(\,\beta^2(|\alpha_1|^2+\sigma_2^2) - \sigma_2^2\beta^2 + \\ &\quad -|\alpha_1|^2\,R_{\dot{p}}(\Delta\tau^{(2,1)})\left(\frac{1}{1-\left(R_p(\Delta\tau^{(1,2)})\right)^2}\right)R_{\dot{p}}(\Delta\tau^{(2,1)})\Big)^{-1}\\ &= \frac{1}{2\,\nu\,|\alpha_1|^2}\left(\beta^2 + \left(\frac{\left(R_{\dot{p}}(\Delta\tau^{(2,1)})\right)^2}{\left(R_p(\Delta\tau^{(1,2)})\right)^2-1}\right)\right)^{-1}\quad. \qquad (3.98)\end{aligned}$$

Appendix E

In this Appendix, we want to derive the Jacobian and the Fisher Information matrices related to the alternative approaches described in 3.4.2. The expression of $(\nabla_{\boldsymbol{\psi}}\,\boldsymbol{\eta})$ that relates the true parameters vector with the measurements can be computed as

- 2nd approach

$$(\nabla_{\boldsymbol{\psi}}\,\boldsymbol{\eta}) = \left[\begin{array}{c:cc} \nabla_{\mathbf{q}}(\boldsymbol{\tau}^T) & \nabla_{\mathbf{q}}(\boldsymbol{\alpha}^T) & \nabla_{\mathbf{q}}(\epsilon^{\mathrm{s}}) \\ \hdashline \nabla_{\boldsymbol{\kappa}}(\boldsymbol{\tau}^T) & \nabla_{\boldsymbol{\kappa}}(\boldsymbol{\alpha}^T) & \nabla_{\boldsymbol{\kappa}}(\epsilon^{\mathrm{s}}) \\ \nabla_{\epsilon^{\mathrm{s}}}(\boldsymbol{\tau}^T) & \nabla_{\epsilon^{\mathrm{s}}}(\boldsymbol{\alpha}^T) & \nabla_{\epsilon^{\mathrm{s}}}(\epsilon^{\mathrm{s}}) \end{array}\right] = \left[\begin{array}{c:c} \nabla_{\mathbf{q}}(\boldsymbol{\tau}^T) & \mathbf{0} \\ \hdashline \mathbf{B} & \mathbf{C} \end{array}\right] \qquad (3.99)$$

- 3rd approach

$$(\nabla_{\boldsymbol{\psi}}\,\boldsymbol{\eta}) = \left[\begin{array}{c:cc} \nabla_{\mathbf{q}}(\boldsymbol{\xi}^T) & \nabla_{\mathbf{q}}(\boldsymbol{\kappa}^T) & \nabla_{\mathbf{q}}(\epsilon^{\mathrm{s}}) \\ \hdashline \nabla_{\boldsymbol{\kappa}}(\boldsymbol{\xi}^T) & \nabla_{\boldsymbol{\kappa}}(\boldsymbol{\kappa}^T) & \nabla_{\boldsymbol{\kappa}}(\epsilon^{\mathrm{s}}) \\ \nabla_{\epsilon^{\mathrm{s}}}(\boldsymbol{\xi}^T) & \nabla_{\epsilon^{\mathrm{s}}}(\boldsymbol{\kappa}^T) & \nabla_{\epsilon^{\mathrm{s}}}(\epsilon^{\mathrm{s}}) \end{array}\right] = \left[\begin{array}{c:c} \nabla_{\mathbf{q}}(\boldsymbol{\xi}^T) & \mathbf{0} \\ \hdashline \mathbf{0} & \mathbf{I} \end{array}\right] \qquad (3.100)$$

where $\mathbf{0}$ is the zero matrix and $\mathbf{I}$ is an identity matrix. Note that the matrices $\nabla_{\mathbf{q}}(\boldsymbol{\tau}^T)$ and $\nabla_{\mathbf{q}}(\boldsymbol{\xi}^T)$ are dependent on the particular array geometry chosen. For what the FIM related to the measurements vector is concerned, (3.28) becomes

- 2nd approach

$$\mathbf{J}_{\boldsymbol{\eta}} = \left[\begin{array}{c:cc} \mathbf{J}^{\mathrm{d}}_{\boldsymbol{\tau}\boldsymbol{\tau}} & \mathbf{J}^{\mathrm{d}}_{\boldsymbol{\tau}\boldsymbol{\alpha}} & \mathbf{J}^{\mathrm{d}}_{\boldsymbol{\tau}\epsilon^{\mathrm{s}}} \\ \hdashline \mathbf{J}^{\mathrm{d}}_{\boldsymbol{\alpha}\boldsymbol{\tau}} & \mathbf{J}^{\mathrm{d}}_{\boldsymbol{\alpha}\boldsymbol{\alpha}} + \mathbf{J}^{\mathrm{p}}_{\boldsymbol{\alpha}\boldsymbol{\alpha}} & \mathbf{J}^{\mathrm{d}}_{\boldsymbol{\alpha}\epsilon^{\mathrm{s}}} \\ \mathbf{J}^{\mathrm{d}}_{\epsilon^{\mathrm{s}}\boldsymbol{\tau}} & \mathbf{J}^{\mathrm{d}}_{\epsilon^{\mathrm{s}}\boldsymbol{\alpha}} & \mathbf{J}^{\mathrm{d}}_{\epsilon^{\mathrm{s}}\epsilon^{\mathrm{s}}} + \mathbf{J}^{\mathrm{p}}_{\epsilon^{\mathrm{s}}\epsilon^{\mathrm{s}}} \end{array}\right] = \left[\begin{array}{cc} \mathbf{J}^{(1,1)}_{\boldsymbol{\eta}} & \mathbf{J}^{(1,2)}_{\boldsymbol{\eta}} \\ \mathbf{J}^{(2,1)}_{\boldsymbol{\eta}} & \mathbf{J}^{(2,2)}_{\boldsymbol{\eta}} \end{array}\right] \tag{3.101}$$

- 3rd approach

$$\mathbf{J}_{\boldsymbol{\eta}} = \left[\begin{array}{c:cc} \mathbf{J}^{\mathrm{d}}_{\boldsymbol{\xi}\boldsymbol{\xi}} & \mathbf{J}^{\mathrm{d}}_{\boldsymbol{\xi}\boldsymbol{\kappa}} & \mathbf{J}^{\mathrm{d}}_{\boldsymbol{\xi}\epsilon^{\mathrm{s}}} \\ \hdashline \mathbf{J}^{\mathrm{d}\,H}_{\boldsymbol{\xi}\boldsymbol{\kappa}} & \mathbf{J}^{\mathrm{d}}_{\boldsymbol{\kappa}\boldsymbol{\kappa}} + \mathbf{J}^{\mathrm{p}}_{\boldsymbol{\kappa}\boldsymbol{\kappa}} & \mathbf{J}^{\mathrm{d}}_{\boldsymbol{\kappa}\epsilon^{\mathrm{s}}} \\ \mathbf{J}^{\mathrm{d}\,H}_{\boldsymbol{\xi}\epsilon^{\mathrm{s}}} & \mathbf{J}^{\mathrm{d}\,H}_{\boldsymbol{\kappa}\epsilon^{\mathrm{s}}} & \mathbf{J}^{\mathrm{d}}_{\epsilon^{\mathrm{s}}\epsilon^{\mathrm{s}}} + \mathbf{J}^{\mathrm{p}}_{\epsilon^{\mathrm{s}}\epsilon^{\mathrm{s}}} \end{array}\right] = \left[\begin{array}{cc} \mathbf{J}^{(1,1)}_{\boldsymbol{\eta}} & \mathbf{J}^{(1,2)}_{\boldsymbol{\eta}} \\ \mathbf{J}^{(2,1)}_{\boldsymbol{\eta}} & \mathbf{J}^{(2,2)}_{\boldsymbol{\eta}} \end{array}\right] \tag{3.102}$$

where

$$\mathbf{J}^{\mathrm{d}}_{\boldsymbol{\eta}_i\boldsymbol{\eta}_j} = -\mathbb{E}_{\mathbf{r},\boldsymbol{\eta}_{\mathrm{r}}}\left\{\nabla^2_{\boldsymbol{\eta}_i\boldsymbol{\eta}_j}\ \ln f\left(\mathbf{r}|\boldsymbol{\eta}_{\mathrm{r}}\right)\right\} = \left(\mathbf{J}^{\mathrm{d}}_{\boldsymbol{\eta}_j\boldsymbol{\eta}_i}\right)^H \tag{3.103}$$

$$\mathbf{J}^{\mathrm{p}}_{\boldsymbol{\eta}_i\boldsymbol{\eta}_j} = -\mathbb{E}_{\mathbf{r},\boldsymbol{\eta}_{\mathrm{r}}}\left\{\nabla^2_{\boldsymbol{\eta}_i\boldsymbol{\eta}_j}\ \ln f\left(\boldsymbol{\eta}_r\right)\right\} = \left(\mathbf{J}^{\mathrm{p}}_{\boldsymbol{\eta}_j\boldsymbol{\eta}_i}\right)^H \tag{3.104}$$

with $\boldsymbol{\eta}_i$ and $\boldsymbol{\eta}_j$ being the generic elements of (3.25) or (3.26).

Now recalling the expression of $\mathbf{J}_{\boldsymbol{\psi}}$ in (3.27), we find that

- 2nd approach

$$\mathbf{J}^{(1,1)}_{\boldsymbol{\psi}} = \nabla_{\mathbf{q}}\left(\boldsymbol{\tau}^T\right)\,\mathbf{J}^{(1,1)}_{\boldsymbol{\eta}}\,\nabla^T_{\mathbf{q}}\left(\boldsymbol{\tau}^T\right) \tag{3.105}$$

$$\mathbf{J}^{(1,2)}_{\boldsymbol{\psi}} = \nabla_{\mathbf{q}}\left(\boldsymbol{\tau}^T\right)\left(\mathbf{J}^{(1,1)}_{\boldsymbol{\eta}}\,\mathbf{B}^T + \mathbf{J}^{(1,2)}_{\boldsymbol{\eta}}\,\mathbf{C}^T\right) \tag{3.106}$$

$$\mathbf{J}^{(2,2)}_{\boldsymbol{\psi}} = \left(\mathbf{B}\,\mathbf{J}^{(1,1)}_{\boldsymbol{\eta}} + \mathbf{C}\,\mathbf{J}^{(2,1)}_{\boldsymbol{\eta}}\right)\mathbf{B}^T + \left(\mathbf{B}\mathbf{J}^{(1,2)}_{\boldsymbol{\eta}} + \mathbf{C}\,\mathbf{J}^{(2,2)}_{\boldsymbol{\eta}}\right)\mathbf{C}^T \tag{3.107}$$

- 3rd approach

$$\mathbf{J}_{\boldsymbol{\psi}}^{(1,1)} = \nabla_{\mathbf{q}} \left(\boldsymbol{\xi}^{T}\right) \mathbf{J}_{\boldsymbol{\eta}}^{(1,1)} \nabla_{\mathbf{q}}^{T} \left(\boldsymbol{\xi}^{T}\right) \tag{3.108}$$

$$\mathbf{J}_{\boldsymbol{\psi}}^{(1,2)} = \nabla_{\mathbf{q}} \left(\boldsymbol{\xi}^{T}\right) \mathbf{J}_{\boldsymbol{\eta}}^{(1,2)} \tag{3.109}$$

$$\mathbf{J}_{\boldsymbol{\psi}}^{(2,2)} = \mathbf{J}_{\boldsymbol{\eta}}^{(2,2)} \tag{3.110}$$

Chapter 4

RFID Relaying and Energy Sprinklers Techniques

4.1 Related works

The evolution of the Internet of Things paradigm foresees the possibility to exploit a plurality of low-cost nodes (tags) spatially distributed in the environments providing identification and localization information about objects and people and able to sense physical parameters [95, 96, 97]. This trend finds applications in different fields such as logistics (tracking of goods in the supply and distribution chains), security (localization and tracking of authorized people or goods is some areas), energy (monitoring of environmental parameters and consumptions), and health-care (monitoring of patients, medical or paramedical personnel, medicines, and health-care equipments) [24]. Nowadays, the identification, localization, and sensing functionalities are offered separately by different wireless technologies such as RFID, WSN, and RTLS.

In this perspective, high-accuracy network localization becomes an essential requirement to be accomplished [76]. Tipically, network localization is based on an infrastructure including tags attached to or embedded in objects (*agents*), and reference nodes (*anchors*) placed in known positions. In the following, we will refer to different tag architectures according to the active or passive nature of the tag.

Generally speaking, active tags have an internal power source meanwhile semi-passive and passive tags must be energized and activated by an outside source, generally the reader. As a consequence, (semi-)passive devices have the capability to store energy for a short period, since they do not have the necessity to feed-up an active transmitter. Another difference between active and passive/semi-passive tags is the RF transmitting section: in fact, active tags have a complete transmitter able to generate and modulate the signal, while passive and semi-passive tags are generally based on backscattering modulation reflecting and modulating the signal generated by the reader. For these reasons and their low complexity, passive and semi-passive tags and backscatter communications are very promising, especially in the perspective of the adoption of efficient energy scavenging techniques to supply power to the control logic.

To enlarge the spectrum of applications and to increase the acceptance of RFID systems as alternative solutions to barcodes, *tags* should satisfy certain requirements, the most important ones are here reported:

- low-cost and complexity: in this perspective, semi-passive or passive tags relying on passive communications have to be preferred in comparison with their active counterpart;

- localizable with sub-meter precision: they could be designed to operate with UWB signalling in order to guarantee a high level of ranging accuracy;

- lightweight: they could work without cumbersome batteries if energy harvesting techniques are developed;

- based on ecofriendly materials and recyclable.

To meet these needs, passive and semi-passive tags are often adopted. In this context, the communication with anchors often relies on backscatter modulation mechanism. This modulation technique is based on the idea of associating the useful information to be communicated with a variation of tags antenna load condition. Intuitively, as the interrogation signal coming from the readers invests the tag, a part of it, that is the *structural mode*, is immediately reflected depending on the antenna's shape and geometry while another part, called *antenna mode*, is modulated by the tag load status and re-irradiated.

Consequently, as the structural mode is fixed once the antenna is fabricated, the backscattering modulation exploits different load status to communicate the informations to be retrieved by anchors (e.g., the tag identification code).

Besides identification, reliable and high-accuracy localization of tags could be enabled by the UWB communication thanks to the short-duration pulses adopted. It also offers low power consumption, robustness to multipath, low detection probability, and coexistence capability via spectrum sharing [28, 29, 30]. Common methods to determine the tags' position are based on received waveform measurements such as TOA, time difference-of-arrival (TDOA), received signal strength indicator (RSSI), and AOA. The type of measurement significantly affects the localization accuracy [76]. The area coverage for network localization is more demanding than that for network communication; in fact, unambiguous localization requires more than one anchor to be visible simultaneously by a tag in each position. Moreover several disadvantages arise when passive systems have to be deployed; the main important ones are:

- *The poor link budget*: due to the two-hop communication scheme and the standard carrier frequency of 4 GHz usually adopted for UWB schemes in Europe, the received signal backscattered by the tag is weak. In order to counteract this effect and ensure proper tag detection, communication and ranging capabilities, the usual approach consists in adopting packets of several pulses per bit in order to enhance the effective SNR. For typical indoor distances of some meters, as investigated in [11], around 10,000 pulses per bit are necessary for a robust tag detection, resulting in a quite long symbol time (e.g., 1 ms symbol time when a 100 ns pulse repetition period (PRP) is considered).

- *The multi-tags management issue*: when adopting UWB backscatter communication, no anti-collision protocol can be implemented due to the extremely simple tag front-end and the absence of any receiver and processing unit at tag side. For this reason, all the complexity must be moved to the reader side by exploiting a code division multiple access (CDMA)-based scheme for the simultaneous communication with multiple tags [11]. Unfortunately such a scheme poses several challenges in terms of tag code design and interference mitigation [11]; moreover, the simultaneous detection, communication and localization of several tags require a dedicated processing unit for each tag tuned on the specific tag code.

- *The energy-related aspects*: although UWB backscattering is an extremely-low power consumption technique since only a UWB switch is required to perform signal modulation, the circuitry at tag side (UWB switch, control logic and sensors) must be properly powered so energy-harvesting techniques have to be considered. Due to the impossibility of extracting significant energy from the UWB link because of regulatory issues, a possibility is to exploit the UHF band to transfer the required energy to the tag as done in Gen.2 RFID.

Considering these issues, the first part of this chapter presents different type of tag architecture that can be designed for each of which their pros and cons are highlighted. For the most promising ones, the reader-tag communication scheme is also reported. Moreover, the idea of a multitastic RFID configuration,[1] will be presented to limit the poor link budget experienced when passive devices are adopted. To this purpose, several low complexity transmitters, called *energy sprinklers*, could be disseminated in a large number in the environment thanks to their simplicity and they could be exploited to spread signals to power up and interrogate tags around them. The backscattered response is then collected by one or more receivers located in different positions. With the proposed configuration, it is expected that

---

[1] Benefits of bistatic and multistatic RFID configurations have been recently highlighted in [98, 25].

even tags placed far from the receiver can be detected and localized with an improved localization accuracy thanks to a reduced transmitter-tag distance.

Therefore, NLOS conditions generated by the presence of obstacles in real environments may drastically limit the area covered by the localization system even if a multistatic configuration is adopted. In such severe propagation conditions, a typical approach to improve the performance and coverage of localization systems consists in increasing the number of receiving nodes at the expense of higher infrastructure and deployment costs.[2] Another approach consists in exploiting prior knowledge of the environment and spatio-temporal cooperation among tags [78, 99, 100]. Unfortunately, cooperation can be exploited only by active tags with transceivers and high computational capability, which is often in contrast with cost and complexity requirements. This calls for flexible and low cost solutions to improve localization accuracy and coverage in RFID for both active and passive tags. To this end, the second part of the chapter will present relaying techniques to be adopted for localization coverage enhancement in severe propagation situations. Relays should represent simpler entities with respect to receiving nodes capable of repeating the signals between anchors and tags beyond obstacles.

4.2 UHF-UWB multistatic RFID using energy sprinklers nodes

4.2.1 Reader-tag architecture solutions

If the UHF and UWB technologies are jointly adopted, tag design should face different issues to guarantee both UHF and UWB operation capabilities. For what the UWB section is concerned, UWB signalling represents the most natural candidate for accurate ranging through round-trip time measurement of the backscattered signal (in case of passive tags) or through precise TDOA measurement of the UWB pulse generated by the tag it self (in case of active

---

[2] Note also that anchors have to be tightly time synchronized if time-based positioning approaches are adopted.

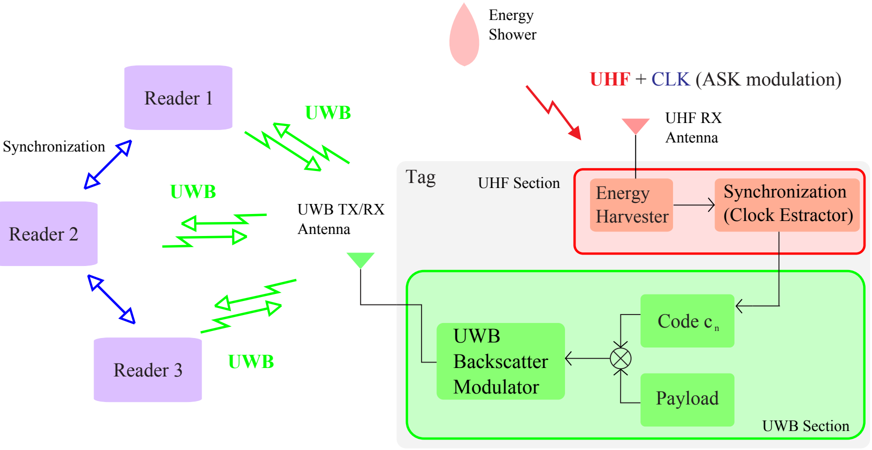

Figure 4.1: Active Tag.

tag). As a consequence, tags' codes generators have to be kept synchronized at pulse level for identification and ranging purposes.
To accomplish this feature, a possible solution is to exploit the UHF signal, used for energy harvesting, for synchronization at chip level (around $1\mu s$ accuracy). This solution does not need an oscillator and it results in a less energy consuming tag. Thus, the joint adoption of these two technologies seems a viable solution to overcome the limitations of UHF and UWB when are separately adopted. Moreover, it would be appreciated to have a backward compatibility with previous RFID technologies to open the way at numerous market-oriented applications.

4.2.2 Tag architectures investigated

We now describe the possible reader-tag solutions that might be adopted to meet the requirement enumerated in Sec. 4.1. For each solution, the advantages and the disadvantages are analysed.

Active Tags The first tag architecture we want to analyse is the active one. As previously stated, the term active refers to the tag capability to generate an UWB signal thanks to a waveform generator included in the tag itself (refer to Fig. 4.1 where the active part is denoted by the UWB Pulse Generator).

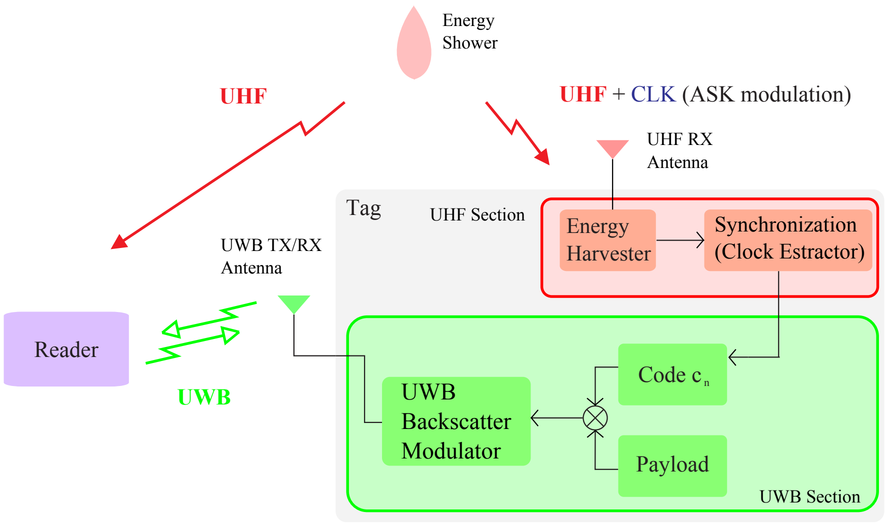

Figure 4.2: Stand-alone UWB-UHF passive tag.

If from one side, this choice translates into an improved coverage, as we have only 1-hop path in the tag-reader communication (from the active tag to the receiver), on the other side the transmitting section makes the tag particularly energy consuming and neither eco-compatible nor recyclable. In addition, another limitation of such architecture is the need of a TDOA scheme with tight synchronized readers to cope with the lack of synchronization in the UWB pulses generation process.

To resume, the advantages and disadvantages of this solution are:

- $\ddot\smile$ improved coverage;
- $\ddot\frown$ energy-consuming tag;
- $\ddot\frown$ non-green tag;
- $\ddot\frown$ synchronization among readers required for TDOA estimation.

As depicted in Fig. 4.1, the tag is composed of an UWB pulse generator, that modulates the signal with the coded sequence produced by the spreading unit to uniquely identify the tag, connected to an UWB antenna (in the diagram the coded sequence is described by the $\{c_n\}$ code-block and the data to be transmitted with the payload-block). On the other side, the UHF

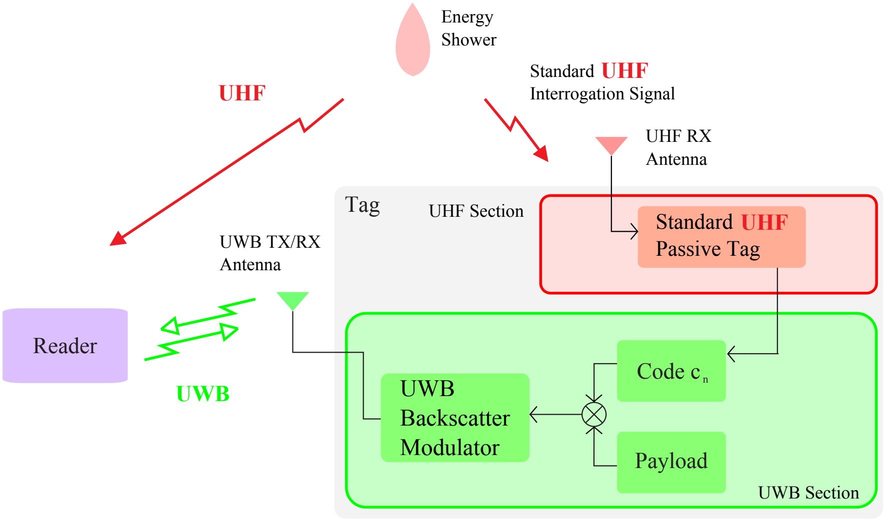

Figure 4.3: UWB as add-on of standard Gen.2 UHF passive tag.

part takes advantages of the UHF showers signalling to activate the energy harvester and to extract the synchronism.

Stand-alone UWB-UHF passive tag We now analyse the possibility to adopt a stand-alone UWB-UHF passive tag (see Fig. 4.2). The main idea is to exploit the UWB signalling for both tags identification and data transmission, performing a precise ranging as well, while UHF energy showers are adopted for energy harvesting and system synchronization only. Additionally, the clock signal to the tag code generator can be extracted from the UHF impinging wave, guaranteeing a good synchronism.

This type of architecture has not a backward compatibility with Second Generation RFID systems but it is totally new, cheap and easy to optimize. Tags are passive and modulate the reflected signal via backscatter modulation: several tags can be interrogated simultaneously as each of them can be characterized by a different spreading code. With this configuration, the tag architecture is simple and potentially green. In fact, the backscatter modulator performs the signal modulation of the electromagnetic waves generated by the reader (or by the "energy shower"'s oscillators) without the need of integrating the pulse generator (as done in active solutions) but just adopting an UWB switch alternating between two different load conditions [12].

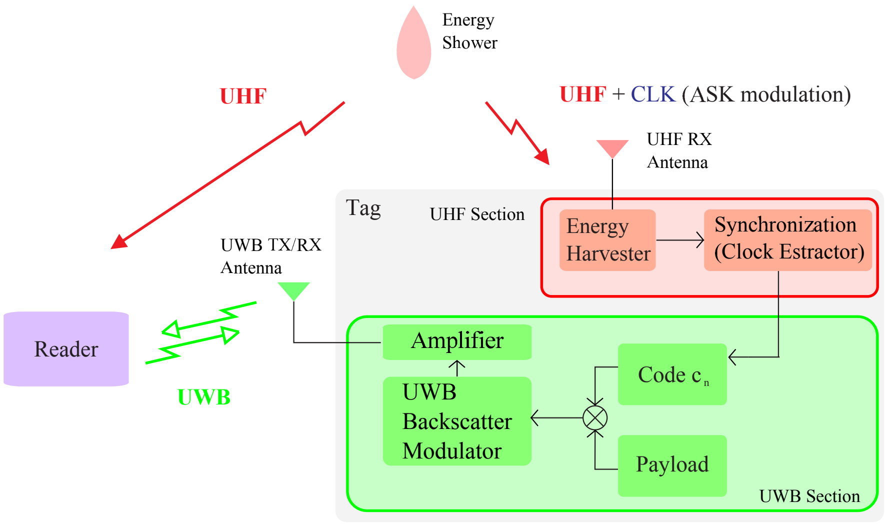

Figure 4.4: Tag operating as an active reflector.

As the modulator reduces to a switch, the complexity of the architecture drastically decreases.

However, to detect several tags at the same time, the reader should have multiple de-spreading units (one for each tag's coded sequences) increasing its complexity and cost at infrastructure level.

The tag's UHF section consists of an energy harvester to activate the tag itself and it provides the clock (thus avoiding the local oscillator in the tag and clock drift problems). In principle, more than one reader could interrogate the same tag simultaneously (using different coded signals), however the inter-reader interference could be detrimental.

Another limitation of this solution is the poor link budget due to the two-hop communication link between readers and tags. Even if several solutions might be adopted to counteract such issue, this effect can dramatically reduce the overall system performance.

As already mentioned this approach does not guarantee backward compatibility, since UHF is only used for energy harvesting (EH) and to provide the clock synchronism but it is non standard-compliant.

To sum up, the positive and negative aspects of this architecture are here listed:

- $\ddot\smile$ low complexity and green tag architecture;
- $\ddot\smile$ good synchronism via UHF signalling;
- $\ddot\frown$ no backward compatibility;
- $\ddot\frown$ poor link budget;
- $\ddot\frown$ high complexity and cost of readers architecture.

UWB as add-on of standard Gen.2 UHF passive tag The solution proposed in Fig. 4.3 aims to integrate UWB tag as add on of a standard Gen.2 UHF tag: backward compatibility opens a wider range of potential applications in current industrial markets. The UWB link is used only for high-accuracy ranging, while the standard Gen.2 protocol is adopted to read and write data from/to the tag. One of the problems to be faced while adopting this approach is an easy integration of the UWB and sensor part with the standard UHF chip.

Among the possible benefits of such a solution, it is important to remark that multiple access is solved by the Gen. 2 UHF protocol: since only one tag per time is allowed to communicate with the reader, there is not multi user interference problem in the UWB link. In addition, the communication is faster as no data are transmitted in the slow UWB communication link, and only 1-2 UWB symbols and 1 unique spreading code are necessary for ranging (1-2 ms interrogation duration). As a consequence, a simple reader is required to perform tag detection and localization, guaranteeing also high refresh rate (the standard guarantees about 200 reads/s).

The benefits and the drawbacks of this solution are:

- $\ddot\smile$ low complexity and ”green” tag architecture;
- $\ddot\smile$ low complexity of reader architecture;
- $\ddot\smile$ backward compatibility with current UHF RFID, which is appealing for industrial applications;
- $\ddot\smile$ high refresh rate;

- ☺☹ market-oriented;
- ☺☹ feasibility of an easy integration of the UWB and sensor part with the standard UHF chip to be investigated.

Tags as Active Reflectors The last solution we propose is the adoption of the tag as an active reflector (see Fig. 4.4). It is a modification of the stand-alone joint UWB-UHF solution in which an UWB power amplifier is added in the architecture to strengthen the backscatter signal and improve the link budget. The coexistence of the received and transmitted signals could be managed by a circulator.

As before, the UHF signal transmitted by the shower is exploited by both readers and tags to perform synchronization, and it is also used as clock signal at tag side and for energy harvesting as well. Such a solution implies an improved coverage and a precise UWB synchronization, but the amount of energy to be stored to power up the UWB amplifier and how to harvest it is still a point under investigation. Again, the main drawback of this solution is a less green solution leading this approach far from the project objectives.

Some benefits and drawbacks are here reported:

- ☺ improved coverage;
- ☺ precise synchronism;
- ☹ no backward compatibility;
- ☹ reduced greenness of tag architecture;
- ☹ high complexity and cost of readers architecture.

Reader-tag architectures

Considering all the features of the proposed solutions, the two main candidates for providing a green architecture are the adoption of UWB as an add-on of standard UHF RFID and the stand-alone UWB solution. In Fig. 4.5 and 4.6 we report the reader's and tag's structure for each solution.

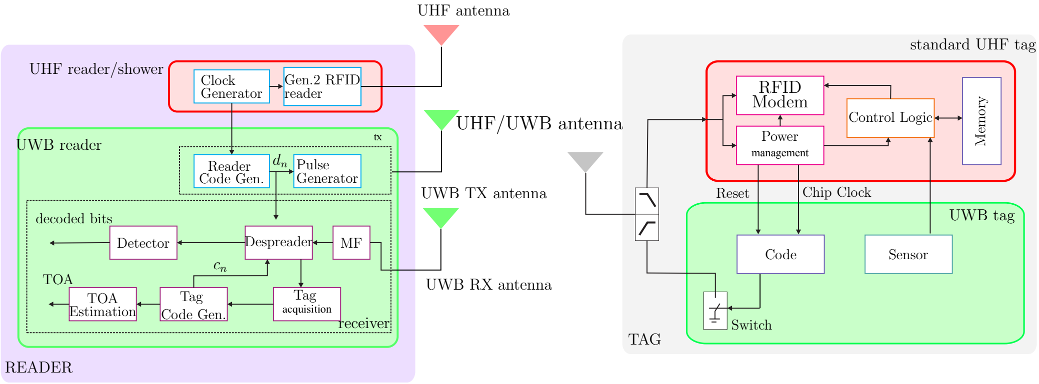

Figure 4.5: UWB as an add-on of standard Gen.2 UHF reader-tag - Block Diagram.

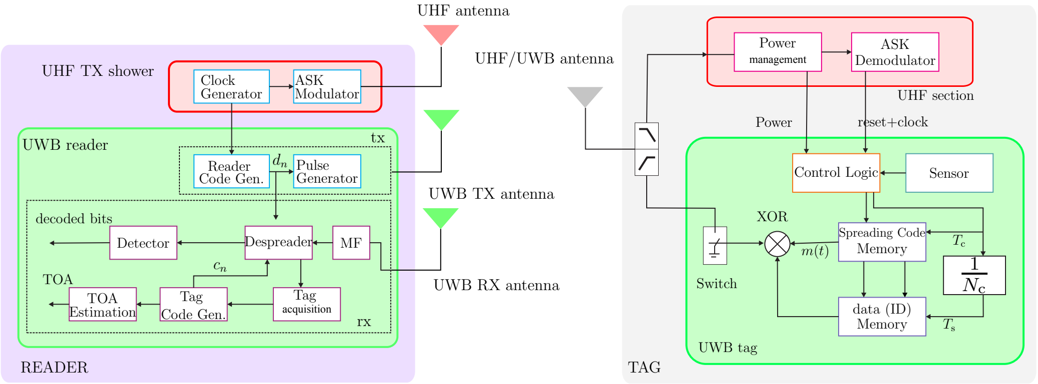

Figure 4.6: Stand-Alone UWB-UHF reader-tag - Block Diagram.

The main difference between the two architectures is the backward compatibility with the standard Gen.2 RFID technology and reader complexity. In fact, consider the UHF section: the joint UWB-UHF stand-alone solution is mainly composed of an amplitude shift keying (ASK) modulator (see Fig. 4.6), while in Fig. 4.5, the UHF section reduces to a Gen.2 RFID reader guaranteeing the backward compatibility with the UHF standard. With reference to the block scheme, the UWB transmitter section is composed of a UWB pulse generator and of a spreading sequence (reader's code) generator that produces an antipodal binary sequence $\{d_n\}$ of length N_c symbols (chips).

The compatible Gen.2 UWB-UHF reader of Fig. 4.5 interacts with a tag whose control logic and memory functions are accomplished by the UHF

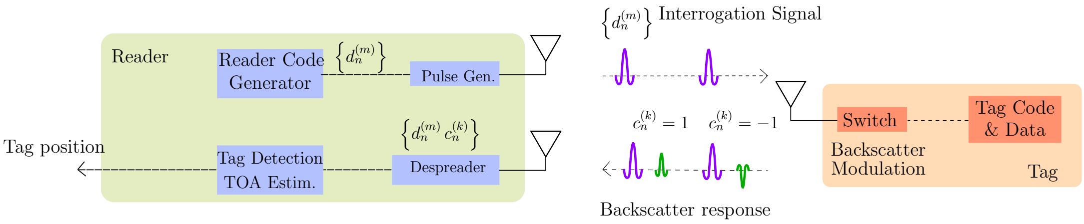

Figure 4.7: Equivalent scheme for the backscatter link.

standard while the UWB section drastically simplifies, as it is exploited only for ranging. As a consequence, it becomes an appealing solution for current industrial applications: the state of the art of UHF RFID systems can be simply equipped with a UWB section (mainly composed of a UWB switch for backscatter modulation, and a sensor) that performs high ranging capabilities while maintaining the compatibility with UHF RFID standard.

Consider now the joint UWB-UHF stand-alone system of Fig. 4.6. It requires a more complex reader and tag's UWB section but with a lower power consumption and a newer structure with respect to the traditional UHF tag, as it is completely based on UWB backscatter communication.

Figure 4.7 reports an equivalent scheme of the UWB reader-tag backscatter communication: pulses radiated by the reader according to the sequence $\{d_n\}$, are received by the tag and multiplied by the code $\{c_n\}$ and the data. Successively they are backscattered and received by the reader. A despreading stage realizes the product of the received signal and the composite sequence given by the reader and tag code, and a decision stage demodulates the data bit sent by the tag [26, 12, 101], where it is evident how the tag modulates the reflected signal according to the information data b_n and the reader's and tag's code.

4.2.3 Reader-tag communication scheme

Stand-alone UWB-UHF tag communication scheme

In Fig. 4.8 the communication between a reader and a stand alone UWB tag is shown, where the UHF link is exploited for energy harvesting and system synchronization, while the UWB link is adopted for tags identification, data transmission and ranging. Note that in this case, the scenario is monostatic, as the reader plays both the transmitting and receiving role.

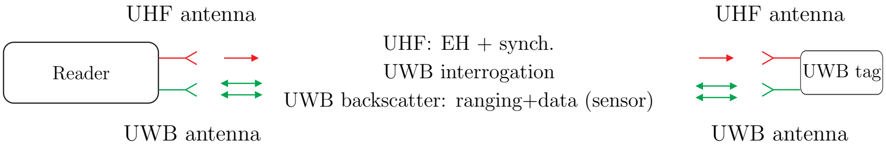

Figure 4.8: Reader and stand-alone UWB tag

A multistatic alternative, depicted in Fig. 4.9, considers the adoption of distributed energy showers consisting of different transmitters. In this alternative version, the UHF and UWB interrogation signals could be generated by energy showers deployed in the environment to facilitate the coverage and the energy harvesting procedure, while the tags' backscattered signals are collected by the UWB readers. The main issue of this architecture could be how to synchronize multiple showers, which is far from being trivial, and the real advantages of adopting a multistatic scenario, which are analysed in the following.

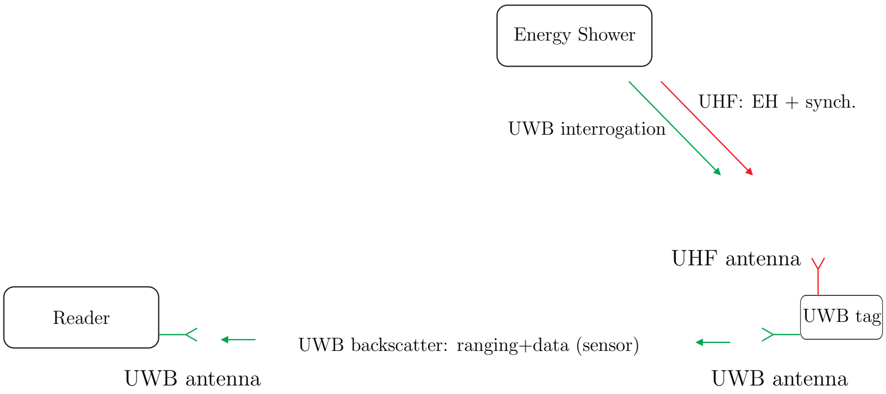

Figure 4.9: Reader and stand-alone UWB tag with energy shower

For the stand alone architecture the interrogation cycle is shown in Fig. 4.10. Reader-tag communication takes place during an interrogation of duration cycle T_{cycle} involving different steps: first of all, the reader interacts with the tag via a UHF wake-up signal in order to power up the tag and activate the UWB switching control responsible of antenna load variations (wake-up period of duration $T_{\text{wake-up}}$). Once the tag has been powered up and the synchronization process has ended (after a fixed time T_{synch}), a sequence of UWB pulses (of duration T_{int}) is transmitted by the reader to interrogate the tag and obtain the data stored on them.

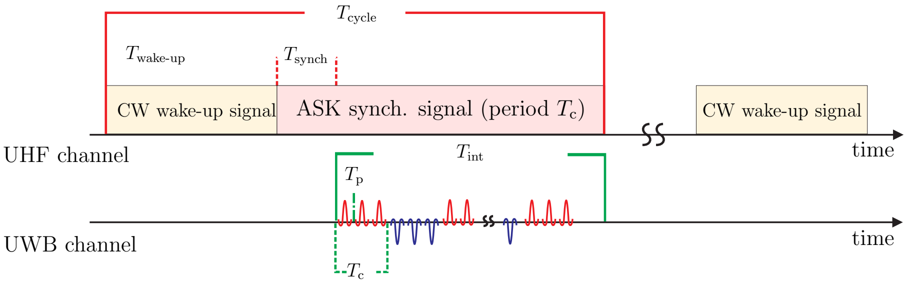

Figure 4.10: Interrogation cycle relative to the UWB stand-alone tag.

The mth reader modulates the UWB transmitted sequence using an antipodal binary code of period T_{s} and length N_{c} given by $\left\{d_n^{(m)}\right\} \in \{-1, +1\}$, which allows to uniquely identify the reader (reader's code).

Each transmitted pulse is backscattered by all tags as well as by all the surrounding scatterers present in the environment determining, at reader side, the clutter component. In particular, at each chip time T_{c}, the kth tag changes its load conditions (short or open circuit) in order to modulate the backscattered signal, according to an antipodal tag's code $\left\{c_n^{(k)}\right\} \in \{-1, +1\}$ of period N_{c}. The backscattered signal associated with this tag is so modulated by $\left\{d_n^{(m)} c_n^{(k)}\right\}$. On the other hand, all the signals coming from other interfering tags are modulated by different tags' codes $\left\{d_n^{(m)} c_n^{(i)}\right\}$ with $i \neq k$. Differently, the environmental reflected signals (i.e., the clutter component, which includes the structural antenna mode) exhibits modulation by the reader's code $\left\{d_n^{(m)}\right\}$ only. Then, to discriminate the useful component (i.e. that reflected back by the kth tag) it is sufficient at reader side to perform a de-spread of the received signal using the $\left\{d_n^{(m)} c_n^{(k)}\right\}$ coded sequence.

The tag UWB interface is adopted also for data transmission, then the tag information symbol $\left\{b_n^{(k)}\right\}$ is associated to each burst of N_{s} pulses with symbol time $T_{\text{s}} = T_{\text{p}} N_{\text{s}}$, and it affects the entire sequence of pulse polarity at each symbol time. In general we consider only one active reader at each time according to a reader time division multiple access (TDMA) protocol

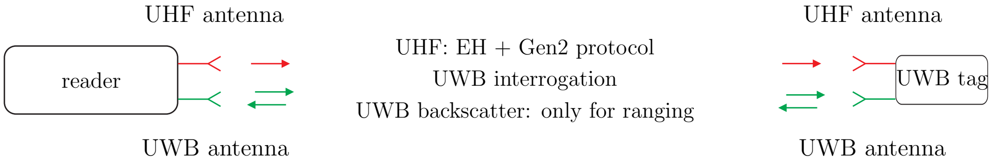

Figure 4.11: Reader and backward Gen2 UHF-UWB tag

to minimize the inter-reader interference.

UWB as add-on of standard Gen.2 UHF tag communication scheme

Consider now the UWB section as an add-on for the standard Gen2 UHF RFID. Figure 4.11 shows the communication scheme reader-tag, where

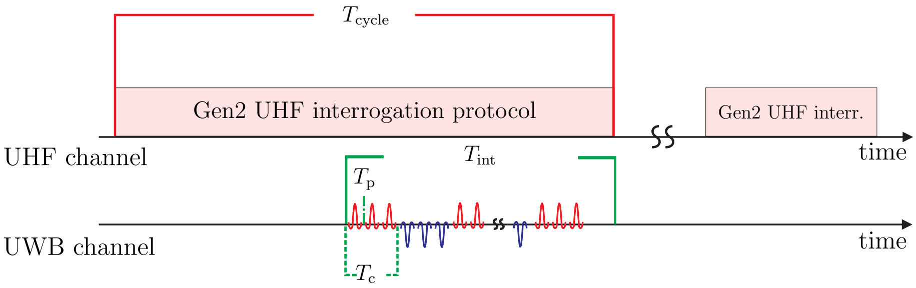

Figure 4.12: Interrogation cycle backward Gen.2 UWB-UWB tag.

the UWB part is exploited only for ranging purposes, while with the UHF link, data are read from the tag. As shown in Fig. 4.12, the reader-tag communication takes place during a period T_{cycle} as before: the UHF channel is dedicated to synchronization and data communication while relegating the UWB channel for ranging transmission. The UWB transmitted sequence is identical to the previous case with the only exception that is not modulated according to the sensor's data but only by the spreading code for localization purposes. Therefore only a limited number of symbols is sufficient for ranging purposes.

4.2.4 Energy sprinklers

Considering the multistatic configuration in Fig. 4.9, in this section the idea of extending the localization coverage using energy sprinklers is put forth.

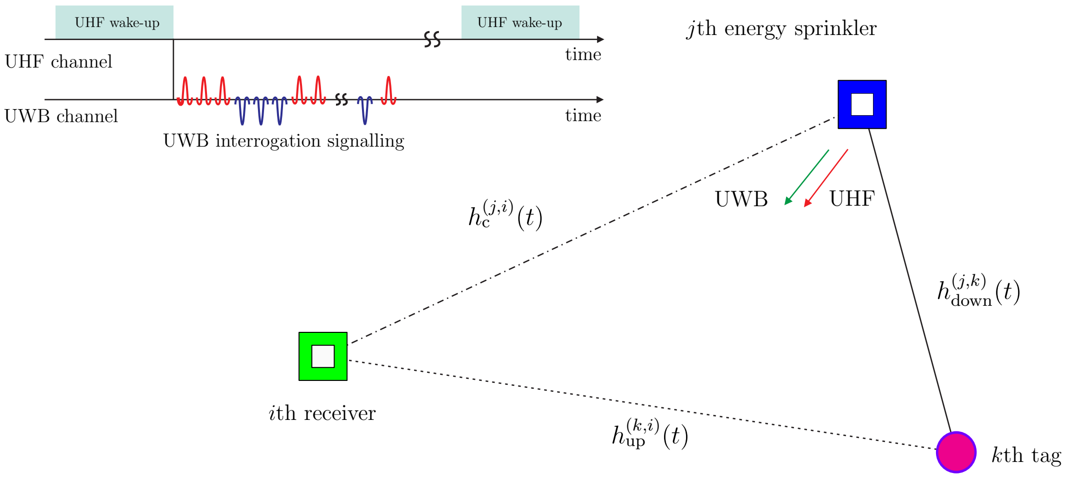

Figure 4.13: System architecture with energy sprinklers.

4.2.5 Signaling with energy sprinklers

Let $\mathcal{T}$ be the set of tags in the environment, $\mathcal{E}$ the set of energy sprinklers and $\mathcal{R}$ the set of receivers. We consider $|\mathcal{E}| = N_{\mathrm{t}}$ energy sprinklers located in known positions $\mathbf{p}_{\mathrm{T}j} = (x_{\mathrm{T}j}, y_{\mathrm{T}j}, z_{\mathrm{T}j})$, with $j = 1, 2, \ldots, N_{\mathrm{t}}$, $|\mathcal{R}| = N_{\mathrm{r}}$ receivers in $\mathbf{p}_{\mathrm{R}i} = (x_{\mathrm{R}i}, y_{\mathrm{R}i}, z_{\mathrm{R}i})$, with $i = 1, 2, \ldots, N_{\mathrm{r}}$ and $|\mathcal{T}| = N_{\mathrm{tag}}$ tags in unknown positions $\mathbf{p}_k = (x_k, y_k, z_k)$, with $k = 1, 2, \ldots, N_{\mathrm{tag}}$. As previously remarked, while in traditional RFID systems the reader is composed of both a transmitting and a receiving section (co-located in the same node), here transmitters and receivers are separated, as the transmitting section is delegated to the energy sprinklers. In this way, receivers complexity is reduced due to the absence of the transmitting part.

Note that the herein described reference nodes are not synchronous. Section 4.2.6 will discuss how the lack of initial synchronism impacts the localization process.

We now provide some details about the sprinkler-tag-receiver communication. Figure 4.13 reports a schematic example of the communication protocol. First, a UHF tone is sent by the transmitter (energy sprinkler) to energize the tags in proximity; all tags retrieving enough energy wake up and start varying the switch condition according to their own code (backscatter modulation). In the meantime, the transmitter sends a UWB interrogation

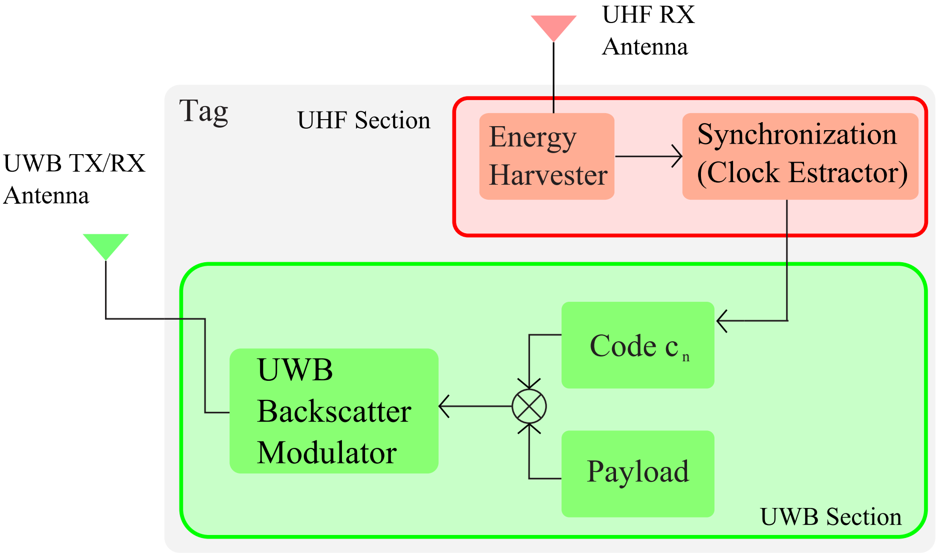

Figure 4.14: UHF-UWB RFID tags.

signal which is backscattered by tags and post-processed by the receiver. The jth energy sprinkler sends an UWB interrogation signal composed of repeated symbols of duration T_s, each given by

$$s_{\mathrm{T}j}(t) = \sum_{m=0}^{N_\mathrm{p}-1} s_j(t - mT_\mathrm{s}) \tag{4.1}$$

where each symbol is a sequence of UWB waveforms modulated according to an antipodal binary spreading code $\left\{d_n^{(j)}\right\}$ of time period T_s specific of that energy sprinkler. Each energy sprinkler adopts a different code $\left\{d_n^{(j)}\right\}$. The symbol is defined as

$$s_j(t) = \sum_{n=0}^{N_\mathrm{c}-1} d_n^{(j)}\, g(t - nT_\mathrm{c}) \tag{4.2}$$

where

$$g(t) = \sum_{i=0}^{N_\mathrm{pc}-1} p(t - iT_\mathrm{p}) \tag{4.3}$$

where $\left\{d_n^{(j)}\right\}$ is the jth energy sprinkler's code, N_c is the number of chips (code length), T_c the chip time, N_pc the number of pulses per chip and $p(t)$

the transmitted UWB pulse, repeated with PRP T_p.

Backscatter modulation

We consider UWB-UHF passive tags exploiting UWB backscatter modulation without active transmitting capabilities.

As previously highlighted, backscatter modulation consists in a variation, between short and open circuit, of the load connected to the tag's antenna [8]. Note that the modulator reduces to a UWB switch lessening the complexity of the tag.

In particular, each tag is designed to alternate its status at each chip time T_c, according to an antipodal binary tag's code $\left\{c_n^{(k)}\right\}$, for $n = 0, 1, \ldots, N_\mathrm{c} - 1$. This ensures the creation of a unique backscattered signal signature allowing the discrimination of the tag among other tags (interference) and clutter.

Considering N_p transmitted symbols, the backscatter modulator signal commanding the switch of the kth tag is

$$m^{(k)}(t) = \sum_{m=0}^{N_\mathrm{p}-1} \sum_{n=0}^{N_\mathrm{c}-1} c_n^{(k)} \cdot \Pi\left(\frac{1}{T_\mathrm{c}}[t - mT_\mathrm{s} - nT_\mathrm{c}]\right) \tag{4.4}$$

with $\Pi(t)$ denoting the rectangular function of unitary duration for $t \in [0, 1]$. In this way, the polarity of the backscattered signal changes at each chip time T_c according to the kth tag's code value $c_n^{(k)}$, with $k \in \mathcal{T}$.

Received signal

Each interrogation signal is backscattered by the tags as well as by the surrounding scatterers of the environment. Specifically, the signal at the ith receiver, response of the interrogation signal from the jth energy sprinkler, can be written as

$$\breve{r}_{i,j}(t) = r_{i,j}^{\mathcal{T}}(t) + r_{i,j}^{\mathcal{S}}(t) + n(t) \tag{4.5}$$

where $r^{\mathcal{T}}_{i,j}(t)$ denotes the tags contribution[3] while $r^{\mathcal{S}}_{i,j}(t)$ accounts for the static contribution[4] (comprehensive of multipath) between energy sprinkler and receiver. Finally, $n(t)$ models the AWGN with one-sided power spectral density N_0.

The tags' contribution is given by[5]

$$r^{\mathcal{T}}_{i,j}(t) = \sum_{k \in \mathcal{T}} \left[\left(s_{\mathrm{T}j}(t) \otimes h^{(j,k)}_{\mathrm{down}}(t) \right) \cdot m^{(k)}(t) \right] \otimes h^{(k,i)}_{\mathrm{up}}(t) \tag{4.6}$$

where $h^{(j,k)}_{\mathrm{down}}(t)$ is the downlink CIR, de-embedded of the propagation time, related to the link jth transmitter - kth tag, $h^{(k,i)}_{\mathrm{up}}(t)$ is the uplink CIR related to the link kth tag - ith receiver. It is possible to rearrange (4.6) as

$$r^{\mathcal{T}}_{i,j}(t) = \sum_{k \in \mathcal{T}} \sum_{m=0}^{N_{\mathrm{p}}-1} \sum_{n=0}^{N_{\mathrm{c}}-1} d^{(j)}_n c^{(k)}_n w^{\mathcal{T}}_{i,j,k}(t - mT_{\mathrm{s}} - nT_{\mathrm{c}} - \tau_{i,j,k}) \tag{4.7}$$

where $\tau_{i,j,k}$ is the signal TOA, considered with respect to the transmitter's clock, and $w^{\mathcal{T}}_{i,j,k}(t) = g(t) \otimes h^{(j,k)}_{\mathrm{down}}(t) \otimes h^{(k,i)}_{\mathrm{up}}(t)$ is the channel response to $g(t)$ of the kth tag. Specifically, we have $\tau_{i,j,k} = (d_{\mathrm{T}j} + d_{\mathrm{R}i})/c$, where $d_{\mathrm{T}j}$ is the distance between the jth energy sprinkler and the tag, $d_{\mathrm{R}i}$ is the distance between the tag and the ith receiver,[6] and c denotes the speed of light.

For what concerns the static contribution $r^{\mathcal{S}}_{i,j}(t)$ in (4.5), we have

$$r^{\mathcal{S}}_{i,j}(t) = s_{\mathrm{T}j}(t) \otimes h^{(j,i)}_{\mathrm{c}}(t) \tag{4.8}$$

having indicated with $h^{(j,i)}_{\mathrm{c}}(t)$ the CIR of the link between the jth energy sprinkler and the ith receiver, which is independent of tags' backscattering. As before, (4.8) can be reformulated as

$$r^{\mathcal{S}}_{i,j}(t) = \sum_{m=0}^{N_{\mathrm{p}}-1} \sum_{n=0}^{N_{\mathrm{c}}-1} d^{(j)}_n w^{\mathcal{S}}_{i,j}(t - mT_{\mathrm{s}} - nT_{\mathrm{c}} - \tau_{i,j}) \tag{4.9}$$

---

[3] Here only the tag's antenna mode component is included [26].

[4] We neglect the presence of fast moving objects and tags in the environment, as well as the effects of diffuse clutter [25].

[5] Operator $\otimes$ denotes the convolution.

[6] Both $d_{\mathrm{T}j}$ and $d_{\mathrm{R}i}$ are function of the tag index k, however this dependence has been omitted for notation convenience.

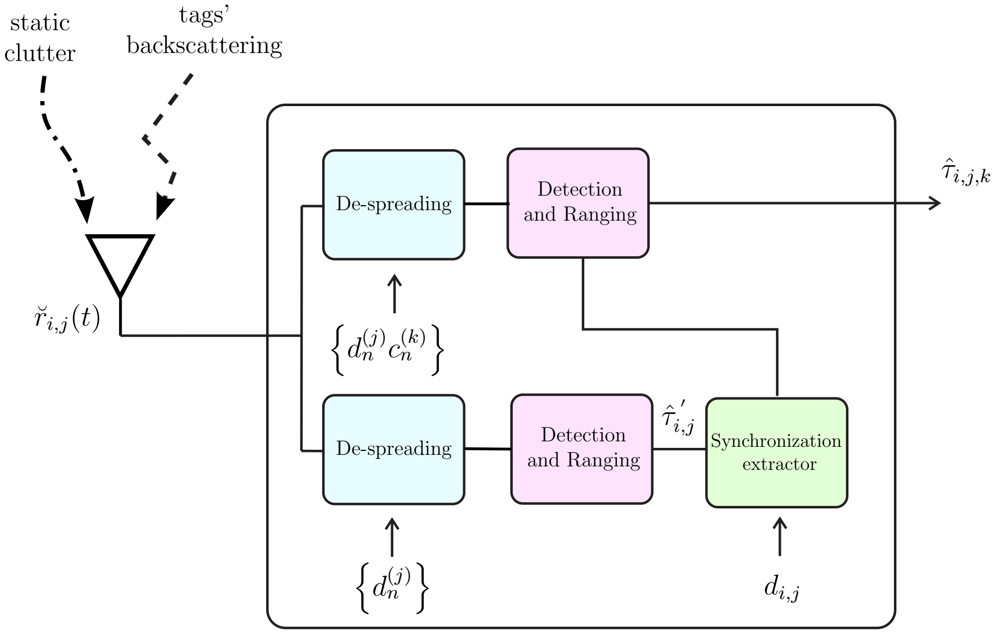

Figure 4.15: Receiver structure.

where $\tau_{i,j}$ is the signal TOA, considered with respect to the transmitter's clock, and $w_{i,j}^{\mathcal{S}}(t) = g(t) \otimes h_{\mathrm{c}}^{(i,j)}(t)$ is the channel response to $g(t)$ for the direct link. Specifically we have $\tau_{i,j} = d_{i,j}/c$, where $d_{i,j}$ is the distance between the jth energy sprinkler and the ith receiver.

Discrimination between the useful contribution backscattered from the kth tag and those reflected by other tags and the direct sprinkler-to-receiver signal is ensured by a de-spreading procedure at the receiver (see Fig. 4.15). Specifically, the separation is enabled by the adoption of different spreading codes, since the tags signals are modulated according to the composed code $\left\{d_n^{(j)} \cdot c_n^{(k)}\right\}$, while the direct contribution independent of tags' backscattering results modulated according to the sprinkler code $\left\{d_n^{(j)}\right\}$ only [25].

4.2.6 Network localization with energy sprinklers

The proposed configuration is classical in radar networks, where transmitters and receivers are often not co-located [102]. In this case the localization can be performed by intersection of ellipses (ellipsoids in 3D space) with foci corresponding to the positions of the transmitter and receiver composing a

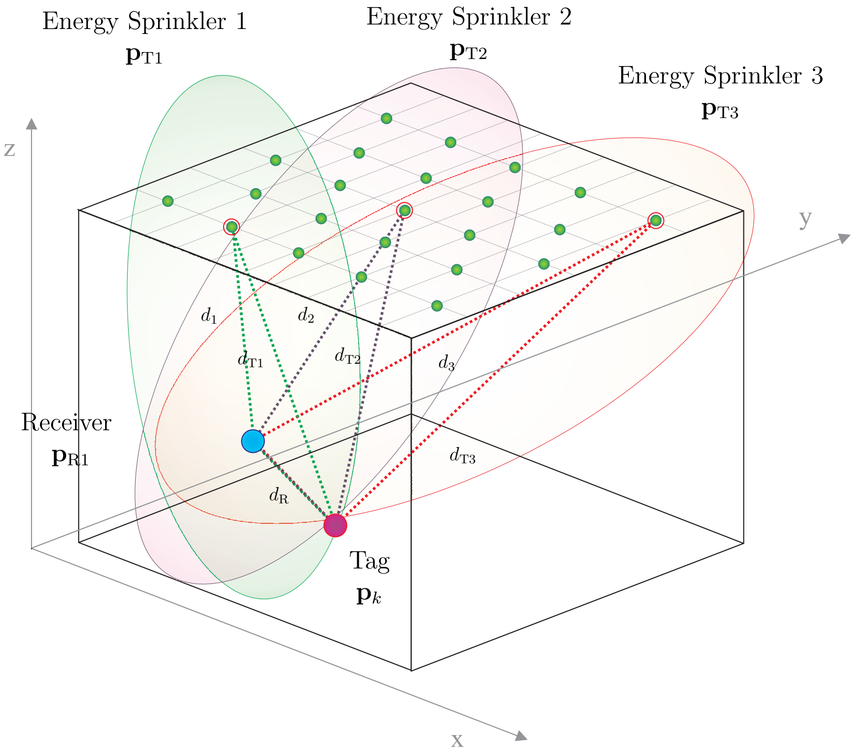

Figure 4.16: Multistatic tag localization.

specific bistatic pair, whose axes are related to the sum $d_{\mathrm{T}j}+d_{\mathrm{R}i}$. In order to exploit this localization technique, the estimation of the distance $d_{\mathrm{T}j}+d_{\mathrm{R}i}$ is necessary. This sum can be obtained starting from the measurements of the propagation time $\tau_{i,j,k}$ resulting from TOA estimation at receiver side. However, since energy sprinklers and receivers are supposed to be asynchronous to avoid a complex network synchronization infrastructure, the receiver must implement a procedure to synchronize with the intended sprinkler's clock.

This initial synchronization process is enabled by two facts: (i) energy sprinklers are placed in known positions; (ii) de-spreading operation is conducted exploiting the energy sprinkler code $\left\{d_n^{(j)}\right\}$ only, resulting in the isolation of the contribution $r^{\mathcal{S}}_{i,j}(t)$ at receiver side. Specifically, by performing TOA estimation on the signal $r^{\mathcal{S}}_{i,j}(t)$, the ith receiver estimates $\widehat{\tau}'_{i,j}=\widehat{\tau}_{i,j}+T_{i,j}$, where $T_{i,j}$ is the unknown clock offset between the jth sprinkler and the ith receiver. Since energy sprinklers' and receivers' positions are known, the true distance $d_{i,j}$ between the transmitter and the receiver composing the bistatic pair can be exploited to determine $T_{i,j}$ and synchronize the receiver with the sprinkler. After this first synchronization step, a second de-spreading conducted with the composed code $\left\{d_n^{(j)} \cdot c_n^{(k)}\right\}$ allows isolating the kth tag component $r_{i,j}^{\mathcal{T}}(t)$. Now, TOA estimation of such a signal gives $\hat{\tau}_{i,j,k}$, and consequently $\hat{d}_{i,j,k} = c\,\hat{\tau}_{i,j,k}$, which corresponds to the estimation of the sum $d_{\mathrm{T}j} + d_{\mathrm{R}i}$. The term $\hat{d}_{i,j,k}$ can be exploited to define the ellipse related to the bistatic pair of interest, with the foci located in the considered energy sprinkler and receiver. With the intersection of several ellipses the tag's position is then determined [103].

Obviously the first TOA estimation operated on the direct sprinkler-receiver link can produce errors which affect tags' localization. Although a deep analysis of the impact of such errors is out of the scope of this paper, the actual effect can be neglected due to the higher SNR deriving from the one-hop of the direct sprinkler-receiver link against to the two-hop propagation link concerning the tag. As example, consider a sprinkler-receiver distance of 10 m and a tag placed at 5 m from both the reference nodes. The difference in SNR, between the direct and the backscattered signals is around 50 dB.[7] Considering, the classical CRB describing TOA localization accuracy [30], this results is about two orders of magnitude of difference in the estimation error.

4.2.7 Results

In this section we introduce the performance metrics and the results adopted to assess the performance of the proposed energy sprinklers solution in terms of detection and localization accuracy. The characterization of energy harvesting properties is out of the scope of the thesis.

First of all, the theoretical localization performance enhancement will be analyzed by exploiting the PEB derived for the proposed multistatic RFID configuration in [25]. PEB is obtained under the assumption of adopting omnidirectional antennas at tag and reader side, and in the case of a 2D scenario. It includes the effects of system parameters (e.g., the signal format),

---

[7] The result has been obtained by considering the parameters indicated in Sec. 4.2.7.

distance between energy sprinklers, tags and receivers, and network topology with the related geometric dilution of precision (GDOP) effects. We remand to [25] for further details on PEB derivation.

For such an analysis, we consider the coherent accumulation, during the de-spreading, of N_s received pulses at receiver side, giving a SNR

$$\mathsf{SNR} = \frac{P_\mathrm{R}(d_{\mathrm{T}j}, d_{\mathrm{R}i})\, T_\mathrm{p}\, N_\mathrm{s}}{N_0} \tag{4.10}$$

where $P_\mathrm{R}(d_{\mathrm{T}j}, d_{\mathrm{R}i})$ is the received power. The noise PSD can be obtained from the receiver characteristics with $N_0 = \kappa\, N_\mathrm{F}\, T_0$, being $T_0 = 290\,\mathrm{K}$ the reference temperature, κ the Boltzmann constant and N_F the receiver noise figure.

As second performance metric, a 3D detection coverage analysis is reported. Differently from the PEB characterization conducted in ideal conditions, here we consider the feasibility of the proposed system architecture in a more realistic scenario taking into account different tag orientations and realistic radiation patterns. In general, the received power $P_\mathrm{R}(d_{\mathrm{T}j}, d_{\mathrm{R}i})$, related to the kth tag, can be expressed as [101]

$$P_\mathrm{R}(d_{\mathrm{T}j}, d_{\mathrm{R}i}) = \int_{f_\mathrm{c}-\frac{W}{2}}^{f_\mathrm{c}+\frac{W}{2}} \frac{S_\mathrm{t}(f) G_\mathrm{es}(f, \boldsymbol{\Theta}) G_\mathrm{ti}(f, \boldsymbol{\Theta}) G_\mathrm{tr}(f, \boldsymbol{\Theta}) G_\mathrm{r}(f, \boldsymbol{\Theta}) c^4}{L_\mathrm{t}(f)(4\pi)^4 f^4 d_{\mathrm{T}j}^{\alpha} d_{\mathrm{R}i}^{\alpha}}\, df \tag{4.11}$$

where we considered a transmitted signal with central frequency f_c, bandwidth W and PSD $S_\mathrm{t}(f)$, which is generally imposed by emission masks. $L_\mathrm{t}(f)$ accounts for losses in the tag (e.g., caused by the backscatter modulator) and we indicated with $G_\mathrm{es}(f, \boldsymbol{\Theta})$, $G_\mathrm{ti}(f, \boldsymbol{\Theta})$, $G_\mathrm{tr}(f, \boldsymbol{\Theta})$ and $G_\mathrm{r}(f, \boldsymbol{\Theta})$, the antenna gains of energy sprinklers, tags (for the incident and reflected signals), and receivers, respectively, with $\boldsymbol{\Theta}$ being the angles defined by the sprinkler-tag-receiver geometry.

Given a tag test position, we simulated M_c random tag 3D orientations and, for each orientation, we compared the received SNR with the minimum SNR_th required at receiver side to detect the tag presence with high reliability [104]. Fixed the nth tag position, the rate at which a tag is detected is given by

$$\mathrm{C}_n(\mathsf{SNR}_{\mathrm{th}}) = \frac{1}{M_{\mathrm{c}}} \sum_{m=1}^{M_{\mathrm{c}}} \mathbf{1}(\mathsf{SNR}_{m,n} - \mathsf{SNR}_{\mathrm{th}}) \tag{4.12}$$

where we have defined the unit step function $\mathbf{1}(x) = 1$ if $x \geq 0$ and 0 otherwise, and $\mathsf{SNR}_{m,n}$ is the SNR at the mth Monte Carlo iteration, evaluated using (4.10) and (4.11). C_n returns the detection coverage rate of the nth position. Similarly, the coverage outage is defined as

$$\mathcal{O}(\mathsf{SNR}_{\mathrm{th}}) = \frac{1}{M_{\mathrm{c}} N_{\mathrm{pos}}} \sum_{n=1}^{N_{\mathrm{pos}}} \sum_{m=1}^{M_{\mathrm{c}}} \mathbf{1}(\mathsf{SNR}_{\mathrm{th}} - \mathsf{SNR}_{m,n}) \tag{4.13}$$

where N_{pos} is the number of tested tag positions.

Simulation results

A UWB-RFID system adopting RRC pulses with $W = 500\,\mathrm{MHz}$ bandwidth centered at $f_{\mathrm{c}} = 4\,\mathrm{GHz}$ is simulated. We consider a PRP $T_{\mathrm{p}} = 128\,\mathrm{ns}$ and a receiver with noise figure $F = 4\,\mathrm{dB}$. Implementation losses of 3 dB have been included to account for tags' losses and non-idealities at receiver side.

To assess the theoretical maximum localization performance gain, we consider the 2D simulated environment is a square room of $10 \times 10\,\mathrm{m}^2$ with one or two receivers placed, respectively, in the points with coordinates $\mathbf{p}_{\mathrm{R1}} = [0, 5]$ and $\mathbf{p}_{\mathrm{R2}} = [10, 5]$. Energy sprinklers are supposed scattered in the environment in random (but known) positions, $N_{\mathrm{s}} = 8192$ coherently accumulated pulses per symbol are considered and Monte Carlo simulations with 100 cycles are conducted to evaluate the average PEB. All the antennas are supposed omni-directional with gain of 2 dBi.

For the coverage analysis, we consider a 3D indoor scenario of $10 \times 10 \times 4\,\mathrm{m}^3$ and we set the number of accumulated pulses to a higher value ($N_{\mathrm{s}} = 65536$) to counteract the poorer link budget caused by the 3D room dimensions. Energy sprinklers' and receivers' antennas are assumed with a constant gain of 2 dBi and 6 dBi respectively, in the semi-space where antennas are directed to. A simulated dipole antenna has been chosen for the tag. Results are obtained by taking into consideration the antenna characteris-

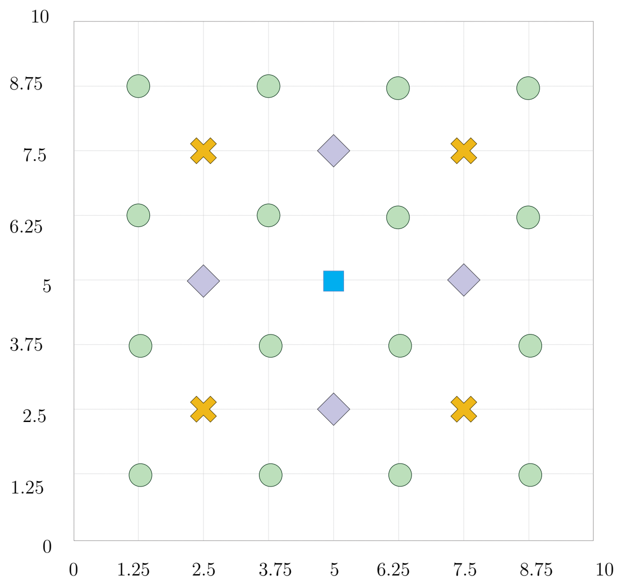

Figure 4.17: Transmitters positions. Blue (□): single sprinkler. Yellow (×): 4 sprinklers. All the non-circle points (□, ×, ⋄): 9 sprinklers. Green (∘): 16 sprinklers.

tics, and a random tag orientation in the 3D space for each of the $M_c = 1000$ Monte Carlo cycles. Energy sprinklers are supposed placed on the ceiling, downward oriented. Their positions are reported on the grid of Fig. 4.17.

Tags can move on a discretized grid of points 0.25 mt spaced in the azimuthal plane while their height is uniformly distributed between 1 and 3 m and changes at each Monte-Carlo iteration together with the antenna radiation pattern. Two receivers are considered placed in positions $\mathbf{p}_{R1} = [0,\ 5,\ 2]$ and $\mathbf{p}_{R2} = [10,\ 5,\ 2]$.

Figure 4.18 reports the localization error outage (LEO) [25] obtained from the PEB as a function of the localization error ϵ_{th} for different number of energy sprinklers, considering one or two receivers. From the figure it is evident that, in the presence of a single receiver, the adoption of 3 or more energy sprinklers is fundamental to guarantee a localization error below 1 m in the 90% of the tag positions (LEO = 0.1). The performance can be further improved by increasing the number of energy sprinklers. Differently, when two receivers are considered, a significant gain is present when moving from a single energy sprinkler to 2 or 3 sprinklers: on the contrary, a less pronounced

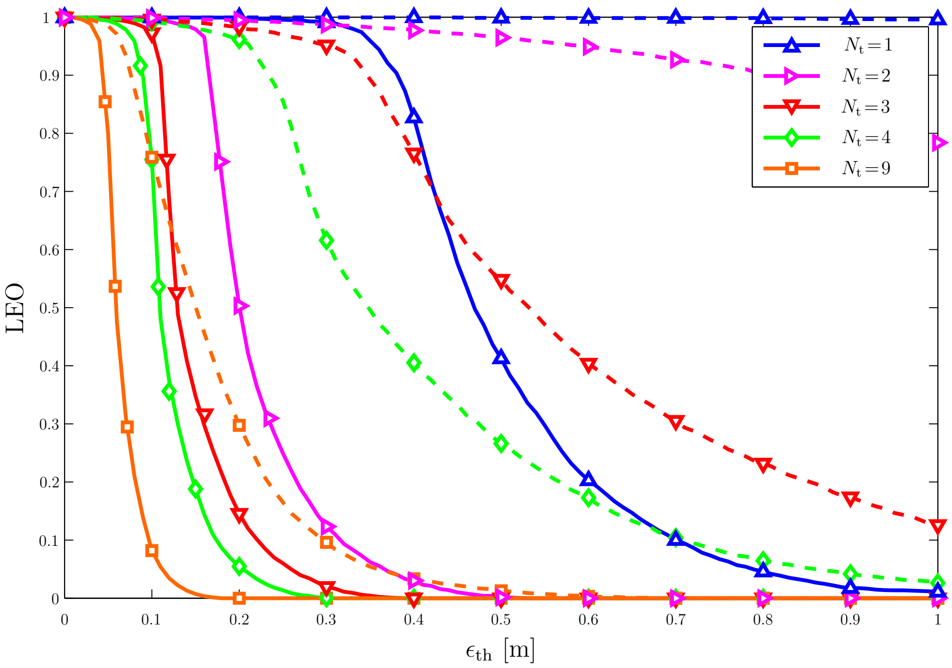

Figure 4.18: Localization error outage. Dashed lines (- -) refer to a single receiver; continuous lines (–) refer to 2 receivers.

incremental gain is obtained through the deployment of additional sprinklers (e.g., moving from 4 to 9). From Fig. 4.18 it is also evident that the adoption of 2 receivers instead of 1 increases significantly the performance. It is important to underline that, in general, at least 3 observations (corresponding to 3 bistatic pairs) are necessary to have an unambiguous localization (e.g. 2 energy sprinklers and 2 receivers). If a configuration with less than 3 bistatic pairs is considered, proper sprinklers/receivers placement must be adopted to avoid ambiguities.

Figure 4.19 shows the coverage $\mathrm{C}_n(\mathsf{SNR}_{\mathrm{th}})$ obtained using (4.10) for $\mathsf{SNR}_{\mathrm{th}} = 15\,$dB,and when a monostatic configuration, or 1, 4, 9 and 16 sprinklers are adopted, respectively. Coverage has been averaged considering multiple tags random locations on the z axis. In particular, the monostatic configuration guarantees high performance when the tags are near the readers, while detection becomes poorer and poorer when the distance from them grows. On the contrary, multistatic configurations help to overcome this limitation, improving the detection coverage for positions not close to the receivers, thus

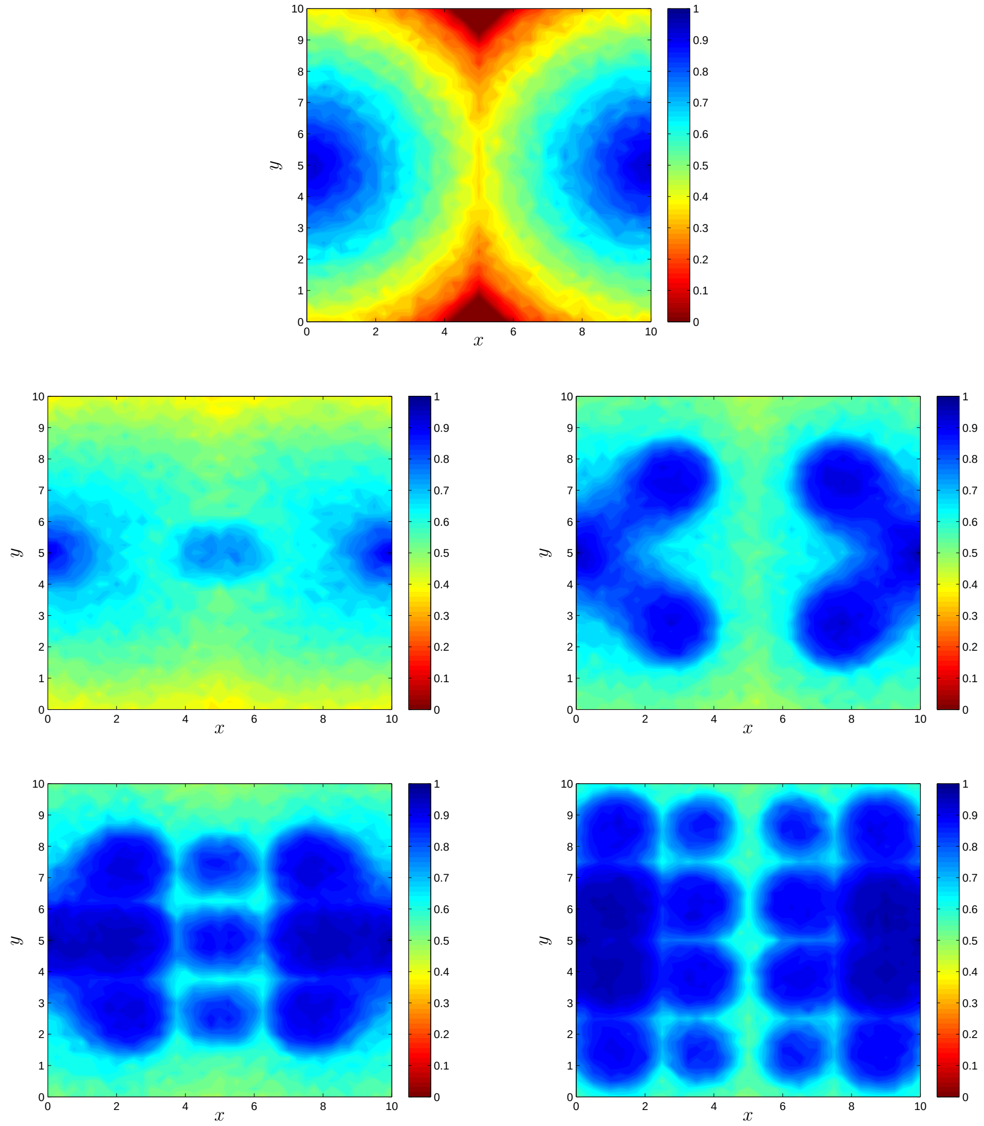

Figure 4.19: Detection coverage maps obtained for $\mathsf{SNR}_{\mathrm{th}} = 15\,\mathrm{dB}$. Top: monostatic configuration. Middle: $N_{\mathrm{es}} = 1$ (left) and $N_{\mathrm{es}} = 4$ (right). Bottom: $N_{\mathrm{es}} = 9$ (left) and $N_{\mathrm{es}} = 16$ (right).

allowing a more equalized performance in the space. The importance of the adoption of energy sprinklers is well evidenced in Fig. 4.20, where the coverage outage is reported for different SNR thresholds. Note that if we fix a detection coverage target to 80% (i.e., $\mathcal{O}(\mathsf{SNR}_{\mathrm{th}}) = 0.2$), we can observe

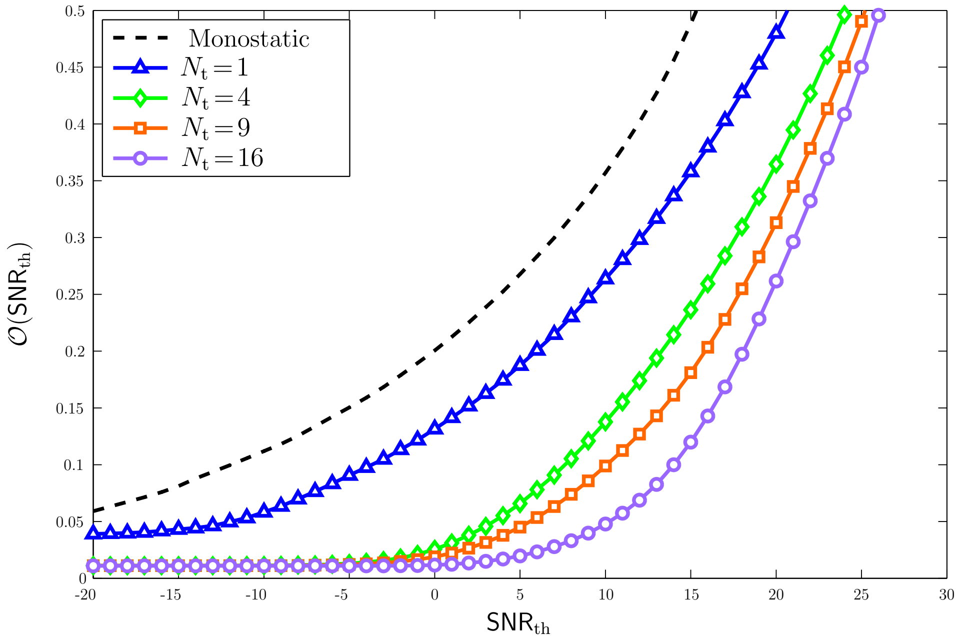

Figure 4.20: Detection coverage outage.

an improvement on the required SNR_th of about 15 dB when moving from a monostatic configuration to $N_\mathrm{es} = 16$.

4.3 Relaying techniques for localization

The second part of this chapter deals with the idea of deploying relays in the environment to increase the localization coverage in presence of obstructions between anchors and tags. The idea of using relaying techniques to extend radio coverage is not new. In particular, regenerative relays, for example employing detect & forward (DF) techniques [105] have been widely investigated for communication systems, but not for localization systems. The adoption of regenerative relays for localization was presented in [106] with the purpose of reducing the overhead and scaling inefficiencies of conventional two-way ranging methods. A similar approach based on secondary anchors performing ranging was described in [107], while in [108] regenerative relays are considered in *ad-hoc* networks composed of master and secondary active nodes for localization without prior nodes' synchronization. The enhancement of localization coverage was also addressed in [109, 110] for locating and tracking passive point scatterers using regenerative relays and UWB signals.

Previous solutions using regenerative relays have similar complexity of anchors because TOA estimation and data communication capabilities are required at the relay side. Moreover, the design of regenerative relays depends on the specific signal format adopted by the localization system, thus preventing generality and reconfiguration of the localization infrastructure.

To overcome the above-mentioned limitations we advocate the use of *non-regenerative relays*, where neither modulator nor demodulator sections are present in the relay and the received signal is directly repeated. Non-regenerative relays can be active, namely AF, or passive, namely JF. JF relays (also referred to as cold repeaters) are composed of a couple of interconnected directive antennas and take advantage of antenna directivity gain to mitigate the additional path-loss caused by the two-hop link. Non-regenerative relaying approach is known in communication networks; for example JF relays are adopted as gap fillers in broadcasting and Wi-Fi systems to cover shadowed areas, especially for indoor environments [111]. Non-regenerative relay-based systems present in the literature are communication-oriented, not localization-oriented.

The goal of this section is to introduce non-regenerative relaying for network localization and to facilitate a deep understanding of its benefits in real environments. Specifically, the basis for the design and analysis of localization systems with UWB non-regenerative relaying is proposed. Both AF and JF relays are considered for localization performance improvement and coverage extension in indoor environment with NLOS propagation conditions.

Non-regenerative relays

We consider a localization system composed of N_a anchors, in known positions $\mathbf{p}_m^{(\mathrm{A})}$, with $m = 1, 2, \ldots, N_\mathrm{a}$, a set of N_r non-regenerative unidirectional relays, in known positions $\mathbf{p}_l^{(\mathrm{R})}$, with $l = 1, 2, \ldots, N_\mathrm{r}$, and a tag in unknown position $\mathbf{p}$ to be inferred (see Fig. 6). Anchors are part of a network controlled by the central processing unit and with a common time scale (i.e.,

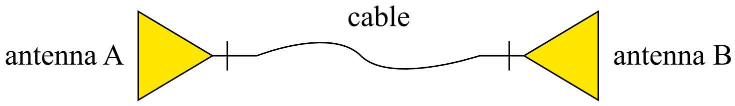

(a) JF relay

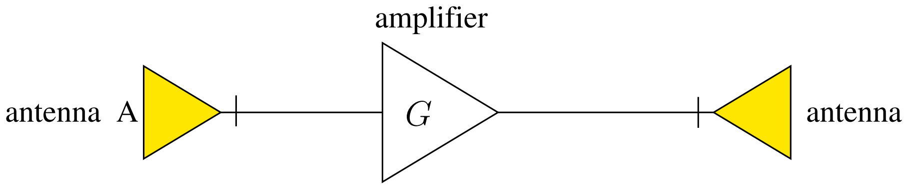

(b) AF relay

Figure 4.21: Non-regenerative relays.

anchors are synchronized). We now describe non-regenerative relaying and the signaling. Relays repeat the signal exchanged between tags and anchors. In particular, non-regenerative relays can be passive (JF) or active (AF). Figure 4.21a shows the JF relay, which is composed of a weak directional antenna (antenna A), an electrical cable, and a high gain directional antenna (antenna B). The JF relay exploits the partial compensation of the additional path-loss caused by the two-hops link (tag-relay-anchor) by the directional gain of the antennas.

Relays can be implemented in different ways: unidirectional relays are used in case of one-way ranging protocols (e.g., for TDOA), while bidirectional relays are used in case of two-way ranging protocols. In the following we focus on unidirectional relays because of their intrinsic lower complexity. Figure 4.21b shows an example of one-way AF relay with an amplifier between antenna A and antenna B to reinforce the signal. The presence of an amplifier suffers from mutual coupling between antennas, which must be controlled through proper isolation and device deployment to avoid unstable loops that could arise due positive feedback.[8] A more complex architecture that adopts echo cancelers can be used to increase the robustness against feedback [112]. Other known solutions require an external synchronization signal [113].

Non-regenerative relays add thermal noise into the system. Specifically, if

---

[8] This effect limits the maximum signal amplification level.

$T_\mathrm{a} = 290\,\mathrm{K}$ is the antenna temperature and G the gain of the relay ($G < 1$ for JF relays), then the equivalent single-side noise PSD results in $k\,F_\mathrm{R}\,T_\mathrm{a}$, where k is the Boltzmann's constant and F_R is the relay noise figure ($F_\mathrm{R} = 1/G$ for JF relays).

As a general guideline, the relays are deployed so that antenna B is in LOS condition with one preferred anchor, and antenna A is in LOS condition to all the possible tag positions covered by the relay. Note that the considered non-regenerative relays do not require synchronization schemes.

4.3.1 Signaling with non-regenerative relays

Each tag emits a signal $s(t)$ with energy E_T which is received by one or more anchors through a direct path (when in LOS condition), reflections from walls and obstacles, or non-regenerative relays.[9] The impulse-radio UWB ranging packet $s(t)$,[10] is composed of a sequence of N_s band-pass pulses $p(t)$ of bandwidth W repeated with PRP T_f. For simplicity of notation in the following derivation we assume $N_\mathrm{s} = 1$, even if the coherent accumulation of $N_\mathrm{s} > 1$ pulses will be accounted for in the numerical results to increase the SNR.

Tags are in general asynchronous, and t_0 is the difference between the tag's clock and the readers' network clock. The initial uncertainty on t_0 can be significantly reduced by partially synchronizing tags through a dedicated control channel (e.g., a narrow band signal in the UHF band) [34].[11]

The received signal at the mth anchor is given by

$$r_m(t) = s_m(t) + n_m(t) \tag{4.14}$$

where $s_m(t)$ is the useful term and $n_m(t) = \sum_{l=0}^{N_\mathrm{R}} n_{l,m}(t)$ accounts for all noise components generated by the receiver and the relays. In particular, $n_{l,m}(t)$, for $l = 1, \ldots, N_\mathrm{r}$, is the thermal noise at the mth anchor, with PSD $N_{l,m}$,

---

[9] Multiple tags can coexist in the same environment by a suitable medium access control (MAC) procedure [114, 115].

[10] Or any generic low duty-cycle signal.

[11] Another approach to reduce uncertainty on t_0 consists in adopting TDOA-based localization schemes accounting for the presence of relays.

due to the lth relay and $n_{0,m}(t)$ is the thermal noise generated at the anchor with PSD $N_{0,m} = N_0$. In (4.14), the useful term $s_m(t)$ can be expressed as

$$s_m(t) = \sum_{l=0}^{N_\mathrm{r}} a_{l,m}\, g_{l,m}(t - \tau_{l,m}) \tag{4.15}$$

where the terms for $l > 0$ account for relayed signals, whereas the term for $l = 0$ accounts for the direct link between the tag and the anchor (even through environmental multipath). The signal $g_{l,m}(t)$, for $l = 1, 2, \ldots N_\mathrm{r}$, is the normalized channel response (NCR) to the signal $s(t)$ of the link tag – lth relay – mth anchor, while $g_{0,m}(t)$ is the NCR of the link tag – mth anchor. The normalization is done with respect to the time-of-flight (TOF) $\tau_{l,m}$ and the average energy, that is $\mathbb{E}\left\{\int_{T_\mathrm{f}} g_{l,m}^2(t)\, dt\right\} = 1$. Note that signals $g_{l,m}(t)$ account for multipath propagation effects and for distortion caused by antennas and circuits frequency selectivity. In the following we will refer to the complete set of $L = N_\mathrm{r} + 1$ signals at anchor m with the name *replicas*.[12] We denote with $T_\mathrm{p}^{(l,m)}$ the duration of the lth replica of the received signal at the mth anchor. Specifically, in (4.15) we defined the quantities

$$a_{l,m} = \begin{cases} \sqrt{E_\mathrm{T}}\, w(\mathbf{p}, \mathbf{p}_m^{(\mathrm{A})})\,, & l = 0\,, \\ \sqrt{E_\mathrm{T}}\, w(\mathbf{p}, \mathbf{p}_l^{(\mathrm{R})})\, \sqrt{G_l}\, w(\mathbf{p}_l^{(\mathrm{R})}, \mathbf{p}_m^{(\mathrm{A})})\,, & l = 1, 2, \ldots, N_\mathrm{r} \end{cases} \tag{4.16}$$

$$\tau_{l,m} = \begin{cases} \tau(\mathbf{p}, \mathbf{p}_m^{(\mathrm{A})}) + t_0\,, & l = 0\,, \\ \tau(\mathbf{p}, \mathbf{p}_l^{(\mathrm{R})}) + \delta_l + \tau(\mathbf{p}_l^{(\mathrm{R})}, \mathbf{p}_m^{(\mathrm{A})}) + t_0, & l = 1, 2, \ldots, N_\mathrm{r} \end{cases} \tag{4.17}$$

where $\tau(\mathbf{p}_1, \mathbf{p}_2) \triangleq \|\mathbf{p}_1 - \mathbf{p}_2\|/c$ is the TOF of the signal to reach position $\mathbf{p}_2$ from $\mathbf{p}_1$, c is the speed of light, G_l and δ_l are the gain and the delay introduced by the lth relay, respectively. The coefficient $w(\mathbf{p}_1, \mathbf{p}_2)$ accounts for the antenna gains and path-loss for a link between $\mathbf{p}_1$ and $\mathbf{p}_2$; in the absence of such a link $w(\mathbf{p}_1, \mathbf{p}_2) = 0$.[13]

---

[12] In this formulation multiple hop paths between relays are considered strongly mitigated by directive antenna radiation patterns. Each NCR $g_{l,m}(t)$ is obviously dependent on the particular link.

[13] The information about radio visibility can be derived from the environmental knowledge [100].

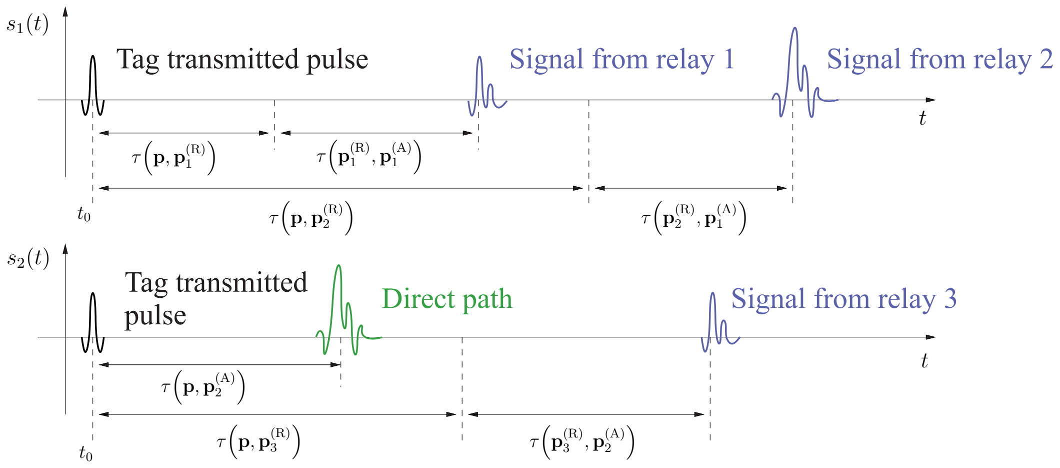

Figure 4.22: Example of signal structure in a scenario adopting active tags with $\delta_l = 0$, where $s_1(t)$ and $s_2(t)$ are the (noise-free) signals received by anchors 1 and 2, respectively.

Figure 4.22 shows an example of signal received by anchors 1 and 2 in the scenario of Fig. 6 in the presence of $N_\mathrm{r} = 3$ relays and $N_\mathrm{a} = 2$ anchors. For the sake of illustration, we have considered the tag in severe NLOS condition with respect to anchor 1 (i.e., $w\left(\mathbf{p}, \mathbf{p}_1^{(\mathrm{A})}\right)=0$), and $w\left(\mathbf{p}_1^{(\mathrm{A})}, \mathbf{p}_3^{(\mathrm{R})}\right)= w\left(\mathbf{p}_1^{(\mathrm{R})}, \mathbf{p}_2^{(\mathrm{A})}\right) = w\left(\mathbf{p}_2^{(\mathrm{R})}, \mathbf{p}_2^{(\mathrm{A})}\right) = 0$. Here $\delta_l = 0$, $\forall l$ is assumed. As can be seen, the impulse emitted by the tag at time $t = t_0$ is received by relay 1 after $\tau\left(\mathbf{p}, \mathbf{p}_1^{(\mathrm{R})}\right)$ seconds and then relayed. The relayed signal arrives at anchor 1 after $\tau\left(\mathbf{p}, \mathbf{p}_1^{(\mathrm{R})}\right) + \tau\left(\mathbf{p}_1^{(\mathrm{R})}, \mathbf{p}_1^{(\mathrm{A})}\right)$ seconds. It has to be remarked that the delay $\tau\left(\mathbf{p}_1^{(\mathrm{R})}, \mathbf{p}_1^{(\mathrm{A})}\right)$ is known from the prior knowledge of anchors and relays positions.

4.3.2 Network localization with non-regenerative relays

In most localization systems, tag's position estimation is obtained in two steps: measurement of position/distance/angle dependent quantities (e.g., TOA,TDOA, RSSI), followed by a localization algorithm (e.g., multi-lateration, least-square, maximum likelihood (ML), etc.) [76]. Single-step (direct) estimators, which infer the position directly from signals, offer in general better performance at the expense of higher complexity. We now derive direct ML position estimators accounting for non-regenerative relaying. Note that the proposed architecture based on non-regenerative relays is not limited to direct ML position estimators [93, 116].[14] Here the ML estimator has been chosen because of its asymptotic efficiency and wide range of applications. In the following, lower complexity ML estimators are also derived based on different levels of channel state information (CSI) availability.

ML estimators

Perfect CSI Here the ML estimator of tag's position is determined for the case of perfect CSI, that is, perfect knowledge of NCRs $g_{l,m}(t)$ and of channel gain coefficients $w(\cdot,\cdot)$. Such estimator serves as performance benchmark for other practical estimators, that will be derived in the following sections.[15]

The ML tag's position estimate $\hat{\mathbf{p}}$ and the estimate of $\hat{t}_0$ are given by

$$(\hat{\mathbf{p}}, \hat{t}_0) = \underset{(\mathbf{p},t_0)\in(\mathcal{P},\mathcal{T})}{\operatorname{argmax}} \; \ell(\mathbf{p}, t_0) \tag{4.18}$$

where $\mathcal{P}$ is the set of admissible locations (e.g. obtained from a priori environment knowledge), $\mathcal{T}$ is the initial uncertainty on t_0, and the log-likelihood function is given by

$$\ell(\mathbf{p}, t_0) = \sum_{m=1}^{N_\mathrm{a}} \left\{ \frac{2}{N_m} \left[\sum_{l=0}^{N_\mathrm{r}} a_{l,m}\, \chi_{l,m}\left(\tau_{l,m}\right) \right] - \frac{E_m}{N_m} \right\} \tag{4.19}$$

with the correlation term

$$\chi_{l,m}(\xi) \triangleq \int_{T_\mathrm{ob}} r_m(t)\, g_{l,m}(t-\xi)\, dt \tag{4.20}$$

---

[14] Other state-of-the-art schemes for TOA and position estimation techniques, for example based on popular two-step approaches, could be considered with proper adaptation to include the presence of relays.

[15] In the scenario with relays obtaining CSI is a more challenging task with respect to conventional communication systems due to the presence of relayed components in the received signal.

and the energy term $E_m \triangleq \int_{T_{\text{ob}}} s_m^2(t)\, dt$. To simplify the notation we do not explicit the dependence of the involved quantities on position $\mathbf{p}$ and transmission time t_0. We have indicated with T_{ob} the observation interval chosen to include all the useful signal replicas, and with $N_m = \sum_{l=0}^{N_{\text{r}}} N_{l,m}$ the overall noise PSD at anchor m.

The ML estimator consists in filtering the received signal at each anchor by a bank of filters matched to $g_{l,m}(t)$ and observing their weighted outputs in time instants depending on the tag's position $\mathbf{p}$. The ML estimator implementation can be drastically simplified by adopting filters matched to a template waveform proportional, for example, to the transmitted signal $s(t)$, instead of replicas $g_{l,m}(t)$ that are in general unknown. This case will be considered in the numerical results in Sec. 4.3.3. Note that, in (4.19), the correlators outputs are weighted by the noise PSD N_m at each anchor to account for different noise levels due to the particular anchor-relay distances.

Partial CSI We now consider practical estimators with different levels of CSI availabilities at the receiver. First we derive the ML estimator in case of unknown amplitudes of the received signal replicas; in this case the localization capability relies only on the delay-distance dependence on the signal's TOA. Then, we analyze the position estimator without knowledge of the NCRs $g_{l,m}(t)$, in the presence only of information on RSSI and TOA of the received signal. Finally, a blind position estimator that does not require any knowledge of the NCRs and exploits only the information on signal TOA is derived.

The discrete signals representation obtained by sampling the original signals with sampling time $\delta t = 1/2W$ provides:[16]

$$\begin{aligned}
r_m(t); t \in (0, T_{\text{ob}}) \quad &\rightarrow \mathbf{r}^{(m)} \in \mathbb{R}^N \; ; \; r_n^{(m)} = r_m(n\delta t) \\
n_m(t); t \in (0, T_{\text{ob}}) \quad &\rightarrow \mathbf{n}^{(m)} \in \mathbb{R}^N \; ; \; n_n^{(m)} = n_m(n\delta t) \\
s_m(t); t \in (0, T_{\text{ob}}) \quad &\rightarrow \mathbf{s}^{(m)} \in \mathbb{R}^N \; ; \; s_n^{(m)} = s_m(n\delta t) \\
g_{l,m}(t); t \in (0, T_{\text{p}}^{(l,m)}) &\rightarrow \mathbf{g}_{\mathbf{l}}^{(m)} \in \mathbb{R}^{M^{(l,m)}}; g_{l,n}^{(m)} = g_{l,m}(n\delta t)
\end{aligned} \tag{4.21}$$

---

[16] This provides a good approximation when $WT_{\text{ob}} \gg 1$ [70], as it is in our case.

$$\breve{\boldsymbol{\chi}}_m = \mathbf{W}_m^{\mathrm{T}}\,\mathbf{r}^{(m)} = \left[\mathbf{w}^{(m)\mathrm{T}}_{\breve{\tau}_{0,m}}\mathbf{r}^{(m)}, \mathbf{w}^{(m)\mathrm{T}}_{\breve{\tau}_{1,m}}\mathbf{r}^{(m)}, \dots, \mathbf{w}^{(m)\mathrm{T}}_{\breve{\tau}_{N_{\mathrm{r}},m}}\mathbf{r}^{(m)}\right] \in \mathbb{R}^L \tag{4.27}$$

where $l = 0, 1, \dots N_{\mathrm{r}}$; $n = 1, 2, \dots, N$; $N = \lceil T_{\mathrm{ob}}/\delta t \rceil$; and $M^{(l,m)} = \lceil T_{\mathrm{p}}^{(l,m)}/\delta t \rceil$.[17]

We now derive the position estimator when the channel amplitudes

$$\mathbf{a}^{(m)} = \left[a_{0,m}, a_{1,m}, \dots, a_{N_{\mathrm{r}},m}\right]^{\mathrm{T}} \in \mathbb{R}^L \tag{4.22}$$

in (4.19) are unknown. From (4.21), it is possible to rewrite (4.14) in vector form as

$$\mathbf{r}^{(m)} = \mathbf{s}^{(m)} + \mathbf{n}^{(m)} = \mathbf{W}_m\,\mathbf{a}^{(m)} + \mathbf{n}^{(m)} \tag{4.23}$$

where $\mathbf{W}_m$ is[18]

$$\mathbf{W}_m = \left[\mathbf{w}^{(m)}_{\breve{\tau}_{0,m}}, \mathbf{w}^{(m)}_{\breve{\tau}_{1,m}}, \dots, \mathbf{w}^{(m)}_{\breve{\tau}_{N_{\mathrm{r}},m}}\right] \in \mathbb{R}^{N\times L} \tag{4.24}$$

with

$$\mathbf{w}^{(m)}_{\breve{\tau}_{l,m}} = \left[\mathbf{0}_{\breve{\tau}_{l,m}}, \mathbf{g}_{\mathbf{l}}^{(m)}, \mathbf{0}_{N-M^{(l,m)}-\breve{\tau}_{l,m}}\right]^{\mathrm{T}} \in \mathbb{R}^N \tag{4.25}$$

having indicated with $\breve{\tau}_{l,m} \triangleq \lceil \tau_{l,m}/\delta t \rceil$ the discretized version of delay $\tau_{l,m}$.

By considering the vector $\mathbf{a}^{(m)}$ unknown deterministic, the position estimation can be obtained from (4.18) and (4.19) by substituting $\mathbf{a}^{(m)}$ with its ML estimate $\hat{\mathbf{a}}^{(m)}$, which can be obtained in closed form for each anchor as

$$\begin{aligned}(\hat{\mathbf{p}}, \hat{t}_0) &= \underset{(\mathbf{p},t_0)\in(\mathcal{P},\mathcal{T})}{\mathrm{argmax}}\ \ell\left(\mathbf{p}, t_0; \{\mathbf{a}^{(m)}\} = \{\hat{\mathbf{a}}^{(m)}\}\right) \\ &= \underset{(\mathbf{p},t_0)\in(\mathcal{P},\mathcal{T})}{\mathrm{argmax}} \left\{-\sum_{m=1}^{N_{\mathrm{a}}} \frac{1}{2\sigma_m^2}\left\|\mathbf{r}^{(m)} - \mathbf{W}_m\,\hat{\mathbf{a}}^{(m)}\right\|^2\right\}\end{aligned} \tag{4.26}$$

where $\sigma_m^2 = N_m W$ is the noise power at anchor m. In [34], this estimator is

---

[17] Notation $\lceil x \rceil$ denotes the smallest integer greater than or equal to x.

[18] $\mathbf{W}_m$ is a function of $\mathbf{p}$ and t_0. However, this dependence will be omitted in the rest of the paper for notation simplicity.

$$\breve{\mathbf{R}}_m = \mathbf{W}_m^{\mathrm{T}} \mathbf{W}_m = \begin{bmatrix} \mathbf{w}^{(m)\mathrm{T}}_{\breve{\tau}_{0,m}} \mathbf{w}^{(m)}_{\breve{\tau}_{0,m}} & \mathbf{w}^{(m)\mathrm{T}}_{\breve{\tau}_{0,m}} \mathbf{w}^{(m)}_{\breve{\tau}_{1,m}} & \cdots & \mathbf{w}^{(m)\mathrm{T}}_{\breve{\tau}_{0,m}} \mathbf{w}^{(m)}_{\breve{\tau}_{N_{\mathrm{r}},m}} \\ \mathbf{w}^{(m)\mathrm{T}}_{\breve{\tau}_{1,m}} \mathbf{w}^{(m)}_{\breve{\tau}_{0,m}} & \mathbf{w}^{(m)\mathrm{T}}_{\breve{\tau}_{1,m}} \mathbf{w}^{(m)}_{\breve{\tau}_{1,m}} & \cdots & \mathbf{w}^{(m)\mathrm{T}}_{\breve{\tau}_{1,m}} \mathbf{w}^{(m)}_{\breve{\tau}_{N_{\mathrm{r}},m}} \\ \vdots & \vdots & \ddots & \vdots \\ \mathbf{w}^{(m)\mathrm{T}}_{\breve{\tau}_{N_{\mathrm{r}},m}} \mathbf{w}^{(m)}_{\breve{\tau}_{0,m}} & \mathbf{w}^{(m)\mathrm{T}}_{\breve{\tau}_{N_{\mathrm{r}},m}} \mathbf{w}^{(m)}_{\breve{\tau}_{1,m}} & \cdots & \mathbf{w}^{(m)\mathrm{T}}_{\breve{\tau}_{N_{\mathrm{r}},m}} \mathbf{w}^{(m)}_{\breve{\tau}_{N_{\mathrm{r}},m}} \end{bmatrix} \in \mathbb{R}^{L \times L} \tag{4.28}$$

derived as given by

$$(\hat{\mathbf{p}}, \hat{t}_0) = \underset{(\mathbf{p},t_0)\in(\mathcal{P},\mathcal{T})}{\operatorname{argmax}} \left\{ \sum_{m=1}^{N_{\mathrm{a}}} \frac{1}{2\sigma_m^2} \breve{\boldsymbol{\chi}}_m^{\mathrm{T}} \breve{\mathbf{R}}_m^{-1} \breve{\boldsymbol{\chi}}_m \right\} \tag{4.29}$$

where the vector $\breve{\boldsymbol{\chi}}_m$ and the matrix $\breve{\mathbf{R}}_m$, both dependent on tag's position $\mathbf{p}$, are defined respectively in (4.27) and (4.28). Even in realistic propagation conditions where overlapped signal replicas might be present, numerical results show the effectiveness of the estimator derived under this assumption. In this case, the ML estimator (4.29) reduces to the continuous-time

$$(\hat{\mathbf{p}}, \hat{t}_0) = \underset{(\mathbf{p},t_0)\in(\mathcal{P},\mathcal{T})}{\operatorname{argmax}} \left\{ \sum_{m=1}^{N_{\mathrm{a}}} \frac{1}{N_m} \sum_{l=0}^{N_{\mathrm{r}}} \frac{1}{E_{l,m}} \chi_{l,m}^2(\tau_{l,m}) \right\} \tag{4.30}$$

with $E_{l,m} = \breve{E}_{l,m}\delta t$. The position estimator (4.30) relies only on the TOA of signal replicas (not on the unknown signal amplitudes $a_{l,m}$). Note also that (4.30) requires the sum of the correlation terms related to all the L replicas at each anchor while, as explained in Sec. 4.3.1, only a subset of the relays and anchors is, in general, in visibility of a tag. This is accounted by the fact that coefficients $w(\cdot,\cdot)$ are zero in the absence of radio visibility. Therefore, prior information on blocked signal replicas[19] can be exploited by setting to zero the corresponding coefficients in (4.22). In such a case, the estimator

---

[19] Such information can be obtained, for example, from the knowledge of the environment.

(4.30) becomes

$$(\hat{\mathbf{p}}, \hat{t}_0) = \underset{(\mathbf{p},t_0)\in(\mathcal{P},\mathcal{T})}{\operatorname{argmax}} \left\{ \sum_{m=1}^{N_\mathrm{a}} \frac{1}{N_m} \sum_{l\in\mathcal{A}_m} \frac{1}{E_{l,m}} \chi^2_{l,m}\left(\tau_{l,m}\right) \right\} \tag{4.31}$$

where $\mathcal{A}_m = \{u : a_{u,m} \neq 0\}$.

It is important to remark that both estimators (4.18)-(4.19) and (4.31) require, in general, the knowledge of the complete NCRs $g_{l,m}(t)$.[20] In the numerical results we will also consider a simplified and practical solution that makes use of the known transmitted signal $s(t)$ as a template in the correlations instead of the actual NCR, with a substantial reduction of the complexity. We now derive a position estimator that does not require the evaluation of the correlation terms in (4.20), and hence can operate at sub-Nyquist rate. Such estimator combines RSSI and TOA information without prior knowledge of the NCRs.

First, consider all replicas $g_{l,m}(t)$ having the same shape $g(t)$ with support T_p. Note that this is not true in general as each replica is characterized by different multipath components. However, as shown afterwards and in the numerical results, this leads to a simple but well-performing estimator even in realistic propagation conditions. By denoting the energy of the NCR $E_g = \int_0^{T_\mathrm{p}} g^2(t)\, dt$ and defining the vector $\mathbf{g} \in \mathbb{R}^M$, with $M = \lceil T_\mathrm{p}/\delta t \rceil$, whose elements are samples of $g(t)$, we have $\|\mathbf{g}\|^2 = \breve{E}_\mathbf{g}$, where $\breve{E}_\mathbf{g} = E_g/\delta t$ [70]. It is possible to rewrite (4.23) in the form

$$\mathbf{r}^{(m)} = \mathbf{H}_m \, \mathbf{g} + \mathbf{n}^{(m)} \tag{4.32}$$

where the matrix $\mathbf{H}_m$ accounts for signal delays and channel gains.[21] In particular,

$$\mathbf{H}_m = \sum_{l=0}^{N_\mathrm{r}} a_{l,m} (\mathbf{\Pi}_N)^{\breve{\tau}_{l,m}} \mathbf{G} \;\in \mathbb{R}^{N\times M} \tag{4.33}$$

where $\mathbf{\Pi}_N$ is the N-order basic circulant permutation matrix [117, p. 26],

---

[20] This is analogue of considering, at each anchor, an ideal all-rake receiver.

[21] Also $\mathbf{H}_m$ is dependent on $\mathbf{p}$ and t_0.

and $\mathbf{G}$ is

$$\mathbf{G} = \begin{bmatrix} \mathbf{I}_M \\ \mathbf{0}_{N-M,M} \end{bmatrix} \in \mathbb{R}^{N \times M} \tag{4.34}$$

with $\mathbf{I}_M$ the M-order identity matrix and $\mathbf{0}_{N-M,M}$ the $(N-M) \times M$ null matrix. To derive a non-coherent position estimator that does not require the knowledge of the NCRs (i.e., the shape of $g(t)$), we substitute $\mathbf{g}$ with its ML estimate $\hat{\mathbf{g}}$, resulting in

$$\begin{aligned} (\hat{\mathbf{p}}, \hat{t}_0) &= \underset{(\mathbf{p},t_0)\in(\mathcal{P},\mathcal{T})}{\operatorname{argmax}} \; \ell\left(\mathbf{p}, t_0; \{\mathbf{g}\} = \{\hat{\mathbf{g}}\}\right) \\ &= \underset{(\mathbf{p},t_0)\in(\mathcal{P},\mathcal{T})}{\operatorname{argmax}} \left\{ -\sum_{m=1}^{N_\mathrm{a}} \frac{1}{2\sigma_m^2} \left\| \mathbf{r}^{(m)} - \mathbf{H}_m \, \hat{\mathbf{g}} \right\|^2 \right\}. \end{aligned} \tag{4.35}$$

In [34], the ML estimator (4.35) is derived as given by

$$(\hat{\mathbf{p}}, \hat{t}_0) = \underset{(\mathbf{p},t_0)\in(\mathcal{P},\mathcal{T})}{\operatorname{argmax}} \left\{ \sum_{m=1}^{N_\mathrm{a}} \frac{1}{2\sigma_m^2} \frac{\sqrt{\breve{E}_\mathbf{g}}}{\|\mathbf{H}_m^+ \, \mathbf{r}^{(m)}\|} \mathcal{E}^{(m)} \left(2 - \frac{\sqrt{\breve{E}_\mathbf{g}}}{\|\mathbf{H}_m^+ \, \mathbf{r}^{(m)}\|} \right) \right\} \tag{4.36}$$

where

$$\mathcal{E}^{(m)} = {\mathbf{r}^{(m)}}^\mathrm{T} \mathbf{H}_m \mathbf{H}_m^+ \mathbf{r}^{(m)} \,. \tag{4.37}$$

Note that, although the estimator (4.36) is in closed form, it can have high complexity due to sampling at Nyquist rate and matrix inversion. Therefore we consider signal replicas being not overlapped at the anchors. Again, even in realistic propagation conditions, numerical results show the effectiveness of the following resulting continuous-time estimator derived in [34] as given by

$$(\hat{\mathbf{p}}, \hat{t}_0) = \underset{(\mathbf{p},t_0)\in(\mathcal{P},\mathcal{T})}{\operatorname{argmax}} \left\{ \sum_{m=1}^{N_\mathrm{a}} \frac{2E_m}{N_m} \left(\sqrt{\frac{1}{E_m} \int_{\mathcal{D}^{(m)}} r_m^2(t)\, dt} - \frac{1}{2} \right) \right\} \tag{4.38}$$

where the set $\mathcal{D}^{(m)}$, function of $\mathbf{p}$, is the union of intervals

$$\mathcal{D}^{(m)} = \bigcup_{l \in \mathcal{A}_m} \left\{ (\tau_{l,m}, \tau_{l,m} + T_{\mathrm{p}}) \right\} \tag{4.39}$$

and $E_m = E_g \sum_{l=0}^{N_{\mathrm{r}}} a_{l,m}^2$ is the overall received energy including the collected L replicas at the anchor m. Note that the ML estimator (4.38) leads to a very simple implementation as it only requires energy measurements within particular time intervals where signal replicas are expected for each test position.

When the signal is completely unknown it is not possible to exploit the amplitude-distance dependence. Therefore, localization can only rely on the expected TOA information obtained by geometrical considerations.

Here, $\mathbf{s}^{(m)}$ in (4.23) is treated as an unknown vector and the ML position estimator is derived as

$$\begin{aligned} (\hat{\mathbf{p}}, \hat{t}_0) &= \operatorname*{argmax}_{(\mathbf{p}, t_0) \in (\mathcal{P}, \mathcal{T})} \ell \left(\mathbf{p}, t_0; \{\mathbf{s}^{(m)}\} = \{\hat{\mathbf{s}}^{(m)}\} \right) \\ &= \operatorname*{argmax}_{(\mathbf{p}, t_0) \in (\mathcal{P}, \mathcal{T})} \left\{ - \sum_{m=1}^{N_{\mathrm{a}}} \frac{1}{2\sigma_m^2} \left\| \mathbf{r}^{(m)} - \hat{\mathbf{s}}^{(m)} \right\|^2 \right\} \end{aligned} \tag{4.40}$$

where $\mathbf{s}^{(m)}$ is substituted by its ML estimate $\hat{\mathbf{s}}^{(m)}$ with elements $\hat{s}_n^{(m)}$, for $n = 1, 2, \ldots, N$. Specifically, according to the available prior information on the expected TOA only, the ML estimates $\hat{\mathbf{s}}^{(m)}$ are those exploiting the knowledge about the replica arrival time, that is,

$$\hat{s}_n^{(m)} = r_n^{(m)} \text{ for } n \in \breve{\mathcal{D}}^{(m)}, \; 0 \text{ otherwise} \tag{4.41}$$

where $\breve{\mathcal{D}}^{(m)}$ is the set of discrete time indexes n for which we expect to receive signal contributions in a test position. By substituting (4.41) in (4.40), and neglecting the terms independent of $\mathbf{p}$ and t_0, we obtain the continuous-time estimator

$$(\hat{\mathbf{p}}, \hat{t}_0) = \operatorname*{argmax}_{(\mathbf{p}, t_0) \in (\mathcal{P}, \mathcal{T})} \left\{ \sum_{m=1}^{N_{\mathrm{a}}} \frac{1}{N_m} \int_{\mathcal{D}^{(m)}} r_m^2(t)\, dt \right\}. \tag{4.42}$$

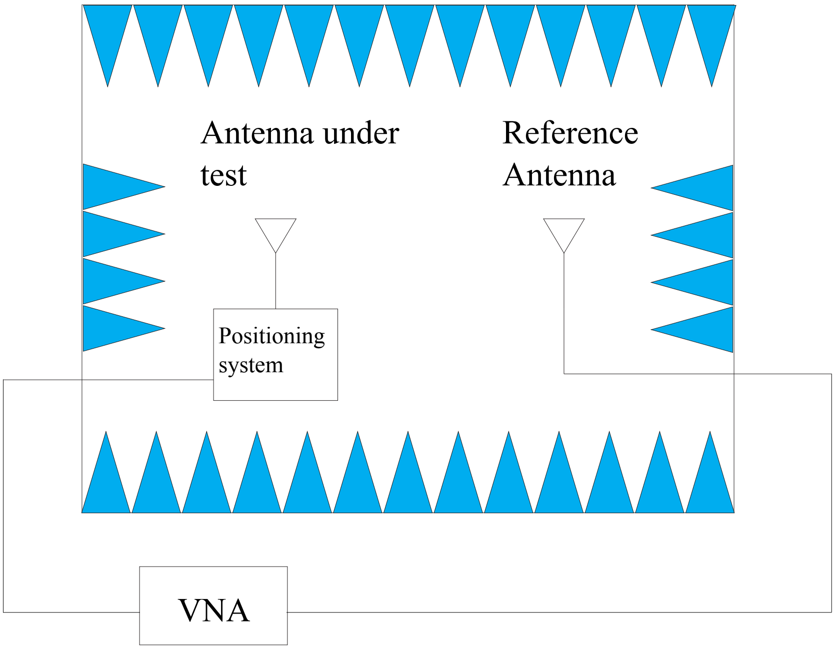

Figure 4.23: Anechoic Chamber Measurement set-up.

The structure of the ML estimator (4.42) is simple and consists in collecting the energy in those time intervals in which, according to $\mathbf{p}$ and t_0, the presence of signal replicas is expected.

4.3.3 Results

We now present a case study for the proposed network localization based on non-regenerative relaying, quantifying the performance of position estimators derived in Sec. 4.3.2.

UWB antenna characterization

The main aim of this section is to highlight the importance of antenna measurements in underlining some antennas parameters (such as radiation pattern) and to stress out how these features could drive the choice of adopting an antenna instead of another in a localization context. First of all, it is necessary to define the equipment used in antenna measurements system. In order to simplify the description we could refer to Fig. 4.23.

As we can see, the measurement process involves two kind of antennas: the *antenna under-test* is the antenna we want to measure and it is connected with a positioning system that controls its orientation while the *reference antenna* presents known figures of merit. Our goal is to measure the radiation pattern and gain of the antenna under test and to associate at each UWB measured antenna a role in a localization contest based on the analysis of measurements results. The measurement takes place in an anechoic chamber which stops reflections thanks to the radiation absorbent materials of which it is made up. As we have anticipated before, the purpose of this work is to understand what is the best role that each measured antenna could play in a localization system and to integrate the results with the simulator previously developed: the antennas which present a quasi omni-directional radiation pattern could, therefore, be a good candidate to perform the functionality of tags, while more directional antennas can be adopted for the development of relay nodes.

Measurements results Figure 4.24 reports the radiation patterns considering the two orthogonal linear vertical and horizontal polarization separately and then the total gain in polar coordinates obtained as the linear sum of the two partial gains for three types of realistic UWB measured antennas. Antennas were characterized in the azimuth plane, corresponding to the 2D plane of the case study for a frequency range between 2.5 and 10.5 GHz by steps of 5 degrees. Figure 4.24a presents the results for a UWB Vivaldi antenna with a peak gain $G_{\mathrm{A}} = 5\,\mathrm{dBi}$ at $f = 4\,\mathrm{GHz}$ and a HPBW of $101°$ degrees. Given this radiation properties, this type of antenna is suitable to be adopted for anchors and relay's antenna A (tag-relay links). Differently, Figure 4.24b considers a four-patch array antenna with peak gain $G_{\mathrm{R}} = 12\,\mathrm{dBi}$ and HPBW of 45 degrees at $f = 4\,\mathrm{GHz}$. These features best fit for the relay's antenna B (relay-anchor links).

It is important to remark how from these results we can conclude that certain types of antenna, such as an omnidirectional antenna (Figure 4.24c), fit with the typical features required for tag nodes while others such as the 4 patches antenna presents a more directive radiation diagram and conse-

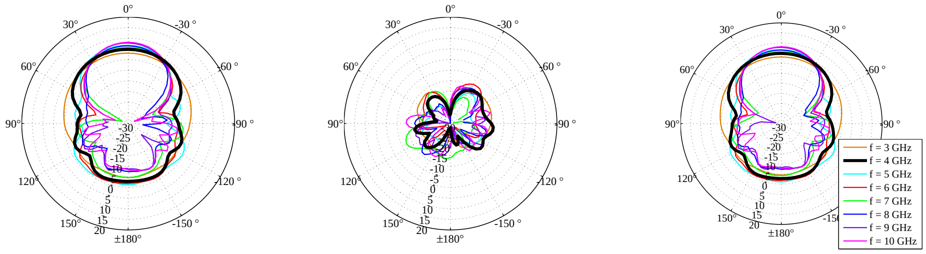

a.i) Co-pol.   a.i) Cross-pol.   a.iii) Total gain

(a) UWB Vivaldi Antenna

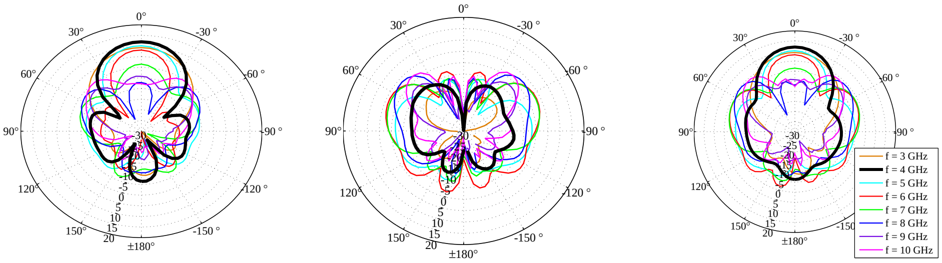

a.i) Co-pol.   a.i) Cross-pol.   a.iii) Total gain

(b) UWB 4-Patch Antenna

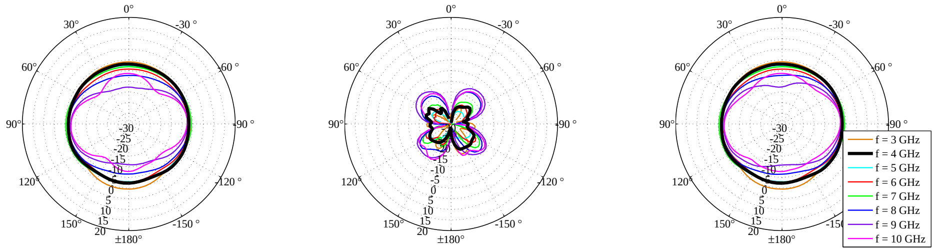

a.i) Co-pol.   a.i) Cross-pol.   a.iii) Total gain

(c) Dipole

Figure 4.24: UWB Antennas measurements results.

quently could be used as relay node.

In the following, frequency selectivity will be neglected, and only the radiation patterns evaluated at $f = 4\,\text{GHz}$ will be included in simulations.

Simulation scenario

Anchors are placed at the 4 corners of the square cell and 4 non-regenerative relays are present in the environment, placed at the corners of the blocking

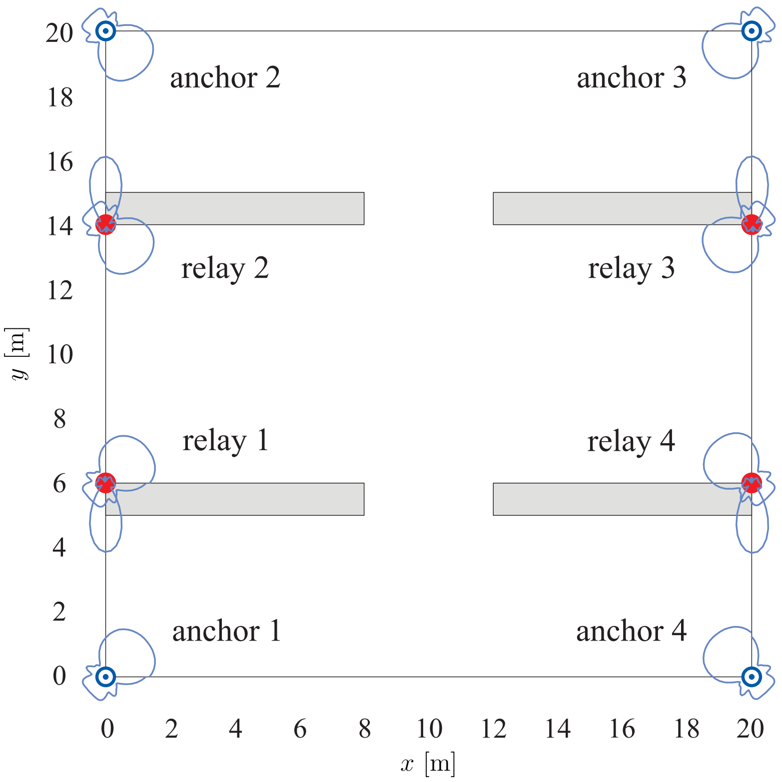

Figure 4.25: The considered scenario. Blue circles refer to anchors, red points refer to relays. Antennas' radiation patterns and orientation are reported. Obstacles are depicted in grey.

obstacles (i.e., at the corners of the area partially shadowed). Each relay points its directional antenna (antenna B) towards the closest anchor and its weak directional antenna (antenna A) towards the shadowed area. In Fig. 4.25, the antenna radiation patterns and orientations of anchors and relays are also depicted.[22]

An IEEE 802.15.4a [118] compliant UWB transmitted signal $s(t)$ is considered, with RRC pulses centered at frequency $f_0 = 4\,\text{GHz}$, roll-off factor $\eta = 0.6$, and pulse width parameter $\tau = 1\,\text{ns}$. The ranging packet is composed of $N_\text{s} = 512$ UWB pulses with PRP $T_\text{f} = 120\,\text{ns}$.

Each tag is equipped with an omnidirectional antenna (gain $G_\text{T} = 0\,\text{dBi}$), and

---

[22] The case study is performed in the 2D space for simplicity of discussion. Moreover only the antenna main polarization is considered and no polarization distribution within the channel is included.

transmits a power compliant with the emission limit of $-41.3\,\text{dBm/MHz}$ in the $3.2\div4.7\,\text{GHz}$ band.

Relays have the same gain (i.e., $G_l = G\ \forall l$). Anchors have a noise figure $F=4$ dB. Additive noise at relays should in principle be taken into account, which scales with $GF_{\text{R}}-1$. However, when received by an anchor, this power is attenuated by the path-loss between the anchor and the relay and in most practical cases the relay noise power received by an anchor is well below the anchor additive noise. Consequently, it is $N_{l,m} \ll N_0$ for $l \neq 0$, and thus they are not considered in the results.

The performance is obtained in different propagation conditions. In particular, three multipath propagation models are considered for the tag-anchor and tag-relay links. The first is a classical TDL channel model with an exponential PDP and a rms channel delay spread of $5\,\text{ns}$ [119, 120, 121]. The paths are separated of $1.5\,\text{ns}$ apart with a probability $b=0.7$ of path presence. Each path is subjected to Nakagami fading (severity factor $m=3$) except for the direct path that is deterministic according to the free-space path-loss model.[23] The second and third channel models are the IEEE 802.15.4a CM7 and CM3 for indoor industrial environments and for indoor office environments, respectively [118].

The coefficients $w(\mathbf{p}_1, \mathbf{p}_2)$ in (4.16) are modeled as

$$w(\mathbf{p}_1, \mathbf{p}_2) = \sqrt{\frac{1}{L(\mathbf{p}_1, \mathbf{p}_2)}} \tag{4.43}$$

where

$$L(\mathbf{p}_1, \mathbf{p}_2) = L_0 \left\|\mathbf{p}_1 - \mathbf{p}_2\right\|^{\beta} \Psi(\mathbf{p}_1, \mathbf{p}_2) \tag{4.44}$$

is the channel path-loss, β is the path-loss exponent, and L_0 is the path-loss at 1 meter. The term $\Psi(\mathbf{p}_1, \mathbf{p}_2)$ accounts comprehensively for antennas' radiation patterns. We consider $\beta = 2$ for the TDL channel model, while we consider the parameters reported in [118] for the 802.15.4a channels. An

---

[23] This seems an optimistic assumption since also the direct path is in general subject to fading. However, it has been shown that the direct path experiences a small variance with respect to an ideal propagation condition [122].

AWGN channel for relay-anchor links is assumed because of the high directivity of the relay antenna oriented to the anchor direction.

Performance metrics

Two different sets have been investigated: the first one considers the tag placed on a discrete grid ($N_\mathrm{p} = 1600$ with 50 cm step), while the second considers the tag uniformly distributed within the monitored area ($N_\mathrm{p} = 1000$ random tag's positions). To keep the simulation time affordable, the likelihood function maximization for position estimation is always performed in test positions located on the grid (discrete search) [123]. The first positions set allows the performance assessment by decoupling the results from the effect of the discrete search on the grid,[24] while the second set provides a more realistic simulation set up with tags not constrained in a fixed grid.

The localization performance is given in terms of estimated CDFs of the localization error, where the error accounts for both the random tag locations and the Monte Carlo iterations over channel realizations. Specifically, $M_\mathrm{c} = 100$ iterations are performed on each potential tag's position.

Results are provided considering a target error $e_\mathrm{th} = 50$ cm.

Localization performance is given in terms of LEO, defined as the rate at which the localization root mean square error (RMSE) is greater than a given target error e_th [124, 100] (i.e., the fraction of spatial test locations that do not fulfill a target error requirement), that is

$$\mathrm{CDF}(e_\mathrm{th}) = \frac{1}{N_\mathrm{p} M_\mathrm{c}} \sum_{n=1}^{N_\mathrm{p}} \sum_{m=1}^{M_\mathrm{c}} \mathbf{1}_{\mathbb{R}^-}(e_{n,m} - e_\mathrm{th}) \tag{4.45}$$

where we have defined the indicator function $\mathbf{1}_{\mathcal{A}}(x) = 1$ if $x \in \mathcal{A}$ and 0 otherwise, and $e_{n,m}$ is the output error in the nth test position for the mth Monte-Carlo iteration, that is $e_{n,m} = \|\hat{\mathbf{p}}_{n,m} - \mathbf{p}_n\|$ with $\hat{\mathbf{p}}_{n,m}$ the estimated

---

[24] Obviously, an improvement in the performance can be obtained considering a finer grid at the expense of higher simulation time [123].

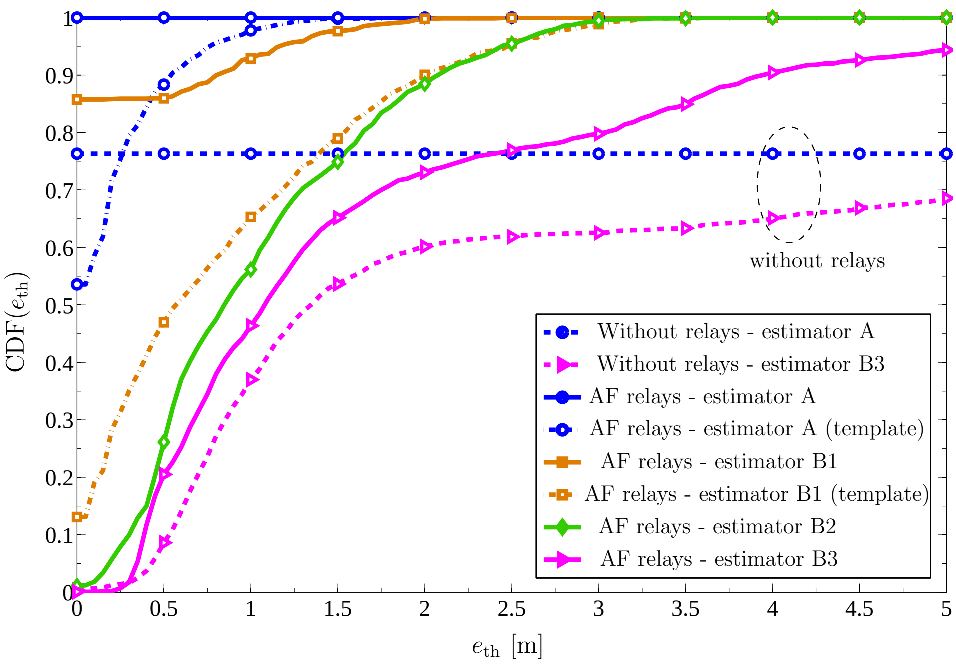

Figure 4.26: Estimated CDF using the TDL channel model for AF relays with $G = 10\,\text{dB}$.

location output of each simulation.

$$\text{CDF}(e_{\text{th}}) = \frac{1}{N_{\text{p}} M_{\text{c}}} \sum_{n=1}^{N_{\text{p}}} \sum_{m=1}^{M_{\text{c}}} \mathbf{1}(e_{\text{th}} - e_{n,m}) \tag{4.46}$$

where we have defined the unit step function $\mathbf{1}(x) = 1$ if $x \geq 0$ and 0 otherwise, and $e_{n,m}$ is the output error in the nth potential tag's position for the mth Monte-Carlo iteration, that is $e_{n,m} = \|\hat{\mathbf{p}}_{n,m} - \mathbf{p}_n\|$ with $\hat{\mathbf{p}}_{n,m}$ the estimated location output of each simulation.

The RMSE in the two-dimensional (2D) environment is also reported for selected configurations to show the spatial distribution of the error in the scenario. Localization RMSE $e_{\text{RMS}}(\mathbf{p}_n)$ in the nth potential tag's position is given by

$$e_{\text{RMS}}(\mathbf{p}_n) = \sqrt{\frac{1}{M_{\text{c}}} \sum_{m=1}^{M_{\text{c}}} \|\hat{\mathbf{p}}_{n,m} - \mathbf{p}_n\|^2}\,. \tag{4.47}$$

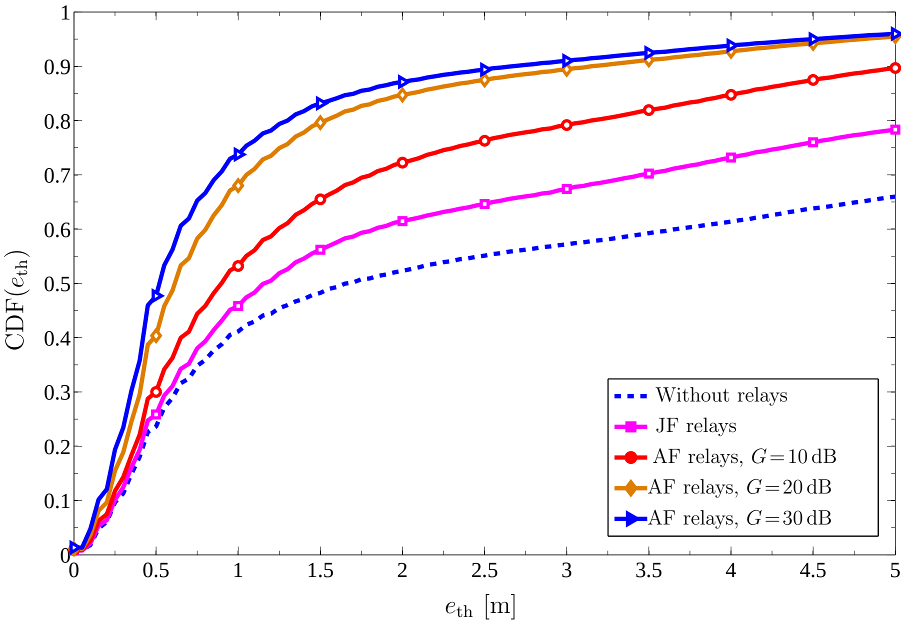

Figure 4.27: Estimated CDF for the IEEE 802.15.4a CM7 for different relays gain.

Simulation results

Figure 4.26 shows the estimated CDF of the localization error as function of a target error e_{th} for the TDL channel model with tags placed on the grid. Dashed lines refer to the absence of relays while continuous lines refer to the presence of AF relays with $G = 10\,\mathrm{dB}$. A performance benchmark in terms of area coverage is given by the estimator A, with perfect CSI. It can be seen that, in the absence of relays, 100% of coverage is not achievable because about 25% of the potential tag's positions are not in visibility of any anchor. Differently, by adopting relays the full localization coverage can be guarantee for any target position. In realistic cases where perfect CSI is not available, it is interesting to observe the performance of the same estimator A implemented according to a sub-optimal and more practical scheme which considers the template waveform at the receiver (indicated with "template") equal to the transmitted signal $s(t)$.[25] It can also be seen the performance of estimator B1 in (4.31) (for both perfect knowledge of the multipath structure

---

[25] This is equivalent to assume a filter matched to the first-path only, without taking advantage of the multipath energy.

and assuming only a template pulse for correlation), estimator B2 in (4.38), and estimator B3 in (4.42). Non-coherent estimators B2 and B3, based on energy detection, have been implemented considering $T_{\mathrm{p}} = 1.6\,\mathrm{ns}$, that is, the time window corresponding, approximately, to the main lobe of the pulse envelope. For comparison, the estimated CDF of the localization error in the absence of relays (i.e., $N_{\mathrm{r}} = 0$) is reported for estimator B3. As expected, the ML coherent estimator A offers the best performance, while estimator B3 (non-coherent TOA-based) is less powerful. In any case the use of relays allows a significant performance improvement with respect to the absence of relays.

In the following, we focus on estimator B3 more appealing for practical and low-complexity positioning solutions. Tags are uniformly distributed in the environment and the IEEE 802.15.4a channel models are considered. To collect some energy from the multipath components and to avoid ambiguities in the case the first path is not the strongest one, a wider integration time is considered. In general, T_{p} should be optimized based on the channel response and the SNR [125].[26] However this would drastically increase the receiver complexity since channel-dependent parameters and the SNR have to be estimated for each location. Therefore, we choose for T_{p} a value suitable for typical UWB channels, that is, close to the channel decay constant [118].

Figure 4.27 shows the CDF of the localization error considering estimator B3 in the IEEE 802.15.4a CM7 (industrial environment) with $T_{\mathrm{p}} = 8\,\mathrm{ns}$, for JF and AF relays with different gains G. It can be observed that the error decreases as G increases, thanks to the additional information carried out by the relayed signal replicas. It can also be observed that JF relays lead to a performance improvement with respect to the absence of relays. However, these results are not completely satisfactory in terms of localization accuracy. This is mainly due to the strong ambiguities (several peaks with close amplitude) that arise in the likelihood function and produce outliers in case of severe propagation conditions. In the following, we adopt an outliers reduction algorithm detailed in [34].

Figure 4.28 compares the results obtained for AF relaying with $G = 20\,\mathrm{dB}$

---

[26] Weighting techniques have been proposed in [126].

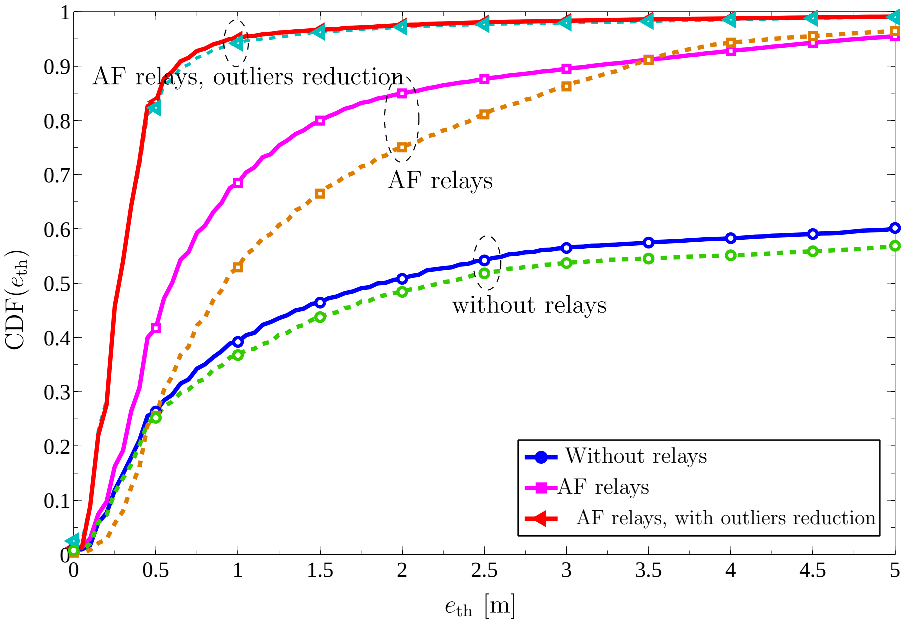

Figure 4.28: Estimated CDF for the IEEE 802.15.4a CM7 (continuous lines) and CM3 (dashed lines) for AF relays with $G = 20\,\mathrm{dB}$.

and for the IEEE 802.15.4a CM7 and CM3 channel models. The estimator B3 in (4.42), is considered with a fixed integration time $T_{\mathrm{p}} = 15\,\mathrm{ns}$ for the CM3 and $T_{\mathrm{p}} = 8\,\mathrm{ns}$ for the CM7, also in conjunction with the outliers reduction algorithm based on the TOA estimation of the first path. It can be observed that the outliers reduction algorithm significantly improves the performance; a localization error lower than 0.5 m in about 90% of the cases is obtained, which makes the relaying approach very appealing even when using simple non-coherent estimators. This improvement highlights how the outlier ambiguity effect in the likelihood function maximum search represents the main source of performance degradation that can be successfully overcome using the algorithm proposed.

Figures 4.29a and 4.29b plot the contour map of the spatial distribution of the localization RMSE in the 2D scenario, in the absence and presence of JF relays, respectively, considering the estimator B3 (energy-based) and the channel model IEEE 802.15.4a CM7. Note that, in the absence of relays, localization capability in the central area, shadowed by obstacles, results significantly degraded due to the lack of anchors visibility, with corresponding

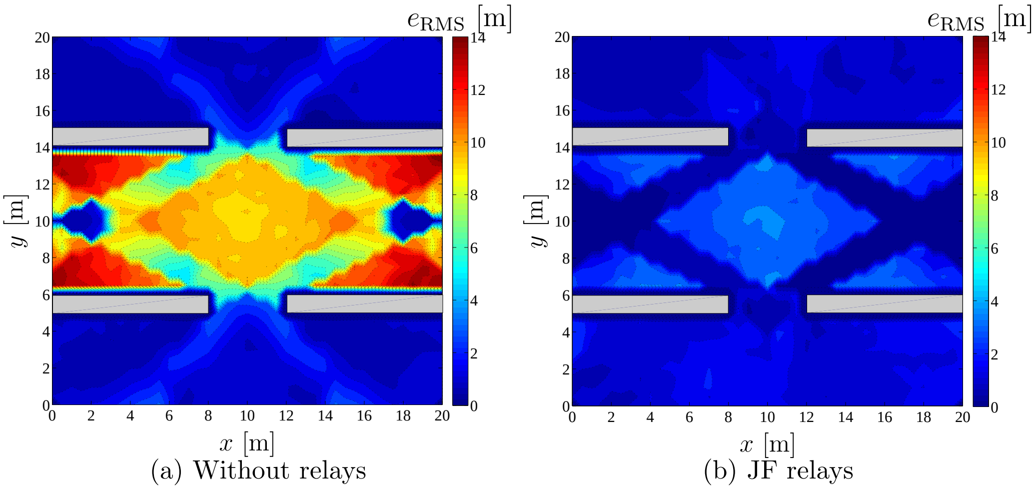

(a) Without relays (b) JF relays

Figure 4.29: RMSE contour map in the 2D environment for the IEEE 802.15.4a CM7.

errors of several meters. By exploiting non-regenerative JF relays, the system coverage in the shadowed areas is considerably extended, and the localization performance improved.

4.4 Conclusions

This chapter presents two different techniques that can be adopted in UWB RFID systems to enhance the localization coverage. Firstly the use of energy sprinklers for tags' detection and localization has been illustrated. Energy sprinklers offer the double functionality of being active transmitters and energy sources. This permits to shorten the two-hop link of traditional RFID configuration and enables the adoption of less expensive and green passive tags. Moreover, thanks to their low-cost and low-complexity, a large number of sprinklers can be disseminated in the environment improving the overall coverage. We have analysed the benefits of this system in terms of localization performance and coverage metrics: in particular, we have derived the theoretical localization bound and we have conducted a 3D coverage analysis adopting simulated radiation pattern for tags. Results show that the multistatic deployment of sprinklers lead to a significant localization performance enhancement and tag detection coverage extension with respect to classic monostatic configuration.

Secondly, to overcome the indoor propagation constraints the concept of non-regenerative relaying for network localization has been introduced as a low complexity approach to increase the service coverage in localization systems when the reduction of the number of anchors is desirable to simplify the network infrastructure. The adoption of UWB JF or AF relays, acting as virtual anchors, increases the number of received signal components that, thanks to a prior knowledge of relays' position, contribute in improving the localization capability in shadowed areas. Results have shown the effectiveness of the relaying technique for network localization, even using simple passive JF relays and low-complexity energy-based position estimators. Localization coverage enhancement through UWB non-regenerative relays is particularly attractive thanks to relays transparency to signals format, which allows the coexistence of different localization systems, and to the use of extremely low cost devices that do not require neither a communication infrastructure nor a power supply (in case of JF relays). This opens the way to a new design methodology for localization systems in severe propagation conditions, a methodology that facilitates the deployment and reduces cost and complexity of the network infrastructure.

Conclusions

The main topic investigated in this thesis is related to the enhancement of the mobile users knowledge of the indoor environment using *radiolocalization and mapping techniques* relying on different technologies. Given this broad objective, different applications have been analysed in order to have a complete overview of the problem. Among all, three of them have been a matter of study: the personal radar application where a mmW massive array maps the environment; a localization system using a single-AP equipped with a large number of antennas; and a UWB-RFID scenario using passive tags.

In this direction, Chapter 1 dealt with the main strengths and weaknesses of massive arrays operating at mmW frequencies. This study aimed at underlying which are the most important parameters to be considered in the array design. Specifically, with the perspective of adopting arrays for mapping and localization purposes, accurate beamforming/beamsteering, high ranging performance and angular resolution become essential requirements. However, a trade-off must be found between the possibility to realize mmW technologies that meet all these specifications and an acceptable array cost and structural complexity. In this chapter, the main sources of errors arising when a low-profile massive array is employed have been analysed in terms of beampointing error and beamwidth spread. The results of Chapter 1 have shown that when employing only phase shifters, the adoption of a high signal bandwidth has a detrimental effect on the pointing error but it increases the ranging accuracy. At the same time, quantization errors coming from the adoption of digital phase shifters slightly affect the scanning angle resolution and the pointing precision. As an example of real-existing massive arrays, TAs have been taken as a case of study and they have been employed in a mmW backscattering measurements campaign as a part of a bistatic radar system. This experimental part aimed at assessing the radar capability in indoor office environment using massive arrays with only 1-bit of phase compensation.

Chapter 2 has been dedicated to the personal radar concept. In particular, a personal radar is based on the idea of adopting a massive array operating at mmW frequencies in a smartphone or a tablet to enable mapping capabilities. To this aim, a new mapping algorithm has been proposed based on a non-coherent receiver scheme taking into account the antenna radiation characteristic and all the raw energy measurements collected. Differently from SLAM technologies where laser-based radars are often used, electronically beamsteering permits to scan the environment and to gather energy measurements from which RCS information could be retrieved. Results obtained for different indoor environments have demonstrated the feasibility of the idea and that a good level of map reconstruction can be achieved even when a reduced number of bits for phase compensation are adopted provided that a large number of antennas is employed. Stimulated by the simulation results obtained, the output of the mmW measurements campaign has been used to derive energy profiles to be processed by the mapping simulator. Considering only 1-bit for phase compensation, the results have shown that for different signal bandwidths the mapping performance are quite accurate. Future investigations will be focus on the refinement of the mapping algorithm considering different scattering regimes and a more realistic observation model.

Chapter 3 presented the idea of equipping not only portable devices but also APs with massive arrays for localization coverage enhancement. More precisely, we considered the possibility to retrieve mobile user position and orientation using a single AP acting as reference node. Different array structures were considered in the analysis: MIMO arrays exploiting signals orthogonality to increase the diversity gain and timed/phased arrays performing beamsteering operation to increase the array gain. The performance of such technologies has been evaluated through a Fisher information analysis by considering quantization errors, synchronization mismatch between the transmitter and the receiver and multipath propagation conditions. Specifically, the results of this chapter have shown that in orientation-aware scenarios, timed and phased arrays outperform the localization accuracy of MIMO arrays thanks the the SNR enhancement provided by the beamforming operation. Nevertheless, when planar array configuration is adopted timed and phased arrays are more sensitive to the orientation angle between the transmitter and the receiver. Moreover when operating at mmW frequencies, the localization performance of timed and phased arrays tend to coincide. Contrarily, in orientation-unaware situations, only the MIMO array results in a non-singular FIM matrix. This work could be extended in order to assess the ultimate performance of personal radars. To this end, different receiver schemes and backscattering communications will be accounted for.

Finally, Chapter 4 focused on the possibility to interact with tagged objects disseminated in the environment retrieving useful information from them. A UWB-RFID system has been considered to accomplish this task: different tags architectures have been shown to find the best compromise between the high ranging accuracy provided by the UWB signalling; the compatibility with previous tags generation technology; and energy autonomy. Passive communications are often adopted to lessen the complexity of tags design and their costs but they suffer from a poor link budget limitation that becomes more and more severe when considering UWB power emission constraints. To counteract this drawback, a multistatic RFID scenario has been investigated where transmitters and receivers are no more collocated in a monostatic configuration, but only 1 receiver and multiple simple transmitting entities are spread in the environment to localize and energize passive tags. Thanks to their simplicity, they could be deployed in a huge number in the environment augmenting the tags localization coverage while reducing the overall system cost. The results have proven the superior performance of this configuration in terms of LEO and detection coverage with respect to the monostatic case. Going a step ahead, in indoor scenarios, harsh propagation conditions could attenuate or completely block the signals exchange between readers and tags. To deal with this situation, non-regenerative relaying techniques were proposed to extend the tags lo-

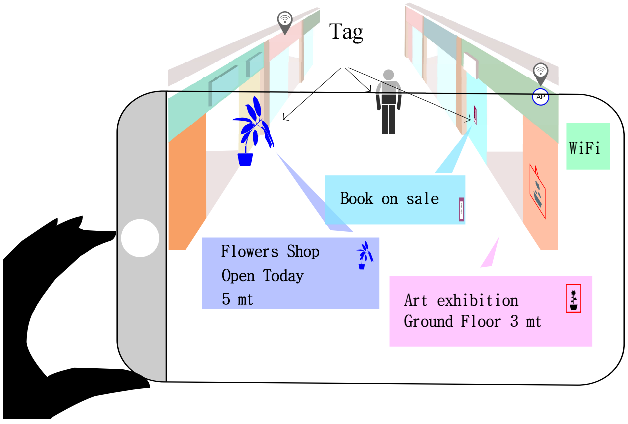

Figure 4.30: Envisioned future scenario: a user, with its own personal device, can interact with tagged objects placed in the surrounding environment.

calization coverage without relying on an increased number of reader nodes. An experimental study has been conducted to assign the best antenna radiation characteristics to each network nodes. The different UWB antenna radiation patterns evaluated through anechoic chamber measurements have been adopted in the localization simulator. The results have shown that the possibility to adopt non-regenerative relays could be a feasible solution to enhance the tags localization coverage even with simple receiver schemes working without any statistical channel prior knowledge available. Finally, future works will investigate cooperation techniques among tags as well as new RFID scenarios operating at mmW and adopting multi-antenna systems at reader side.

Future Perspectives

One of the key technology for future context-aware systems could be represented by mmW and, more in perspective, by the THz band. The incoming 5G smartphones will integrate mmW interfaces to boost the communication data rate beyond 1 Gbps. A part from the extremely large bandwidth available at such frequencies, which is beneficial for accurate positioning, mmW technologies offer also some other interesting opportunities. Thanks to the extremely narrow beam formed, the possibility to focus the power flux

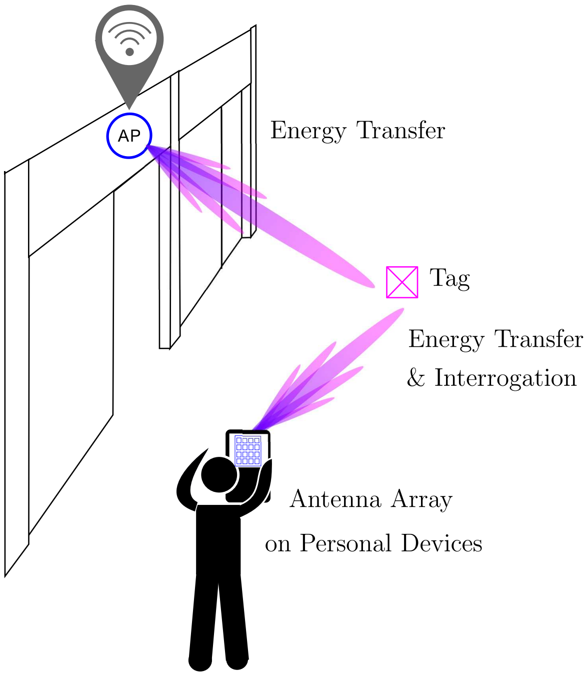

Figure 4.31: Energy transfer mechanism to energize passive tags using mmW/THz massive arrays.

towards the tag and transfer the energy at several meters will become possible with much higher efficiency than that achievable with today technology. Therefore there will be the possibility to energize, detect and localize tagged items using smartphones at several meters of distance enabling augmented reality applications (Fig. 4.30).

Moreover, no dedicated infrastructure would be required as large antenna arrays already used for communication could be employed as reference nodes with the advantage of permitting both accurate TOA and AOA estimations.

Another possible scenario is that in which access points deployed for indoor communications and equipped with mmW antenna arrays localize the tags present in the surrounding environment, and transfer the energy allowing the tag to accumulate the energy (e.g., during the night) so that they will be operative whenever a mobile device interrogates them, as shown in Fig. 4.31. Efficient and smart energy transfer together with high-performance energy accumulation (e.g., using supercap [127]) could open the possibility to exploit more efficient active communications (active tags) in place of backscatter communication.

In addition, as previously stated, tags will have to be eco-compatible and energy autonomous. In such context, the use of paper for the implementation of microwave components and systems is receiving an increasing attention, because paper is a cheap, renewable and biocompatible material. Among the available technologies for manufacturing and integration of microwave components, the substrate integrated waveguide (SIW) technique appears as a very promising candidate to satisfy the requirements of the future Internet of Things systems [128].

In conclusion the technological shift towards next-generation localization systems will require a significant research effort and synergy between different but tightly intertwined fields such as low-power electronics, antenna design, communication theory and signal processing.

Publications

Journal papers

- [J1] A. Guerra, F. Guidi , and D. Dardari: "Single-Anchor Position and Orientation Performance Limits using Millimeter-Wave Massive Arrays", *in preparation for submission*, 2015.
- [J2] F. Guidi, A. Guerra, A. Clemente, R. D'Errico and D. Dardari, "Joint Energy Detection and Massive Arrays Design for Localization and Mapping ", submitted to *IEEE Transactions on Wireless Communications*, March 2016.
- [J3] F. Guidi, A. Guerra, and D. Dardari: "Personal Mobile Radars with Millimeter-Wave Massive Arrays for Indoor Mapping ", *IEEE Transactions on Mobile Computing*, 2015.
- [J4] N. Decarli, A. Guerra, A. Conti, R. D'Errico, A. Sibille, and D. Dardari, "Non-Regenerative Relaying for Network Localization "*IEEE Transactions on Wireless Communications*, January 2014

Conference papers

- [C1] D. Dardari, N. Decarli, A. Guerra, F. Guidi, "The Future of Ultra-Wideband Localization in RFID ", accepted for presentation to *2016 IEEE International Conference on RFID*, IEEE RFID 2016, Orlando, Florida (invited paper).
- [C2] F. Guidi, A. Guerra, A. Clemente, R. D'Errico and D. Dardari, "Energy Detection Performance with Massive Arrays for Per-

sonal Radar Applications ", accepted for presentation to *11th International Conference on Cognitive Radio Oriented Wireless Networks 2016*, Crowncom 2016, Grenoble, France.

- [C3] A. Guerra, F. Guidi, A. Clemente, R. D'Errico and D. Dardari, "Delay Spread Characterization of Millimeter-Wave Indoor Backscattering Channel ", submitted to *IEEE European Conference on Antennas and Propagation*, EuCAP 2016, Davos, Switzerland.

- [C4] A. Guerra, F. Guidi, A. Clemente, R. D'Errico, L. Dussopt and D. Dardari, "Millimeter-wave Backscattering Measurements with Transmitarrays for Personal Radar Applications ", in *IEEE Globecom*, Globecom 2015, San Diego, CA, USA.

- [C5] N. Decarli, A. Guerra, F. Guidi, M. Chiani, D. Dardari, A. Costanzo, M. Fantuzzi, D. Masotti, S. Bartoletti, J. Shafiei Dehkordi, A. Conti, A. Romani, M. Tartagni, R. Alesii, P. Di Marco, F. Santucci, L. Roselli, M. Virili, P. Savazzi, and M. Bozzi, "The GRETA Architecture for Energy Efficient Radio Identification and Localization ", in *Proc. EURASIP RFID Workshop*, Rosenheim, Germany, Oct. 2015.

- [C6] S. Bartoletti, N. Decarli, A. Guerra, F. Guidi, D. Dardari, and A. Conti, "Energy-based order of arrival estimation via UWB-UHF RFID ", in *Proc. EURASIP RFID Workshop*, Rosenheim, Germany, Oct. 2015.

- [C7] A. Guerra, F. Guidi, A. Clemente, R. D'Errico, L. Dussopt, and D. Dardari, "Application of Transmitarray Antennas for Indoor Mapping at Millimeter-Waves ", in *IEEE European Conference on Networks and Communications*, EUCNC 2015, Paris, France.

- [C8] A. Guerra, F. Guidi, and D. Dardari, "Position and Orientation Error Bound for Wideband Massive Antenna Arrays ", in *IEEE International Conference on Communications*, ICC 2015, London, United Kingdom.

- [C9] A. Guerra, F. Guidi, and D. Dardari, “Millimeter-Wave Personal Radars for 3D Environment Mapping ”, in *IEEE Asilomar Conference on Signals, Systems, and Computers*, Asilomar, USA, 2014 (invited paper).

- [C10] A. Guerra, F. Guidi, and D. Dardari, “Energy sprinklers for passive UWB RFID ”in *IEEE International Conference on Ultra-Wideband*, ICUWB 2014, Paris, France, September 2014. **Best Student Paper Award**

- [C11] F. Guidi, A. Guerra, and D. Dardari, “Millimeter-wave massive arrays for indoor SLAM ”in *IEEE International Conference on Communications- Workshop ANLN*, ICC 2014, Sydney, Australia, June 2014.

- [C12] S. Bartoletti, N. Decarli, A. Guerra, F. Guidi, D. Dardari, and A. Conti, “Order of arrival estimation via UHF-UWB RFID ”in *IEEE International Conference on Communications- Workshop ANLN*, ICC 2014, Sydney, Australia, June 2014.

- [C13] D. Dardari, N. Decarli, A. Guerra, and A. Conti, Enhanced localization coverage with non-regenerative UWB relays”in *2012 Proceedings of the 20th European Signal Processing Conference (EUSIPCO)*, Bucharest, August 2012.

Technical Documents

- [D1] H2020 XCYCLE Deliverable 3.1: “Specification of in-vehicle and on-bicycle systems”, March 2016.

- [D2] PRIN GREen TAgs (GRETA) Deliverable 2: “Report on the First Year of Activity ”, April 2014.

- [D3] PRIN GREen TAgs (GRETA) Deliverable 1: “Reference Scenarios and Applications Requirements Definition”, July 2013.

- [D4] FP7 SELECT Deliverable 2.3.2: “Multi-functional network design: final system specification”, June 2012.

Acknowledgements

At the end of my PhD I would like to express my deepest gratitude and appreciation to all people who in different ways have guided and supported me in these years.

First of all, sincere thanks to my advisor, Prof. Davide Dardari; without his inspirational ideas, patience and guide this dissertation would not have been possible. His daily presence and humanity have allowed me to grow along the way, not only professionally, but also as a person. His encouragement to work hard with perseverance and dedication, even in research "difficulties", as well as to attend various conferences and training courses have instilled passion for this work. I always felt privileged to be your student.

I would also like to thank Dr. Raffaele D'Errico for welcoming and having hosted me twice at the CEA (Grenoble) and to be able to make the time spent with his research team rich of precious stimuli for my preparation. Thanks for having shared your thoughts and for the patience you have shown me, although sometimes I have tried to put it under test. Thank you for your accurate and timely suggestions in the thesis review, that have permitted to improve the work also in the final stage.

A special thank to Luc Vandendorpe for having reviewed the thesis and for all the insightful comments and suggestions that have helped in improving the quality of the manuscript.

Un grazie particolare a tutto il gruppo di telecomunicazioni di Cesena. Francesco, grazie per essere stato sempre presente, disponibile al dialogo e per avermi seguito e motivato in questi anni. Un grazie speciale a Nicoló che mi ha accompagnato dalla tesi di laurea a quella di dottorato e che oltre al lavoro, ha organizzato splendide escursioni che ci hanno unito sempre piú come gruppo. Grazie a Simone che ha iniziato e condiviso con me tutto il periodo del dottorato; la nostra amicizia si é via via rafforzata tra pause tisana e momenti yogici. Grazie a Ashraf e al suo continuo cercare la condivisione sui "misteri" della ricerca e della vita. Infine, un ringraziamento anche a tutti i docenti, Prof. Marco Chiani, Prof. Enrico Paolini, Prof. Andrea Giorgetti che mi hanno accompagnata durante il percorso universitario e a tutti i compagni di laboratorio, Mario, Matteo, Danilo, Roberto, Alex, Sara, Chiara, Andrea, Ahmed con i quali ho condiviso giornate di lavoro divertenti e allegre. Grazie a Vincenzo che trova sempre un minuto libero per chiamarmi e leggermi una storia. Grazie anche agli amici del treno con cui ho condiviso numerosi viaggi e racconti in questi anni.

Un remerciement á l'équipe du LAP (CEA) avec laquelle j'ai très bien travaillé grâce á l'accueil chaleureux, la complète disponibilité et la cordialité infinie dont vous m'avez fait part. Je me sens enrichie au niveau professionnel puisque j'ai pu profiter de vos excellentes compétences. Donc de tout cœur je vous remercie pour cette expérience merveilleuse que j'ai pu partager avec vous. Grazie agli amici italiani d'oltrealpe; Francesco, Luca e Lorenzo: é stato spassoso convidere Grenoble con voi. Un très grand merci à Lotfi avec qui j'ai partagé la période du stage et la thèse et qui a été toujours disponible et infiniment gentil. Un grazie di cuore a Antonio, il mio angelo custode al CEA!, per avermi accolto e aver trovato il tempo per consigliarmi e aiutarmi durante tutto il periodo francese.

Ultimo ma non meno importante, un grazie immenso alla mia famiglia per non avermi mai fatto mancare il proprio amore, sostegno morale e senza la quale nulla sarebbe stato possibile. Grazie nonni, mi avete sempre seguito nei miei spostamenti e guidato con il vostro esempio. Grazie Mamma e Papá per avermi sempre appoggiato in ogni scelta e aver minimizzato le mie difficoltá insormontabili. Grazie Matteo per le critiche costruttive e dissacranti che mi hai rivolto nel corso del tempo. E infine, grazie Alice per tutte le avventure che abbiamo passato insieme, le interminabili chiacchierate e per la grinta con cui affronti ogni cosa.

List of Figures

Bibliography

[1] C. Floerkemeier, M. Langheinrich, E. Fleisch, F. Mattern, and S. E. Sarma, *The Internet of Things.* Springer, 2008, vol. 4952.

[2] R. Di Taranto, S. Muppirisetty, R. Raulefs, D. Slock, T. Svensson, and H. Wymeersch, "Location-aware communications for 5G networks: How location information can improve scalability, latency, and robustness of 5G," *IEEE Signal Processing Mag.*, vol. 31, no. 6, pp. 102–112, Nov 2014.

[3] K. Witrisal, P. Meissner, E. Leitinger, Y. Shen, C. Gustafson, F. Tufvensson, K. Haneda, D. Dardari, A. F. Molisch, A. Conti, and Z. Moe, "High-accuracy localization for assisted living," *IEEE Signal Processing Mag.*, 2016.

[4] A. Guerra, F. Guidi, and D. Dardari, "Position and orientation error bound for wideband massive antenna arrays," in *Proc. IEEE Int. Conf. Commun. (ICC)*, June 2015.

[5] F. Guidi, A. Guerra, and D. Dardari, "Personal mobile radars with millimeter-wave massive arrays for indoor mapping," *IEEE Trans. Mobile Comp.*, vol. 14, no. 99, 2015.

[6] A. Guerra, F. Guidi, A. Clemente, R. D'Errico, L. Dussopt, and D. Dardari, "Application of transmitarray antennas for indoor mapping at millimeter-waves," in *Proc. IEEE European Conf. Networks and Commun. (EUCNC)*, 2015.

[7] ——, “Millimeter-wave backscattering measurements with transmitarrays for personal radar applications,” in *2015 IEEE Global Telecommun. Conf. (GLOBECOM 2015)*, 2015.

[8] K. Finkenzeller, *RFID Handbook: Radio-frequency identification fundamentals and applications.* Wiley, 1999.

[9] A. Costanzo, D. Masotti, T. Ussmueller, and R. Weigel, “Tag, you’re it: Ranging and finding via RFID technologies,” *IEEE Microwave Mag.*, vol. 14, no. 5, pp. 36–46, July 2013.

[10] P. V. Nikitin and K. S. Rao, “Theory and measurement of backscattering from RFID tags,” *IEEE Antennas Propagat. Mag.*, vol. 48, no. 6, pp. 212–218, 2006.

[11] F. Guidi, N. Decarli, S. Bartoletti, A. Conti, and D. Dardari, “Detection of multiple tags based on impulsive backscattered signals,” *IEEE Trans. Commun.*, vol. 62, no. 11, pp. 3918–3930, 2014.

[12] D. Dardari, F. Guidi, C. Roblin, and A. Sibille, “Ultra-wide bandwidth backscatter modulation: Processing schemes and performance,” *EURASIP J. Wireless Commun. and Networking*, vol. 2011, no. 1, pp. 1–15, 2011.

[13] F. Boccardi, R. Heath, A. Lozano, T. Marzetta, and P. Popovski, “Five disruptive technology directions for 5G,” *IEEE Commun. Mag.*, vol. 52, no. 2, pp. 74–80, Feb. 2014.

[14] T. Rappaport, R. J. Heath, R. C. Daniels, and J. N. Murdock, “Millimeter wave wireless communications.” Prentice Hall, 2014.

[15] R. Daniels and R. Heath, “60 GHz wireless communications: emerging requirements and design recommendations,” *IEEE Mag. Veh. Tech.*, vol. 2, no. 3, pp. 41–50, 2007.

[16] F. Giannetti, M. Luise, and R. Reggiannini, “Mobile and personal communications in 60 GHz band: A survey,” *Wireless Personal Commun.*, vol. 10, pp. 207–243, 1999.

[17] W. Hong, K.-H. Baek, Y. Lee, Y. Kim, and S.-T. Ko, "Study and prototyping of practically large-scale mmWave antenna systems for 5G cellular devices," *IEEE Commun. Mag.*, vol. 52, no. 9, pp. 63–69, 2014.

[18] H. Kaouach, L. Dussopt, J. Lantéri, T. Koleck, and R. Sauleau, "Wideband low-loss linear and circular polarization transmit-arrays in V-band," *IEEE Trans. Antennas and Propag.*, vol. 59, no. 7, pp. 2513–2523, 2011.

[19] A. Clemente, L. Dussopt, R. Sauleau, P. Potier, and P. Pouliguen, "Focal distance reduction of transmit-array antennas using multiple feeds," *IEEE Antennas and Wireless Propag. Lett.*, vol. 11, pp. 1311–1314, 2012.

[20] ——, "Wideband 400-element electronically reconfigurable transmitarray in X band," *IEEE Trans. Antennas and Propag.*, vol. 61, no. 10, pp. 5017–5027, 2013.

[21] A. Guerra, F. Guidi, and D. Dardari, "Millimeter-wave personal radars for 3D environment mapping," in *Proc. IEEE Asilomar Conf. Signals, Syst. and Comput.*, Pacific Grove, USA, Nov. 2014.

[22] R. J. Mailloux, "Phased array antenna handbook," *Boston, MA: Artech House, 1994.*, 1994.

[23] http://www.selectwireless.eu/.

[24] http://www.greentags.eu/.

[25] N. Decarli, F. Guidi, and D. Dardari, "A novel joint RFID and radar sensor network for passive localization: Design and performance bounds," *IEEE J. Sel. Topics Signal Process.*, vol. 8, no. 1, pp. 80–95, 2014.

[26] D. Dardari, R. D. Errico, C. Roblin, A. Sibille, and M. Z. Win, "Ultrawide bandwidth RFID: The next generation?" *Proc. IEEE*, vol. 98, no. 9, pp. 1570–1582, 2010.

[27] R. Verdone, D. Dardari, G. Mazzini, and A. Conti, *Wireless sensor and actuator networks: technologies, analysis and design.* Academic Press, 2010.

[28] M. Z. Win and R. A. Scholtz, "Impulse radio: How it works," *IEEE Commun. Lett.*, vol. 2, no. 2, pp. 36–38, 1998.

[29] S. Gezici, Z. Tian, G. B. Giannakis, H. Kobayashi, A. F. Molisch, H. V. Poor, and Z. Sahinoglu, "Localization via ultra-wideband radios: a look at positioning aspects for future sensor networks," *IEEE Signal Processing Mag.*, vol. 22, no. 4, pp. 70–84, 2005.

[30] D. Dardari, A. Conti, U. Ferner, A. Giorgetti, and M. Z. Win, "Ranging with ultrawide bandwidth signals in multipath environments," *Proc. IEEE*, vol. 97, no. 2, pp. 404–426, 2009.

[31] M. Z. Win, D. Dardari, A. F. Molisch, W. Wiesbeck, and J. Zhang, "History and applications of UWB," *Proc. IEEE*, vol. 97, no. 2, pp. 198–204, 2009.

[32] A. Guerra, N. Decarli, F. Guidi, and D. Dardari, "Energy sprinklers for passive UWB RFID," in *2014 IEEE Int. Conf. Ultra-WideBand (ICUWB).* IEEE, 2014, pp. 356–361.

[33] R. D'Errico, M. Bottazzi, F. Natali, E. Savioli, S. Bartoletti, A. Conti, D. Dardari, N. Decarli, F. Guidi, F. Dehmas *et al.*, "An UWB-UHF semi-passive RFID system for localization and tracking applications," in *2012 IEEE Int. Conf. on RFID-Technologies and Applications (RFID-TA).* IEEE, 2012, pp. 18–23.

[34] N. Decarli, A. Guerra, A. Conti, R. D'Errico, A. Sibille, and D. Dardari, "Non-regenerative relaying for network localization," *IEEE Trans. Wireless Commun.*, vol. 13, no. 1, pp. 174–185, 2014.

[35] C. A. Balanis, *Antenna theory: analysis and design.* John Wiley & Sons, 2005, vol. 1.

[36] J. Huang and J. Encinar, “Reflectarray antennas, by institute of electrical and electronics engineers,” 2008.

[37] A. Clemente, L. Dussopt, R. Sauleau, P. Potier, and P. Pouliguen, “Multiple feed transmit-array antennas with reduced focal distance,” in *2012 42nd European Microwave Conf. (EuMC)*. IEEE, 2012, pp. 826–829.

[38] L. Di Palma, A. Clemente, L. Dussopt, R. Sauleau, P. Potier, and P. Pouliguen, “Circularly polarized transmit-array with sequentially rotated elements in Ka band,” in *2014 8th European Conf. on Antennas and Prop. (EuCAP),*. IEEE, 2014, pp. 1418–1422.

[39] J. Y. Lau and S. V. Hum, “Reconfigurable transmitarray design approaches for beamforming applications,” *IEEE Trans. Antennas and Propag.*, vol. 60, no. 12, pp. 5679–5689, 2012.

[40] P. Padilla, A. Muñoz-Acevedo, M. Sierra-Castañer, and M. Sierra-Pérez, “Electronically reconfigurable transmitarray at Ku band for microwave applications,” *IEEE Trans. Antennas and Propag.*, vol. 58, no. 8, pp. 2571–2579, 2010.

[41] L. Di Palma, A. Clemente, L. Dussopt, R. Sauleau, P. Potier, and P. Pouliguen, “1-bit unit-cell for transmitarray applications in Ka-band,” in *EuCAP 2015*.

[42] C.-C. Cheng, A. Abbaspour-Tamijani, and B. Lakshminarayanan, “Reconfigurable lens-array with monolithically integrated MEMS switches,” in *38th European Microwave Conf., 2008. EuMC 2008.* IEEE, 2008, pp. 112–115.

[43] J. D. Krieger, C.-P. Yeang, and G. W. Wornell, “Dense delta-sigma phased arrays,” *IEEE Trans. Antennas and Propag.*, vol. 61, no. 4, pp. 1825–1837, 2013.

[44] L. Rondinelli, "Effects of random errors on the performance of antenna arrays of many elements," in *1958 IRE Int. Conv. Record*, vol. 7. IEEE, 1966, pp. 174–189.

[45] W. Wagner, "Radiometric calibration of small-footprint full-waveform airborne laser scanner measurements: Basic physical concepts," *ISPRS J. Photogrammetry and Remote Sensing*, vol. 65, no. 6, pp. 505–513, 2010.

[46] K. Sarabandi, E. S. Li, and A. Nashashibi, "Modeling and measurements of scattering from road surfaces at millimeter-wave frequencies," *IEEE Trans. Antennas and Propag.*, vol. 45, no. 11, pp. 1679–1688, 1997.

[47] V. Degli-Esposti, F. Fuschini, E. M. Vitucci, and G. Falciasecca, "Measurement and modelling of scattering from buildings," *IEEE Trans. Antennas and Propag.*, vol. 55, no. 1, pp. 143–153, 2007.

[48] L. M. Correia and P. O. Françês, "Estimation of materials characteristics from power measurements at 60 Ghz," in *5th IEEE Int. Symp. on Personal, Indoor and Mobile Radio Commun., 1994. Wireless Networks-Catching the Mobile Future.* IEEE, 1994, pp. 510–513.

[49] FCC, "Revision of Part 15 of the Commissions Rules Regarding Operation in the 57-64 GHz Band. August 2013."

[50] J. A. Zevallos Luna and L. Dussopt, "A V-band switched-beam transmit-array antenna," *Int. J. Microwave and Wireless Technol.*, vol. 6, no. 01, pp. 51–56, 2014.

[51] K. Haneda, J. Jarvelainen, A. Karttunen, M. Kyro, and J. Putkonen, "A statistical spatio-temporal radio channel model for large indoor environments at 60 and 70 ghz," *IEEE Transactions on Antennas and Propagation,*, vol. 63, no. 6, pp. 2694–2704, 2015.

[52] P. F. Smulders, "Statistical characterization of 60-GHz indoor radio channels," *IEEE Trans. Antennas and Propag.*, vol. 57, no. 10, pp. 2820–2829, 2009.

[53] R. S. Elliot, *Antenna theory and design.* John Wiley & Sons, 2006.

[54] http://robotics.ccny.cuny.edu/web/.

[55] W. Morris, I. Dryanovski, J. Xiao *et al.*, "3D indoor mapping for micro-uavs using hybrid range finders and multi-volume occupancy grids," in *RSS 2010 workshop on RGB-D: Advanced Reasoning with Depth Cameras, Zaragoza, Spain*, 2010.

[56] H. Whyte and T. Baliey, "Simultaneous localization and mapping (slam) part 1 the essential algorithms," *IEEE Robot. Automat. Mag.*, 2006.

[57] http://www.openstreetmap.org/.

[58] K. Zheng, M. Li, and H. Jiang, "Mobile and ubiquitous systems: Computing, networking, and services."

[59] M. Alzantot and M. Youssef, "Crowdinside: automatic construction of indoor floorplans," in *Proc. of the 20th Int. Conf. on Advances in Geographic Information Systems.* ACM, 2012, pp. 99–108.

[60] A. Rai, K. K. Chintalapudi, V. N. Padmanabhan, and R. Sen, "Zee: zero-effort crowdsourcing for indoor localization," in *Proc.s of the 18th annual Int. Conf. on Mobile Computing and Networking.* ACM, 2012, pp. 293–304.

[61] R. Faragher, C. Sarno, and M. Newman, "Opportunistic radio SLAM for indoor navigation using smartphone sensors," in *2012 IEEE/ION Position Location and Navigation Symposium (PLANS).* IEEE, 2012, pp. 120–128.

[62] M. Dissanayake, P. Newman, S. Clark, H. F. Durrant-Whyte, and M. Csorba, “A solution to the simultaneous localization and map building (SLAM) problem,” *IEEE Trans. Robot. Automat.*, vol. 17, no. 3, pp. 229–241, 2001.

[63] E. Jose and M. D. Adam, “Relative RADAR cross section based feature identification with millimeter wave RADAR for outdoor SLAM,” in *2004 IEEE/RSJ Int. Conf. on Intelligent Robots and Systems (IROS 2004)*, vol. 1. IEEE, 2004, pp. 425–430.

[64] E. Jose and M. D. Adams, “An augmented state SLAM formulation for multiple line-of-sight features with millimetre wave radar,” in *2005 IEEE/RSJ Int. Conf. on Intelligent Robots and Systems (IROS 2005).* IEEE, 2005, pp. 3087–3092.

[65] E. Jose, M. Adams, J. S. Mullane, and N. M. Patrikalakis, “Predicting millimeter wave radar spectra for autonomous navigation,” *IEEE Sensors J.*, vol. 10, no. 5, pp. 960–971, 2010.

[66] C. Wu, Z. Yang, and Y. Liu, “Smartphones based crowdsourcing for indoor localization,” *IEEE Trans. Mobile Computing*, vol. 14, no. 2, pp. 444–457, 2015.

[67] https://www.google.com/atap/projecttango/.

[68] J. Ruze, “The effect of aperture errors on the antenna radiation pattern,” *Il Nuovo Cimento (1943-1954)*, vol. 9, pp. 364–380, 1952.

[69] D. Dardari, P. Closas, and P. M. Djuric, “Indoor tracking: Theory, methods, and technologies,” *IEEE Trans. Veh. Technol.*, vol. 64, no. 4, pp. 1263–1278, 2015.

[70] H. Urkowitz, “Energy detection of unknown deterministic signals,” *Proc. IEEE*, vol. 55, no. 4, pp. 523–531, 1967.

[71] K. M. Wurm, C. Stachniss, and G. Grisetti, “Bridging the gap between feature-and grid-based SLAM,” *Robotics and Autonomous Systems*, vol. 58, no. 2, pp. 140–148, 2010.

[72] O. Ozisik and S. Yavuz, “An occupancy grid based SLAM method,” in *IEEE Int. Conf. on Computational Intelligence for Measurement Systems and Applications (CIMSA 2008).* IEEE, 2008, pp. 117–119.

[73] S. Y. Chun and A. Shapiro, “Normal versus noncentral chi-square asymptotics of misspecified models,” *Multivariate Behavioral Research*, vol. 44, no. 6, pp. 803–827, 2009.

[74] J. Xiong and K. Jamieson, “Arraytrack: A fine-grained indoor location system.” in *NSDI*, 2013, pp. 71–84.

[75] “5G: A Technology Vision.” [Online]. Available: http://www.huawei.com/5gwhitepaper/

[76] D. Dardari, E. Falletti, and M. Luise, *Satellite and terrestrial radio positioning techniques: a signal processing perspective.* Academic Press, 2011.

[77] S. Mohammad Razavizadeh, M. Ahn, and I. Lee, “Three-dimensional beamforming: A new enabling technology for 5G wireless networks,” *IEEE Signal Processing Mag.*, vol. 31, no. 6, pp. 94–101, 2014.

[78] Y. Shen and M. Z. Win, “Fundamental limits of wideband localization-part i: A general framework,” *IEEE Trans. Inf. Theory*, vol. 56, no. 10, pp. 4956–4980, 2010.

[79] H. Godrich, A. M. Haimovich, and H. V. Poor, “An analysis of phase synchronization mismatch sensitivity for coherent mimo radar systems,” in *2009 3rd IEEE Int. Workshop on Computational Adv. in Multi-Sensor Adaptive Process. (CAMSAP).* IEEE, 2009, pp. 153–156.

[80] M. Pardini, F. Lombardini, and F. Gini, “The hybrid cramér–rao bound on broadside DOA estimation of extended sources in presence of array errors,” *IEEE Trans. Signal Process.*, vol. 56, no. 4, pp. 1726–1730, 2008.

[81] A. Mallat and L. Vandendorpe, “Joint estimation of the time delay and the clock drift and offset using UWB signals,” in *2014 IEEE Int. Conf. on Commun. (ICC)*. IEEE, 2014, pp. 5474–5480.

[82] ——, “CRBs for the joint estimation of TOA and AOA in wideband MISO and MIMO systems: comparison with SISO and SIMO systems,” in *IEEE International Conference on Communications, 2009. ICC’09.* IEEE, 2009, pp. 1–6.

[83] Y. Shen, H. Wymeersch, and M. Z. Win, “Fundamental limits of wideband localizationpart ii: Cooperative networks,” *IEEE Trans. Inf. Theory*, vol. 56, no. 10, pp. 4981–5000, 2010.

[84] Y. Han, H. Meng, Y. Shen, and X. Zhang, “Performance Limits and Geometric Properties of Narrowband Array Localization,” *arXiv preprint arXiv:1405.4372*, 2014.

[85] A. G. Amigo, P. Closas, A. Mallat, and L. Vandendorpe, “Cramér-rao bound analysis of UWB based localization approaches,” in *2014 IEEE Int. Conf. on Ultra-WideBand (ICUWB)*. IEEE, 2014, pp. 13–18.

[86] J. Li and P. Stoica, “MIMO radar with colocated antennas,” *IEEE Signal Processing Mag.*, vol. 24, no. 5, pp. 106–114, 2007.

[87] E. Fishler, A. Haimovich, R. S. Blum, L. J. Cimini Jr, D. Chizhik, R. Valenzuela *et al.*, “Spatial diversity in radars-models and detection performance,” *IEEE Trans. Signal Process.*, vol. 54, no. 3, pp. 823–838, 2006.

[88] A. Hassanien, S. Vorobyov *et al.*, “Phased-MIMO radar: A tradeoff between phased-array and MIMO radars,” *IEEE Trans. Signal Process.*, vol. 58, no. 6, pp. 3137–3151, 2010.

[89] F. C. Robey, S. Coutts, D. Weikle, J. C. McHarg, and K. Cuomo, “MIMO radar theory and experimental results,” in *Conf. Rec. of the Thirty-Eighth Asilomar Conf. on Signals, Syst. and Comput., 2004*, vol. 1. IEEE, 2004, pp. 300–304.

[90] Q. He, R. S. Blum, H. Godrich, and A. M. Haimovich, “Target velocity estimation and antenna placement for mimo radar with widely separated antennas,” *IEEE J. Sel. Topics Signal Process.*, vol. 4, no. 1, pp. 79–100, 2010.

[91] A. M. Haimovich, R. S. Blum, and L. J. Cimini, “Mimo radar with widely separated antennas,” *IEEE Signal Processing Mag.*, vol. 25, no. 1, pp. 116–129, 2008.

[92] K. Witrisal and P. Meissner, “Performance bounds for multipath-assisted indoor navigation and tracking (mint),” in *2012 IEEE Int. Conf. on Commun. (ICC).* IEEE, 2012, pp. 4321–4325.

[93] H. L. Van Trees, *Detection, estimation, and modulation theory.* John Wiley & Sons, 2004.

[94] G. E. Garcia, W. Hu, W. P. Tay, and H. Wymeersch, “Joint scheduling and localization in uwb networks,” in *2015 IEEE Int. Conf. Commun. Workshop (ICCW).* IEEE, 2015, pp. 724–729.

[95] C. Floerkemeier, M. Langheinrich, E. Fleisch, F. Mattern, and S. E. Sarma, *The Internet of Things: First International Conference, IOT 2008, Zurich, Switzerland, March 26-28, 2008, Proceedings.* Springer, 2008, vol. 4952.

[96] J. Zheng, D. Simplot-Ryl, C. Bisdikian, and H. T. Mouftah, “The internet of things [guest editorial],” *IEEE Commun. Mag.*, vol. 49, no. 11, pp. 30–31, 2011.

[97] H. Soganci, S. Gezici, and H. V. Poor, “Accurate positioning in ultra-wideband systems,” *IEEE Wireless Commun.*, vol. 18, no. 2, pp. 19–27, 2011.

[98] J. Kimionis, A. Bletsas, and J. N. Sahalos, “Increased range bistatic scatter radio,” *IEEE Trans. Commun.*, vol. 62, no. 3, pp. 1091–1104, 2014.

[99] M. Z. Win, A. Conti, S. Mazuelas, Y. Shen, W. M. Gifford, D. Dardari, and M. Chiani, "Network localization and navigation via cooperation," *IEEE Commun. Mag.*, vol. 49, no. 5, pp. 56–62, 2011.

[100] A. Conti, M. Guerra, D. Dardari, N. Decarli, and M. Z. Win, "Network experimentation for cooperative localization," *IEEE J. Sel. Areas Commun.*, vol. 30, no. 2, pp. 467–475, 2012.

[101] F. Guidi, N. Decarli, D. Dardari, C. Roblin, and A. Sibille, "Performance of UWB backscatter modulation in multi-tag RFID scenario using experimental data," in *2011 IEEE Int. Conf. on Ultra-Wideband (ICUWB).* IEEE, 2011, pp. 484–488.

[102] E. Paolini, A. Giorgetti, M. Chiani, R. Minutolo, and M. Montanari, "Localization capability of cooperative anti-intruder radar systems," *EURASIP J. Adv. Signal Process.*, vol. 2008, no. 1, p. 726854, 2008.

[103] M. Malanowski and K. Kulpa, "Two methods for target localization in multistatic passive radar," *IEEE Trans. Aerosp. and Electron. Syst.*, vol. 48, no. 1, pp. 572–580, 2012.

[104] E. Savioli, M. Bottazzi, F. Natali, N. Decarli, F. Guidi, N. Hadaschik, R. D'Errico, and L. Ouvry, "Semi-passive UHF-UWB RFID: Architecture and localization performance," in *2013 IEEE Int. Conf. Commun. Workshops (ICC)*, 2013.

[105] R. Pabst, B. H. Walke, D. C. Schultz, P. Herhold, H. Yanikomeroglu, S. Mukherjee, H. Viswanathan, M. Lott, W. Zirwas, M. Dohler *et al.*, "Relay-based deployment concepts for wireless and mobile broadband radio," *IEEE Commun. Mag.*, vol. 42, no. 9, pp. 80–89, 2004.

[106] Z. Sahinoglu, "Method and system for target positioning and tracking in cooperative relay networks," Sep. 4 2012, uS Patent 8,259,699.

[107] L. W. Fullerton, M. D. Roberts, K. Loum, I. Dodoukh, S. S. O'Hanian *et al.*, "Method and system for extensible position location," Oct. 13 2009, uS Patent 7,602,339.

[108] C. Villien and D. Norbert, "Systeme de radiolocalisation/posionment au moyen d'un resau ad hoc," France Patent 2 924 818/ 07 59 611, Jun. 12, 2009.

[109] M. Rydström, E. G. Ström, A. Svensson, and L. Reggiani, "An algorithm for positioning relays and point scatterers in wireless systems," *IEEE Signal Process. Lett.*, vol. 15, pp. 381–384, 2008.

[110] L. Reggiani, M. Rydström, G. Tiberi, E. G. Ström, and A. Monorchio, "Ultra-wide band sensor networks for tracking point scatterers or relays," in *6th Int. Symp. Wireless Commun. Syst. (ISWCS 2009)*. IEEE, 2009, pp. 1–5.

[111] Y. Huang, N. Yi, and X. Zhu, "Investigation of using passive repeaters for indoor radio coverage improvement," in *IEEE Antennas and Propag. Soc. Int. Symp., 2004.*, vol. 2. IEEE, 2004, pp. 1623–1626.

[112] G. Chiurco, M. Mazzotti, F. Zabini, D. Dardari, and O. Andrisano, "Fpga design and performance evaluation of a pulse-based echo canceller for DVB-T/H," *IEEE Trans. Broad.*, vol. 58, no. 4, pp. 660–668, 2012.

[113] M. Nakagawa, "UWB repeater with pulse delay and UWB communication system," U.S. Patent US 7,359,673 B2, Apr. 15, 2008.

[114] P. C. Pinto, A. Giorgetti, M. Z. Win, and M. Chiani, "A stochastic geometry approach to coexistence in heterogeneous wireless networks," *Selected Areas in Communications, IEEE Journal on*, vol. 27, no. 7, pp. 1268–1282, 2009.

[115] A. Rabbachin, T. Q. Quek, H. Shin, and M. Z. Win, "Cognitive network interference," *IEEE J. Sel. Areas Commun.*, vol. 29, no. 2, pp. 480–493, 2011.

[116] M. Steven, "Fundamentals of statistical processing: Estimation theory," *Prectice Hall*, 1993.

[117] R. A. Horn and C. R. Johnson, *Matrix analysis.* Cambridge university press, 2012.

[118] A. F. Molisch, K. Balakrishnan, D. Cassioli, C.-C. Chong, S. Emami, A. Fort, J. Karedal, J. Kunisch, H. Schantz, U. Schuster *et al.*, "Ieee 802.15. 4a channel model-final report," *IEEE P802*, vol. 15, no. 04, p. 0662, 2004.

[119] D. Cassioli, M. Z. Win, and A. F. Molisch, "The ultra-wide bandwidth indoor channel: from statistical model to simulations," *IEEE J. Sel. Areas Commun.*, vol. 20, no. 6, pp. 1247–1257, 2002.

[120] T. Q. Quek and M. Z. Win, "Analysis of UWB transmitted-reference communication systems in dense multipath channels," *IEEE J. Sel. Areas Commun.*, vol. 23, no. 9, pp. 1863–1874, 2005.

[121] T. Q. Quek, D. Dardari, and M. Z. Win, "Energy efficiency of dense wireless sensor networks: To cooperate or not to cooperate," *IEEE J. Sel. Areas Commun.*, vol. 25, no. 2, pp. 459–470, 2007.

[122] B. Dewberry and W. Beeler, "Increased ranging capacity using ultrawideband direct-path pulse signal strength with dynamic recalibration," in *2012 IEEE/ION Position Location and Nav. Symp. (PLANS).* IEEE, 2012, pp. 1013–1017.

[123] D. Dardari and A. Conti, "A sub-optimal hierarchical maximum likelihood algorithm for collaborative localization in ad-hoc network," in *2004 First Annual IEEE Commun. Soc. Conf. Sensor and Ad Hoc Commun. and Networks, 2004.* IEEE, 2004, pp. 425–429.

[124] D. B. Jourdan, D. Dardari, and M. Z. Win, "Position error bound for UWB localization in dense cluttered environments," *IEEE Trans. Aerosp. Electron. Syst.*, vol. 44, no. 2, pp. 613–628, 2008.

[125] N. Decarli, A. Giorgetti, D. Dardari, and M. Chiani, "Blind integration time determination for uwb transmitted reference receivers," in *2011*

IEEE Global Telecommun. Conf. (GLOBECOM 2011). IEEE, 2011, pp. 1–5.

[126] F. Wang, Z. Tian, and B. M. Sadler, “Weighted energy detection for noncoherent ultra-wideband receiver design,” *IEEE Trans. Wireless Commun.*, vol. 10, no. 2, pp. 710–720, 2011.

[127] S. Sudevalayam and P. Kulkarni, “Energy harvesting sensor nodes: Survey and implications,” *IEEE Communications Surveys & Tutorials,*, vol. 13, no. 3, pp. 443–461, 2011.

[128] S. Moscato, N. Delmonte, L. Silvestri, M. Pasian, M. Bozzi, and L. Perregrini, “Compact substrate integrated waveguide (SIW) components on paper substrate,” in *2015 European Microwave Conference (EuMC).* IEEE, 2015, pp. 24–27.